Synthesis of Metal-Oxide Monoliths and Metallic Nanoparticles: Applications in Sustainable Development

Thesis Submitted

By

Manisha Sharma

(Regd. No. 901409012)

In Fulfilment of the Requirement for the degree of

Doctor of Philosophy

Under the supervision of

Dr. Soumen Basu

(Associate Professor)

SCHOOL OF CHEMISTRY AND BIOCHEMISTRY

THAPAR UNIVERSITY

PATIALA-147004

PUNJAB, INDIA

August 2017

Certificate

*This is to certify that the thesis entitled "**Synthesis of Metal-Oxide Monoliths and Metallic Nanoparticles: Applications in Sustainable Development**" being submitted by Ms. Manisha Sharma in fulfilment of the requirement for the award of the Degree of Doctor of Philosophy in the School of Chemistry and Biochemistry, Thapar University, Patiala, is a record of candidate's own independent and original research work carried out by her under supervision my supervision and guidance. The material embodied in thesis has not been submitted in part or full to any other University or Institute for the award of any degree.*

(Supervisor)

Dr. Soumen Basu

Associate Professor

School of Chemistry and Biochemistry

Thapar University, Patiala-147004

Punjab (India)

Candidate's Declaration

*I hereby declare that the present work in the thesis entitled "**Synthesis of Metal-Oxide Monoliths and Metallic Nanoparticles: Applications in Sustainable Development**" in the fulfilment of the requirement for the award of the Degree of Doctor of Philosophy in the School of Chemistry and Biochemistry, Thapar University, Patiala, is authentic record of my own work carried out under the supervision of Dr. Soumen Basu, Associate Professor, School of Chemistry and Biochemistry, Thapar University, Patiala, India. The material embodied in thesis has not been submitted in part or full to any other University or Institute for the award of any degree in India or Abroad.*

Manisha Sharma

(Supervisor)

Dr. Soumen Basu

Associate Professor

School of Chemistry and Biochemistry

Thapar University, Patiala-147004

Punjab (India)

Acknowledgements

I devotedly thank the Almighty for providing me the potency to persist on the path to success.

A statement of thanks is not evident to inculcate my deep sense of gratitude and obligation to all those who helped me in one way or another in completion of thesis. I would like to take this opportunity to thank many people who helped and encouraged me throughout this research.

First and foremost, I would like to thank my Parents (Mother, Mrs. Kanta Dev and Father, Mr. Saurp Singh Sharma), Siblings (Brother, Mr. Jagpravesh Sharma and Sister, Mrs. Nisha Sharma) without their love and support over the years none of this would have been possible. They have been there for me and I am thankful for everything they have helped me achieve. My special thanks to my Fiancé, Mr. Chaitanya Gangwar who has always encouraged and supported me in every aspect.

Next, I would like to thanks to my research supervisor, ***Dr. Soumen Basu****, Associate Professor, School of Chemistry and Biochemistry, for his valuable supervision, scholar inputs and consistent encouragement throughout the research work. He always made a point of available to clarify my doubts despite his busy schedules and I consider it as a great opportunity to do my doctoral programme under his guidance and to learn from his research expertise. His guidance was of paramount importance in providing a well-rounded understanding of my research for long term career goals.*

I gratefully acknowledge the DAE-BRNS, Mumbai, India, for providing me fellowship for the year of research.

I am also thankful to my doctoral committee members ***Dr. Amjad Ali, Dr. Satnam Singh and Dr. B. N. Chudasama*** *for their encouragement, constructive criticism and inspirations.*

Many thanks to all the faculty members of School of Chemistry and Biochemistry, Thapar University, Patiala for providing necessary guidance during my research work. I am also thankful to Mr. Chandar Thakur and Mr. Mayank Sharma, School of Chemistry and Biochemistry for the constant official help and cooperation.

I would like to extend my thank to SAI Labs, Thapar University, Patiala and sprint Testing for analysis of prepared samples.

Special thanks to seniors Dr. Richa Goel, Mr. Rayees Ahmad, Dr. Akul Sen Gupta, Mr. Yuvraj, Ms. Suraksha, Ms. purnima and Ms. Tanushree Basu who have extended their support in a very special way. I gained a lot from them, through their personal and scholarly interactions, their suggestions at various points in my research programme.

I am also thankful to my lab mates and friends Mrs. Ruhi, Ms. Jyoti Sharma, Ms. Richa Bansal, Ms. Sehaspreet Kaur, Mrs. Akansha Sachdeva, Ms. Shagun Kainth, Mr. Amit Mishra, Mr. Iqbal Brar, Mr. Jasminder Singh and Ms. Ramandeep Kaur for always standing by my side and sharing a great relationship as compassionate friends. I will always cherish the warmth shown by them, whose smiling faces always inspired me.

Besides this, I am thankful to the persons who knowingly and unknowingly helped me during the successful completion of this work.

Manisha.

Manisha Sharma

Table of Content

List of Figures

Chapter -4

Chapter -5

List of Tables

List of Abbreviations

NPs	Nanoparticles
4-NP	4-nitrophenol
4-AP	4-aminophenol
Pb(II)	Lead ions
Cd(II)	Cadmium ions
TRIX	Triton X-100
FA	Furfuryl alcohol
OA	Oxalic acid
CAC	Critical aggregation concentration
SDAs	Structure directing agents
BET	Brunner– Emmett– turner
BJH	Barrett–Joyner–Halenda
XRD	X-ray diffraction analysis
SEM	Scanning electron microscopy
TEM	Transmission electron microscopy
FTIR	Fourier Transmission Infrared
UV-Vis	UV-Visible
DLS	Dynamic Light Scattering
XPS	X-ray photo- electron spectroscopy
AAS	Atomic adsorption spectrophotometer
IC_{50}	Half maximum inhibitory concentration
EDS	Energy Dispersive X-ray Spectroscopy
TEOS	Tetraethoxysilane
PEG	Poly ethylene glycol
C_{12}TAB	Dodecyltrimethylammonium bromide
C_{14}TAB	Tetradecyltrimethylammonium bromide
C_{16}TAB	Cetyltrimethylammonium bromide

C_{18}TAB	Octadecyltrimethylammonium bromide
BTMAC	Benzyltrimethylammonium chloride
TMB	1,3,5-trimethylbenzene
SDS	Sodium dodecyl sulphate
ml	Milliliter
mg	Milligram
a.u.	Arbitrary Unit
T	Temperature
ΔH	Enthalpy
ΔS	Entropy
ΔG	Gibbs free energy
K	Kelvin
TOF	Turnover frequency

List of Publications

1. **Manisha Sharma**, Satyajit Hazra, Soumen Basu, "ZnO@SiO_2 Monolithic System as Adsorbent for Removal of Toxic Pollutants from Aqueous Solution" *Journal of Colloid and Interface Sciences* 504, **2017**, 669–679. (IF=4.233)

2. **Manisha Sharma**, Diptiman Choudhary, Satyajit Hazra and Soumen Basu, "Effective Removal of Metal Ions by Enlarged MnO_2 and TiO_2 Monoliths with Tuneable Mesopore Size: Kinetic and Equilibrium Modelling" *Journal of Alloys and Compounds,* 720, **2017** 221- 229. (IF=3.133)

3. **Manisha Sharma**, Pallavi Jain, Amit Mishra, Akansha Mehta, Diptiman Choudhary, Satyajit Hazra and Soumen Basu, "Variation of Surface Properties of Silica Monoliths by Controlling Ionic Character/Chain Length of Surfactants and Polymers" *Material Letters,* 194, **2017**, 213–216. (IF=2.572)

4. Amit Mishra, Akansha Mehta, **Manisha Sharma**, Soumen Basu, "Enhanced heterogeneous photodegradation of VOC and dye using microwave synthesized TiO_2/Clay nanocomposites: A comparison study of different type of clays" *Journal of Alloys and Compounds* 694, **2017**, 574-580. (IF=3.133)

5. **Manisha Sharma**, Amit Mishra, Akansha Mehta, Diptiman Choudhury, Soumen Basu, "Effect of Surfactants on the Structure and Adsorption Efficiency of Hydroxyapatite Nanorods" *Journal of Nanoscience and Nanotechnology* **2017** (**In press**). (IF=1.556)

6. Jyoti Sharma, **Manisha Sharma**, Soumen Basu, "Mesoporous MgO Nanostructures Using Cat-anionic Surfactants: Enhanced Adsorption and Antimicrobial activity" *Journal of Environmental Chemical Engineering* 5, 2017, 3429-3438. (IF=)

7. Amit Mishra, Akansha Mehta, **Manisha Sharma**, Soumen Basu, "Impact of Ag nanoparticles on photomineralization of chlorobenzene by TiO2/bentonite nanocomposites" *Journal of Environmental Chemical Engineering* 5 (2017) 644–651. (IF=)

8. **Manisha Sharma**, Amit Mishra, Akansha Mehta, Diptiman Choudhury, Soumen Basu, "Enhanced catalytic and antibacterial activity of nanocasted mesoporous silver monoliths: kinetic and thermodynamic studies" *J Sol-Gel Sci Technol*, 81, **2016**, 704. (IF=1.660)

9. **Manisha Sharma**, Amit Mishra, Vinod Kumar, Soumen Basu, "Green Synthesis of Silver Nanoparticles with Exceptional Colloidal Stability and its Catalytic Activity towards Nitrophenol Reduction" *NANO*, 11(4), **2016**, 1-10. (IF=1.11)

10. Akansha Mehta, Amit Mishra, **Manisha Sharma**, Soumen Basu, "Effect of silica/titania ratio on enhanced photooxidation of industrial hazardous materials by microwave treated mesoporous SBA-15/TiO_2 nanocomposites" *J Nanopart Res* 18, **2016**, 209. (IF=2.278)

11. Amit Mishra, **Manisha Sharma**, Akansha Mehta, Soumen Basu, "Microwave Treated Bentonite Clay Based TiO_2 Composites: An Efficient Photocatalyst for Rapid Degradation of Methylene Blue" *Journal of Nanoscience and Nanotechnology*, 16, **2016**, 1-7. (IF=1.556)

12. **Manisha Sharma**, Satyajit Hazra, Soumen Basu, "Synthesis of Heterogeneous Ag-Cu Bimetallic Monolith with Different Mass Ratios and Their Performance for Catalysis and Antibacterial Activity" (Communicated).

13. **Manisha Sharma**, Satyajit Hazra, Soumen Basu, "Removal of Heavy Metal Ions from Aqueous Solution using Mesoporous ZnO and TiO_2@ZnO Monoliths: Adsorption and Kinetic Studies" (Communicated)

14. Vanshita Goel, **Manisha Sharma**, Pawandeep Kaur, Soumen Basu, Diptiman Choudhury, "pH modulated green synthesis of silver nanoparticles for its antibacterial and catalytic activity" (Communicated)

15. Love Dashairya, **Manisha Sharma**, Soumen Basu, Partha Saha, "Enhanced Dye Degradation using Hydrothermally Synthesized Nanostructured Sb_2S_3/rGO Under Visible Light Irradiation" (Communicated)

16. **Manisha Sharma**, Jasminder Singh, Satyajit Hazra and Soumen Basu, "Remediation of Heavy Metal Ions from Water Using Microporous Carbon Monolith Synthesis via Nanocasting Method" (communicated)

17. **Manisha Sharma**, Soumen Basu, "Co-SiO_2 monolithic system as an efficient catalyst for synthesis of benzimidazole and its derivatives" (Manuscript under preparation)

18. **Manisha Sharma,** Iqbal brar, Kamaldeep Paul, Soumen Basu, "High catalytic performance of Pd-SiO_2 monoliths for Suzuki coupling reaction" (Manuscript under preparation)

19. **Manisha Sharma** Satyajit Hazra, Soumen Basu, "Pb(II) and Cd(II) adsorption by Fe-Ni monoliths derived from sol-gel method." (Manuscript under preparation)

Conferences and Workshops

1. Presented poster in *2nd Conference on Microscopy in Material Science* (AMST-2016) held at Thapar University, Patiala during Feburary 25-27, 2016.

2. Presented poster in *International conference on Nanoscience and Technology* (ICONSAT-2016) organised by IISER Pune, India from 29th February to 2nd March 2016.

3. Presented oral presentation in *International Conference on Recent Advances in Emerging Technologies* (ICRAET-2016) held at Shri Guru Granth Sahib World University, Fatehgarh Sahib.

4. Participated in National Workshop on *Advanced Techniques for surface Characterization* held at Thapar University, Patiala from October 28 – 30, 2015.

Abstract

Mesoporous metal/metal-oxides are of great interest in such application as photocatalytic degradation, catalysis, adsorption and separation, fuel cells and batteries. Mesoporous materials can be synthesized via soft templating and hard templating process. Out of them nanocasting method in hard template process, provides a sacrificial template as a monolithic replica. These replicated monoliths contain ordered micro/ meso/ macropores with high surface area, which allow adsorption and reduction of pollutants present in water.

Chapter 1: This chapter includes a brief discussion about hierarchically porous materials, e.g. monoliths. Green approach for the synthesis of metal nanoparticles along with mesoporous materials synthesized via hard template (nanocasting) process has also been presented in detail. Some selected applications for sustainable development by metal or metal-oxide nanostructures have been reported which is relevant with other chapters of the thesis.

Chapter 2: In this Chapter, to achieve maximum pore diameter and surface area of porous silica monoliths different structure directing agents (SDAs) (Cationic/ anionic/ neutral/ mixture) were used. BET study showed alteration of SDA's chain length, composition or concentration have a cumulative effect on controlling the surface area and pore size. PEG in combination with other SDAs like CTAB, SDS, BTMAC, Triton-X100 etc. controlled internal agglomeration along with particles size. The maximum amount of surface area was observed by using maximum chain length of PEG and CTAB.

Chapter 3 Section - A: In this chapter, ordered hierarchically porous silica (by sol-gel method) and metal-oxide monoliths (through nanocasting method) were synthesized. Porous silica and metal oxide monoliths (MnO_2 and TiO_2) exhibited excellent adsorption for heavy metal ions such as Pb(II) & Cd(II). The morphological and structural study of the synthesized silica and metal oxide monoliths were done by FESEM and XRD analysis. The adsorption studies were conducted in different batches. The maximum adsorption of Pb(II) on SiO_2, MnO_2 and TiO_2 varied from 91-125, 166-200 and 769-857 mg/g respectively depending upon the choice of PEG, which is used as a structure directing/controlling agent. Similarly, the maximum adsorption of Cd(II) on SiO_2, MnO_2 and TiO_2 varied from 90-100, 100-125 and 667-770 mg/g respectively. The effects of

contact time (0-80 min), temperature (at 303, 313 and 323 K) and pH (3-10) on the Pb(II) & Cd(II) removal were also explored.

Section - B: Up till now, the excessive and unconstrained release of Pb(II) and Cd(II) ions in water becomes a foremost concern by way of threatening human health seriously. Therefore, for removal of Pb(II) and Cd(II) ions from waste water, adsorbent with high efficacy and low cost technologies is most needed to alleviate the situation. In this Chapter, robust, mesoporous ZnO & TiO_2@ZnO monoliths with specific surface area (120-332 mg^2/g) were synthesized via nanocasting process and their performance as an adsorbent for removal of Pb(II) and Cd(II) ions from water was successfully evaluated. The adsorption data shows better fit at pH 6 to Freundlich isotherm model. Applicability of pseudo-second order kinetic model specifies the chemisorption process. Thermodynamic parameters confirmed that removal of Pb(II) and Cd(II) ions was endothermic process. The maximum adsorption efficacy of Pb(II) ions based on monolayer adsorption was found to be 909 and 1250 mg/L for ZnO and TiO_2@ZnO monoliths, respectively whereas the maximum adsorption efficacy of Cd(II) ions based on monolayer adsorption was found to be 833 and 1000 mg/L for ZnO and TiO_2@ZnO monoliths respectively. Besides, used mesoporous ZnO & TiO_2@ZnO monoliths could be efficiently reused for at least three times after treatment with NaOH. The high uptake capacity for Pb(II) and Cd(II) ions with good reusability of ZnO & TiO_2@ZnO monoliths made them a potentially attractive adsorbent.

Section - C: Novel innovation regarding synthesis of most promising and robust adsorbent to purify water has been developed as a great concern among the most promising fields. Many adsorbents based on carbon material have been explored worldwide due to high surface area, high chemical stability, and compact structure and appropriate for bulk production. Here, carbon monoliths (CM) with micro/ mesopore have been synthesized via nanocasting method, using silica monoliths as solid template. On the micrometer scale, synthesized CMs are considered as positive replica of parent silica monolith. CMs with high surface area (1103 m^2/g) is tested first time as adsorbent for removal of Pb(II) and Cd(II) ions from aqueous solution. Also, through batch experiments various effective and applicable parameters were successfully studied for instance pH, contact time, adsorbate/ adsorbent concentration, temperature etc. The maximum monolayer adsorption efficiency for Pb(II) and Cd(II) ions is 1128 mg/g and 989 mg/g, respectively. Kinetic data for the adsorption process shows best fit to pseudo second order.

Chapter 4: Removal of toxic effluents (like dyes and pesticides) by cost effective and user-friendly method is needed to provide sustaining the environment for civilization. Here, low-cost mesoporous silica monolith (SiO_2) and silica supported metal-oxide ($ZnO@SiO_2$) monolith were synthesized to reduce the solemn impact of toxic effluents. Batch experiments were performed to remove Alizarin (AZ), Paradol (PD), Acid blue-113 (AB) and Rhodamine-B (RD) from aqueous water via synthesized monoliths. The influence of various parameters (like pH, contact time, temperature and adsorbate concentration) has been optimized. The maximum adsorption capacity of $ZnO@SiO_2$ monolith is 625, 500, 714.2 and 555.5 mg/g for AZ, PD, AB, and RD respectively. The adsorption for AZ, PD, AB, and RD is spontaneous and exothermic. The adsorption process can be well described by the pseudo-second-order kinetic model (high regression coefficients) and the Freundlich isotherm model (R^2 = 0.97‑0.99).

Chapter 5 Section - A: In this chapter, silver nanoparticles were synthesized by one-step process in the presence of kollicoat as capping, reducing and stabilizing mediator. The synthesized nanoparticles were characterized by using FTIR, TEM, DLS, XRD, EDS, and UV-vis spectroscopy. The resulted silver nanoparticles were having an incomparable colloidal stability against the salt addition and change of pH. The effect of different synthesis parameters and the catalytic property of the nanoparticles were examined.

Section - B: Use of low-cost renewable catalysts is essential for effective removal of a chemical contaminant like 4-nitrophenol (4-NP) from water bodies. In the present study, for the first time use of surface enhanced (14 m^2/g) nanocasted mesoporous silver monolith (AgM) through impregnation into silica monoliths (prepared by sol-gel method) has been demonstrated for its catalytic and antibacterial activity. Highly efficient catalytic reduction rate (2.43 min^{-1}) of 4-NP to 4- aminophenol (4-AP) was demonstrated using 0.2 g L^{-1} of AgM. Enhancement of reduction rate also observed with increase in temperature (from 25-40 °C). Removal of microbial contamination from drinking water is also a prime concern for water purification. Mesoporous AgM showed effective antimicrobial activity against gram negative (*E. coli*) and gram positive (*B. subtilis*) with IC_{50} values of 75.86 ± 0.173 and 74.56 ± 0.103 respectively at 24 h of incubation.

Section - C: Combination of two or more metallic particles along with high surface area and porous structure exhibits enhanced catalytic as well as antibacterial activity. Here, Ag-Cu bimetallic monoliths were synthesized by nanocasting method by strictly adjusting the molar ratio

of Ag-Cu. This work is mainly focused on the effect of molar ratio (Ag:Cu) on surface area (14-110 m^2/g) and porous size of bimetallic monoliths, which has great influence on enhancement of catalytic and antimicrobial activity. The catalytic activity of bimetallic Ag-Cu monoliths was evaluated for the reduction of 4-nitrophenol (4-NP) to 4-aminophenol (4-AP) in the presence of excess $NaBH_4$. The reaction rate follows pseudo-first order for reduction of 4-NP with a reduction efficacy of ~95%. In comparison with pristine Ag monometallic monoliths, bimetallic Ag-Cu monoliths exhibit high catalytic performance on the reduction of 4-NP. These heterogeneous catalysts were effortlessly recovered and reused (upto 8 cycles) after completion of catalytic reaction. As bimetallic Ag-Cu particles are well-known for antibacterial activity, so bactericidal properties of synthesized monoliths are tested against *E. coli* and *B. subtilis* bacteria by minimum inhibitory concentration method (MIC). The calculated EC_{50} (half maximum effective concentration) after 24 h of incubation, against *E. coli* and *B. subtilis* were 22.87 ± 0.015 and 23.33 ± 0.09 respectively using Ag/Cu-3 bimetallic monolith.

Chapter-1

Introduction, Literature Review and Scope of work

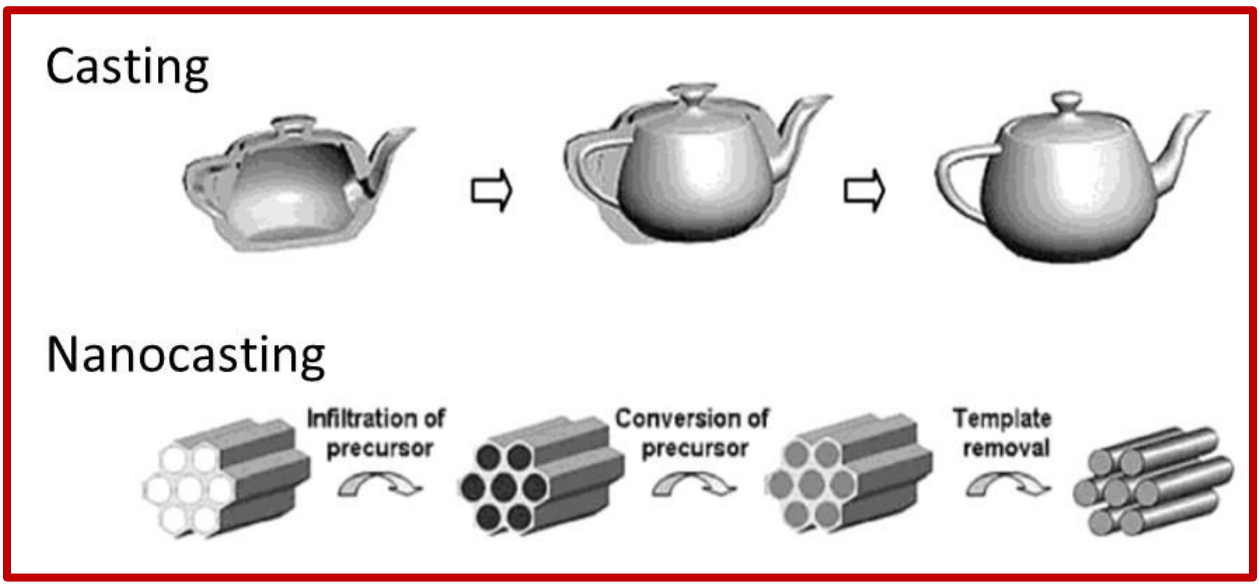

This chapter includes a brief discussion about hierarchically porous materials, e.g. monoliths. Green approach for the synthesis of metal nanoparticles along with mesoporous materials synthesized via hard template (nanocasting) process has also been presented in detail. Some selected applications for sustainable development by metal or metal-oxide nanostructures have been reported which is relevant with other chapters of the thesis.

1.1 Introduction to nanoscience and nanotechnology

Nanoscience and nanotechnology are recent, innovatory development in science and engineering that are evolving at a very fast pace. It is driven by the desire to fabricate materials with novel and improved properties that are likely to impact virtually all areas of the physical and chemical sciences, biological sciences, and health sciences. Nanomaterials are usually considered to be materials with at least one external dimension that measures 100 nanometers or less. They may be in the form of particles, tubes, rods or fibres[1].

1.2 Metallic nanomaterials

Metallic nanoparticles are of great interest in both technology and research, due to their certain properties not available in insulated molecules or bulk metals. Due to these properties, metal nanoparticles have many important applications in sensing, imaging, and catalysis[2]. Out of other metallic nanoparticles, silver nanoparticles (Ag NPs) are considered as one of the main remarkable materials because of its exceptional properties such as chemical stability, good conductivity, catalysis and antimicrobial activity[3]. These properties of Ag NPs acutely depend on their size and morphology. Several studies have made (Table 1.1) to know the size, stability, morphology and (chemical and physical) properties of the Ag NPs, which are strongly influenced by the experimental condition, the kinetics of contact of silver ions with reducing agents, and adsorption process of stabilizing agent with Ag NPs[4].

Table 1.1: Silver nanoparticles with different shapes reported in the literature.

Polymer used	Shape	Size/properties	References
PVA	Octahedral	The largest side has 33.33 nm length and shortest 27.77 nm length	[7]
PEG	Sphere	Average diameters of the particles were found to be 10 - 25 nm	[8]
PVP	Cube	Self-assembled nanocubes were obtained	[9]
$NaBH_4$/SDS	Sphere	Particle diameter ranges from 30 to 40 nm)	[10]

1.3 Porous materials

The porous material is a solid substance with interconnected pores (voids). Due to the interconnection between pores or voids, various atoms, molecules, and ions are able to interact among themselves at the surface as well in the bulk of material[5]. As a result, they exhibit potential applications in the area of catalysis, ion exchange, adsorption, pollutant remediation, sensors, drug delivery systems, bactericides etc. Different porous substances are clays, bones, rocks, ceramics, metal-oxides and carbonaceous material. Out of them, massive porous stone or rocks like structures are considered as monoliths. According to IUPAC classification, porous materials can be described as materials that have porosity across several length scales, including micropores (<2 nm), mesopores (2-50 nm), and/or macropores (> 50 nm). Among various porous material, silica and silica based solids have been chosen for extensive research as the internal chemistry of silica offers a flexible state that allows a better control of mesostructures[6].

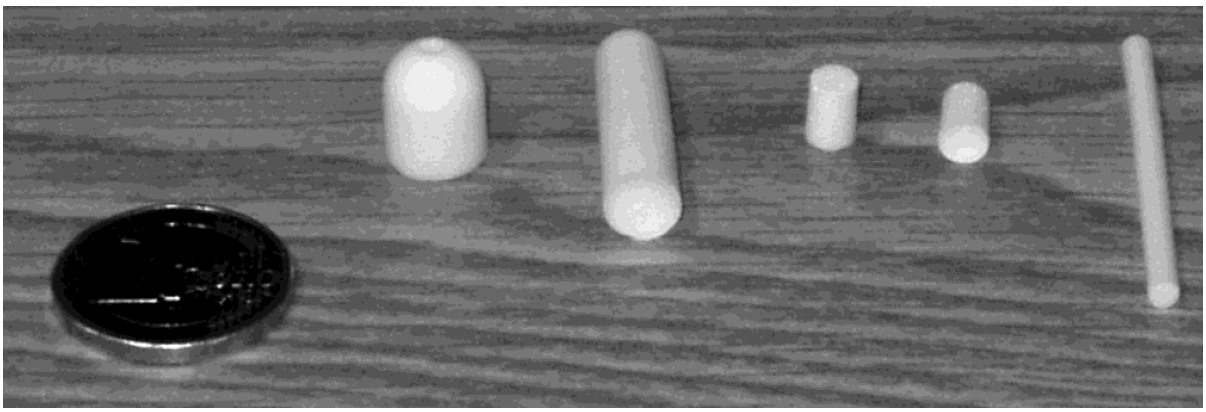

Fig. 1.1: Photograph of silica monoliths of different shapes (diameter of the coin is 23 mm).

1.3.1 Historical background of monolithic system

Mesoporous silica based material was discovered by two research groups in the USA and in Japan at the same time in the early 90s. These two groups succeeded in the synthesis of this new material by ensuing two different routes but with common silica source and surfactant (alkylammonium) as structuring and self-assembling agents for silica[11]. Silica was synthesized in alkaline medium (in which silica is normally soluble) along with the low concentration of surfactant and as a result, unexpectedly first hexagonal silica mesophase material was formed

(Fig 1.1). Structure directing agents (amphiphilic polymer and different surfactant molecules) and experimental conditions were recognized as a way to control pore size and geometry of synthesized silica monoliths[12].

1.3.2 Hard templating or nanocasting process

Ordered silica based mesoporous materials are amorphous in nature. Through silica based mesoporous materials, synthesis of non-siliceous ordered mesoporous solids can be achieved by using templating approaches. Hard templating or nanocasting is an extension of the traditional casting process down to the nanometer scale. During the nanocasting process, a liquid precursor is introduced into the micrometer or nanometer size pores. The liquid precursor then undergoes a chemical conversion to the desired end product (Scheme 1.1). With the exception of the carbon nanocasting process, there is normally a drastic volume reduction during this conversion, with the final product only occupying 6-12% of that of the precursor solution. Due to this volume reduction, repeated infiltrations with the precursor solution are required if complete pore filling is desired[13]. Since then, there have been many reports of nanocasting into mesoporous silica templates. The most common metal precursor used is the nitrate salt due to its high solubility.

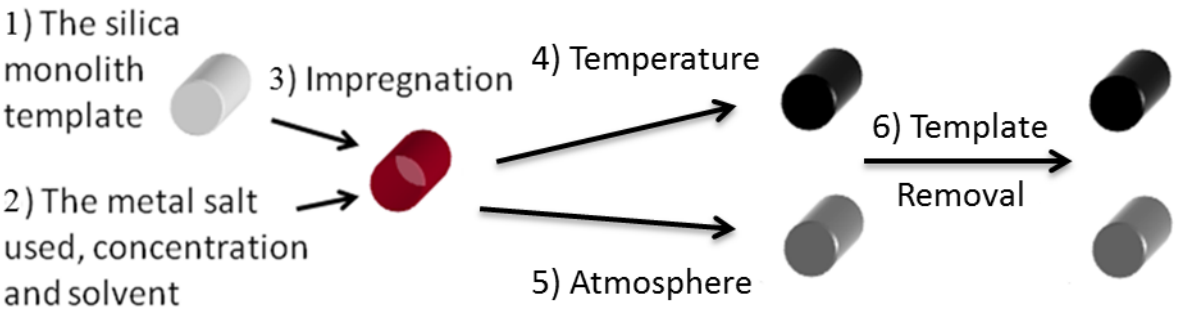

Scheme 1.1: Schematic representation of nanocasting process.

Table 1.2: Based on literature various metal-oxide monoliths synthesized using nanocasting.

Support	Synthesis method	Metal-oxide monolith	Surface area (m^2/g)	Gaps	References
Silica monoliths	Nanocasting route	Co_3O_4, SnO_2, MnO_2 and Mn_2O_3		Alteration in pore size of monoliths has not been explored so far	[5]
Silica monoliths	Impregnation	α-Fe_2O_3, ZrO_2, Nickel and silver	65.3 84 10.7 17.9	Change in surface area and pore size of synthesized monoliths has not been done	[14]
SBA-15 and KIT-6	Impregnation	Co_3O_4, NiO, CeO_2, and Cr_2O_3	-	Not worked on the surface area of monoliths	[15]
Silica templates	Impregnation	cerium oxides	198	Adsorption of pollutants and metal ions has not been done along with the change in pore size of monoliths	[16]
Silica monoliths	Nanocasted using chemical vapor depostion	Carbon	1090	Change in pore size of synthesized monoliths has not been done by changing the chain length of polymer/surfactant along with the adsorption experiments for metal ions	[17]
1-butyl-3-methylimidazolium tetrafluoroborate ($BMIM^+BF_4^-$)	Sol-gel method with a peptization process	TiO_2	118-498	Change in pore size of synthesized monoliths has not been done by changing the chain length of polymer/surfactant	[18]
SBA-15 and KIT-6	Nanocasting route	Ferrihydrite	222	Modulation in pore size of monoliths has not been done	[19]

1.3 Adsorption of toxic pollutants

Toxic pollutants containing metal ions, dyes and pesticides need to be treated before being delivered to the environment due to their toxic and carcinogenic effects on the living system including human beings by causing skin irritations, allergies etc.[20-22]. Among several physical or chemical methods, adsorption process can be used as a conventional method as it is utmost effective, cost effective, eco-friendly and easy to use. Adsorption method is tested as one alternative effective process without chemical degradation of solid adsorbents used for toxic pollutant removal from water. Some advantages like high efficiency, most effective, sludge free, insensitivity to toxic material made adsorption techniques most apt to work[23]. Numerous adsorbents like zeolites, metal oxides, clays, functionalized polymers, activated carbons, etc. have been well-known and verified for the adsorption of heavy metal ions[24]. Nowadays, metal-oxide based nanomaterials are considered as suitable material for water treatment.

MnO_2 loaded D301 resin were synthesized to check its removal capacity for cadmium at the wide range of pH 3–8. Langmuir adsorption was best fitted and obtained maximum adsorption efficacy was 77.88 mg/g for Cd(II)[25]. Adsorption mechanism for adsorption of Hg (II) and Pb (II) ions were analyzed using as prepared nanoTPFR. The kinetic study shows that adsorption mechanism follows pseudo second order[26]. Amine functionalized SBA-15 was synthesized via grafting and co-condensation technique. Amine grafted SBA-15 showed a significant amount of adsorption efficacy for Cu(II), Cd(II), Pb(II), Ni(II) and Zn(II) in aqueous solution in comparison to SBA prepared via co-condensation method[27]. Fe_2O_3–ZnO–$ZnFe_2O_4$/C were prepared as adsorbents for the removal of BPB dye from aqueous solution. The adsorption process was analyzed by equilibrium kinetic and isotherm models[28]. Mesoporous ZnO–SnO_2 mixed oxide nanoparticles were used to remove completely malachite green oxalate (MGO) and hexavalent chromium (Cr) from contaminated water[29]. The MnO_2-loaded resin had been used as an adsorbent for lead and cadmium removal and the maximum removal efficiency was calculated as 80.64 mg/g for Pb(II) and 21.45 mg/g for Cd(II)[30]. Some research had been done on the removal of Cd^{2+}, Cu^{2+}, Ni^{2+}, and Pb^{2+} from synthetic solutions using nanoparticle sorbents (TiO_2, MgO, and Al_2O_3) with a range of experimental approaches[31]. Flower-like TiO_2-graphene oxide was used for the removal of heavy metal ions from water[32]. The removal capacity of TiO_2-graphene oxide was measured 88.9, 72.8 and 65.6 mg/g for Zn^{2+}, Cd^{2+}, and Pb^{2+}, respectively[32].

The adsorption of Pb (II), Cu (II) and Zn (II) by TiO_2 can be accomplished from simulated polluted water and up to 94% removal was achieved[33]. The titania beads were used to remove Cr(VI), Cd(II), Cr(III), Cu(II), and Co(II) ions from simulated wastewater and the adsorption capacities were found to be 9.39, 8.94, 8.93, 8.40, and 7.62 mg/g, respectively[34].

Table 1.3: Literature based data for the adsorption efficiency of different metal-oxide nanostructures for the removal of metal-ions and organic pollutants.

Adsorbents	**Surface area (m^2/g)**	**Metal-ions**	**Maximum adsorption**		**Conditions**	**Refer-ences**
			(mg/g)	**%**		
TiO_2 nanoparticles	--	Pb(II) Cd(II)	--	44.7 25	Time- 60 to 90 min	[31]
GO-TiO_2	--	Pb(II) Cd(II)	65.6 72.8	--	pH- 5.6 Time- 12h	[32]
TiO_2		Pb(II) Cu(II)				[33]
Nano- TiO_2	--	Pb(II)	--	100	pH-2	[34]
ß-MnO_2	83.5	Cd(II)	12.9	--	Temp-20-50°C pH-4-6	[35]
$MnFe_2O_4$- G composite	79.30	Pb(II) Cd(II)	100 76.9	--	pH- 2-8 Time-220 min	[36]
Silica nanotubes (SNT)	--	Pb(II)	42.85	--	pH-4, 7, 9, Temp-30°C Time-240 min	[37]
Mesoporous silica	198.3	Cu(II)	36.38	--	pH-2-7	[38]
Silica monoliths	565	Cu(II)	145.98	--	pH-7	[39]
IOARM	--	Cd(II)	117.6	--	pH -6 Time-90 min Temp-20°C	[40]
TiO_2	220	Pb(II) Cd(II)	857 770	--	pH-6 Temp-30°C Time-80 min	[41]
AF-Fe_3O_4	25.94	Pb(II) Cd(II)	369 446.4	--	pH -7 Time-120 min	[24]
Fe_2O_3	79.35	Pb(II)	68.9	--	pH -5 Temp-45°C	[42]
CPA/ZnO hybride	45.9	Orange 16 dye	476.2	--	Time -60 min	[43]
ZnO-NR-AC	--	Bromoph enol red	200	--	pH- 1-9 Time-24 min	[44]
Activated carbon	981	Pesticide (Methox	112.0	--	pH-2 Temp-25°C	[45]

		ychlor)			Time -60 min	
ZnO nanoparticles	--	Victoria Blue	163.9	--	pH- 2-10	[46]
ZnO/$ZnFe_2O_4$	94.4	Methylene Blue	37.27	--	pH- 3-11	[47]
ZnO nanopowder	--	Reactive black	27.6	--	pH- 3-9	[48]
MWCNTs	--	Alizarin red S	161.29	--	pH-1-6	[49]
Functionalized ZnO NPs		Brilliant blue R-250	59.9	--	pH-2-12	[50]

1.4 Catalysis by different nanostructures

Study keen on catalysis is a foremost field in applied science and contains many areas of chemistry and materials science. Catalytic reactions are preferred in chemistry (environmentally friendly) due to the reduced amount of waste generated, in contrast to stoichiometric reactions in which all reactants are consumed and more side products are formed. Out of all catalytic reactions, catalytic properties of the heterogeneous catalyst with respect to the reduction of toxic aromatic nitro compounds such as 4-NP is of enormous importance. As, 4-NP can be converted to its useful derivatives such as 4-AP, a precursor of antipyretic and analgesic drugs[51].

There are numerous metal and metal oxide nanostructures were used as a catalyst for the reduction of 4-NP to 4-AP. Ultra-small Ag NPs were synthesized using PAA as stabilizing agent to test the catalytic performance for 4-NP[52]. As synthesized PAA stabilized displayed a good catalytic activity for the reduction of 4-NP to 4-AP[52]. One step synthesis of Au/g-C_3N_4 contact system using a different ratio of Au resulted in bi-functionality for catalytic and visible-light-driven photocatalytic activities for 4-NP to 4-AP reduction reaction[53]. Hierarchical silver nano dendrites were synthesized via galvanic replacement reaction (GPR) using copper foil as a template[54]. Synthesized dendritic microstructures displayed better catalytic activity for 4-NP to 4-AP reduction[54]. Metal nanoparticles were synthesized using PAMAM dendrimers as both stabilizing agent and template to analyze the reduction rate for 4-NP to 4-AP with $NaBH_4$[55].

Table 1.4: Literature data for the catalytic activity of metal nanoparticles for 4-NP reduction reaction.

Catalyst	Catalyst Amount (g/L)	4-NP (M)	Rate (s^{-1})	Reference
Au/CA	1.2	1×10^{-4}	1.4×10^{-4}	51
Au particle	0.6	10^{-2}	0.632×10^{-2}	56
Au@CMK-3-O	0.15	0.27×10^{-5}	0.274	57
Cu- DENs Ag- DENs	--	0.6×10^{-3}	2.43×10^{-2} 0.7×10^{-2}	55
Au/PMMA	--	9×10^{-5}	7.9×10^{-3}	58
Au/g-C_3N_4	--	1×10^{-2}	0.6180×10^{-3}	59
Au-SPB	--	1×10^{-4}	2.301×10^{-4}	60

1.5 Antibacterial activity of different nanomaterials

An antibacterial material is an agent that stops the growth of bacterial infection or kills bacteria. In general, antibacterial are present in most commonly used drugs. Most the bacteria have developed resistance against commonly available antibacterial drugs. This fact has promoted the research for alternative approaches to deal with the bacterial diseases/ infections. Consequently, nanoscale materials like silver nanoparticles have been aroused as novel antibacterial agents.

Silver doped carbon monolith was used to confirm the antibacterial activity against *E. coli*, *S. aureus* and *C. albicans* using standard microbiology method[61]. Ag entrapped in polystyrene nanocomposites were used as an antimicrobial agent against *E. coli*[62]. Spherical mesoporous Ag_3PO_4−pectin microspheres were synthesized by facile precipitation method and due to high intrinsic crystal stability, it shows an increase in bacteriocide activity against *E. coli* and *S. aureus*[63]. AgNPs@silica microcapsule was reported to show that microcapsule with the high surface area will enhance the antibacterial activity and recyclability of synthesized catalyst[56].

1.6 Research gaps

The literature was reviewed in detail to find the gaps in the present study. It has been found that the following areas are not explored in detail till now:

- Synthesis of silica monoliths with different pore size and pore volume by changing the chain length of PEG.
- Synthesis of metal/metal-oxide monoliths with different pore size by nanocasting on silica monoliths.
- Adsorption of organic pollutants (dyes/pesticides) and metal ions (Pb, Cd) by metal oxide monoliths.
- Synthesis of biocompatible polymer capped silver nanoparticles with exceptional colloidal stability and monodispersity.

1.7 Objective of present study

1. Green synthesis of biopolymer capped metal nanomaterials (eg. Ag).
2. To explore the catalytic activities of nanomaterials using green concepts for reduction reaction.
3. Effect of structure directing agents on metal-oxide synthesis (eg. MnO_2, TiO_2).
4. Use of synthesized nanomaterials in wastewater treatment for heavy metal ions, pesticides, and dyes.

1.8 Materials

Tetraethoxysilane (TEOS) and manganese nitrate were purchased from Alfa Aesar. Lead nitrate, cadmium carbonate, and titanium tetrachloride were obtained from Spectrochem. PEG (MW 400–35,000 g/mol) and dodecyl trimethyl ammonium bromide (C_{12}TAB), tetradecyltrimethylammonium bromide (C_{14}TAB), cetyltrimethylammonium bromide (C_{16}TAB), and octadecyltrimethylammonium bromide (C_{18}TAB) were purchased from Sigma Aldrich. Benzyltrimethylammonium chloride (BTMAC) and triton X-100 were purchased from Loba Chemie, India. Nitric acid (69%), ammonia (28-30%), zinc nitrate hexahydrate

($Zn(NO_3)_2 \cdot 6H_2O$), silver nitrate, cupric nitrate, furfuryl alcohol (FA), oxalic acid (OA) 1,3,5-trimethylbenzene (TMB) and sodium dodecyl sulphate (SDS) were purchased from Merck, India. All the reagents were of analytical grade. All reagents were used without further purification. All synthetic solutions of metal ions were prepared with Milli-Q water.

1.9 Characterization

Table 1.5: Specification and details of instruments used for characterization of samples.

Instruments	Specifications
Transmission electron microscopy (TEM)	Transmission electron microscopy (TEM) images were obtained with the FEI Technai G2 F20, operating at 200KV.
Surface area analyzer	Surface area was analyzed through BET surface area analyzer of Microtrac BEL Corp. Pvt. Ltd, Japan (Microtec Belsorp Mini–II). Before each set of measurements, samples were degassed at 200 °C in vacuum for more than 3 h.
Fourier transmission infrared (FTIR)	FTIR spectra were recorded using Agilent Resolution Pro-carry 660.
UV-visible spectrophotometer	Adsorption spectra and kinetic data of reduction reaction was analyzed by UV- Vis spectrophotometer (Champion 500).
Field emission scanning electron microscopy (FESEM)	For field emission scanning electron microscopy (FESEM), JEOL- 7000 FESEM equipped with Energy Dispersive X-ray Spectroscopy (EDS) detector was used.
X-ray diffraction analysis (XRD)	X-ray diffraction analysis (XRD) was performed using PANALYTICAL X'Pert PRO X-ray diffractometer having Cu Kα (λ=1.540Å) radiation operated at 45 KV.
Dynamic light scattering unit	Particle size distribution was determined by Microtrac's DLS model Nanotrac.
Atomic adsorption spectrophotometer	Atomic adsorption spectrophotometer (AAS) of GBC 932AA was used to analyze the metal ion concentrations.
X-ray photo- electron spectroscopy (XPS)	The oxidation state of Ag-Cu monolith was determined from PHI 5200 mode X-ray photo- electron spectroscopy (XPS) system.

1.11 Applications of nanomaterials for sustainable development

1.11.1 Process of adsorption study

Metal ions adsorption on the metal-oxide monoliths was executed in a batch system at ambient temperature using favorable conditions. Dry silica/metal-oxide monolith (0.02 g) was added into a 100 ml aqueous solution of a toxic pollutant (10-50 mg L^{-1}) and agitated for different time periods at a speed of 200-300 rpm. After the adsorption period, the solution was centrifuged for 10 min at 6000 rpm and the supernatant solutions were analyzed to determine the residual metal ion concentration left in the solution by AAS. AAS was used to analyze the dissolved Pb(II) & Cd(II) from a standard solution of lead nitrate and cadmium carbonate respectively, using calibration curve. Whereas UV-Vis spectrophotometer was used for the analysis of organic pollutants. The adsorption capacity (q_e) was calculated by the uptake amount of pollutants adsorbed per mass unit of monoliths (mg/g) using the formula:

$$q_e = \frac{(C_o - C_e)}{m} \times V \qquad (1.1)$$

where C_o is the initial and C_e is the equilibrium concentration (mg/L), while V is the volume of the solution (L) and m is the weight of the adsorbent (g). To control precision, each one of the adsorption experiments was performed in triplicates and the average value was reported.

1.11.2 Process of antibacterial studies

The antimicrobial activity of synthesized mesoporous mono/ bimetallic monolith was evaluated by minimum inhibitory concentration (MIC) method against *E. coli* (MTCC-77) and *B. subtilis* (MTCC-441). Luria broth (LB) was taken as a medium for growing and preserving the bacterial liquid cultures. 10 ml of bacterial culture was developed from a single colony. 5 ml of LB was used to inoculate the bacterial cells in glass test tubes. Mono/ bimetallic monoliths were added to the bacterial culture and the cultures were transferred to the incubator with constant agitation (130 rpm) for 24h at 37 °C (under aerobic conditions). Optical density was recorded at 600 nm after treatment. The results were plotted as the mean value of 3 mutually independent experiments. IC_{50} (half maximum inhibitory concentration), was also determined to measure the concentration of mono/ bimetallic monolith required to attain the 50% reduction in bacterial growth.

1.11.3 Process of catalytic reduction of the nitro compound

A catalytic stability and activity of heterogeneous mono/ bimetallic catalysts were evaluated for reduction process of 4-NP. The standard procedure for reduction reaction as used by Pradhan *et al.* [64] was performed in a quartz cuvette (3 ml). Initially, 200 µL of 0.1 M freshly prepared $NaBH_4$ solution was mixed with a solution containing 30 µL of 0.001 M 4-NP and 2 mL of deionized water. The reaction process does not start at all without the addition of catalyst. But with the addition of catalyst, it drives to accomplish to conversion of 4-AP. The solution was mixed by frail shaking after addition of catalyst and excitation of 4-NP was investigated by UV-Vis spectrophotometer.

References:

1. M. L. Grieneisen and M. Zhang, *Small*, 2011, **7**, 2836-2839.
2. R. D. Glover, J. M. Miller and J. E. Hutchison, *ACS nano*, 2011, **5**, 8950-8957.
3. A. Pal, S. Shah and S. Devi, *Colloids and Surfaces A: Physicochemical and Engineering Aspects*, 2007, **302**, 483-487.
4. H. R. Ghorbani, A. A. Safekordi, H. Attar and S. M. R. Sorkhabadi, *Chemical and Biochemical Engineering Quarterly*, 2011, **25**, 317-326.
5. J.-H. Smått, C. Weidenthaler, J. B. Rosenholm and M. Lindén, *Chemistry of Materials*, 2006, **18**, 1443-1450.
6. H. Huang, L. Wang, Y. Cai, C. Zhou, Y. Yuan, X. Zhang, H. Wan and G. Guan, *CrystEngComm*, 2015, **17**, 1318-1325.
7. T. A. Kareem and A. A. Kaliani, *Arabian Journal of Chemistry*, 2011, **4**, 325-331.
8. K. Shameli, M. B. Ahmad, S. D. Jazayeri, S. Sedaghat, P. Shabanzadeh, H. Jahangirian, M. Mahdavi and Y. Abdollahi, *International journal of molecular sciences*, 2012, **13**, 6639-6650.
9. Y. Sun and Y. Xia, *Science*, 2002, **298**, 2176-2179.
10. K. C. Song, S. M. Lee, T. S. Park and B. S. Lee, *Korean Journal of Chemical Engineering*, 2009, **26**, 153-155.
11. T. Yanagisawa, T. Shimizu, K. Kuroda and C. Kato, *Bulletin of the Chemical Society of Japan*, 1990, **63**, 988-992.
12. K. Nakanishi, R. Takahashi, T. Nagakane, K. Kitayama, N. Koheiya, H. Shikata and N. Soga, *Journal of Sol-Gel Science and Technology*, 2000, **17**, 191-210.
13. X. Deng, K. Chen and H. Tüysüz, *Chemistry of Materials*, 2017, **29**, 40-52.
14. J.-H. Smått, F. M. Sayler, A. J. Grano and M. G. Bakker, *Advanced Engineering Materials*, 2012, **14**, 1059-1073.
15. Yue and Zhou, *Chemistry of Materials*, 2007, **19**, 2359-2363.
16. S. C. Laha and R. Ryoo, *Chem. Commun.*, 2003, 2138-2139.
17. Y. Xia and R. Mokaya, *The Journal of Physical Chemistry C*, 2007, **111**, 10035-10039.
18. Y. Liu, J. Li, M. Wang, Z. Li, H. Liu, P. He, X. Yang and J. Li, *Crystal Growth & Design*, 2005, **5**, 1643-1649.

19. H. Tuysuz, E. L. Salabas, C. Weidenthaler and F. Schuth, *Journal of the American Chemical Society*, 2008, **130**, 280-287.
20. E. N. El Qada, S. J. Allen and G. M. Walker, *Chemical Engineering Journal*, 2008, **135**, 174-184.
21. L. Zhuannian, Z. Anning, W. Guirong and Z. Xiaoguang, *Chinese Journal of Chemical Engineering*, 2009, **17**, 942-948.
22. Z. Ajji and A. M. Ali, *Nuclear Instruments and Methods in Physics Research Section B: Beam Interactions with Materials and Atoms*, 2007, **265**, 362-365.
23. T. A. Saleh and V. K. Gupta, *Environmental science and pollution research international*, 2012, **19**, 1224-1228.
24. X. Xin, Q. Wei, J. Yang, L. Yan, R. Feng, G. Chen, B. Du and H. Li, *Chemical Engineering Journal*, 2012, **184**, 132-140.
25. Z. L. Zhu, H. M. Ma, R. H. Zhang, Y. X. Ge and J. F. Zhao, *Journal of Environmental Sciences*, 2007, **19**, 652-656.
26. M. Ilayaraja, M. Sameem, S. G. Sankari and R. S. Kannan, *Journal of Environmental Analytical Chemistry*, 2014, **01**.
27. J. Aguado, J. M. Arsuaga, A. Arencibia, M. Lindo and V. Gascon, *Journal of hazardous materials*, 2009, **163**, 213-221.
28. A. Mohammadzadeh, M. Ramezani and A. M. Ghaedi, *Journal of the Taiwan Institute of Chemical Engineers*, 2016, **59**, 275-284.
29. K. Yogesh Kumar, H. B. Muralidhara, Y. Arthoba Nayaka and J. Balasubramanyam, *Desalination and Water Treatment*, 2013, **52**, 4568-4582.
30. L. Dong, Z. Zhu, H. Ma, Y. Qiu and J. Zhao, *Journal of Environmental Sciences*, 2010, **22**, 225-229.
31. S. Mahdavi, M. Jalali and A. Afkhami, *Chemical Engineering Communications*, 2013, **200**, 448-470.
32. Y.-C. Lee and J.-W. Yang, *Journal of Industrial and Engineering Chemistry*, 2012, **18**, 1178-1185.
33. N. Wu, H. Wei and L. Zhang, *Environmental science & technology*, 2012, **46**, 419-425.
34. J. Hu and H. J. Shipley, *Environmental science and pollution research international*, 2013, **20**, 5125-5137.

35. M. I. Zaman, S. Mustafa, S. Khan and B. Xing, *Journal of colloid and interface science*, 2009, **330**, 9-19.
36. S. Chella, P. Kollu, E. V. P. R. Komarala, S. Doshi, M. Saranya, S. Felix, R. Ramachandran, P. Saravanan, V. L. Koneru, V. Venugopal, S. K. Jeong and A. Nirmala Grace, *Applied Surface Science*, 2015, **327**, 27-36.
37. P. Wang, M. Du, H. Zhu, S. Bao, T. Yang and M. Zou, *Journal of hazardous materials*, 2015, **286**, 533-544.
38. X. Xue and F. Li, *Microporous and Mesoporous Materials*, 2008, **116**, 116-122.
39. M. R. Awual, T. Yaita, S. A. El-Safty, H. Shiwaku, S. Suzuki and Y. Okamoto, *Chemical Engineering Journal*, 2013, **221**, 322-330.
40. T. A. Khan, S. A. Chaudhry and I. Ali, *Journal of Molecular Liquids*, 2015, **202**, 165-175.
41. M. Sharma, D. Choudhury, S. Hazra and S. Basu, *Journal of Alloys and Compounds*, 2017, **720**, 221-229.
42. S. Rajput, L. P. Singh, C. U. Pittman, Jr. and D. Mohan, *Journal of colloid and interface science*, 2017, **492**, 176-190.
43. P. Kannusamy and T. Sivalingam, *Colloids and surfaces. B, Biointerfaces*, 2013, **108**, 229-238.
44. M. Ghaedi, M. Ghayedi, S. N. Kokhdan, R. Sahraei and A. Daneshfar, *Journal of Industrial and Engineering Chemistry*, 2013, **19**, 1209-1217.
45. V. K. Gupta, B. Gupta, A. Rastogi, S. Agarwal and A. Nayak, *Water research*, 2011, **45**, 4047-4055.
46. N. Kataria, V. K. Garg, M. Jain and K. Kadirvelu, *Advanced Powder Technology*, 2016, **27**, 1180-1188.
47. J. Feng, Y. Wang, L. Zou, B. Li, X. He, Y. Ren, Y. Lv and Z. Fan, *Journal of colloid and interface science*, 2015, **438**, 318-322.
48. Z. Monsef Khoshhesab, K. Gonbadi and G. Rezaei Behbehani, *Desalination and Water Treatment*, 2014, **56**, 1558-1565.
49. M. Ghaedi, A. Hassanzadeh and S. N. Kokhdan, *Journal of Chemical & Engineering Data*, 2011, **56**, 2511-2520.

50. S. Chaudhary, Y. Kaur, A. Umar and G. R. Chaudhary, *Journal of Molecular Liquids*, 2016, **220**, 1013-1021.
51. S. Panigrahi, S. Basu, S. Praharaj, S. Pande, S. Jana, A. Pal, S. K. Ghosh and T. Pal, *The Journal of Physical Chemistry C*, 2007, **111**, 4596-4605.
52. C. Kastner and A. F. Thunemann, *Langmuir : the ACS journal of surfaces and colloids*, 2016, **32**, 7383-7391.
53. Y. Fu, T. Huang, B. Jia, J. Zhu and X. Wang, *Applied Catalysis B: Environmental*, 2017, **202**, 430-437.
54. W. Zhang, F. Tan, W. Wang, X. Qiu, X. Qiao and J. Chen, *Journal of hazardous materials*, 2012, **217-218**, 36-42.
55. M. Nemanashi and R. Meijboom, *Journal of colloid and interface science*, 2013, **389**, 260-267.
56. H. Yang, Y. Liu, Q. Shen, L. Chen, W. You, X. Wang and J. Sheng, *Journal of Materials Chemistry*, 2012, **22**, 24132.
57. P. Guo, L. Tang, J. Tang, G. Zeng, B. Huang, H. Dong, Y. Zhang, Y. Zhou, Y. Deng, L. Ma and S. Tan, *Journal of colloid and interface science*, 2016, **469**, 78-85.
58. K. Kuroda, T. Ishida and M. Haruta, *Journal of Molecular Catalysis A: Chemical*, 2009, **298**, 7-11.
59. Y. S. Fu, T. Huang, B. Q. Jia, J. W. Zhu and X. Wang, *Appl Catal B-Environ*, 2017, **202**, 430-437.
60. S. Wunder, Y. Lu, M. Albrecht and M. Ballauff, *ACS Catalysis*, 2011, **1**, 908-916.
61. V. Marija, K. Ana and D. B. Suzana, *Sci Tech Adv Mater* 2008, **9**, 1-7.
62. M. Palomba, G. Carotenuto, L. Cristino, M. A. Di Grazia, F. Nicolais and S. De Nicola, *Journal of Nanomaterials*, 2012, **117**, 185029.
63. B. Bayón, V. Bucalá and G. R. Castro, *Microporous and Mesoporous Materials*, 2016, **226**, 71-78.
64. N. Pradhan, A. Pal and T. Pal, *Colloids and Surfaces A: Physicochemical and Engineering Aspects*, 2002, **196**, 247-257.

Chapter-2

Synthesis of Mesoporous Silica Monolith to Analyze the Effect of Ionic Character of Surfactants/Polymers

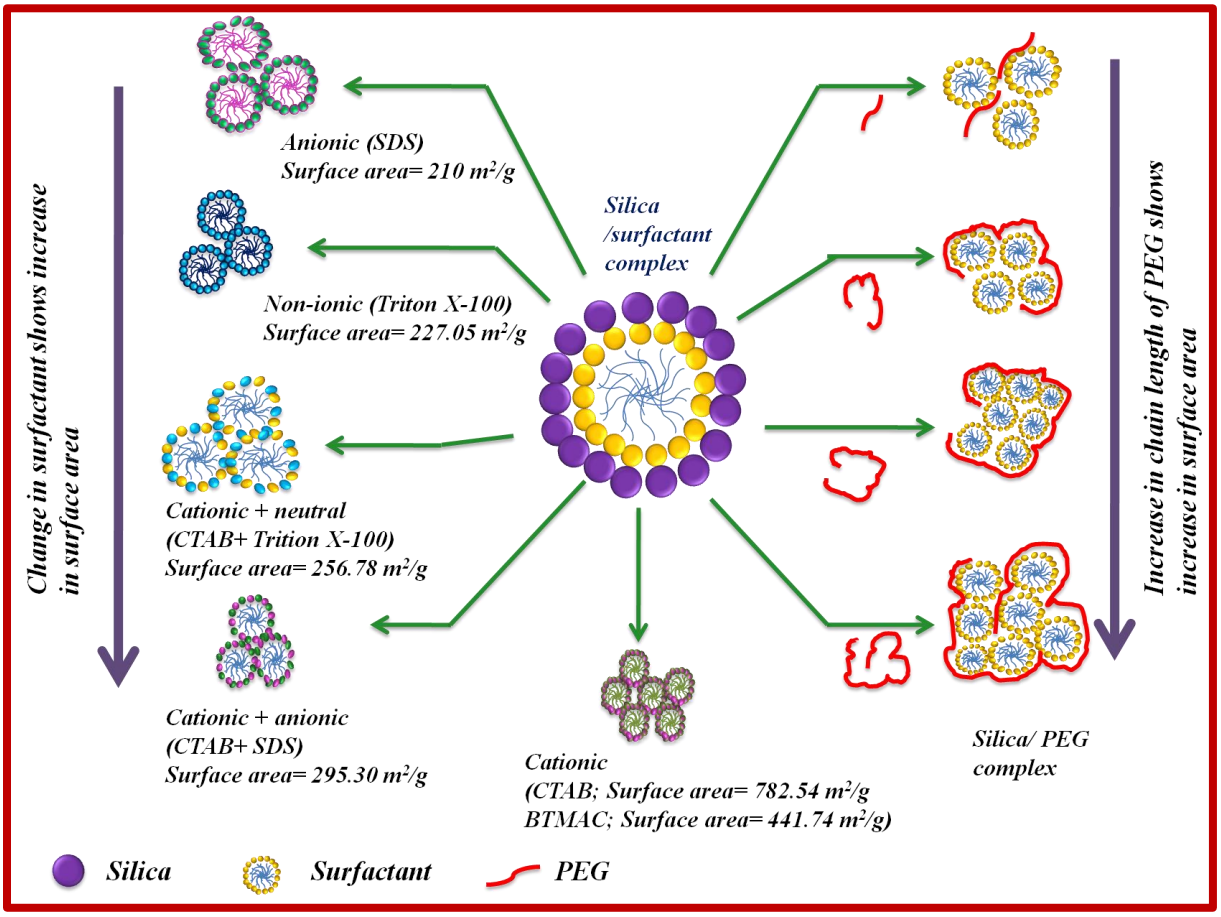

In this chapter, to achieve maximum pore diameter and surface area of porous silica monoliths different structure directing agents (SDAs) (Cationic/ anionic/ neutral/ mixture) were used. BET study showed alteration of SDA's chain length, composition or concentration have a cumulative effect on controlling the surface area and pore size. PEG in combination with other SDAs like CTAB, SDS, BTMAC, Triton-X100 etc. controlled internal agglomeration along with particles size. The maximum amount of surface area was observed by using maximum chain length of PEG and CTAB.

2.1 Introduction

Porous materials have received significant attention because they have an ability to interact with metal ions or nanomaterials due to tunable pore size, pore volume and high surface area[1, 2]. Pores of silica gels are heterogeneous in nature and are ranges from micropore (<2 nm) to mesopore (2-50 nm). The porosity of the gel determines its distribution depending on the preparation conditions[3]. Silica monoliths mostly composed of mesoporous silica supports and are characterized by long parallel channels separated by thin walls[3]. Monoliths of silica having a trimodal, stratified pore structures are commonly made using sol-gel-process[4]. Sol-gel method to prepare silica monolith was first introduced by Nakanishi and Soga in 1991[5]. Later; modification of sol-gel techniques such as phase separation and sol–gel reaction together with a successive solvent exchange treatment was successfully done to generate macroporous and mesoporous (double-pore) silica gel monoliths[6, 7]. More recently, structure directing agents such as long chain water soluble polymers/surfactants had attracted much attention for mesoporous monolith synthesis[4, 8]. Till now, the effect of the cationic surfactant (concentration as well as their chain length) in the formation of lamellar mesoporous silica structure with various degrees of crystallinity had been studied[9]. Few research works had been done on the stability of colloidal mesoporous silica structure, showing huge surface areas (1000–1300 m^2/g), uniform pore diameters (3–4 nm) and pore volumes (about 1 cm^3/g) [10]. Husing *et al.* described the hierarchical network structure of silica monoliths using Pluronic P123 as nonionic block copolymer surfactant through a bimodal pore size distribution[11]. It has already been reported that amorphous mesoporous structures can be produced from anionic surfactants such as SDS; whereas with the non-ionic surfactant such as Triton X-100 (TRIX) produces proper ordered and steady mesoporous structures[12]. Smatt *et al.* synthesized silica monoliths by using a cationic surfactant (CTAB) and water-soluble polymer (PEG) and studied their effect on the alternation of mesopore structures[4]. They have described the influence of CTAB/TEOS ratio and CTAB chain length on the mesoporous structure of silica monolith. But the effect of surfactant nature (cationic, anionic, neutral or mixture) on the properties of mesoporous silica structure is not revealed yet.

For stabilization of mesoporous structures water soluble polymer is needed because they have a direct effect on hydrophilicity and flexibility of these structures. In this chapter, various molecular weight PEG had been used as the water-soluble polymer. The surface coatings of

surface-grafted PEG chains or crosslinked PEG gels are amongst the most effective surface modifier for mesoporous silica monoliths[14-17]. The incorporation of long chain polymers improves the porosity of inner and outer surface of the mesoporous particles. Smatt *et al.* have described the influence of the PEG/TEOS ratio on the mesoporous structure of silica monoliths[4]. But till to date, there is no report on the effect of chain length of hydrophilic polymer on the porous structure of silica monoliths.

Viscosity, hydroxyl group content, and polarity are the determining properties of surfactants/polymers which control the characteristics such as pore size and architecture of the silica monoliths. In this regard, we have synthesized silica monoliths with tunable mesopore size by altering the chain length as well as the ionic nature/concentration of different structure directing agents to investigate their effect on the silica gel ordered structures.

2.2.1 Synthesis process of silica monoliths

TEOS was added to a mixture of nitric acid (30% v/v) and PEG (6.25% w/v) solution then the mixture was stirred at room temperature for 5-10 min until a translucent sol was obtained. After that, solid CTAB (0.1 M) was added to the sol with continuous stirring until the surfactant dissolved completely. 8-12 h time was required for sol to gel formation and then at least 72 h (may vary depending upon type and concentration of surfactant) aging of the gel was done at 40 °C for the complete aging process. The time required for aging by cationic, anionic and non-ionic surfactants is different. Cationic surfactants such as C_nTAB (n=16, 18) and BTMAC and the mixture of cationic and nonionic surfactant ($C_{18}TAB$ + TRIX) took three days for aging process. Whereas mixture of cat-anionic ($C_{18}TAB$+ SDS) and C_nTAB (n=12, 14) required more than five days for aging process. Due to the variation of surfactant as well as gelation time, the size of the synthesized monoliths also differed.

To increase the degree of condensation and stability of the SiO_2 monoliths, the solvent exchange was performed. Silica monoliths were soaked in NH_4OH (1 M) solution at 90 °C for 9 h for the hardening process. The volume of the NH_4OH solution used was kept 10 times higher than the volume of SiO_2 monoliths for that purpose. Later, the solution of SiO_2 monoliths was acidified using HNO_3 (0.1 M). After washing with deionized water monoliths were kept in an oven at 40 °C for 4-5 days for proper drying. Finally, monoliths were calcinated at 550 °C for 5 h with 1 °K/min heating ramp.

2.2.2 Characterizations:

As synthesized silica monoliths were characterized by various techniques; details of the techniques are given in **chapter 1, section 1.9.**

2.3 Results and discussion

2.3.1 Effect of the PEG chain length

PEG was used to improve the phase separation and to control the 3D structure of the hierarchical network in relation with a pore size distribution. High water solubility and condensation reactions could be the advantages of using PEG. Here, silica monoliths were prepared at constant CTAB/TEOS (0.9) and PEG/TEOS (0.003) molar ratios where different chain length PEG was used (MW – 400 to 35, 000 g) (Fig. 2.1). In all cases, white monolithic gel rods with an interconnected mesoporous structure were obtained.

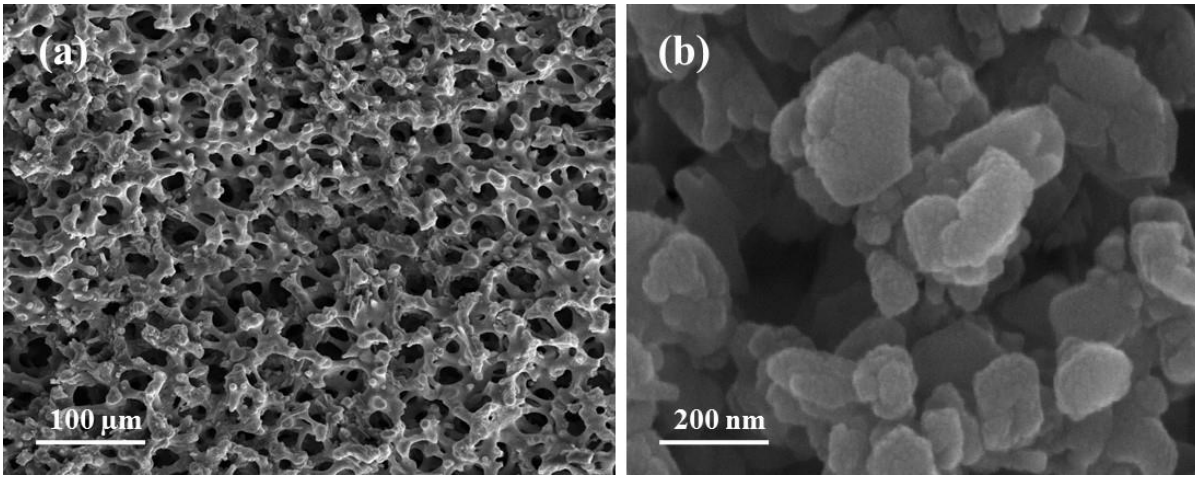

Fig. 2.1: SEM image of porous silica monolith (S-350) showing the textural porosity.

The N_2 sorption of silica monoliths synthesized with different MW of PEG is shown in Fig. 2.2a. It is clearly seen that the relative pressure (P/P_0) at which a fixed increase in the adsorption was observed which was shifted to higher values with increasing molecular weight. BET surface area along with the pore volume and pore size in relation with PEG chain lengths are listed in Table 2.1. The BET areas increased from 638 m^2/g to 760 m^2/g, with an increase of MW of PEG from MW 400 to 35000 gm. For all synthesized samples, type IV isotherms could be observed as confirmed from the IUPAC classification. The uniformity of pore sizes and shape

were defined by the sharp adsorption and desorption branches in H1 hysteresis loops of the synthesized mesoporous silica monoliths. The increase in polymer chain length resulted in an increase of the textural mesopore size (Fig. 2.2b). On the other hand, a pore volume of the silica monolith significantly varied due to the variation of mesopore size (1.1 - 3.1 $cm^3 g^{-1}$).

Table 2.1: Textural characteristics for the silica monoliths with different chain length determined from nitrogen sorption measurements.

Sample name	PEG (MW) (g/mol)	Surface area ($m^2 g^{-1}$)	Mesopore diameter (nm)	Mesopore volume ($cm^3 g^{-1}$)
S-4	400	638	7.01	1.11
S-6	600	654	13.69	2.71
S-10	1000	688	15.83	2.27
S-40	4000	691	13.21	2.38
S- 60	6000	649	4.78	1.77
S-80	8000	669	18.80	3.14
S-100	10000	686	17.39	2.85
S-200	20000	703	15.48	2.92
S-350	35000	760	7.46	1.42

*where S denotes silica.

With the addition of hydrogen bonding polymer, a phase separation between silica rich and polymer rich phase could be achieved. PEG is the main component for sol-gel forms of the interconnected macropores in monolithic silica structure[18, 19]. Under the acidic conditions with the adjustment of chain length of PEG transformation of silica (from liquid to gel) is easily achievable. Silica gel with long chain length PEG can alter interconnected macroporosity and mesoporosity of monolith structures. While interacting with silica gel increase in the chain length of PEG resulted in an increase of volume fraction of polymer[20]. Also, increase the chain length of PEG resulted in the steric stabilization and interconnected colloid formation process which led to the formation of higher textural mesopore size due to an increase of particle volume fraction.

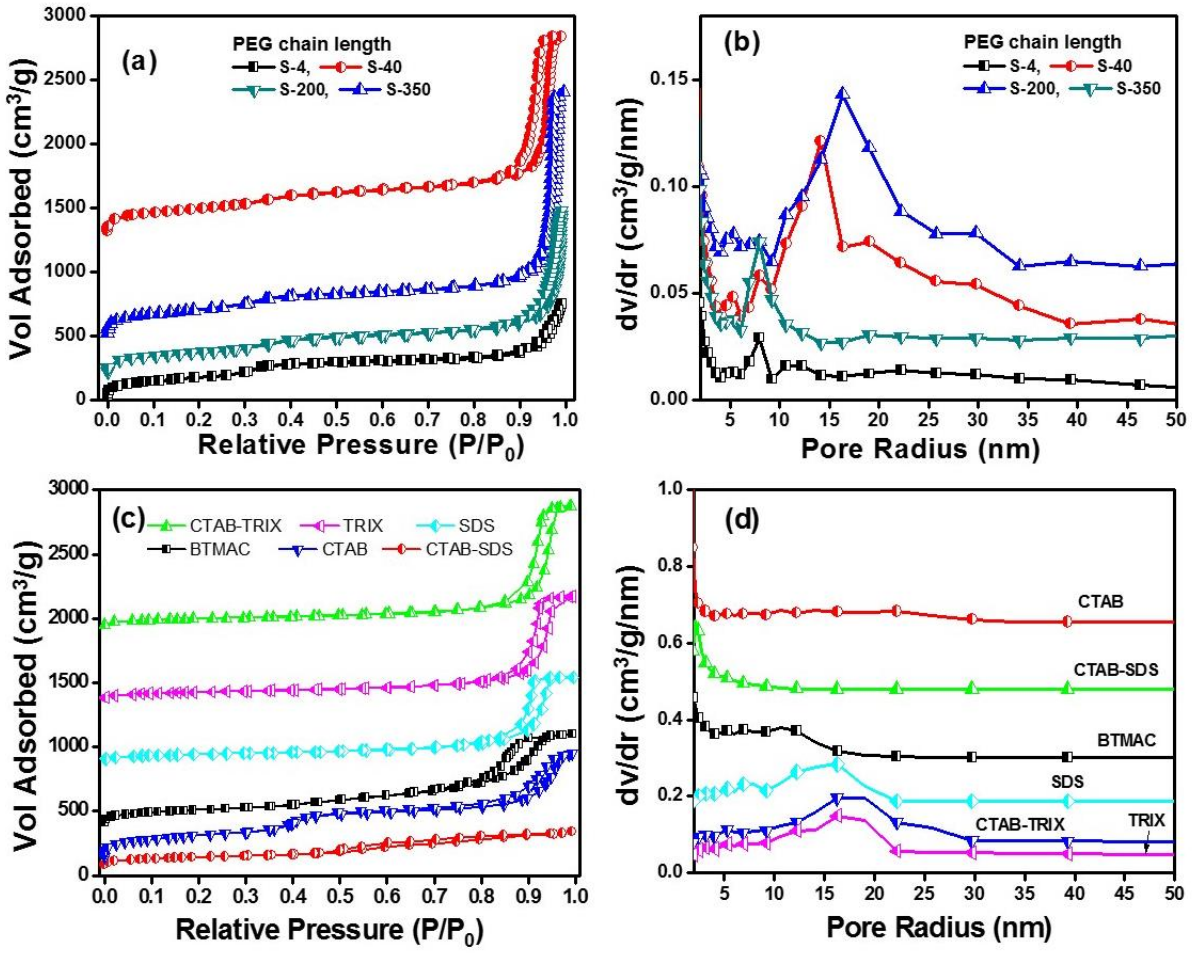

Fig. 2.2: Nitrogen sorption isotherm plots for silica monolith with different a) PEG chain length, c) surfactants; differential pore volume distribution using BJH plots for silica monolith with different b) PEG chain length, d) surfactants. (In case of, Fig. a-b surfactant used: C_{16}TAB and c-d polymer used: PEG-35,000 g/mol).

2.3.2 Effect of ionic characters of surfactant

To check the effect of nature of surfactants on the pore size as well as surface area; cationic (CTAB, BTMAC), anionic (SDS), neutral (TRIX) as well as a mixture of (cationic-anionic and cationic-neutral) surfactants were used to prepare silica monoliths. The batches had a general molar composition of H_2O/HNO_3/TEOS/ PEG (MW 35,000g)/surfactant molar ratio of these monoliths was $8.2:0.53:2.2:9.54\times10^{-4}:0.2$, in which either a single surfactant or an equimolar mixture of surfactants was present. Fig. 2.2c shows the nitrogen adsorption-desorption

isotherm for the SiO_2 monoliths with different surfactants. It has been observed that the BET surface area for cationic surfactant ($C_{18}TAB$) was 782.54 m^2g^{-1}, while the pore volume and pore diameters were 1.26 cm^3g^{-1} and 6.4 nm respectively. But for the anionic surfactant (SDS) the BET surface area and pore volume decreased to 210.21 m^2g^{-1} and 1.013 cm^3g^{-1} whereas its mesopores diameter had increased to 19.31 nm with respect to $C_{18}TAB$ (Table 2). The surface area for another cationic surfactant (BTMAC) was more than that of the anionic surfactant (SDS); having a value of 441.74 m^2g^{-1} while its pore volume and pore diameter was less (1.097 cm^3/g and 9.93 nm, respectively). For non-ionic surfactant (TRIX) the surface area 227.05 m^2g^{-1} was lesser than the cationic surfactants but more than that of the anionic surfactant. Whereas for the cationic-anionic mixture (CTAB + SDS) the surface area obtained was higher (295.30 m^2g^{-1}) than that of the cationic-nonionic mixture (CTAB + TRIX). This could be attributed to the fact that, on the addition of CTAB it formed positively charged rod-like uni-lamellar micelles which induced the formation of the template of large mesoporous size.

Table 2.2: Nitrogen physisorption data of silica monoliths containing a different surfactant.

Name of surfactant	**Ionic nature of surfactant**	**BET surface area ($m^2\ g^{-1}$)**	**Mesopore volume ($cm^3\ g^{-1}$)**	**Mesopore diameter (nm)**
CTAB	Cationic	782	1.26	6.4
BTMAC	Cationic	441	1.09	9.93
SDS	Anionic	210	1.01	19.31
TRIX	Non-ionic	227	1.24	21.89
CTAB + SDS	Cationic-anionic	295	0.43	5.86
CTAB +TRIX	Cationic-nonionic	256	1.46	22.74

Because of charge neutralization between cationic surfactant (CTAB) and a negatively charged silica source, TEOS particles become more hydrophobic in nature. Chain-chain interaction by surfactant adsorption resulted in an increment of micelle size as well as pore size (Fig. 2.2d). SDS formed negatively charged micelles with small mesoporous size and upon addition of TEOS (negatively charged) strong electrostatic repulsions forces generated. This interaction decreased the pore size as well as the surface area in comparison with the cationic surfactant[21]. Due to low electrostatic force in nonionic surfactant intermediate surface area formed. Similarly, due to electro-neutrality of an equimolar mixture of CTAB-SDS upon

interaction with TEOS, generated a weak electrostatic attraction causing an increase in the critical aggregation concentration (CAC)[22] and surface area. In cationic-nonionic mixture, positively charged micelle neutralized the negative charges of TEOS leading to decrease in surface area.

2.3.3 Effect of surfactant concentration

The concentration of surfactants strongly influenced the textural and morphological properties of mesoporous monoliths[23]. It can also be observed that the surface area increased with the increase in the molar concentration of CTAB (Fig. 2.3a). The BET areas increased from 316 m^2/g to 994 m^2/g, with an increase of the molar concentration of CTAB (0.1 to 0.5M). Some physical parameters (such as surface area, pore size, and pore volume) are summarized in Table 3. Specific surface area was found to be directly proportional to surfactant concentration. The critical micelle concentration (CMC) of CTAB in aqueous solution is 0.9−1 mM[24]. Above the CMC transition of spherical shape to rod-like structures occurred[25]. Therefore, on the addition of higher concentration of CTAB positively charged, larger mesoporous, rod-like micelles formed (Fig. 2.3b). The increase in the concentration of CTAB caused strong electrostatic attraction with the TEOS resulting in an increment in pore size and surface area.

Table 2.3: Nitrogen physisorption data of silica monoliths containing a different molar concentration of C_{18}TAB concentration.

C_{18}TAB Concentration (Mol)	**BET surface area ($m^2\ g^{-1}$)**	**Mesopore volume ($cm^3\ g^{-1}$)**	**Mesopore diameter (nm)**
0.1	316	1.23	15.61
0.2	782	1.26	6.40
0.3	831	1.09	5.28
0.5	995	1.77	7.12

2.3.4 Effect of chain length of CTAB

The chain length of CTAB also influenced the textual and morphological properties of mesoporous monoliths. The chain length of CTAB is directly proportional to surface area of monoliths (Fig. 2.3c). Some physical parameters (such as surface area, pore size, and pore volume) are summarized in Table 2.4. Smatt *et al*. synthesized silica monoliths by varying chain length of CTAB and found all are giving the similar surface area of 755 ± 30

m^2/g^4. But we found an increase in the BET surface areas from 528 m^2/g to 782.54 m^2/g with an increase of chain length of C_nTAB (n= 12-18). The increase in C_nTAB chain length resulted in a decrease of the textural mesopore size (Fig. 2.3d).

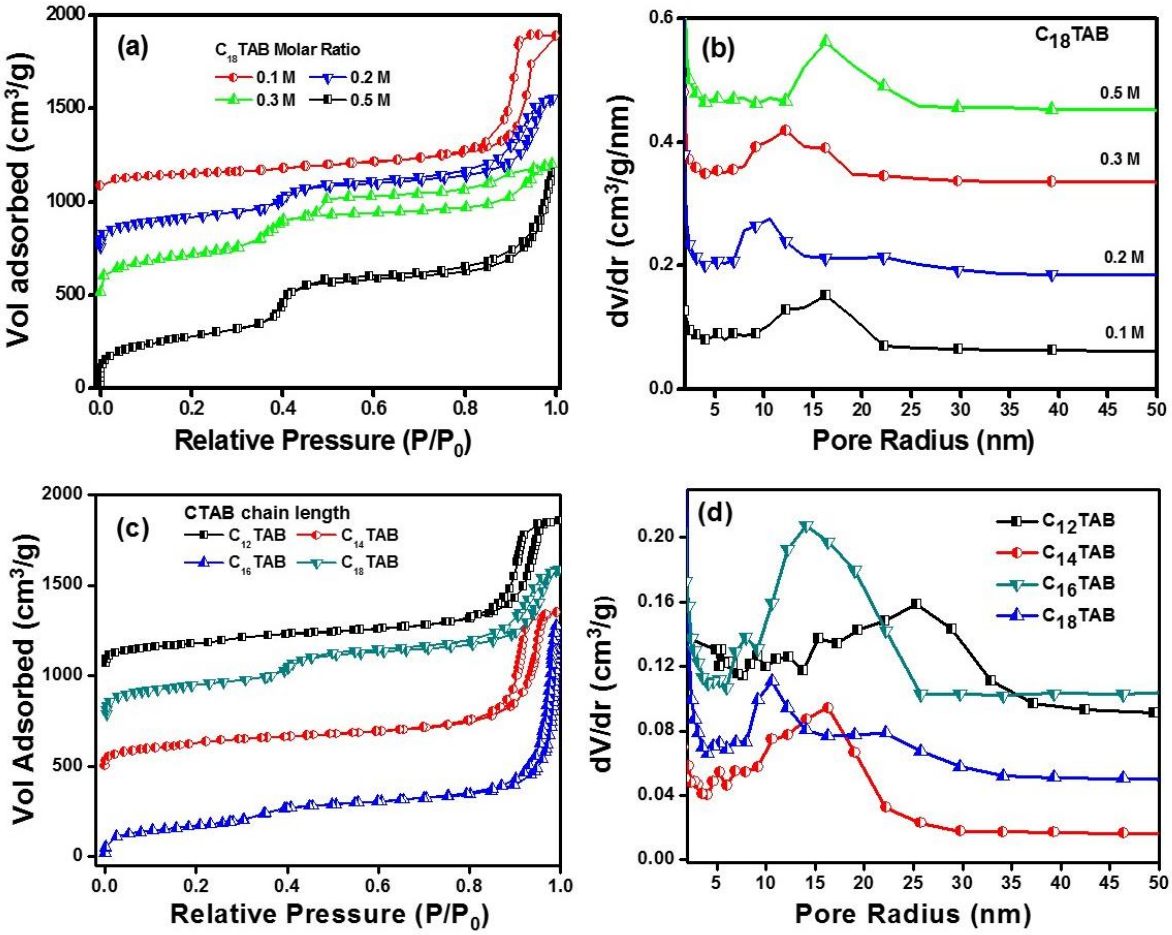

Fig. 2.3: Nitrogen sorption isotherm plots for silica monolith with different a) molar ratio of $C_{18}TAB$, c) CTAB chain length; differential pore volume distribution using BJH plots for silica monolith with different b) molar ratio of $C_{18}TAB$, d) CTAB chain length. (In all cases polymer used: PEG-35,000 g/mol).

Cationic surfactants can form long worm like micelle in combination with TEOS by forming packed entanglement network with enhanced viscoelasticity. Primarily, during the synthesis process, CTAB completely dissolve with a mixture of TEOS and PEG and results in small micelle formation. While increasing the hydrocarbon chain length of surfactants (C_nTAB,

n=12-18) resulted in the conversion of spherical micelle into the uniaxial micellar close packed structure because of the usual mass-action effects. The diameter of micelle can increase by increasing hydrocarbon chain of CTAB which reflects the osmotic compressibility due to increase in surface area of close packed micelles[26].

Table 2.4: Nitrogen physisorption data of samples containing different CTAB chain length.

Chain length of surfactant	BET surface area ($m^2 g^{-1}$)	Mesopore volume ($cm^3 g^{-1}$)	Mesopore diameter (nm)
C_{12}TAB	529	1.34	10.15
C_{14}TAB	690	1.39	9.04
C_{16}TAB	761	1.41	7.46
C_{18}TAB	783	1.65	6.40

2.4 Conclusion

In summary; the effect of chain length of PEG on network structure, packing along with the effect of different surfactants (cationic, anionic, neutral or mixture) over the formation of silica monolith has been presented in detail. Alteration of chain length or composition along with the concentration of surfactant showed a synergistic effect on the surface area and pore size of monoliths. Enhancement in synergistic effect imparts viscoelastic properties of the solution to form flexible and long worm like or unilamellar micelles structures. Controlling of internal structure and agglomeration of particles can be possible by changing the chain length of PEG. It is also possible to vary pore size of mesopores using composition of surfactant/polymer.

References

1. W. Li, Z. Wu, J. Wang, A.A. Elzatahry and D. Zhao, *Chem. Mater.*, 2014, **26**, 287−298.

2. D. Chen, F. Huang F, Y.B. Cheng and R.A. Caruso, *Adv. Mater.*, 2009, **21**, 2206–2210.

3. K. Nakanishi, T. Nagakane and N. Soga, *J. Porous Mater.*, 1998, **5**,103-110.

4. J-H. Smått, S. Schunk and M. Lindén, *Chem. Mater.*, 2003, **15**, 2354- 2361.

5. K. Nakanishi and N. Soga, *J. American Ceramic Society*, 1991, **74**, 2518-2530.

6. K. Nakanishi and N. Soga, *J. non-crystalline solids*, 1992, **139**, 1-13.

7. A-M. Siouffi, *J. Chromat. A*, 2003, **1000**, 801-818.

8. J-H. Smått, C. Weidenthaler, J.B. Rosenholm and M. Linden, *Chem. Mater.*, 2006, **18**, 1443-1450.

9. K Nakanishi, R Takahashi, T Nagakane, K. Kitayama, N. Koheiya, H. Shikata and N. Soga," *J. Sol-Gel Sci. Technol.*, 2000, **17**, 191.

10. D. Brandhuber, V. Torma, C. Raab, H. Peterlik, A. Kulak and N. Huesing, *Chem. Mater.*, 2005, **17**, 4262-4271.

11. N. Huesing, C. Raab, V. Torma, A. Roig, H. Peterlik, *Chem. Mater.*, 2003, **15**, 2690-2692.

12. Z.S. Chao and E. Ruckenstein, *Langmuir*, 2002, **18**, 734-743

13. Schmidt SM, McDonald J, Pineda ET, Verwilst AM, Chen Y, Josephs R and Ostafin AE, *Microporous and Mesoporous Mater.*, 2006, **94**, 330–338

14. Y. Uyama, K. Kato and Y. Ikada, *Adv Polym Sci*, 1998, **137**, 1–39.

15. A. Kidane, T. McPherson, H.S. Shim and K. Park, *Colloids Surf. B*, 2008, **18**, 347–353.

16. G.M. Cruise, O.D. Hegre, D.S. Scharp and J.A. Hubbell, *Biotechnol. Bioeng*., 1998, **57**, 655–665.

17. B.S. Kim, J.S. Hrkach and R. Langer, *Biomaterials* 2000, **21**, 259–265.

18. Q. He, J. Zhang, J. Shi, Z. Zhu, L. Zhang, W. Bu, L. Guo and Y. Chen, *Biomaterials*, 2010, **31**, 1085–1092

19. X. Huang, L. Li, T. Liu, N. Hao, H. Liu, D. Chen and F. Tang, *ACS NANO*, 2011, **5**, 5390–5399.

20. S.Y. Kim, H.W. Meyer, K. Saalwachter and C.F. Zukoski, *Macromolecules*, 2012, **45**, 4225-4237.

21. E.W. Kaler, K.L. Herrington, D.J. Iampietro, B.A. Coldren, H.-T. Jung and J.A. Zasadzinski ed. M. Abe and J.F. Scamehorn, NewYork, 2nd edition, vol. 124, (2004), ch. 9, pp. 289-338.

22. G. Kume, M. Gallotti and G. Nunes, *J. Surfact. Deterg.*, 2008, **11**, 1–11.

23. S.V. Vattikuti and C. Byon, *Sci. Adv. Mater.*, 2015, **7,** 2639-2645.

24. D.C. Culita, C.M. Simonescu, M. Dragne, N. Stanica, C. Munteanu, S. Preda, O. Oprea, *Ceramics International*, 2015, **41**, 13553-13560.

25. K. Shiba, S. Motozuka, T. Yamaguchi, N. Ogawa, Y. Otsuka, K. Ohnuma, T. Kataoka and M. Tagaya, *Cryst. Growth Des.*, 2016, **16**, 1463–1471.

26. M.E. Catest and S.J. Candau, *J. phys.: Condens. Matter*., 1990, **2**, 6869-6892.

Chapter-3

Section-A: Lead and Cadmium Removal in Synthetic Wastewater Using SiO_2, MnO_2 and TiO_2 Monoliths

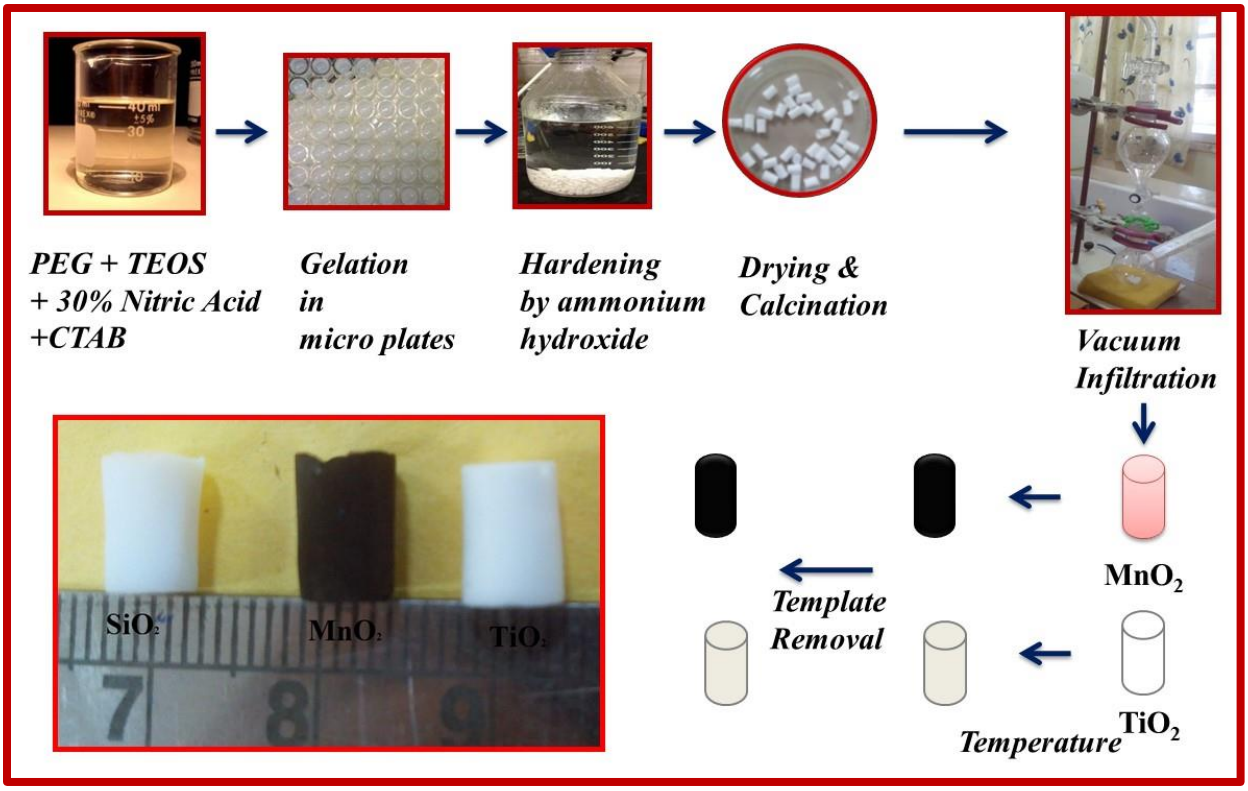

Ordered hierarchically porous silica (by sol-gel method) and metal-oxide monoliths (through nanocasting method) were synthesized. Porous silica and metal oxide monoliths (MnO_2 and TiO_2) exhibited excellent adsorption for heavy metal ions such as Pb(II) & Cd(II). The morphological and structural study of the synthesized silica and metal oxide monoliths were done by FESEM and XRD analysis. The adsorption studies were conducted in different batches. The maximum adsorption of Pb(II) on SiO_2, MnO_2 and TiO_2 varied from 91-125, 166-200 and 769-857 mg/g respectively depending upon the choice of PEG, which is used as a structure directing/controlling agent. Similarly, the maximum adsorption of Cd(II) on SiO_2, MnO_2 and TiO_2 varied from 90-100, 100-125 and 667-770 mg/g respectively. The effects of contact time (0-80 min), temperature (at 303, 313 and 323 K) and pH (3-10) on the Pb(II) & Cd(II) removal were also explored.

3.1 Introduction

Removal of heavy metals from wastewater is very important to reduce the environmental toxicant load. Heavy metals are non biodegradable and cause serious consequences when present in aquatic and soil ecological system. The pollutant in water hinders aquatic life[1] and bioaccumulation of pollutants in the ecosystem and their potential health risks are of great concern[2] such as multiple organ damages, change in cell cycle and may cause carcinogenic diseases[3]. From the economic, environmental, human, animal and microbial health perspective, removal of heavy metals from water is mandatory. Heavy metal's leaching is an important issue. From various sources including chemical industrial waste such as printing waste, battery waste, paper manufacturing, chemical manufacturing, food, pharmaceutical, textile,[4] smelting, commercial fertilizer, pesticides, sewage sludge, metal evaporation from water resource to soil and groundwater,[5] water get polluted with heavy metals.

Among the various heavy metal ions, lead and cadmium have been accepted as one of the main concern pollutants[6]. Porous materials are very effective for removal of these toxicants. At present, most of the available adsorbents are specific for a particular type of metal ion and hence can be useful for removal of only that one. Since water get polluted by different heavy metal contaminants; it would be useful to synthesize a single nanomaterial that can absorb/trap different types of heavy metal ions. Various metal oxides such as MgO, CuO, Fe_2O_3, ZnO, TiO_2 and MnO_2; can be utilized to make useful mesoporous nanomaterials[7]. These metal oxides are non-toxic and less expensive and therefore very useful to purify large water bodies.

Porous metal-oxides (MnO_2 and TiO_2) are very attractive for this purpose because of their surface active properties[8, 9]. Also, MnO_2 and TiO_2 shows promising catalytic properties and remarkable potential for waste water treatment to remove a wide range of metal ions (e.g. lead and cadmium)[10, 11]. In literature, it is found that MnO_2-coated MWCNTs were used for removal of Pb(II) from water using packed column and removal was measured up to 95%[12]. Zaman *et al*. in 2009 investigated the effect of phosphate complexation on Cd(II) adsorption by β-MnO_2 and maximum adsorption efficiency measured was 3.515×10^{-5} mol/g[13]. The MnO_2-loaded resin had been used as an adsorbent for lead and cadmium removal and the maximum removal efficiency was calculated as 80.64 mg/g for Pb(II) and 21.45 mg/g for Cd(II)[14]. Some research had been done on the removal of Cd(II), Cu(II), Ni(II), and Pb(II) from synthetic solutions using nanoparticle sorbents (TiO_2, MgO, and Al_2O_3) with a range of experimental approaches[7].

Flower-like TiO_2-graphene oxide was used for the removal of heavy metal ions from water. The removal capacity of TiO_2-graphene oxide was measured 88.9, 72.8 and 65.6 mg/g for Zn(II), Cd(II), and Pb(II), respectively[15]. The adsorption of Pb (II), Cu (II) and Zn (II) by TiO_2 can be accomplished from simulated polluted water and up to 94% removal was achieved[16]. The titania beads were used to remove Cr(VI), Cd(II), Cr(III), Cu(II), and Co(II) ions from simulated wastewater and the adsorption capacities were found to be 9.39, 8.94, 8.93, 8.40, and 7.62 $mg \cdot g^{-1}$, respectively[17]. So, from these studies, it is obvious that there is a huge demand to synthesize hierarchically porous MnO_2 and TiO_2 materials with the tunable high surface area and high selective adsorption efficiency. In spite of huge demand, most of the available materials are not user-friendly and eco-friendly. Mostly metal-oxide nanomaterials are available in powder form which has disadvantages since they make a miscible suspension with water. Therefore; for their extraction from solution, expensive high-quality filters, and instruments are necessary. So, in this regard, we tried to make hierarchically porous MnO_2 and TiO_2 metal-oxide monoliths (single rock like structure) for metal-ion adsorption which is cost-effective and user-friendly. The efficient removal of metal-ions using solid monoliths synthesized by nanocasting method has not been studied yet.

Metal-oxide monoliths with hierarchically porous structures can be prepared by using nanocasting process. In this method at first pores of the parental silica monoliths have been saturated with a choice of metal salt solution. Thereafter by heat treatments, the metal salt is converted to corresponding metal oxides. At the end, silica part gets removed by either KOH or NaOH[18]. This process has already been used to prepare porous nanomaterials and monoliths of carbon, NiO, TiO_2, Co_3O_4, SnO_2, MnO_2, ZrO_2, Cr_2O_3, In_2O_3, CeO_2, Fe_2O_3, Y_2O_3 and various or mixed-oxides[19-23]. Ordered porous oxides because of their large surface areas, large pore volumes and ordered pore networks have a wide range of potential applications in energy storage, nanoreactors, semiconductors, electronic devices, catalysis and gas sensors[24]. The application of these metal oxide monoliths is highly dependent on their pore diameter as well as their surface properties. By altering the pore diameter of the parental monolith, it is possible to change the porous structure of progeny metal oxide monoliths. The formation of meso/ micropores is highly dependent on the nature and concentration of structure directing agents (e.g. surfactants/water soluble polymers).

As the metal oxide monoliths are the inverse replicas of parental monoliths, so it is possible to control the porosity of the replica monolith by changing the porosity of parent silica monoliths. By exploring this fact, we have synthesized various pore size controlled TiO_2 and MnO_2 monoliths by a nanocasting method using parent mesoporous silica monoliths. To explore the effect of pore diameter/surface area on the application of metal oxide monoliths, we have thoroughly studied the adsorption efficiency of these metal-oxide monoliths for the removal of metal ions such as Pb(II) & Cd(II). The effects of contact time, temperature, pH and adsorbent concentration for removal of metal ions were also explored. The kinetic and equilibrium studies of the monoliths were done by Langmuir and Freundlich Isotherms.

3.2.1 Synthesis of silica monoliths

TEOS (8.1 ml) was added to a mixture of PEG (9.54×10-4 M) and 1.38 ml nitric acid (30%) solution in 8.25 ml distilled water and then mixed by stirring at room temperature for 5-10 min until a translucent sol was obtained. After that, 1.3 g CTAB was added to the sol with continuous agitation until the surfactant was dissolved completely. Here, CTAB was used as surfactant template for the formation of mesoporous structures in monoliths. The obtained sol was transferred to microplates and 8-12 h time was required for sol to gel formation at 40°C. Thereafter aging of the gel was done at 40°C for 72 h. To increase the degree of condensation and stability of the SiO_2 monoliths, the solvent exchange was performed. Silica monoliths were soaked in (1M) NH_4OH solution for 9 h at 90 °C. Later, SiO_2 monoliths were acidified by using (0.1 M) HNO_3 solution. After washing with de-ionized water, monoliths were kept in an oven at 40 °C for 4-5 days for proper drying. Finally, freshly prepared monoliths were calcined at 550 °C for 5 h using 1 K/min heating ramp.

3.2.2 Synthesis of MnO_2 and TiO_2 monoliths

SiO_2 monoliths were degassed using a vacuum pump and then impregnated with aqueous metal salt solutions [3.1 M $Mn(NO_3)_2 \cdot 4H_2O$ and 2.7 M $TiCl_4$] by incipient wetness. After the first cycle of impregnation, monoliths appeared transparent. After that, the monoliths were heated for 10 h at 150 °C and 100 °C for MnO_2 and TiO_2 respectively. These two steps were repeated for 5 times. Afterward, composites of MnO_2 were calcined at 300 °C for 6 h with 1 K/min heating ramp. Finally, silica part was leached out from both of the composites to get metal-oxide monoliths by using NaOH (2 M). By changing the chain length of polymer (PEG), it

is possible to alter the morphology of the silica monoliths along with the morphology of the metal-oxide monoliths as well. Synthesized monoliths were in the cm range scale (0.5 cm in diameter and 0.8 cm in length). The final MnO_2 monoliths appeared black while the TiO_2 was beige in color.

3.2.3 Characterization of monoliths

As synthesized silica and TiO_2 and MnO_2 monoliths were characterized by various techniques; details of the techniques are given in **Chapter 1, section 1.9**

3.2.4 Adsorption Study

Adsorption efficacy of synthesized adsorbents was evaluated through AAS; detail procedure has been given in **Chapter 1, Section 1.10.1**

3.3 Results and discussion

As mentioned above nanocasting is a simple method for synthesis of porous metal-oxide monoliths. For stabilization of mesoporous silica monoliths, the water-soluble polymer is needed because they have a direct effect on hydrophilicity and flexibility of the porous structure. Bimodal interconnected porous structures obtained by phase separation and gelation after interaction (hydrogen bonding) between gelling silica/CTAB micelles and polymer. White gels having bimodal structures can be obtained by addition of polymer with increasing chain length due to a decrease in phase separation time[25].

Table 3.1: Textural characteristics for the silica and metal-oxide monoliths determined from nitrogen sorption measurements.

Sample Name	MW of PEG (g mol^{-1})	BET area (m^2 g^{-1})	Pore diameter (nm)	Pore volume (cm^3 g^{-1})
SiO_2-40	4000	691	13.2	2.3
SiO_2-350	35000	761	18.4	1.4
MnO_2-40	4000	19	47.7	0.2
MnO_2-350	35000	27	25	0.1
TiO_2-40	4000	140	18	0.6
TiO_2-350	35000	220	9.4	0.5

In this regard, PEG with different chain length/molecular weight (4000 and 35000 g/mol) had been used as the water-soluble polymer. In Fig. 3.1a, the nitrogen sorption isotherms of the

SiO_2, MnO_2 & TiO_2 monoliths with a different chain length of PEG are plotted. The surface area and pore volume decreased whereas pore size increased when SiO_2 monoliths were replaced by metal oxide monoliths (Table-3.1). For all synthesized samples, type IV isotherms could be observed as confirmed from the IUPAC classification.

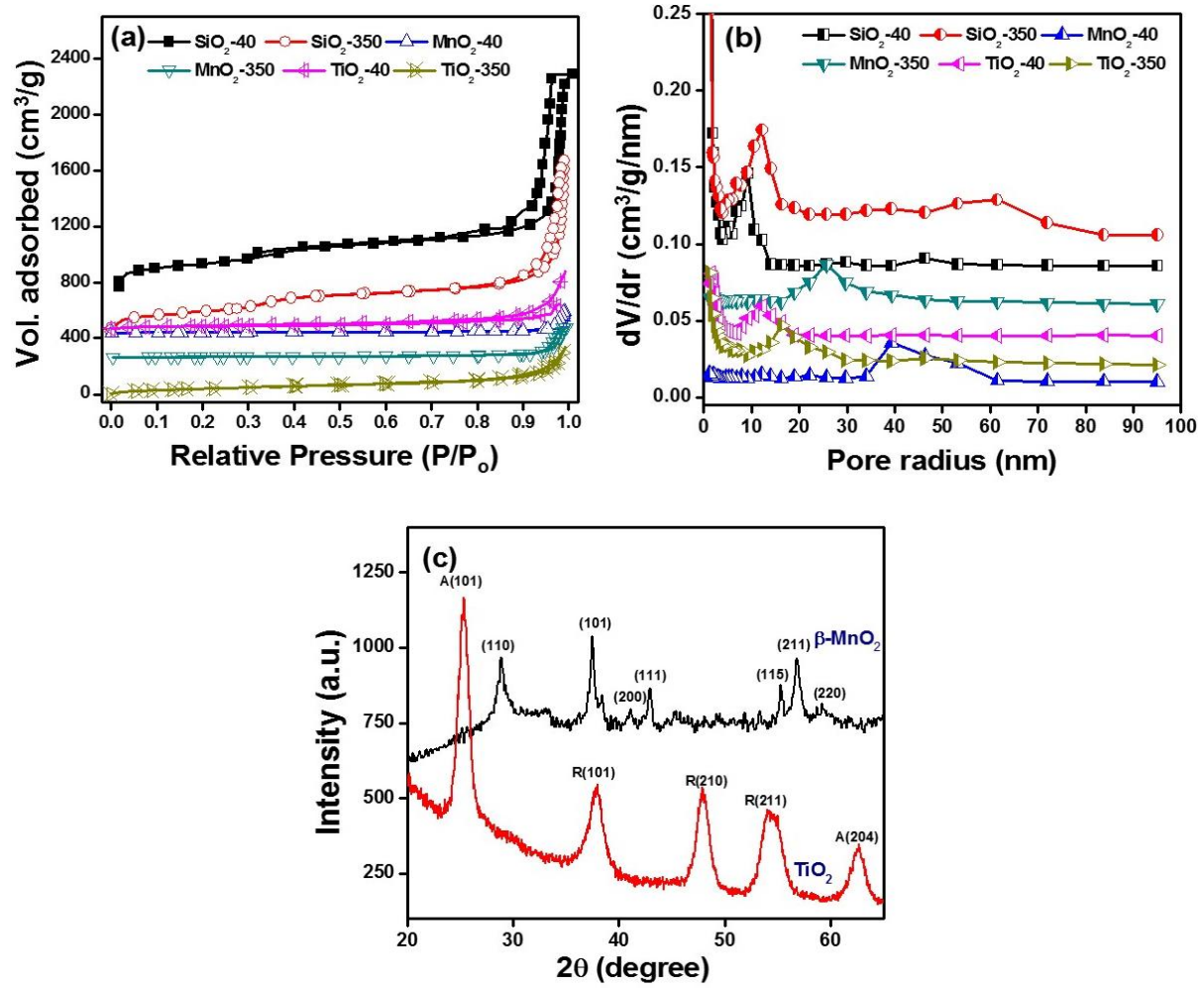

Fig. 3.1: a) Nitrogen adsorption-desorption isotherm, b) pore size distribution (by BJH method) plots for the monoliths and c) XRD pattern of metal-oxide monoliths.

The uniformity of pore sizes and shape were defined by the sharp adsorption and desorption branches in H1 hysteresis loops of the synthesized hierarchically porous silica monoliths. Fig. 3.1b shows the pore size distribution by using the Barrett–Joyner–Halenda (BJH) method of as synthesized monoliths, which confirms the mesoporosity nature of the monoliths.

After the removal of silica part, the crystal phase composition of the metal-oxide monoliths was determined by XRD analysis.

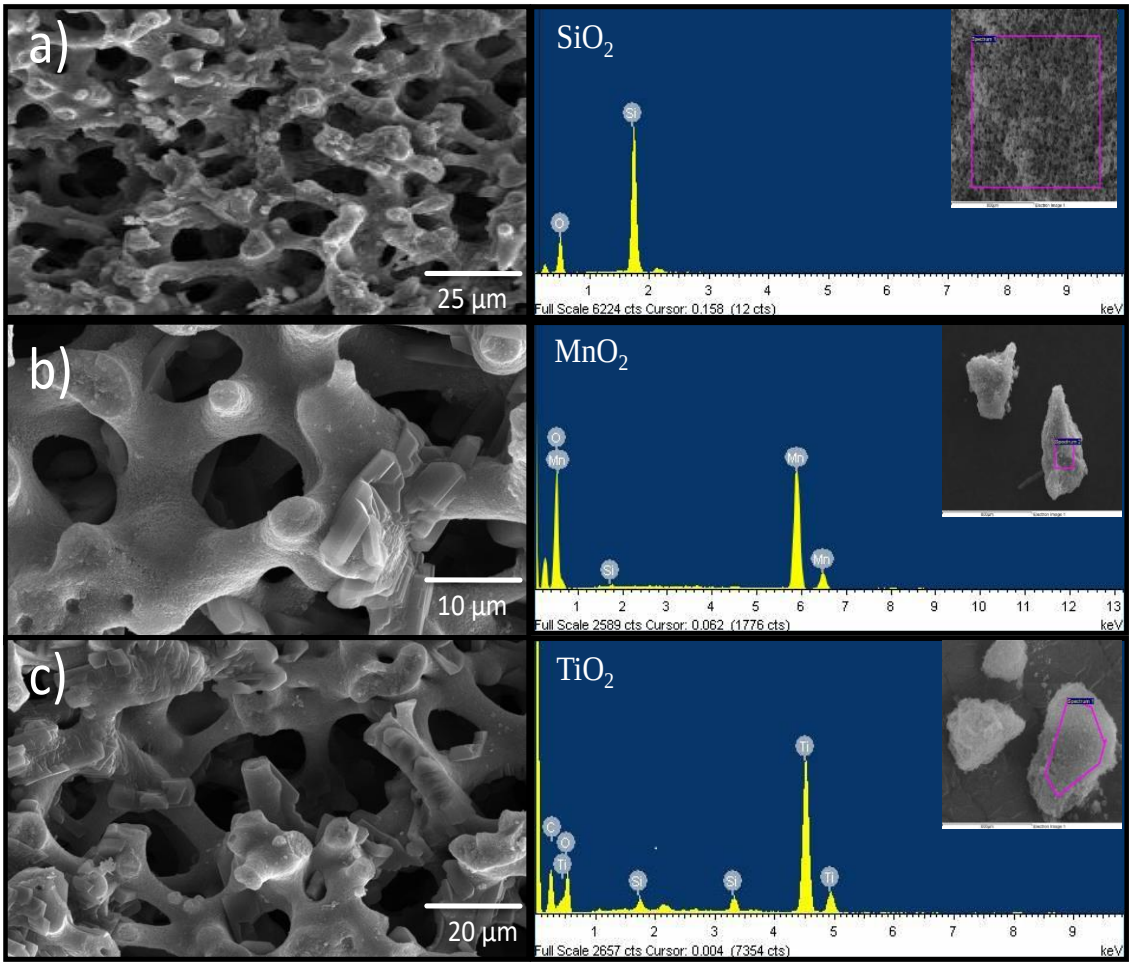

Fig. 3.2: FESEM images and corresponding energy-dispersive spectrum of a) SiO_2 – 350 b) MnO_2- 350 and C) TiO_2- 350 monoliths.

Fig. 3.1c shows the diffraction patterns of metal-oxide monoliths. It was observed that after calcining at 300 °C, monoliths impregnated with manganese nitrate resulted in the formation of β-MnO_2. The diffraction peaks were confirmed by JCPDS card No. 24-0735[26]. While TiO_2 was obtained from $TiCl_4$ and the peaks for rutile and anatase were confirmed by JCPDS card No. 21-1272[27].

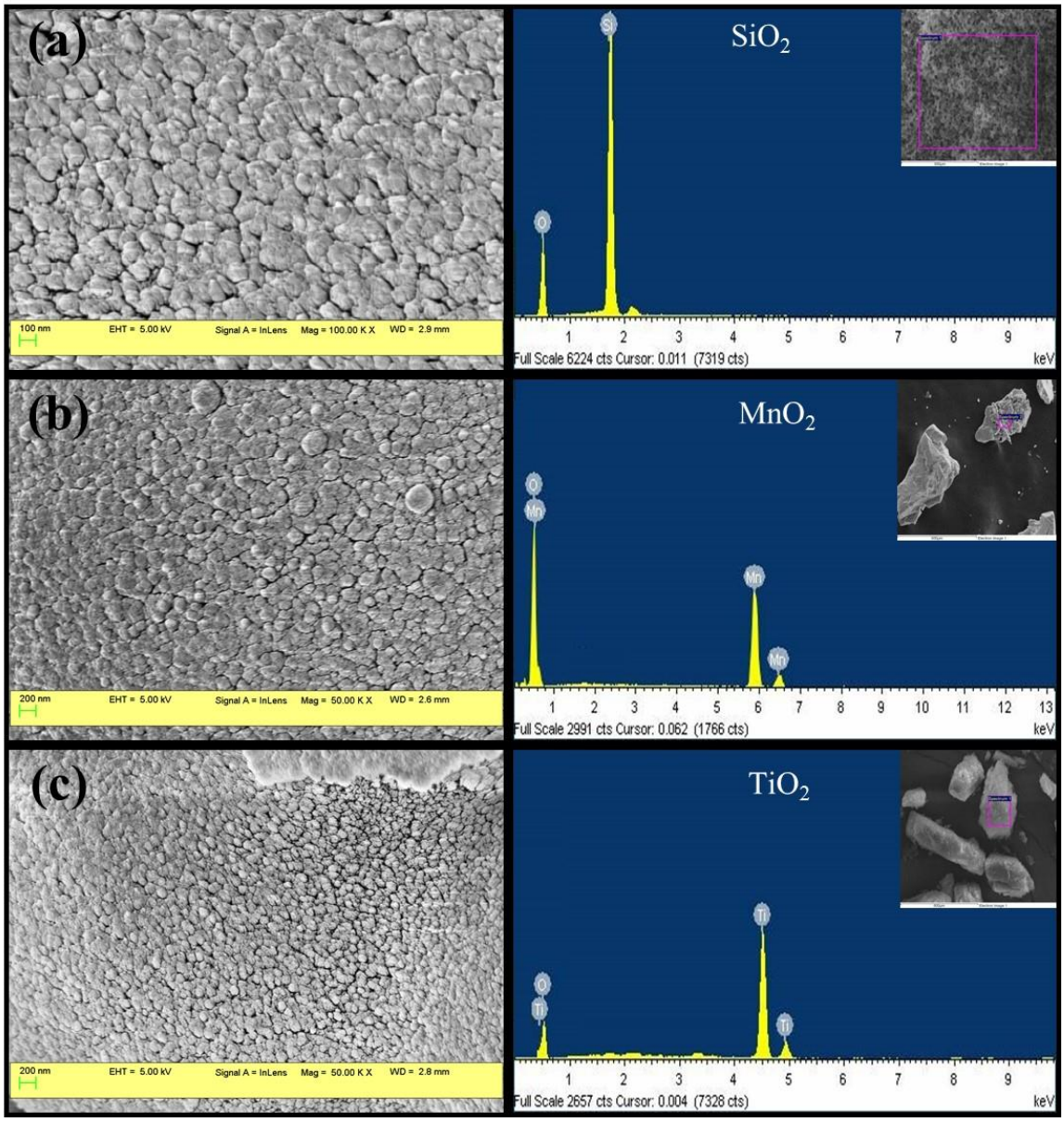

Fig. 3.3: FESEM images and corresponding energy-dispersive spectrum of a) SiO_2 – 40, b) MnO_2- 40 and c) TiO_2- 40 monoliths.

Mechanically steady metal-oxide monoliths were retrieved by nanocasting method upon the leaching of the silica portion. Influence on the homogeneity of monoliths structure of the SiO_2, MnO_2 and TiO_2 was analyzed using FESEM. Fully interconnected pores were formed by the phase separation in metal-oxides monoliths. The porous structures of the monoliths with

different PEG are shown in Fig. 3.2 (molecular weight 35,000 series) and in Fig. 3.3 (molecular weight 4,000 series).

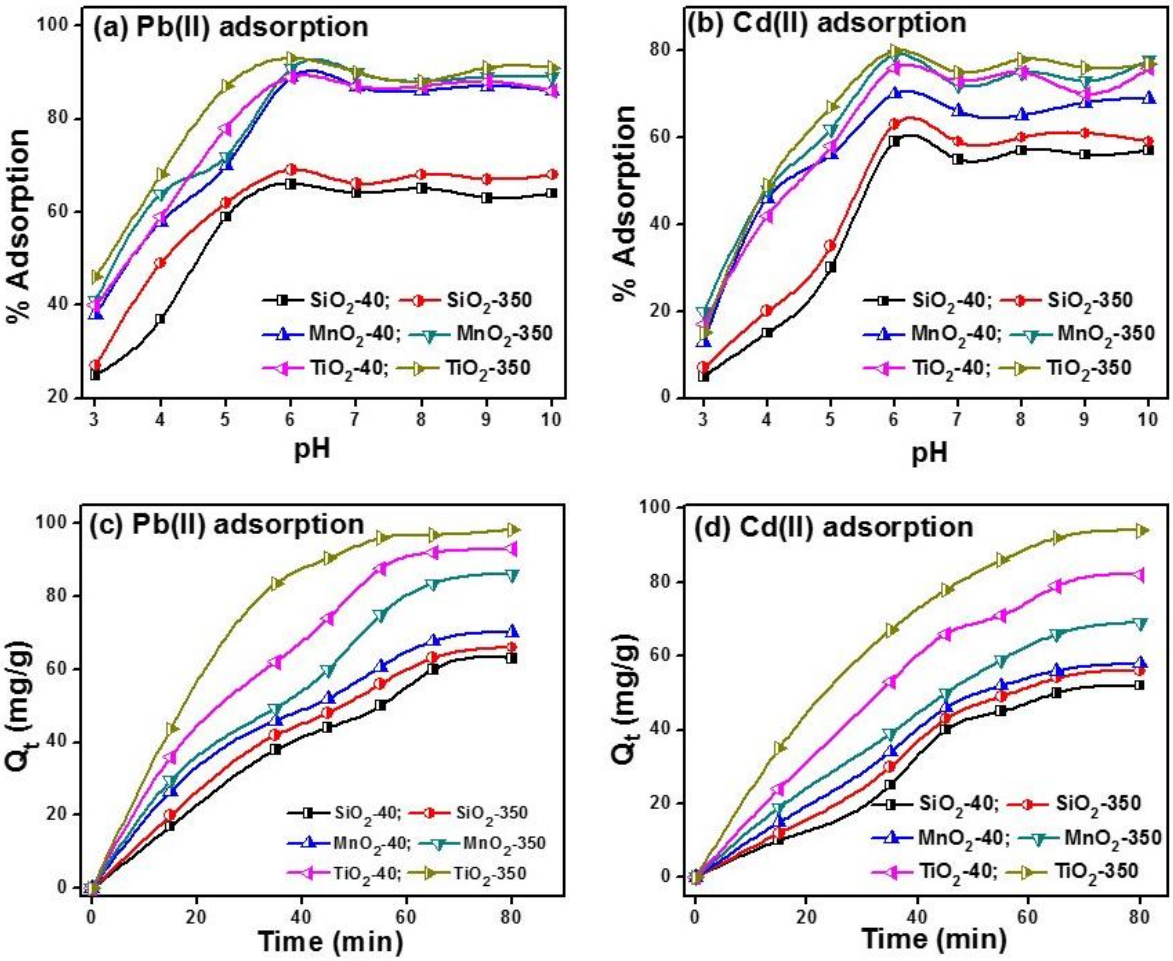

Fig. 3.4: Adsorption capacity of silica and metal oxide monoliths to show effect of pH on the metal ions a) & b) and effect of time on with initial concentration (100 mg/L) c) & d).

There appear to be fine mesoporous structures within the walls, but higher magnification images are difficult to obtain due to the charging of the sample. Metal-oxide monoliths have rough mesoporous walls as compared to silica monoliths. The purity of the metal oxide monoliths (almost complete removal of SiO_2) was confirmed by EDS analysis (Fig. 3.2 and 3.3). Uniform distribution of the precursor metal salts throughout the core of the SiO_2 monoliths was responsible for chemical homogeneity.

3.3.1 Adsorption studies

3.3.1.1 Effect of pH

Adsorption of Pb(II) & Cd(II) in the pores of monoliths depends on the pH of the solution, because of the degree of ionization, surface binding sites of adsorbents and the chemistry of adsorbates. Adsorption of Pb(II) & Cd(II) by silica and metal oxide monoliths were studied at a pH range from 3 to 10. pH values were adjusted by addition of either NaOH or HNO_3 in the synthetic solution of Pb(II) & Cd(II)[28-30]. Fig. 3.4 (a-b) shows plots for the effect of pH on Pb(II) & Cd(II) adsorption efficiency of metal-oxide monoliths. Maximum metal ion removal was observed at pH 6 for all the monoliths. Under the acidic conditions (at low pH), the surface of the adsorbents was surrounded by H^+ ions that compete with metal ions, which prevented the metal ions from approaching the binding sites on the adsorbent. Whereas at high pH values, metal ions were adsorbed due to the negatively charged ions. With the increase of pH, metal-oxides form deprotonated oxides and results in an increase in adsorption of metal ions on the surface of metal oxides due to which electrostatic repulsion force between surface and metal ions decreases.

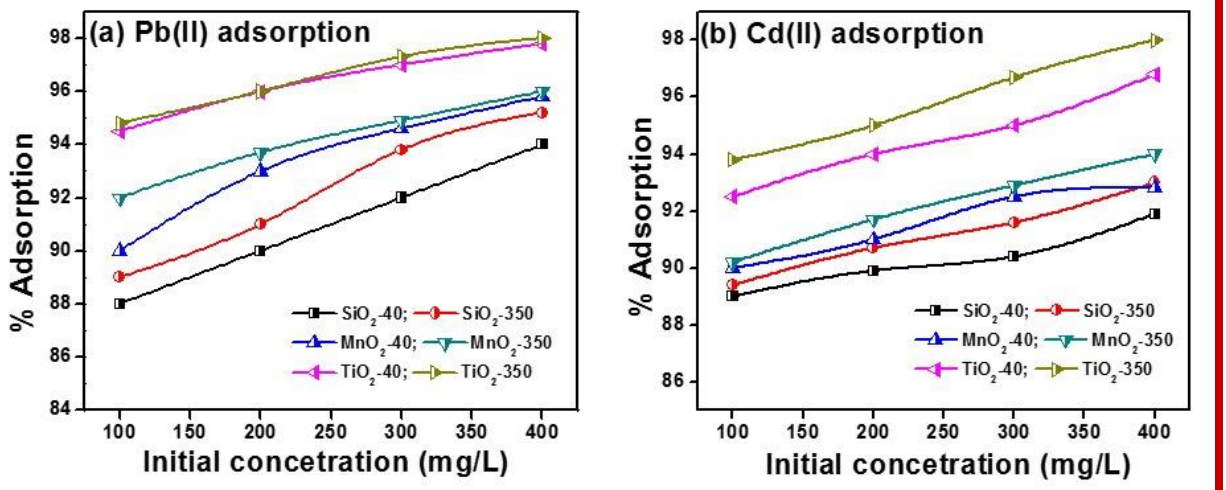

Fig. 3.5: Effect of metal ions concentration a) Pb(II) and b) Cd(II) on the adsorption capacity of metal oxides.

3.3.1.2 Effect of contact time

The effect of contact time was analyzed between 15 to 80 min for the adsorption of metal ions by monoliths (Fig. 3.4(c-d)). The initial concentration of metal salts was kept 100 mg/L at

pH 6. The equilibrium time depends on upon the initial concentration of Pb(II) & Cd(II) ions in the solution. Pb(II) & Cd(II) ions were quantitatively absorbed by the metal oxide monoliths from the synthetic solution even after a short time of exposure (<15 min). Since there was no significant increase in metal ions sorption after 65 min, the reaction time of 80 min was kept for auxiliary experiments[31, 32].

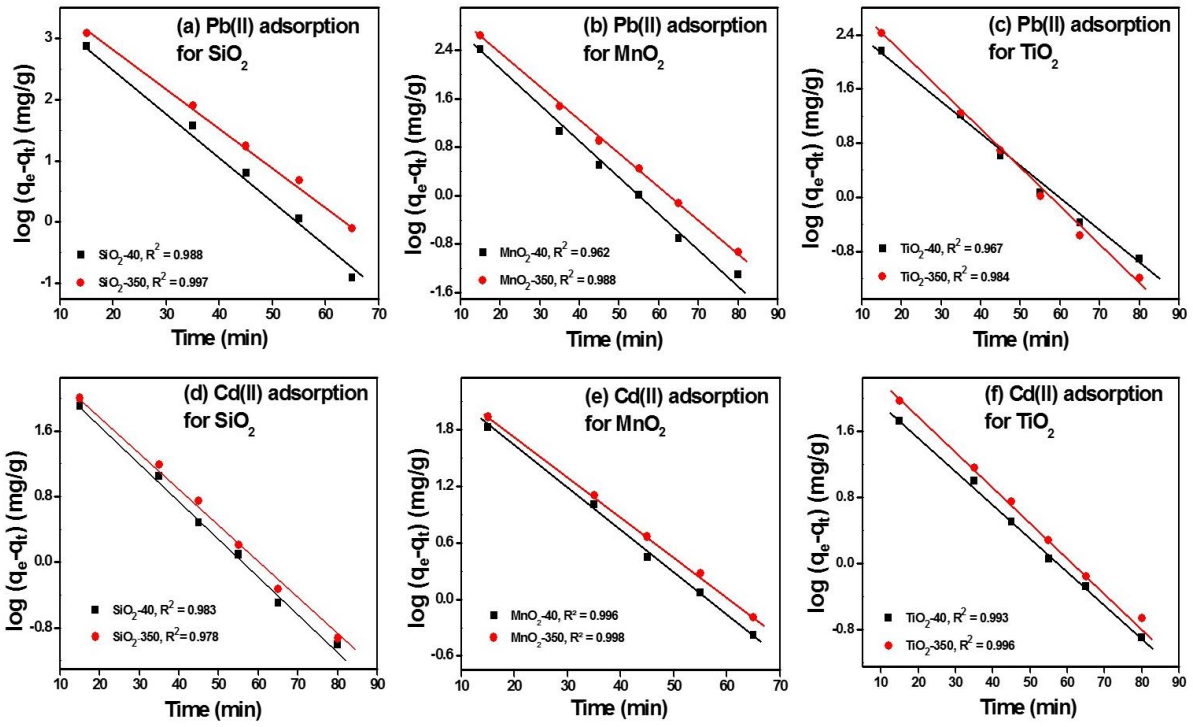

Fig. 3.6: Linear fit plots of pseudo-first-order for the adsorption of Pb (II) and Cd (II).

3.3.1.3 Effect of metal ions concentration

Effect of the metal ions concentration on the monolith (0.02 g) dependent adsorption process was studied by changing the initial Pb(II) & Cd(II) concentrations in the range of 10-50 mg/L at most effective pH (6) and at room temperature (Fig. 3.5). The adsorption of metal-ions at different concentrations was fast during the early stage, which slowly decreases with further adsorption process until equilibrium was reached. Fast adsorption at the small time was due to the large availability of adsorption sites on the surface of metal-oxides. The results confirmed that the removal efficiency of metal ions was directly proportional to the initial concentration of the metal ions[33, 34]. The removal percentage of Pb(II) & Cd(II) by SiO_2, MnO_2, and TiO_2

monoliths were found to be 88-94%, 94-96% and 92-98% respectively of different metal ion concentration (Fig. 3.5).

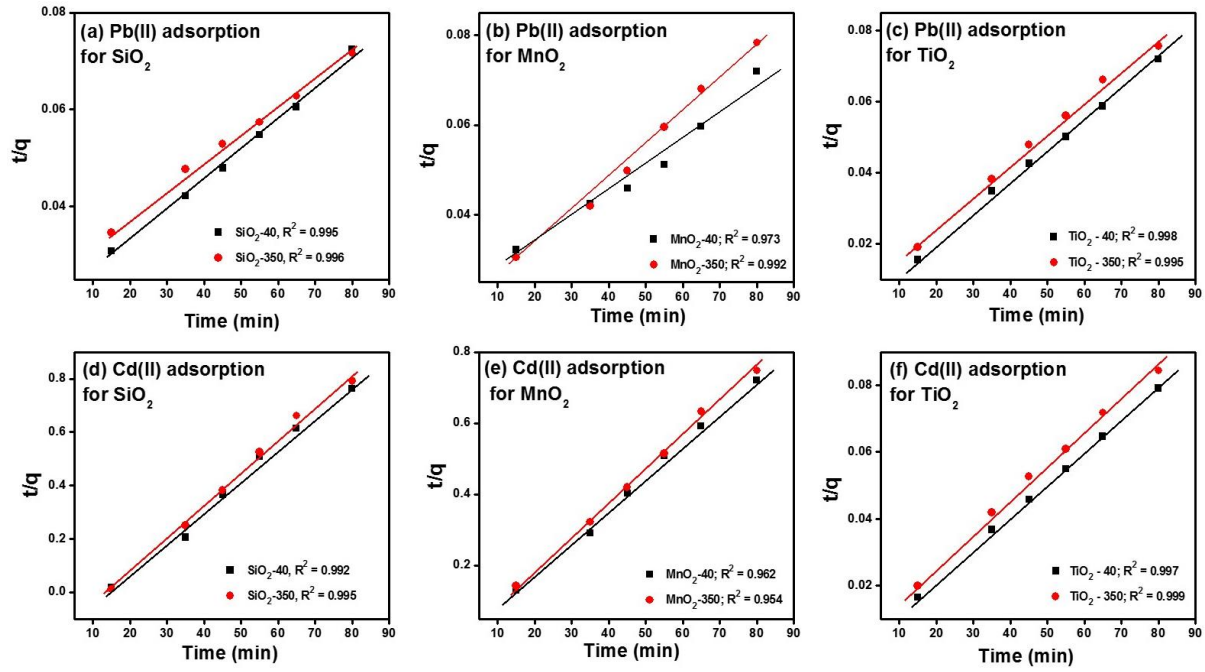

Fig. 3.7: Linear fit plots of pseudo-second-order for the adsorption of Pb(II) and Cd (II).

3.3.2 Adsorption Kinetics

The kinetics of Pb(II) & Cd(II) adsorption on metal oxides were also evaluated using Lagergren's first order rate equation and pseudo-second-order kinetic model[35, 36]. The Lagergren's first-order rate equation is usually used to predict adsorption kinetics and is expressed as;

$$\log(q_e - q_t) = \log(q_e) - \frac{K_1}{2.303} t \qquad (3.1)$$

The pseudo-second-order rate equation is expressed as;

$$\frac{t}{q_t} = \frac{1}{k_2 q_e^2} + \frac{t}{q_e} \qquad (3.2)$$

where q_e and q_t are a number of metal ions (mg/g) adsorbed at equilibrium and at any given time t (min) respectively. While K_1 is the rate constant for the pseudo-first order reaction for adsorption (min^{-1}) and K_2 is the rate constant for pseudo-second order reaction (g/mg min)[37].

Linear fit plots of pseudo-first order and pseudo-second order for SiO_2, MnO_2 and TiO_2 monoliths on the adsorption of Pb(II) & Cd(II) ions are shown in Fig. 3.6 and 3.7, respectively. The pseudo-second order kinetic model coordinates well with the adsorption of metal ions, which suggested that the metal-ions adsorption process might be mostly controlled by chemisorption.

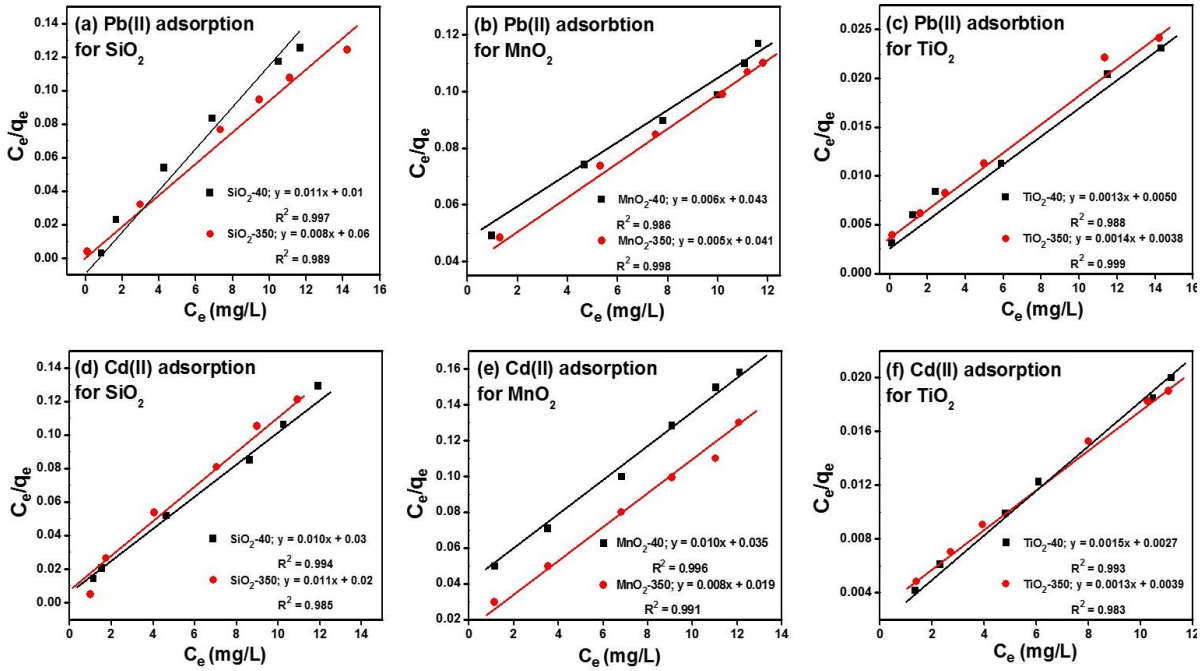

Fig. 3.8: Langmuir isotherm plot for Pb(II) and Cd(II) adsorption on SiO_2 and metal oxide monoliths.

3.3.3 Adsorption isotherms

Adsorption isotherm gives proper quantitation of effectiveness of adsorption. The relationship between the concentration of adsorbed and dissolved adsorbate at equilibrium along with the interactive behavior between the adsorbate and adsorbent can also describe by adsorption isotherm. In this study, Langmuir and Freundlich isotherm models were used to analyze the adsorption mechanisms, through which experimental results of metal ions can be explained in a wide range of concentrations.

The Langmuir equation is expressed as follows;

$$\frac{C_e}{q_e} = \frac{1}{Q_o b} + \frac{C_e}{Q_o} \quad (3.3)$$

where the adsorption capacity at equilibrium is q_e (mg/g) and the maximum amount of the Pb(II) & Cd(II) adsorbed per unit weight of the adsorbent is Q_0 (mg/g). When the surface is entirely covered with metal ions, Q_0 represents the adsorption capacity, helping in the assessment of adsorption act of different adsorbents. Langmuir equilibrium constant (b) which is interrelated to the similarity of the connecting spots, shows the bond energy for the adsorption reaction. The linear plots of C_e/q_e vs. C_e propose the validity of the Langmuir isotherms and the values of Q_0 and b are obtained from slope and intercepts of the plots[38, 39]. Plots for Langmuir isotherm for adsorption on silica and metal-oxide monoliths for Pb(II) & Cd(II) are shown in Fig. 3.8.

The Freundlich isotherm is a resultant model of multilayer adsorption on the adsorbent. It can be described as:

$$\log q_e = \log K_f + \frac{\log C_e}{n} \quad (3.4)$$

Freundlich constants, K_f ($mg^{1-1/n}L^{1/n}\ g^{-1}$) and n, depict the adsorption capacity and intensity, respectively[40]. Freundlich isotherm plot for Pb(II) and Cd(II) adsorption on SiO_2, MnO_2 and TiO_2 are shown in Fig. 3.9.

Although, SiO_2 monolith has high surface area resulted in a decrease in maximum adsorption. As, adsorption mechanism is generally based on an ion exchange or formation of bidentate binuclear surface complexes between metal oxides and metal ions, so metal oxides are more competent to hold other metal ions. In both cases (MnO_2 and TiO_2 monoliths), the bond between heavy metal ions and metal oxide surface is strong due to which metal oxides can adsorb metal ions from very diluted metal ion solutions. Therefore; in spite of having a lesser surface area, MnO_2 monoliths (in compared to SiO_2 monoliths) has maximum adsorption value almost as high as SiO_2 monoliths. The maximum adsorption capacities for Pb(II) & Cd(II) were described in Table 3.2. Monolayer adsorption capacity calculated from the Langmuir model indicates the better applicability due to higher values of correlation coefficients (R^2). Table 3.3 shows a comparison study of maximum sorption capacities of metal ions reported in the literature. Therefore, it could be conceived that the as synthesized metal oxide monoliths could be employed as an alternative adsorbent for Pb(II) & Cd(II) adsorption at low concentrations.

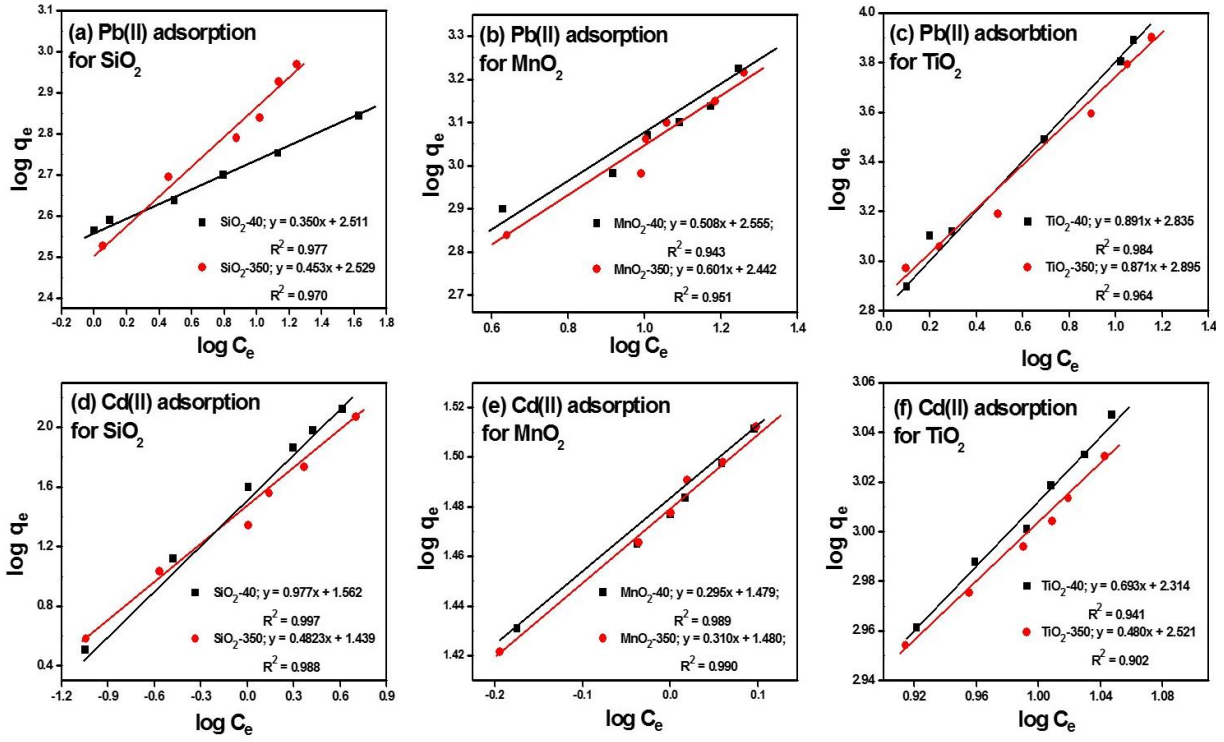

Fig. 3.9: Freundlich isotherm plot for Pb(II) and Cd(II) adsorption on SiO_2 and metal oxide monoliths.

Table 3.2: Langmuir and Freundlich constants and correlation coefficients for adsorption of Pb(II) & Cd(II) on metal-oxide monoliths.

Sample Name	Metal ions	Langmuir			Freundlich		
		Q_0*	b	R^2	K_f**	n	R^2
SiO_2-40	Pb(II)	90.9	1.1	0.997	383.7	6.02	0.983
	Cd(II)	100	0.3	0.998	36.47	1.02	0.997
SiO_2-350	Pb(II)	125	0.1	0.996	338.06	2.20	0.970
	Cd(II)	90.9	0.5	0.999	27.4	1.21	0.988
MnO_2-40	Pb(II)	166.6	0.13	0.995	358.9	1.96	0.943
	Cd(II)	100	0.28	0.999	30.13	3.38	0.989
MnO_2-350	Pb(II)	200	0.12	0.995	276.69	1.66	0.951
	Cd(II)	125	0.42	0.984	30.19	3.22	0.990
TiO_2-40	Pb(II)	769.2	0.245	0.988	683.9	1.12	0.984
	Cd(II)	667	0.555	0.993	206.06	1.44	0.941
TiO_2-350	Pb(II)	857	0.307	0.999	785.23	1.14	0.964
	Cd(II)	770	0.333	0.983	331.8	2.08	0.902

*(mg g^{-1}), **($mg^{1-1/n}L^{1/n}$ g^{-1})

Table 3.3: A comparative account of the adsorption efficiency of heavy metal ions by different metal-oxide nanostructures.

Adsorbents	Surface area (m^2/g)	Metal-ions	Maximum adsorption (mg/g)	Maximum adsorption %	Conditions	References
TiO_2 nanoparticles	--	Pb(II) Cd(II)	--	44.7 25	Time- 60 to 90 min	[7]
ß-MnO_2	83.5	Cd(II)	12.9	--	Temp-20-50°C pH-4-6	[13]
GO-TiO_2	--	Pb(II) Cd(II)	65.6 72.8	--	pH- 5.6 Time- 12h	[15]
Nano- TiO_2	--	Pb(II)	--	100	pH-2	[17]
$MnFe_2O_4$- G composite	79.30	Pb(II) Cd(II)	100 76.9	--	pH- 2-8 Time-220 min	[41]
Silica nanotubes (SNT)	--	Pb(II)	42.85	--	pH-4, 7, 9, Temp-30°C Time-240 min	[42]
Mesoporous silica	198.3	Cu(II)	36.38	--	pH-2-7	[43]
Silica monoliths	565	Cu(II)	145.98	--	pH-7	[44]
SiO_2 monolith	761	Pb(II) Cd(II)	125 90.9	--	pH-6 Temp-30°C	Present study
MnO_2 monolith	27	Pb(II) Cd(II)	200 125		Time-80 min	
TiO_2 monolith	220	Pb(II) Cd(II)	857 770			

3.3.4 Effect of temperature on adsorption

To determine the effect of temperature on the surface of hierarchically porous metal oxides for Pb(II) & Cd(II) adsorption, adsorption experiments were monitored at various temperatures (303, 313 and 323 K). Increase in temperature results in a decrease of the values of $\ln(q_e/C_e)$ and also 1000/T which specifies the exothermic nature of the adsorption process[45]. At different temperatures, the values of $\ln(q_e/C_e)$ are treated according to Van't Hoff equation;

$$\ln\left(\frac{q_e}{C_e}\right) = \frac{-\Delta H}{RT} + \frac{\Delta S}{R} \qquad (3.5)$$

where R is the universal gas constant (8.314 $Jmol^{-1}K^{-1}$) and T is the absolute temperature. The slope ($\Delta H/R$) and intercept ($\Delta S/R$) were evaluated from the plot between $\ln(q_e/C_e)$ and 1/T as

shown in Fig. 3.10. At higher temperature, the adsorption process was also increased as Pb(II) and Cd(II) were adsorbed on the surface of mesoporous metal oxides. Gibbs free energy (ΔG) for adsorption of metal ions was calculated as of the following relation; (3.6)

$$\Delta G = \Delta H - T\Delta S$$

Table 3.4 shows the negative values of ΔG which confirms the spontaneity of the adsorption reactions.

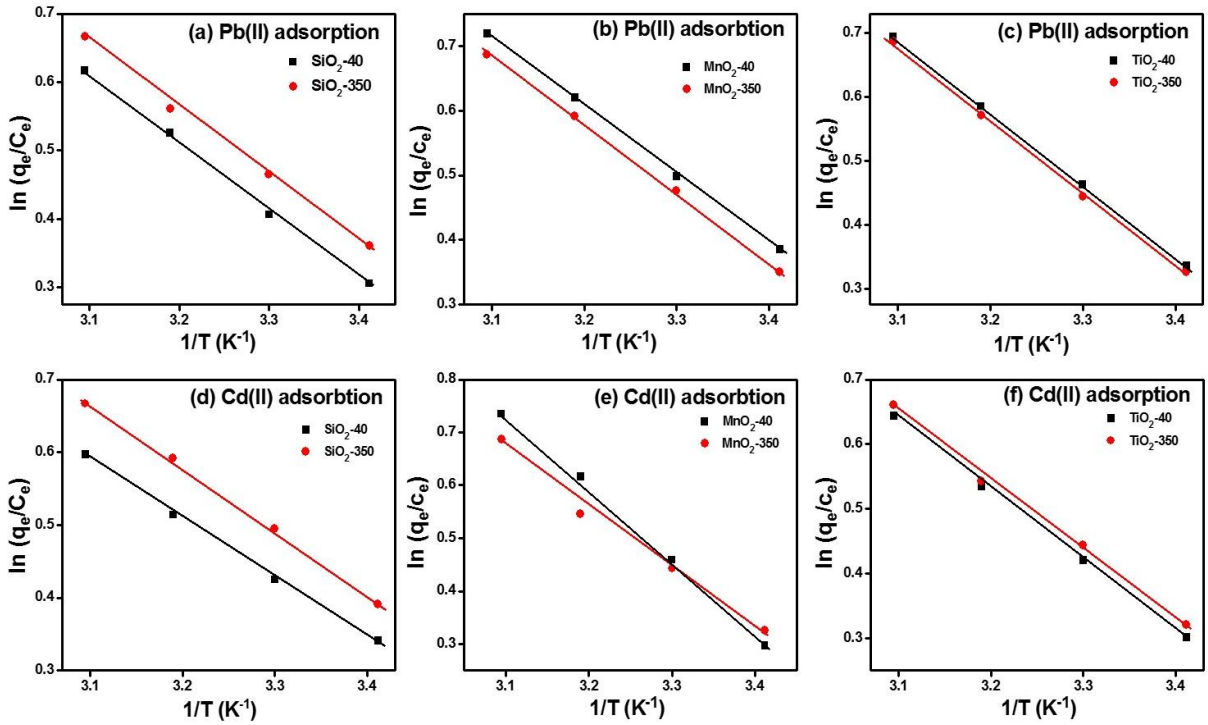

Fig. 3.10: Van't Hoff plots for the adsorption of Pb(II) and Cd (II).

Table 3.4: Thermodynamic parameters for Pb(II) & Cd(II) removal at different temperatures.

Sample Name	Metal Ions	ΔH (kJ mol^{-1})	ΔS (J mol K^{-1})	ΔG (kJ mol^{-1})		
				303(K)	313(K)	323(K)
SiO_2 40	Pb(II)	9.9	36.83	-8.91	-12.5	-16.2
	Cd(II)	8.07	30.92	-9.89	-12.98	-16.07
SiO_2 350	Pb(II)	9.95	36.16	-6.4	-10.06	-13.68
	Cd(II)	8.72	33.72	-11.59	-14.9	-18.34
MnO_2 40	Pb(II)	7.42	29.23	-11.4	-14.3	-17.2
	Cd(II)	7.53	28.56	-8.38	-11.2	-14
MnO_2 350	Pb(II)	9.54	36.15	-10.59	-14.13	-17.74
	Cd(II)	9.2	34.82	-10	-13.5	-16.9

TiO_2 40	Pb(II)	8.16	30.63	-8.05	-11.1	-14.17
	Cd(II)	8.42	32.18	-10.08	-13.3	-16.5
TiO_2 350	Pb(II)	8.55	32.49	-9.6	-12.9	-16.19
	Cd(II)	7.79	30.4	-11.1	-14.2	-17.2

3.3.5 Reusability

As stated in above, a strong bond formed between metal-oxides and metal ions at the time of adsorption, which is essential for complete removal of metal ions from the water. In this case, no specific filtration techniques are required for metal-oxide extraction due to its large size. Also, the metal oxide monoliths possess a robust and strong mechanical structure that can sustain water flow for extended periods of time, which will increase the adsorption capacity. The micrometer-sized overall structure with mesoporosity of monoliths provides the necessary mechanical robustness against wear and tear; while their nanostructure provides the high surface area as well as the high removal capacity for heavy metal ions.

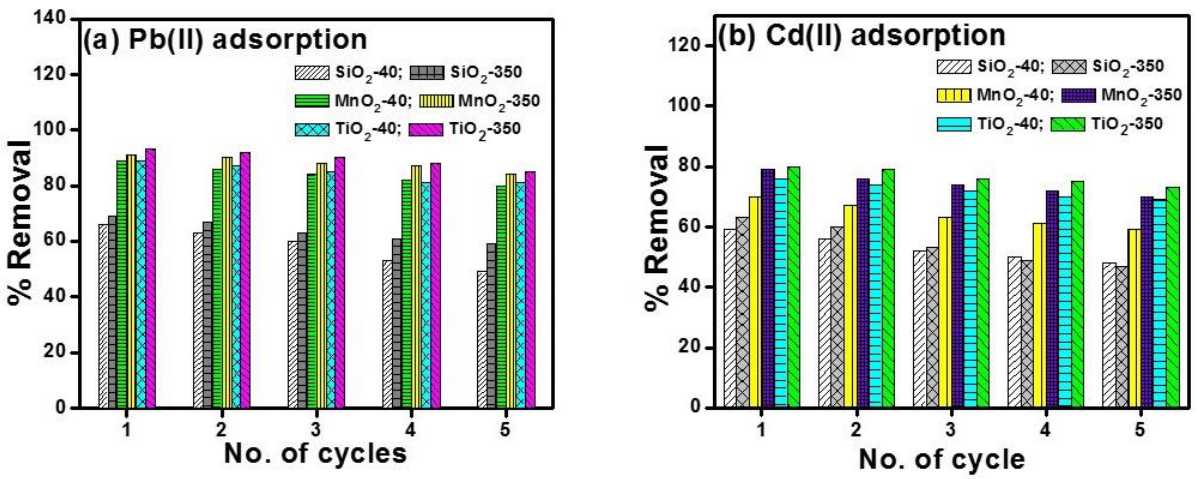

Fig. 3.11: Percentage removal against number of cycles (a) for Pb(II) and (b) for Cd(II) ions.

Though regeneration or reusability of metal oxide bear great challenges, still, by treating the saturated metal-oxides by 2M NaOH for 5 h, moderately regenerated metal-oxides can be obtained[46]. Here, we have checked the reusability of synthesized monoliths for 3 cycles and observed that the removal efficiency decreases up to 35-40% (Fig. 3.11).

3.4 Conclusion

Two different high surface area SiO_2 monoliths were turning out to porous MnO_2 and TiO_2 monoliths via nanocasting method. Hierarchically porous metal oxide monoliths exhibited excellent adsorption performance for Pb(II) & Cd(II). The adsorption studies were conducted in different batches. The removal percentage of Pb(II) & Cd(II) by SiO_2, MnO_2, and TiO_2 monoliths were observed 88-94%, 94-96% and 92-98%, respectively. Thermodynamic studies on the surface of hierarchically porous metal oxides for Pb(II) & Cd(II) adsorption were monitored at various temperatures (303, 313 and 323 K). Negative ΔG value suggests that the adsorption process was spontaneous. Synthesized monoliths are in the cm range scale (0.5 cm in diameter and 0.8 cm in length) which gave a unique advantage in the form of efficient and low-cost recovery over existing systems. Porous monoliths with large structure are highly efficient for heavy metal ions removal and results were found to be comparable or better than other metal oxide nanocomposites in literature. These advantages will make the nanocasted metal oxide monolithic system a potential candidate for development of a user-friendly, low-cost device for the treatment of large polluted water bodies.

<u>Section-B</u>: Mesoporous ZnO and TiO_2@ZnO Monoliths for Removal of Heavy Metal Ions from Aqueous Solution

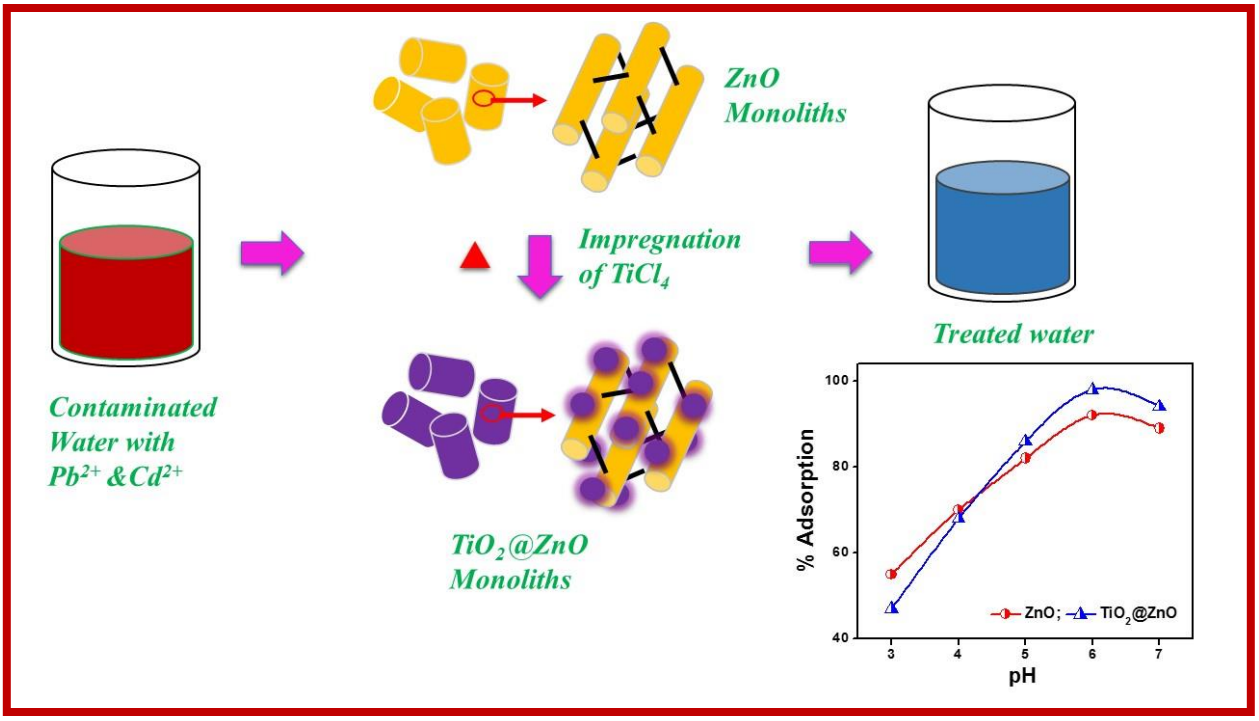

In this chapter, robust, mesoporous ZnO & TiO_2@ZnO monoliths with the specific surface area (120-332 mg^2/g) were synthesized via nanocasting process and their performance as an adsorbent for removal of Pb(II) and Cd(II) ions from water was successfully evaluated. The adsorption data shows better fit at pH 6 to Freundlich isotherm model. The maximum adsorption efficacy of Pb(II) ions based on monolayer adsorption was found to be 909 and 1250 mg/L for ZnO and TiO_2@ZnO monoliths, respectively whereas the maximum adsorption efficacy of Cd(II) ions based on monolayer adsorption was found to be 833 and 1000 mg/L for ZnO and TiO_2@ZnO monoliths respectively. Besides, used mesoporous ZnO & TiO_2@ZnO monoliths could be efficiently reused for at least three times after treatment with NaOH. The high uptake capacity for Pb(II) and Cd(II) ions with good reusability of ZnO & TiO_2@ZnO monoliths made them a potentially attractive adsorbent.

3.5 Introduction

Shortage of drinking water became a serious matter worldwide in consequence of a change in a global climate model. Raw sewage waste containing dyes, heavy metal ions and other toxic compounds from industries get directly released into the environment without any treatment or extraction of the harmful compounds due to which the main source of drinking water e.g. lakes, river and ground water get contaminated[47, 48]. Heavy metals (like lead and cadmium), are counted as most toxic elements among the priority pollutants because of their non-degradable and accumulative nature[49]. To overcome the ongoing drinking water shortage, researchers are working on to find a conventional method for waste water treatment prior to discharge. Till now, a few of conventional methods like reverse osmosis, ion exchange, ultra-filtration, and precipitation have been encountered for metal ions removal with specific disadvantages such as high cost of treatment, incomplete removal or production of high concentration of waste, the complexity of treatment and high energy requirements[14, 50, 51].

Adsorption method is tested as one alternative effective process without chemical degradation of solid adsorbents used for metal ion removal from water. Some advantages like high efficiency, most effective, sludge free, insensitivity to toxic material made adsorption techniques most apt to work[12]. Numerous adsorbents like zeolites, metal oxides, clays, functionalized polymers, activated carbons, etc. have been well-known and verified for the adsorption of heavy metal ions[52]. Nowadays, metal-oxide based nanomaterials are considered as suitable material for water treatment. Despite huge demand, most of the available nanomaterials are not user-friendly and eco-friendly. Also, separation of the metal-oxides from aqueous solution is very challenging because of nanoscale particle size. Moreover, metal-ions at the time of absorption occupied most of the surface of nanomaterials, due to the large size of metal ions, adsorption efficacy gets decreased. In recent years, substantial research has been focused on to encounter mesoporous adsorbents with high adsorption capacity and low cost.

For adsorption of heavy metal ions, mesoporous metal oxides with the high specific surface area, great density, and uniform pore size distribution can act as unprecedented adsorbents. In past few years, worldwide research gets focused on structures with hierarchically ordered porous material that combine mesopores with macropores like silica, carbon, and metal-oxides. The hierarchically ordered porous monolithic system will act as an advantage due to

large size, high porosity in consequence of bimodal porous nature[53]. Even though numerous papers have been published on heavy metal ions adsorption by using mesoporous structure, but only a few are focused on the synthesis of mesoporous metal-oxides in monolithic form like titanium oxide (TiO_2) and zinc oxide (ZnO) as adsorbents. TiO_2 and ZnO, both metal-oxide individually has advantages of chemical and physical stability, ease of availability, low cost, high surface area and porosity [54]. The coupling of these two metal oxides enhanced individual and combined properties. TiO_2 and ZnO heterojunctions has been well reported in the literature but most are focused on photocatalytic reactions and photovoltaic processes[55-57] but not a single has reported the adsorption efficacy. Therefore, for the first time, we have reported ZnO core - TiO_2 shell monolithic system having both mesoporous and microporous nature, synthesized via nanocasting method. The adsorbents prepared in this work are eco-friendly with low cost and high surface area. The purpose of this finding was to analyze the adsorption efficacy of both ZnO and TiO_2@ZnO for removal of Pb(II) and Cd(II) from aqueous solution. Both kinetic and equilibrium features were discussed in order to explain the adsorption process for Pb(II) and Cd(II) in detail.

3.6.1 Synthesis of ZnO monolith

The detailed procedure for the synthesis of silica monolith via sol-gel method has been discussed in **chapter 2, section 3.2.1.** Zinc nitrate hexahydrate solution (3 M) was used as precursor for ZnO monolith synthesis. Zinc nitrate solution was impregnated into as prepared silica monoliths after degassing them under vacuum. The wet monoliths were dried at 150 °C for 10 h (1 °C/min). Impregnation process was repeated for at least five times to get uniform ZnO-SiO_2 monoliths. Later, synthesized composites were calcined at 400 °C for 5 h (1 °C /min). Finally, silica part was leached out from composite of ZnO-SiO_2 to get pure ZnO monoliths by using HF (10%).

3.6.2 Synthesis of TiO_2@ZnO monolith

Above synthesized ZnsO monoliths were impregnated with $TiCl_4$ solution (2.5 M) after degassing them under vacuum. The wet monoliths were dried at 100 °C for 10 h (1 °C/min) and at least 5 impregnation cycles were repeated to get uniform ZnO core-TiO_2 shell monolith.

3.6.3 Characterization of monoliths

As synthesized silica, ZnO and TiO_2@ZnO monoliths were characterized by various techniques; details of the techniques are given in **Chapter 1, section 1.9**

3.6.4 Adsorption Study:

Adsorption efficacy of synthesized adsorbents was evaluated through AAS; detail procedure has been given in **Chapter 1, Section 1.10.1**

3.7 Result and discussion

Porosity of synthesized solid ZnO and TiO_2@ZnO monoliths was evaluated by Brunner–Emmett– Turner analyzer along with Barrett–Joyner–Halenda (BJH) plot. As per IUPAC classification, synthesized ZnO and TiO_2@ZnO monoliths exhibits N_2 sorption isotherms adjacent to typical Langmuir type – IV isotherm and categorized as H1 type hysteresis loop (with relative pressure, P/P_0 = 0.30 to 0.90) which confirms the mesoporous characteristics (Fig. 3.12a). Textural and porous properties of synthesized monoliths are discussed in Table 3.5 and the data from BET equation shows that specific surface area of ZnO gets increase after coating of TiO_2. According to pore size distribution (Fig. 1b), synthesized monoliths holds mesoporous nature along with a small number of micropores (inset of Fig. 3.12b) and such kind of structures are favorable for water treatment.

Table 3.5: Textural properties of ZnO and TiO_2@ZnO monoliths.

Monoliths	**S_{BET} ($m^2 g^{-1}$)**	**Mesopore diameter (nm)**	**Micropore diameter (nm)**	**Mesopore volume ($cm^3 g^{-1}$)**	**Micropore volume ($cm^3 g^{-1}$)**
ZnO	120	9.49	1.9	0.28	0.14
TiO_2@ZnO	332	3.06	0.6	0.25	0.10

Fig. 3.12c, display XRD patterns for the phase and purity of synthesized ZnO and TiO_2@ZnO monoliths. XRD confirms the formation of hexagonal structure of ZnO on the surface of SiO_2 monolith. ZnO monolith shows dominant peaks for ZnO, 2Θ at 31.8°, 34.4°, 36.23, 47.5, 56.6 and 62.8° corresponding to lattice planes of (100), (002), (101), (102), (110) and (103) respectively, which is confirmed by JCPDS card no. 36-1451 [58]. Where as in case of

TiO_2@ZnO monoliths, a few peaks in the XRD patterns corresponding to anatase TiO_2 were observed (JCPDF no. 21-1272). UV-visible spectroscopy for ZnO and TiO_2@ZnO monoliths was performed to point out the influence on the optical properties (Fig. 3.12d) as a function of the wavelength in the region between 250 and 1100 nm.

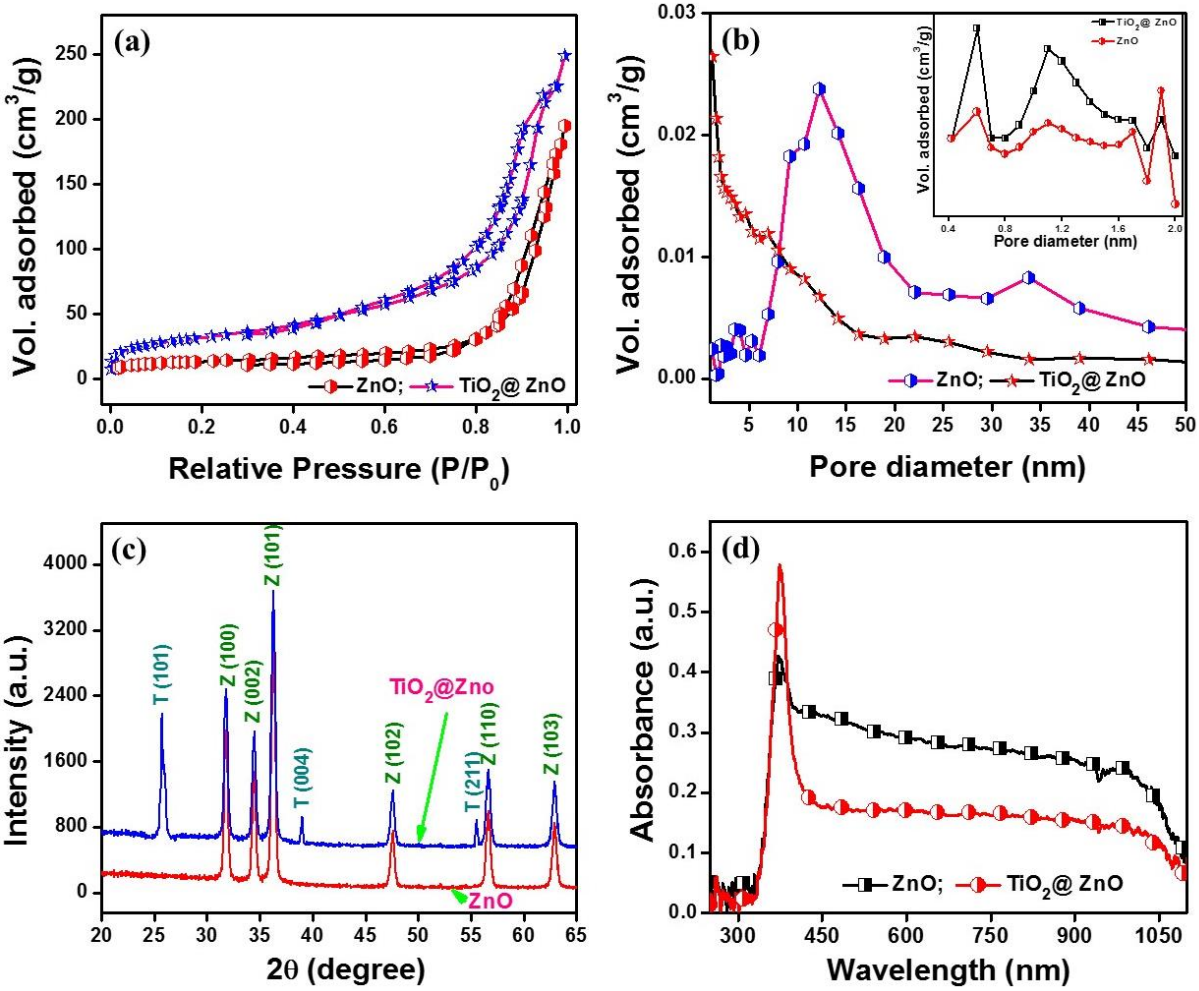

Fig. 3.12: a) N_2 sorption curve, b) BJH plot showing pore size distribution (inset contains micropore distribution curves through MP plot) c) XRD pattern and d) UV-vis spectrum for ZnO and TiO_2@ZnO monoliths.

TiO_2 shell over ZnO core enhances the light absorption which further enhances the semiconducting properties as compare to pure ZnO. The morphological structures of synthesized monoliths determined by FESEM are shown in Fig. 3.13. Similar kind of interconnected macroporous structures having mesopores and micropores (a little amount) with in wall are

obtained, but higher magnification images are difficult to obtain due to the charging of the sample. The purity of the metal oxide monoliths was confirmed by EDS analysis. Uniform distribution of the precursor TiO_2 salt throughout the core of the ZnO monoliths was responsible for chemical homogeneity.

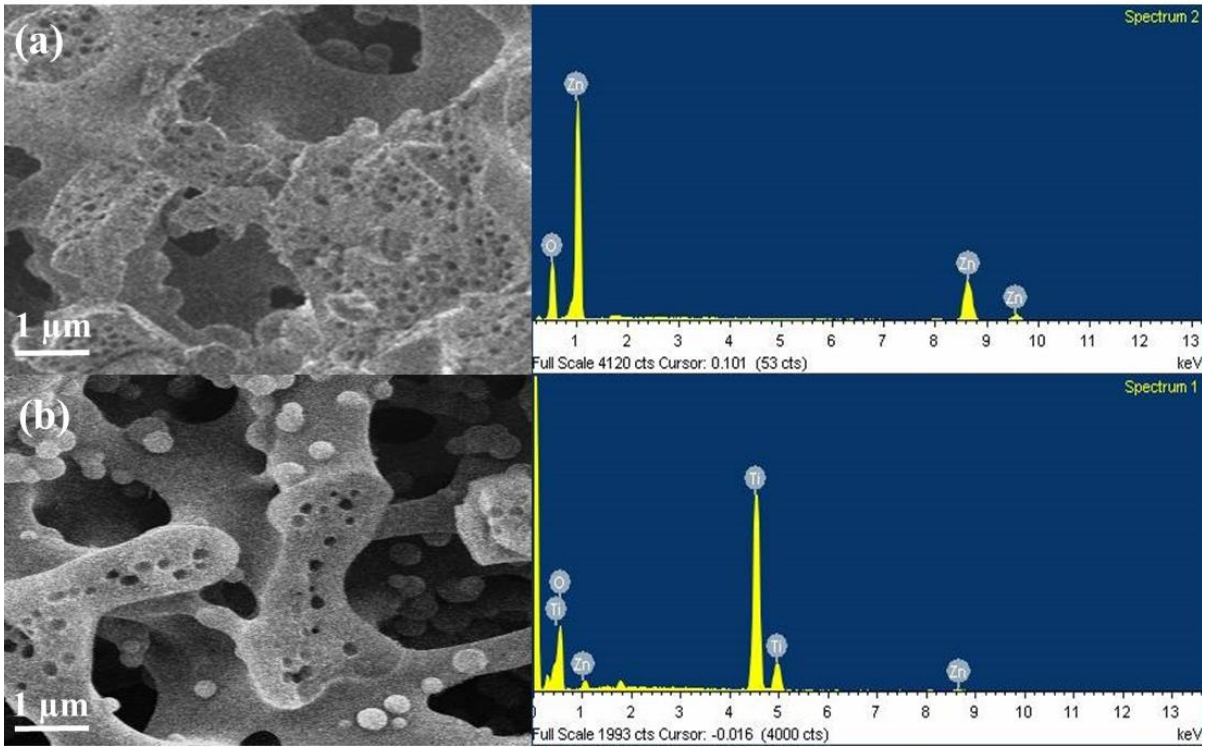

Fig. 3.13: FESEM and EDS spectra for a) ZnO and b) TiO_2@ ZnO monoliths.

3.7.1 Adsorption study

3.7.1.1 Effect of pH

In adsorption process, pH parameter plays an important role in governing the Pb(II) and Cd(II) ions adsorption. So, the impact of pH on adsorption efficiency was investigated over the range from 2.0 to 7.0 because above pH 7 precipitation of Pb(II) and Cd(II) ions may occur. From Fig. 3.14 (a-b), it was observed that the adsorption efficacy increases with increase of pH from 1 to 6. At pH 6, adsorption of metal ions on the surface of metal oxide surface can be explained on the basis of number of active sites present. Under acidic conditions, most of the surface of metal-oxide get surrounded by H^+ ions due to which competition between H^+ and the metal ions get increased for available adsorption sites [30].

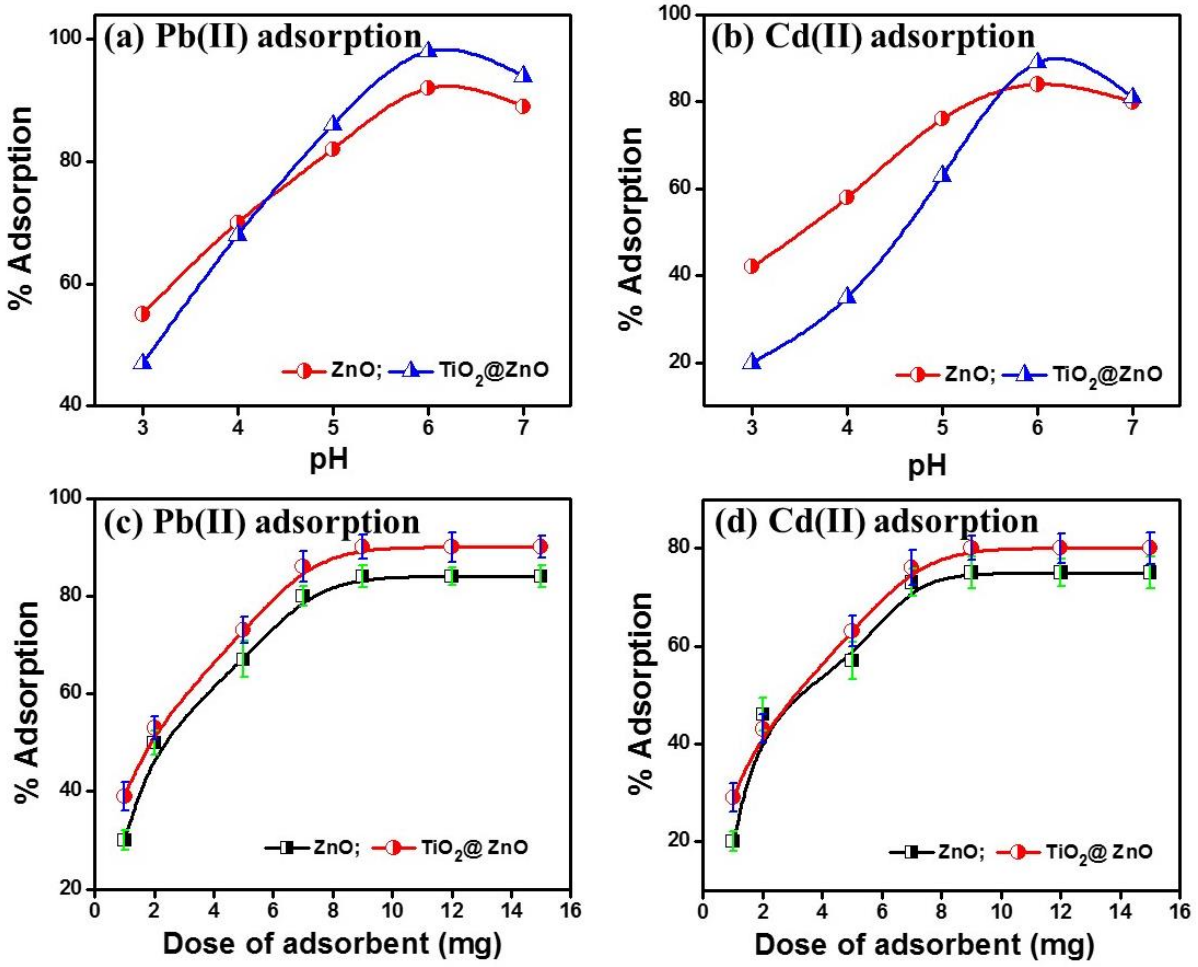

Fig. 3.14: Plot for effect of pH (a- Pb(II) and b- Cd(II)) [adsorbent amount: 0.02 g/L]; effect of adsorbent dose (c- Pb(II) and d- Cd(II)) for ZnO and TiO_2@ZnO monoliths. [Agitation speed: 200 rpm, temperature: 25 °C].

3.7.1.2 Effect of adsorbent dosage

Mass of adsorbent also has a major persona in adsorption process. With the increase of dosage of metal-oxide (2- 15 mg), increase in percentage of metal-ions (10 mg/L) adsorption was observed. Fig. 3.14 (c-d) shows that the removal of approximately 100 % metal ions was attained by using 10 mg of metal-oxides in 50 ml metal ion solution, due to availability of high surface area and more active sites for adsorption. The results confirmed that the removal efficacy of metal ions was directly proportional to the dosage of the metal oxides.

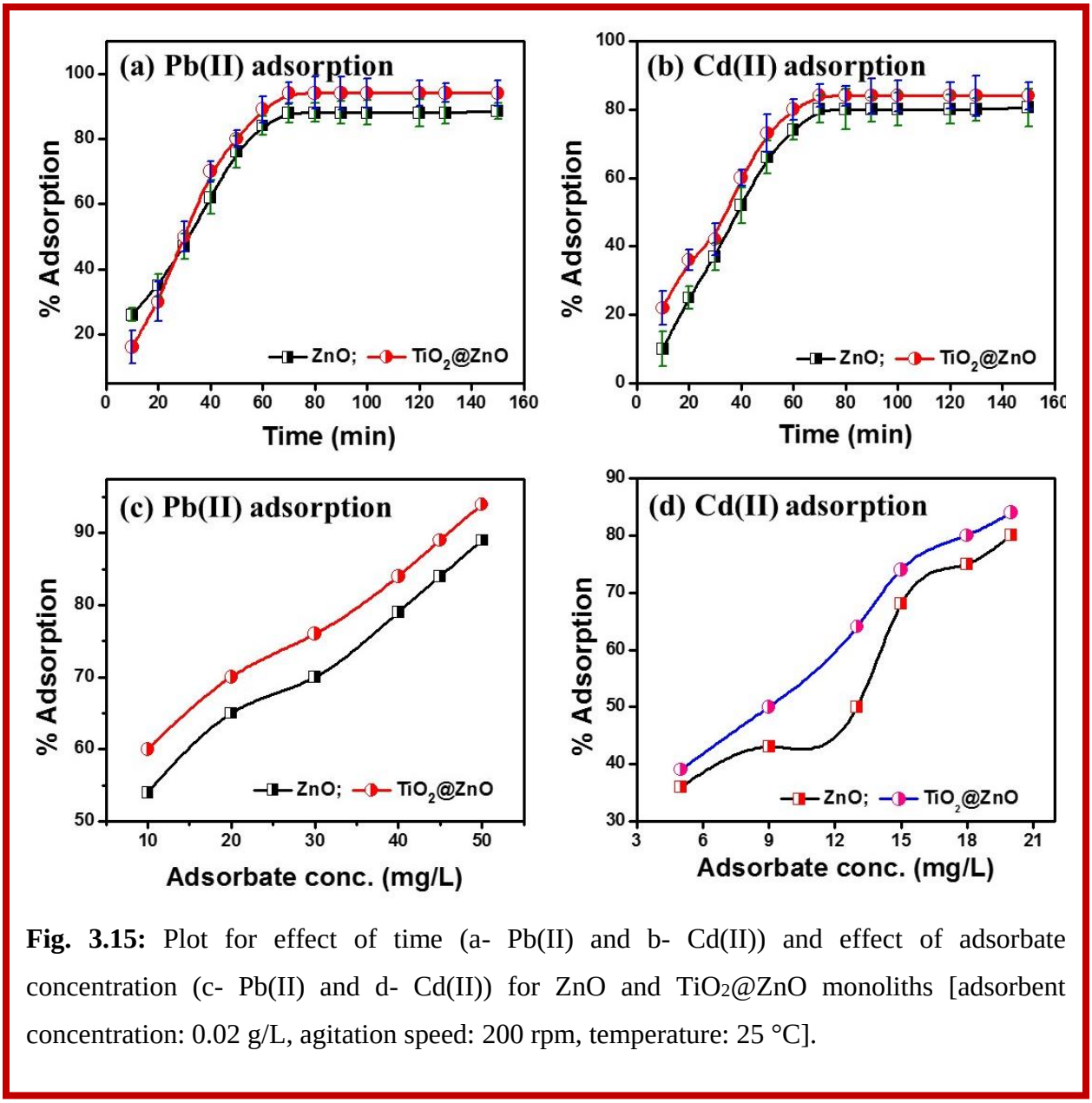

Fig. 3.15: Plot for effect of time (a- Pb(II) and b- Cd(II)) and effect of adsorbate concentration (c- Pb(II) and d- Cd(II)) for ZnO and TiO_2@ZnO monoliths [adsorbent concentration: 0.02 g/L, agitation speed: 200 rpm, temperature: 25 °C].

3.7.1.3 Effect of contact time

The optimization of contact time for removal of Pb(II) and Cd(II) has been shown in Fig. 3.15 (a-b). The agitation time was kept 10-150 min for initial concentration of 20 mg/L for both Pb(II) and Cd(II) ion solution. In this study, moderately fast adsorption of metal ions was observed in first 30 min followed by the slow adsorption in which adsorption efficacy increases until equilibrium achieved (60 min).

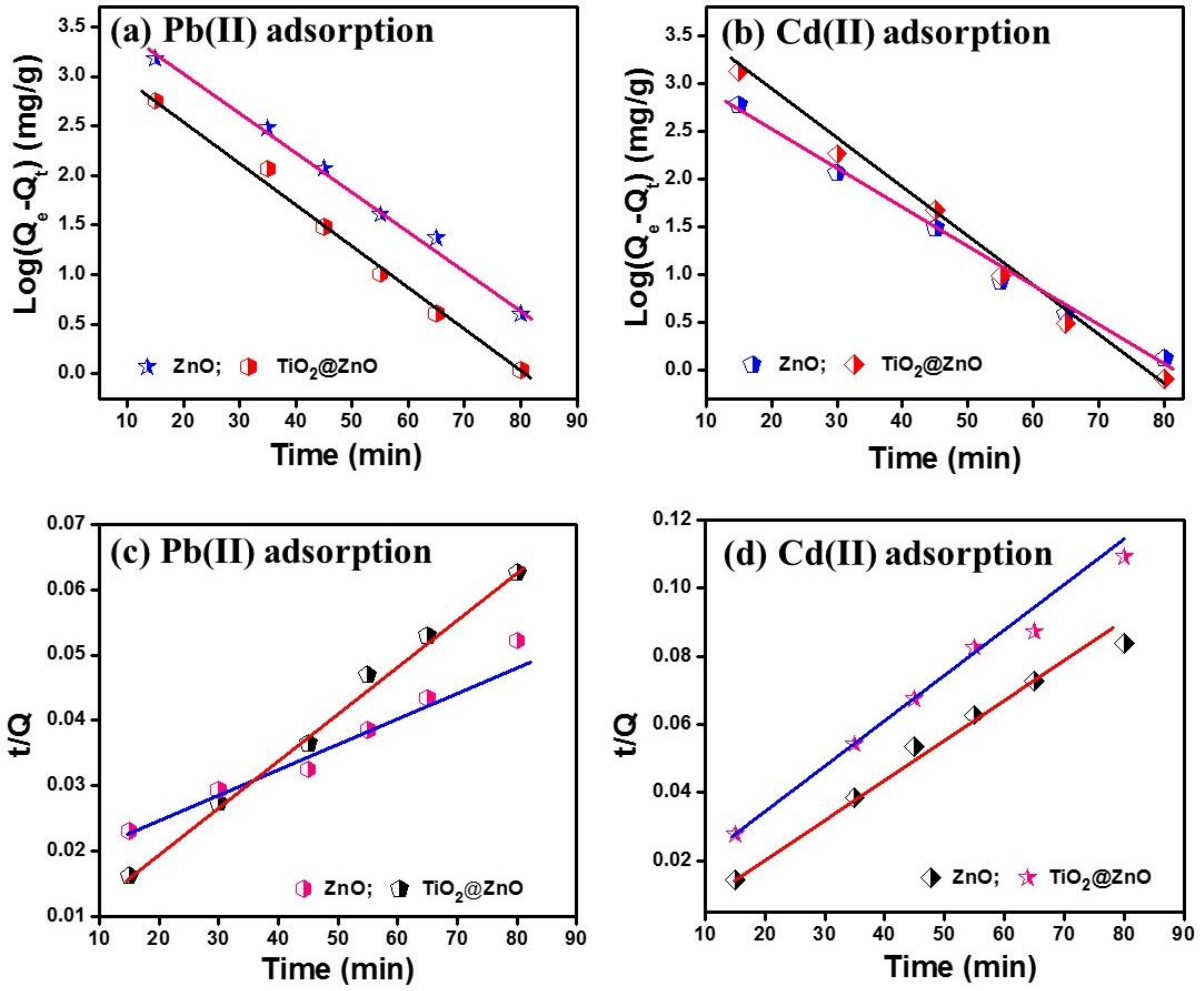

Fig. 3.16: Linear fit curves for pseudo first order (a- Pb(II) and b- Cd(II)) and pseudo second order (c- Pb(II) and d- Cd(II)), for ZnO and TiO_2@ZnO monoliths [adsorbent concentration: 0.02 g/L, agitation speed: 200 rpm, pH: 6, temperature: 25 °C].

3.7.1.4 Effect of adsorbate concentration

Effect of initial concentration of adsorbate (Pb(II) and Cd(II)) on adsorption capacity is shown in Fig. 3.15 (c-d). It was observed that the percentage adsorption was increased with increase of initial concentration of adsorbate[59]. In other words, more than 90% and 80% adsorption was accomplished for aqueous water containing Pb(II) (5-50 mg/L) and Cd(II) (2-20 mg/L), respectively. The initial concentration offers the desired driving forces to overcome the

resistance to mass transfer of Pb(II) and Cd(II) ions between aqueous and solid phase. Accordingly, increase in initial concentration also enhances the interaction between Pb(II) and Cd(II) ions and ZnO and TiO_2@ZnO monoliths.

3.7. 2 Adsorption kinetics

In an attempt to study the adsorption process of Pb(II) and Cd(II) ion on solid ZnO and TiO_2@ZnO monoliths, various kinetic models like pseudo-first-order, pseudo-second-order, Elovich and intra particle diffusion were used to observe the adsorption mechanism. Based on literature, the proposed models define the adsorption process and adsorption efficacy of adsorbents. Linear kinetic equations for these models are as follow[60, 61]:

$$pseudo-first-order \Rightarrow \log(Q_e - Q_t) = \log(Q_e) - \frac{K_1}{2.303} \times t \quad (3.7)$$

$$pseudo-second-order \Rightarrow \frac{t}{Q_t} = \frac{1}{K_2 Q_e^2} + \frac{1}{Q_e} \times t \quad (3.8)$$

$$Elovich's\ equation \Rightarrow Q_t = \frac{1}{b}\ln(ab) + \frac{1}{b}\ln(t) \quad (3.9)$$

$$Intra-particle\ diffusion\ model \Rightarrow Q_t = k_i t^{0.5} + I \quad (3.10)$$

Where Q_e (mg/g) is the amount of metal-ions adsorbed at equilibrium, Q_t (mg/g) is the quantity of metal ions adsorbed at time t, K_1 is the rate constant for the pseudo-first order reaction for adsorption (min^{-1}), K_2 is the rate constant for pseudo-second order reaction (g/mg min), a is the primary adsorption rate (mg/g min), b is the desorption constant (g/mg), k_i is the diffusion rate constant (mg/(g $min^{1/2}$)) and I is the intercept.

Table 3.6: Kinetic parameters and correlation coefficients for the kinetic models.

Model	Parameters	ZnO		TiO_2@ZnO	
		Pd(II)	Cd(II)	Pd(II)	Cd(II)
Pseudo-first order	Q_e	33.3	31.4	47.6	45.4
	K_1	0.083	0.10	0.092	0.13
	R^2	0.942	0.975	0.984	0.974
Pseudo-second order	Q_e	142.8	90.9	200	110.4
	K_2	0.0011	0.0008	0.002	0.0011
	R^2	0.9816	0.989	0.993	0.990

Elovich's model	a	60.9	51.6	83.6	74.3
	b	0.010	0.016	0.021	0.019
	R^2	0.921	0.894	0.9676	0.957
Intra particle diffusion model	k_i	21.7	7.93	24.5	10.02
	I	1.63	1.79	2.06	3.45
	R^2	0.950	0.944	0.971	0.961

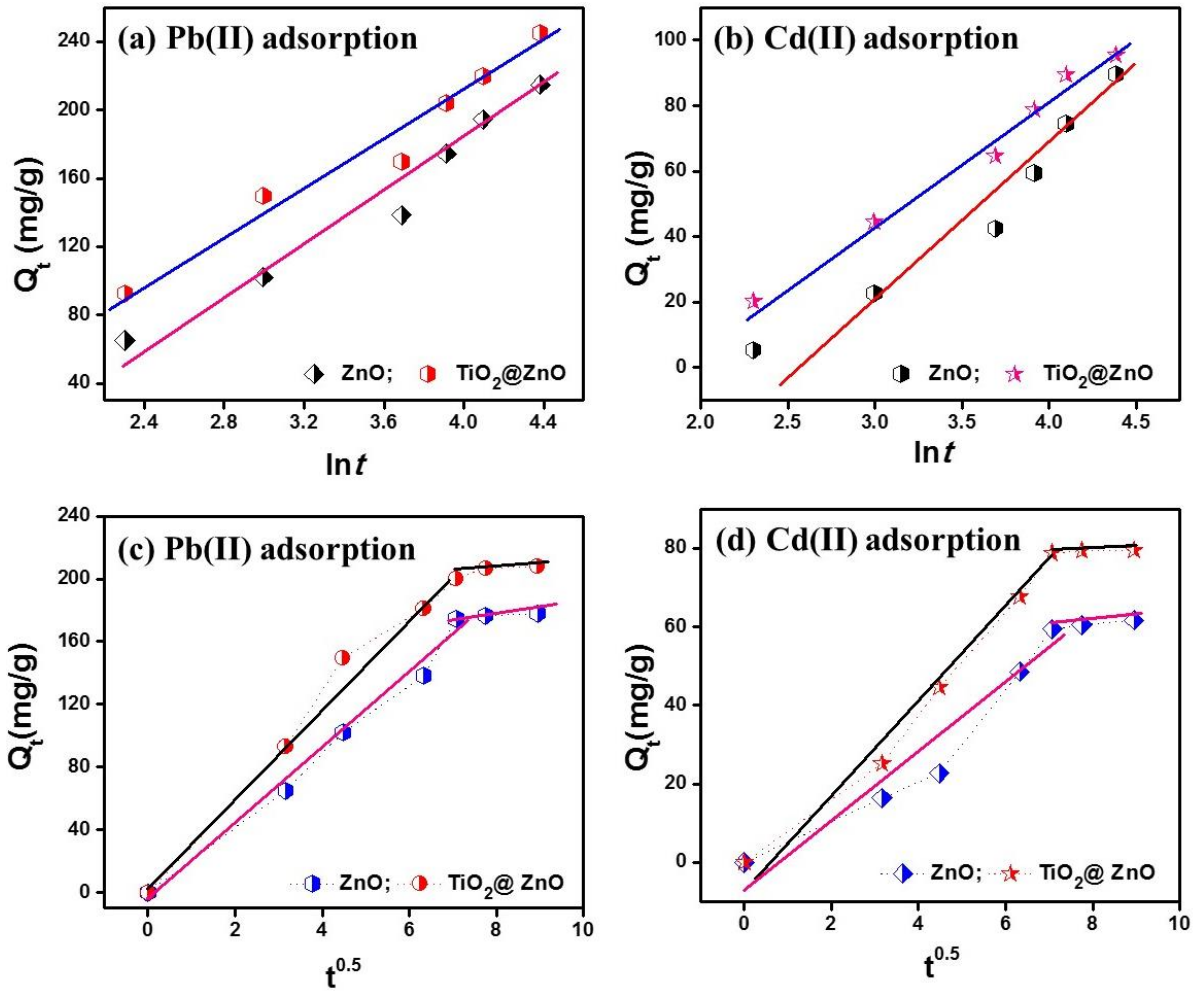

Fig. 3.17: Linear fit curves for elovich's model (a- Pb(II) and b- Cd(II)) and intra-particle diffusion model (c- Pb(II) and d- Cd(II)) for ZnO and TiO_2@ZnO monoliths [adsorbent concentration: 0.02 g/L, agitation speed: 200 rpm, pH: 6, temperature: 25 °C].

The plot for intra particle diffusion for adsorption Pb(II) and Cd(II) ions shows multi-linearity and adsorption process occurred in two steps. At first, in instantaneous diffusion stage adsorption process take place at external surface of adsorbent. After attaining equilibrium at surface, diffusion resistance increased leading to decrease in diffusion rate. Linear fit plots of pseudo-first order and second order for ZnO and TiO_2@ZnO monoliths on the adsorption of Pb(II) and Cd(II) ions are shown in Fig. 3.16, respectively.

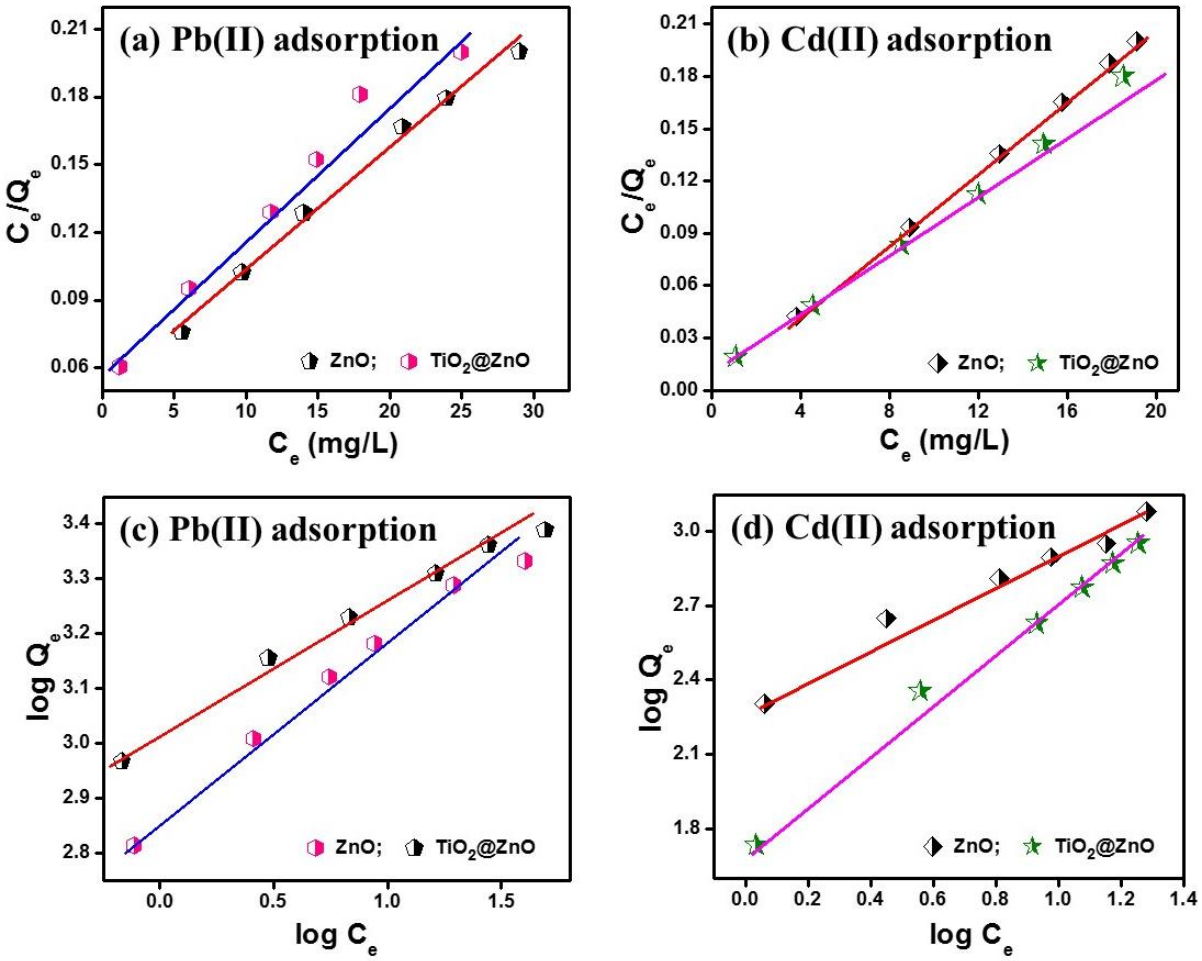

Fig. 3.18: Linear plots for Langmuir (a- Pb(II) and b- Cd(II)) and Freundlich isotherms (c- Pb(II) and d- Cd(II)) for ZnO and TiO_2@ZnO monoliths [adsorbent concentration: 0.02 g/L, agitation speed: 200 rpm, pH: 6, temperature: 25 °C].

Fig. 3.17 shows linear fit curves for Elovich's model and intra-particle diffusion model. For metal-ion adsorption on ZnO and TiO_2@ZnO monoliths, pseudo-second order kinetic model

shows better fitting corresponding to other models which suggests that adsorption process in this study characteristically controlled by chemisorption as displayed in Table 3.6.

3.7.3 Equilibrium studies and modeling

The interaction between adsorbate and adsorbent can be described by adsorption isotherm through optimization of adsorption process. In this study, adsorption data was evaluated by fitting Langmuir and Freundlich isotherm models. The batch experiments were executed at 25 °C with 0.02 g/L adsorbent dose to provide better understanding for single or multi–layer adsorption mechanism.

Langmuir isotherm

Langmuir model is utmost well-known isotherm model for monolayer formation of adsorbate layer on the adsorbent surface. This model is based on the concept that binding energy of all active sites are constant and no transmigration is possible on the surface of adsorbate. Formerly, this model was recognized for gas phase adsorption phenomena, then it had been extensively efficient for adsorbate-adsorbent interaction in liquid phase. The Langmuir isotherm model is given as follows [62]:

$$Langmuir \Rightarrow \frac{C_e}{Q_e} = \frac{1}{Q_o b} + \frac{C_e}{Q_o} \qquad (3.11)$$

where C_e (mg/L) is the equilibrium of metal ions concentration (Pd(II) and Cd(II)), Q_e (mg/g) is the amount of adsorbate adsorbed per gram of adsorbent. Q_0 (mg/L) and b are the Langmuir constants correlated to maximum adsorption capacity and energy of adsorption, respectively. The slope and intercept of linear plots of C_e/Q_e vs. C_e defines the values of Q_0 and b. Plots for Langmuir isotherm for adsorption of Pb(II) and Cd(II) on ZnO and TiO_2@ZnO monoliths are displayed in Fig. 3.18 (a-b).

Freundlich isotherm

Freundlich model is use to define the adsorption process based on both homogeneous and heterogeneous surfaces. According to this model, strong binding site gets occupied first. Meanwhile increase of degree of site occupation results in decrement of binding strength. It can be described as [63]:

$$Freundlich \Rightarrow \log Q_e = \log K_f + \frac{\log C_e}{n} \qquad (3.12)$$

Freundlich constants, K_f ($mg^{1-1/n}L^{1/n}$ g^{-1}) and n, depict the adsorption capacity at unit concentration and intensity, respectively and these constants can be evaluated through plot of log Q_e vs. log C_e. Freundlich isotherm plots for Pb(II) and Cd(II) adsorption on ZnO and TiO_2@ZnO monoliths are shown in Fig. 3.18 (c-d).

The fitting constants and regression coefficients evaluated using Langmuir and Freundlich isotherms are given in Table 3.7. For promising results 'n' values should lies between 1-10. By comparing the data of Pb(II) and Cd(II) ion adsorption and regression coefficients indicates better fitting to Freundlich adsorption model at equilibrium. A comparative study for maximum monolayer adsorption efficiency of different adsorbents for Pb(II) and Cd(II) ions is listed in Table 3.8 and here it could be concluded that the as-synthesized monoliths could be employed as an alternative adsorbent for metal ions adsorption at low concentrations.

Table 3.7: Isotherm parameters for adsorption of Pb(II) and Cd(II) ions.

Model	**Parameters**	**ZnO**		**TiO_2@ZnO**	
		Pd(II)	**Cd(II)**	**Pd(II)**	**Cd(II)**
Langmuir Model	Q_0	909	833	1250	1000
	b	1.25	0.28	2.34	1.1
	R^2	0.965	0.926	0.984	0.954
Freundlich Model	K_f	17.9	5.64	20.78	10.34
	n	3.25	1.02	4.53	1.83
	R^2	0.975	0.957	0.991	0.973

Table 3.8: A comparative account for the adsorption efficiency of heavy metal-ions by different adsorbents.

Adsorbents	**Surface area (m^2/g)**	**Maximum adsorption (mg/g)**		**Conditions**	**References**
		Pb(II)	**Cd(II)**		
GO-TiO_2	--	65.6	72.8	pH- 5.6 Time- 12h	[15]
Silica nanotubes (SNT)	--	42.85		pH-4, 7, 9, Temp-30°C Time-240 min	[42]
AF-Fe_3O_4	25.94	369	446.4	pH -7 Time-120 min	[52]
Fe_2O_3	79.35	68.9	--	pH -5 Temp-45°C	[64]
IOARM	--	--	117.6	pH -6	[65]

				Time-90 min Temp-20°C	
TiO_2	220	857	770	pH-6 Temp-30°C Time-80 min	[66]
ZnO	120	909	833	pH-6 Temp-30°C Time-150 min	Present study
TiO_2@ZnO	332	1250	1000		

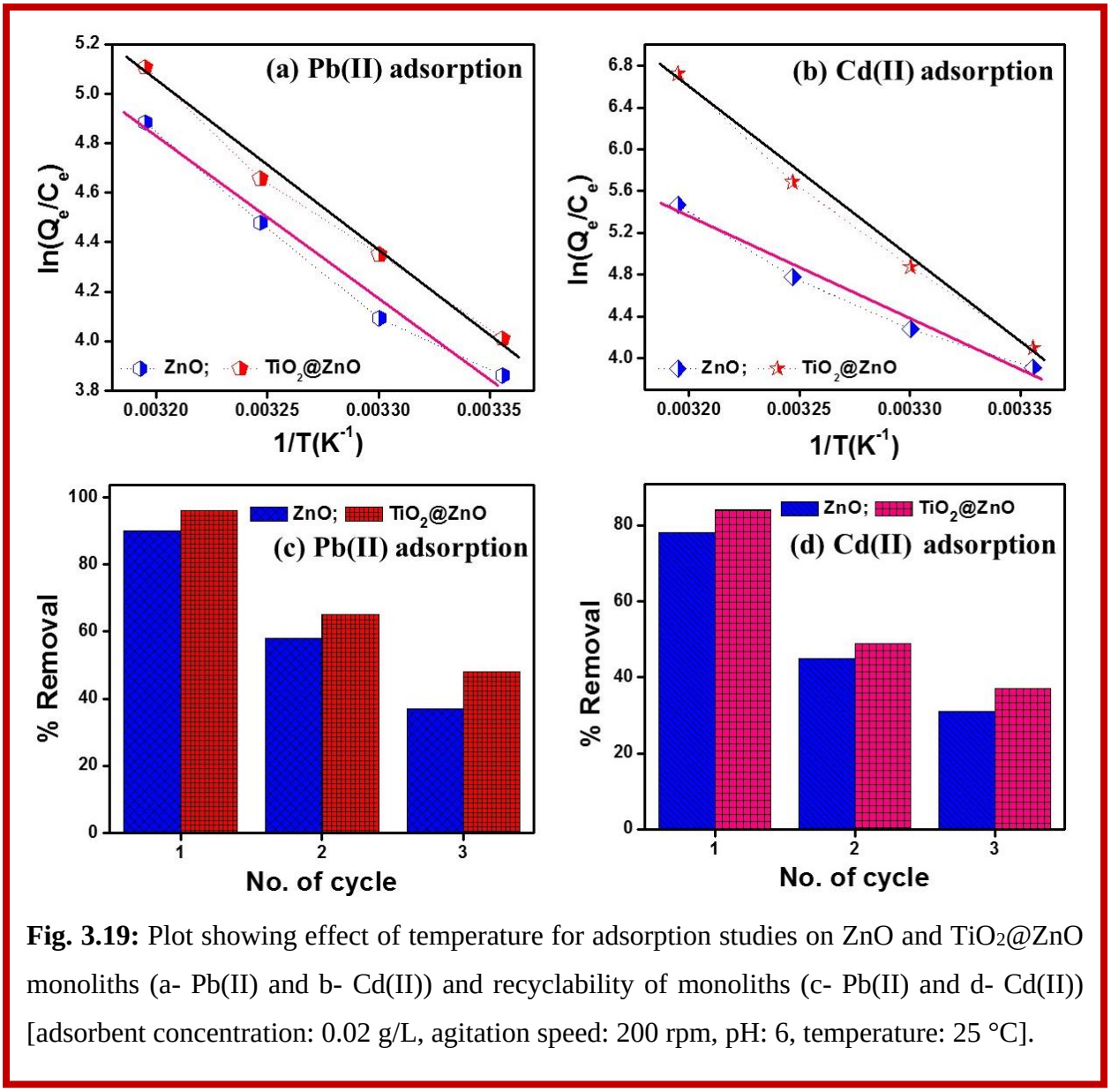

Fig. 3.19: Plot showing effect of temperature for adsorption studies on ZnO and TiO_2@ZnO monoliths (a- Pb(II) and b- Cd(II)) and recyclability of monoliths (c- Pb(II) and d- Cd(II)) [adsorbent concentration: 0.02 g/L, agitation speed: 200 rpm, pH: 6, temperature: 25 °C].

3.7.4 Thermodynamic parameters

The influence of thermodynamic parameters like change in entropy, enthalpy and Gibb's free energy on heavy metal ions adsorption onto the surface of porous ZnO and TiO_2@ZnO monoliths was investigated at temperature ranging from 298 to 323 K. The mathematical representation for free energy change and equilibrium distribution of adsorption can be described by Van't Hoff equation as follow [67]:

$$\Delta G^{\circ} = -RT \ln(\frac{Q_e}{C_e}) \quad (3.13)$$

Where R is the universal gas constant (8.314 $Jmol^{-1}K^{-1}$) and T is the absolute temperature. In other representation, change in entropy and enthalpy can be calculated by:

$$\ln(\frac{Q_e}{C_e}) = \frac{\Delta S}{R} - \frac{\Delta H}{RT} \quad (3.14)$$

Nature of adsorption process can be defined by evaluation of these thermodynamic parameters (Fig. 3.19 (a-b)). For instance, the adsorption process is known as spontaneous and endothermic when ΔG° has negative values and ΔH° has positive values. Thermodynamic parameters of adsorption for Pb(II) and Cd(II) are listed in Table 3.9. The increase of negative values of ΔG° along with increase of temperature represents better adsorption and favorable adsorption.

Table 3.9: Thermodynamic parameters for adsorption of Pb(II) and Cd(II) ions at different temperatures.

Metal-ions	Temperature	ZnO			TiO_2@ZnO		
		ΔH (kJ mol^{-1})	ΔS (J mol K^{-1})	ΔG (kJ mol^{-1})	ΔH (kJ mol^{-1})	ΔS (J mol K^{-1})	ΔG (kJ mol^{-1})
Pd(II)	298	6.1	2.4	-0.93	6.4	2.5	-0.92
	303			-1.28			-1.36
	313			-1.53			-1.61
	323			-1.78			-1.87
Cd(II)	298	9.2	3.4	-0.95	15.5	5.6	-0.97
	303			-1.36			-1.55
	313			-1.69			-2.06
	323			-2.09			-2.67

3.7.5 Reusability of adsorbent

To access the reusability of used porous ZnO and TiO_2@ZnO monoliths as adsorbent, their regeneration using NaOH (2M)[11] and reusability for adsorption of heavy meta-ions (Pb(II) and Cd(II)) were carried out up to 3 cycles which has been shown in Fig. 3.19 (c-d). The adsorption efficacy for both Pb(II) and Cd(II) ions decreases steadily with increased number of cycles because most of the adsorption sites get occupied due to bond formation between adsorbent and adsorbate. The good reusability of mesoporous ZnO and TiO_2@ZnO monoliths is due to the micrometer-sized structure with high surface area, which has a benefit of reducing overall cost for adsorption process. Furthermore, desorption conditions are more simple and accessible as no specific filtration techniques are required for adsorbent extraction due to its large size.

3.8 Conclusion

Mesoporous ZnO and TiO_2@ZnO monoliths synthesized via nanocasting method were utilized as an adsorbent for adsorption of Pb(II) and Cd(II) ions from aqueous solution. Kinetic and thermodynamic experiments verified that metal ion adsorption process was chemisorption, spontaneous and endothermic in nature. The maximum adsorption efficacy of Pb(II) ions based on monolayer adsorption was found to be 909 and 1250 mg/L for ZnO and TiO_2@ZnO monoliths, respectively whereas the maximum adsorption efficacy of Cd(II) ions based on monolayer adsorption was found to be 833 and 1000 mg/L for ZnO and TiO_2@ZnO monoliths respectively, which outperformed most of the reported adsorbents. Mesoporous ZnO and TiO_2@ZnO monoliths can be regenerated by 2 M NaOH and reused for at least three times for metal ions adsorption from aqueous solution.

Section-C: Remediation of Heavy Metal Ions from Waste Water Using Microporous Carbon Monolith

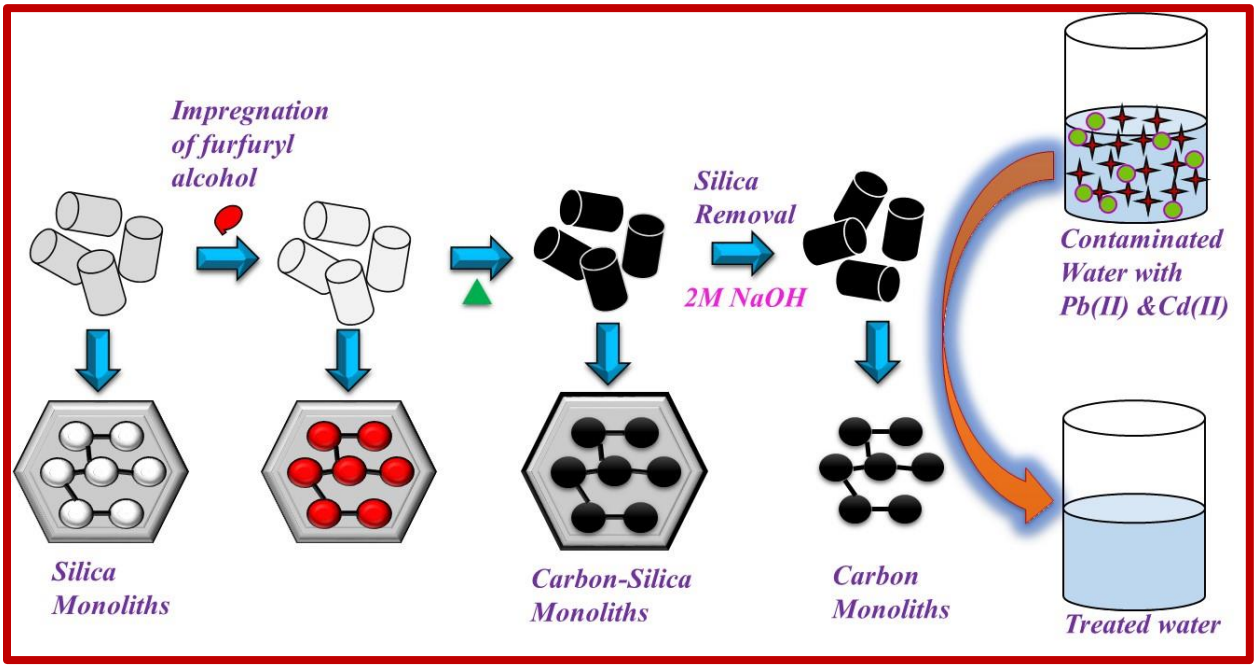

Novel innovation regarding synthesis of most promising and robust adsorbent to purify water has been developed as a great concern among the most promising fields. Many adsorbents based on carbon material have been explored worldwide due to high surface area, high chemical stability, and compact structure and appropriate for bulk production. Here, carbon monoliths (CM) with micro/ mesopore have been synthesized via nanocasting method, using silica monoliths as solid template. On the micrometer scale, synthesized CMs are considered as positive replica of parent silica monolith. CMs with high surface area (1103 m^2/g) is tested first time as adsorbent for removal of Pb(II) and Cd(II) ions from aqueous solution. Also, through batch experiments various effective and applicable parameters were successfully studied for instance pH, contact time, adsorbate/ adsorbent concentration, temperature etc. The maximum monolayer adsorption efficiency for Pb(II) and Cd(II) ions is 1128 mg/g and 989 mg/g, respectively. Kinetic data for the adsorption process shows best fit to pseudo second order.

3.9 Introduction

We all are familiar with a fact that; water is an important resource on the earth for life. For healthy lifestyle, people should have clean water (without toxic chemicals and germs) for drinking and other purposes[68]. With the development of high horizons in science and technology, various consequences has been increasing regarding environmental disorder due to rapid growth in generation of hazardous waste from developed industries and population expansion [59, 62].Therefore, industrial world legislation over worldwide has been advanced in concern to industrial discharge. Removal of heavy metal ions (e.g. lead and cadmium) from industrial waste water can be achieved by physical or chemical treatment processes like ion exchange, adsorption, membrane filtration, precipitation and reverse osmosis etc.[64, 65, 69, 70] Among all aforementioned processes, adsorption is considered as adequate and economically feasible and even effective for removal of heavy metal ions at trace levels. Researchers all over globe are carrying out work on development of cheaper and highly effective adsorbents for removal of heavy metal ions from waste water. A number of adsorbents for removal of toxic pollutants have been already reported in literature includes zeolites, activated carbon, chitosan, silica, CNT, porous metal oxides, clay materials etc.[48, 60, 71-73]

Mesoporous adsorbents due to high surface area, uniform and ordered pore size distribution possess incomparable adsorption efficiency[74]. Although the expenditure may get increase for development of mesoporous adsorbent which can be turned into economical by development in bulk and by performing regeneration experiments for removal of heavy metal ions. Monoliths containing bi/tri modal porosity are universally known porous materials, are very desirable theme in separation science due to their extraordinary surface properties[75]. Owing to solid rock like structure, monolithic system has an advantage over powder porous particles in separation media[76]. Without using any expensive filtration devices, monoliths can be easily extracted from separation media and be capable of reuse for several times. So, in this regard, carbon monoliths with micropores have various benefits and individuality as compare to other known adsorbents from literature. Carbon monoliths have low toxicity, high surface area/ porosity, thermal/ chemical stability, high adsorption capacity and resistance to acidic and basic medium. Considering these advantages, carbon monoliths can be counted as incomparable adsorbent for metal ion removal form waste water. In our previous studies[66], novel silica monoliths via sol-gel method and metal-oxides monoliths via nanocasting process were

successfully synthesized, aiming to boost the adsorption efficiency of adsorbent for toxic pollutants. Here, carbon monoliths were prepared by nanocasting method as negative replica of previously synthesized silica monoliths. Up to know, no systematic investigation of heavy metal ion adsorption by CM has been reported. Hence, we anticipated that synthesized carbon monoliths have favorable potential to be used as adsorbent for Pb(II) and Cd(II) removal.

3.10.1 Synthesis of Carbon Monoliths

Mesoporous silica monoliths synthesized in previous studies[77] have been used as mold for synthesis of carbon monoliths. Furfuryl alcohol (FA) and oxalic acid (OA) in ratio $\eta_{FA} = \eta_{OA}$ (200-300) were mixed in 1,3,5-trimethylbenzene (TMB) and the obtained solution was impregnated into the pore of parent silica monoliths. After completion of impregnation the white monoliths became transparent. Afterward transparent monoliths were heated at 80 °C for polymerization of FA and later heated to 300°C, at heating rate of 1°C/min. At last, the temperature was increased up to 800°C for 4 h, at heating ramp of 1°C/min. Finally, the CM were obtained after silica removal using 2M NaOH solution.

3.10.2 Characterization of monoliths (adsorbent)

As synthesized carbon monoliths were characterized by various techniques; details of the techniques are given in **Chapter 1, section 1.9.**

3.10.3 Adsorption Study

Adsorption efficacy of synthesized adsorbents was evaluated through AAS; detail procedure has been given in **Chapter 1, Section 1.10.1**

3.11 Results and Discussion

3.11.1 Characterization of the adsorbent

The specific surface area of synthesized carbon monoliths was described by N_2 sorption measurement and calculated through multipoint BET equation which was found to be 1103 m^2/g. Synthesized CM exhibits an uptake for nitrogen between 0.4 -0.5 relative pressure (P/P_0) (Fig. 3.20a). The mesopore size and pore volume obtained by Barrett-Joyner-Halenda (BJH) analysis were found to be 3.68 nm and 0.67 cm^3/g, respectively (inset of Fig. 3.20a). Synthesized CMs are mostly microporous in nature, which is confirmed by micropore analysis and the obtained micropore size and pore volume is 1.3 nm and 0.56 cm^3/g, respectively (Fig. 3.20b). The relative

adsorption performance of CM is mainly dependent on surface area and pore size. Due to huge surface area, along with micropores, CM would become most consistent adsorbent for adsorbate adsorption. Fig. 3.20c shows diffraction patterns for mesoporous CM, and revealed two main characteristic peaks at nearby 24.5° and 43.04° representing mesoporous carbon through index reflection pattern of 002 and 110 respectively. Successful synthesis of CM was achieved because of thermally stable precursor of furfuryl alcohol (FA) and trimethyl benzene.

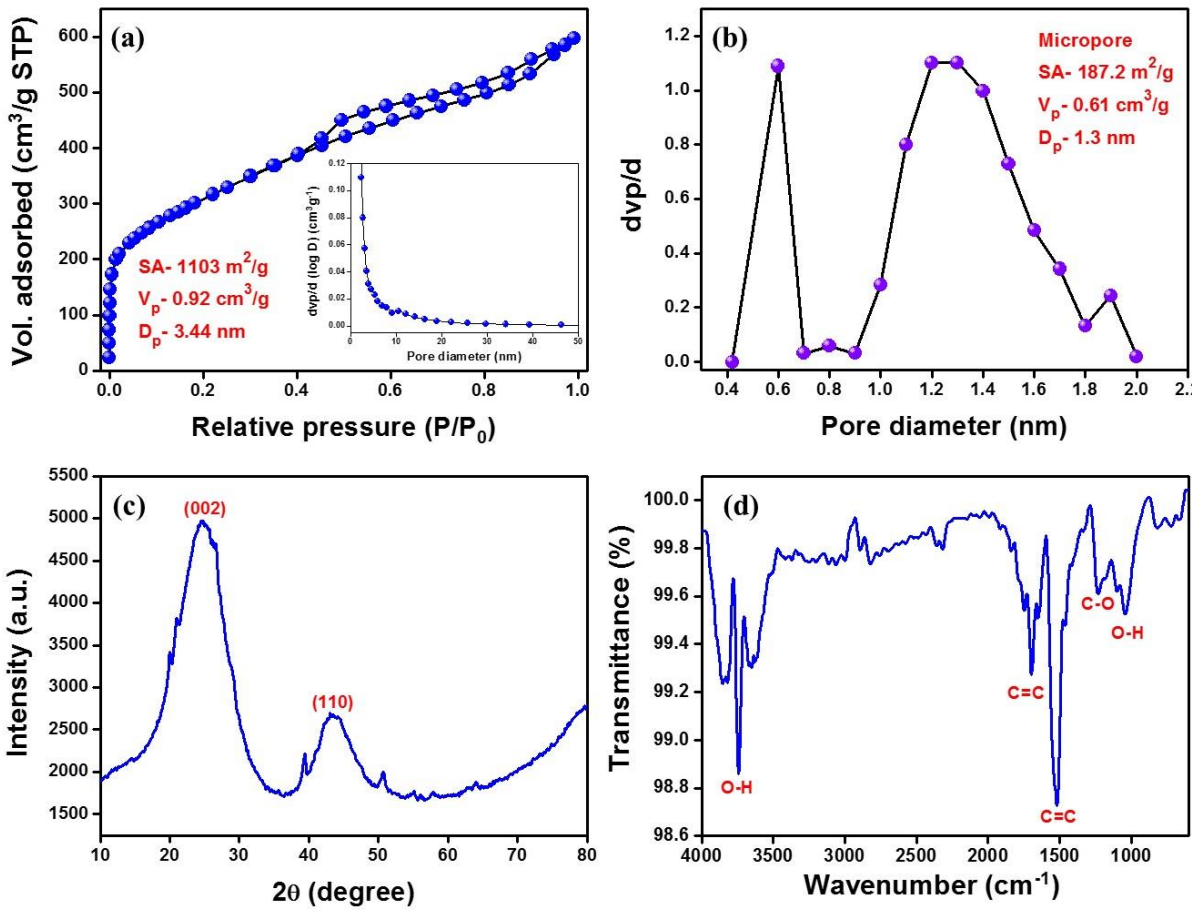

Fig. 3.20: a) N_2 sorption curve (inset contains BJH plot) b) MP plot showing micropore size distribution c) XRD pattern and d) FTIR spectrum for carbon monoliths.

FTIR spectrum for synthesized carbon monoliths has been shown in Fig. 3.20d. Peaks in the region of 3615-3856 cm^{-1} are corresponding to stretching vibrations of O–H. The characteristic C=C vibrations are seen at 1520-1705 cm^{-1}. Also, peaks at 1232 cm^{-1} and 1040 cm^{-1} are corresponding to C-O stretching and O-H bending, respectively. As discussed above, FA and OA is used as precursor which is mixed in TMB for CM synthesis and later impregnated inside the pores of parent silica monoliths. Fig. 3.21a shows the digital photograph of synthesized solid CM after calcination. Pure CM with micropore diameter of 1.3 nm has been synthesized after removal of silica content which is be confirmed by EDS analysis (Fig. 3.21b). The result of EDS analysis represents that diffusion of silica content from micro/ mesopores of CM. Also, morphological structure of prepared CM was investigated using FESEM at different magnification scale (Fig. 3.21 c-d).

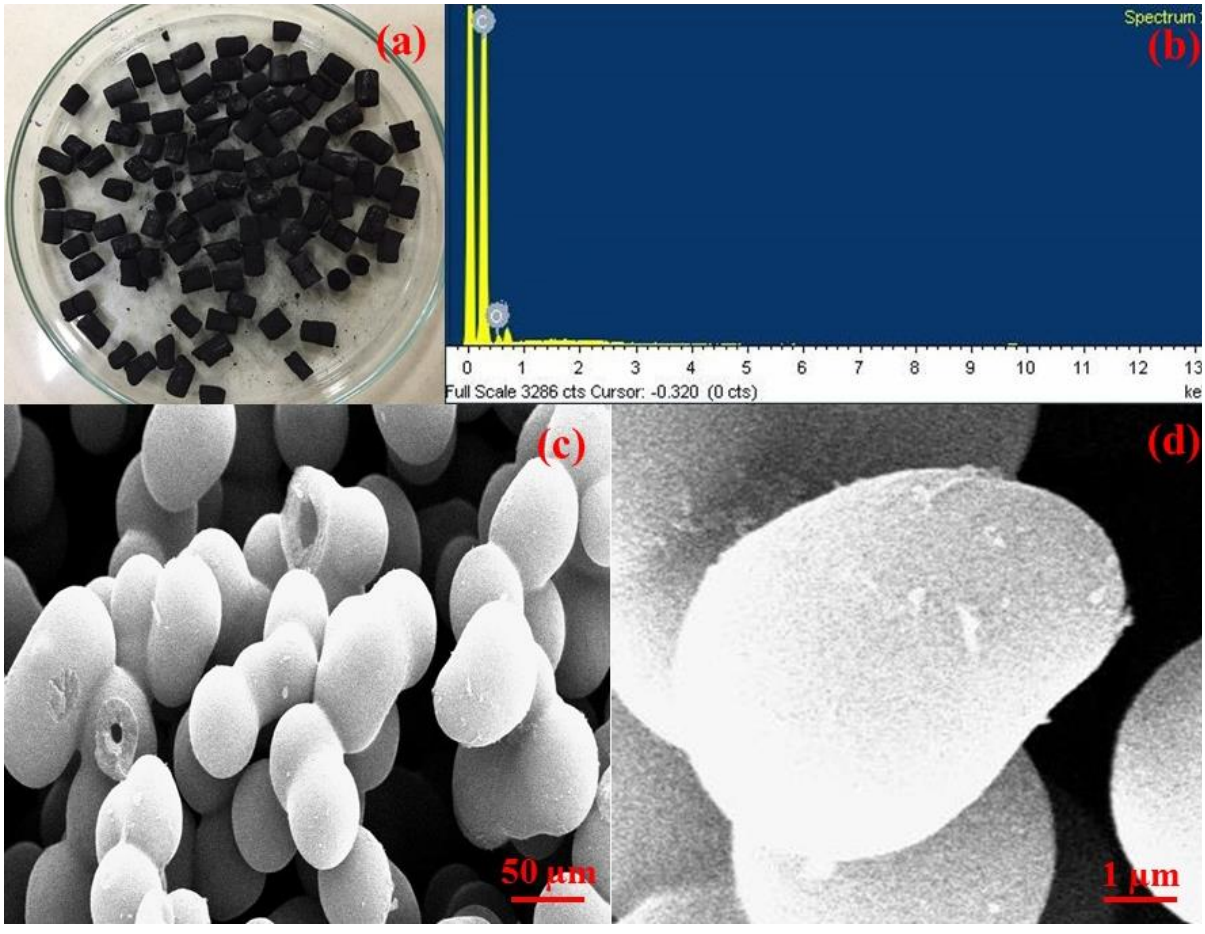

Fig. 3.21: a) synthesized carbon monoliths, b) EDS spectra and c) & d) FESEM for carbon monoliths

Though we have discussed about structure of silica monoliths in detail previously[77], here we have focused only on effect of FA and OA on micro mesoporous structure of monoliths for adsorption process. Accordingly, we have tried to emphasis on micro/ mesoporous structure of synthesized CM, but due to charging effect in FESEM, proper porous structure of positive carbon replica can't be shown.

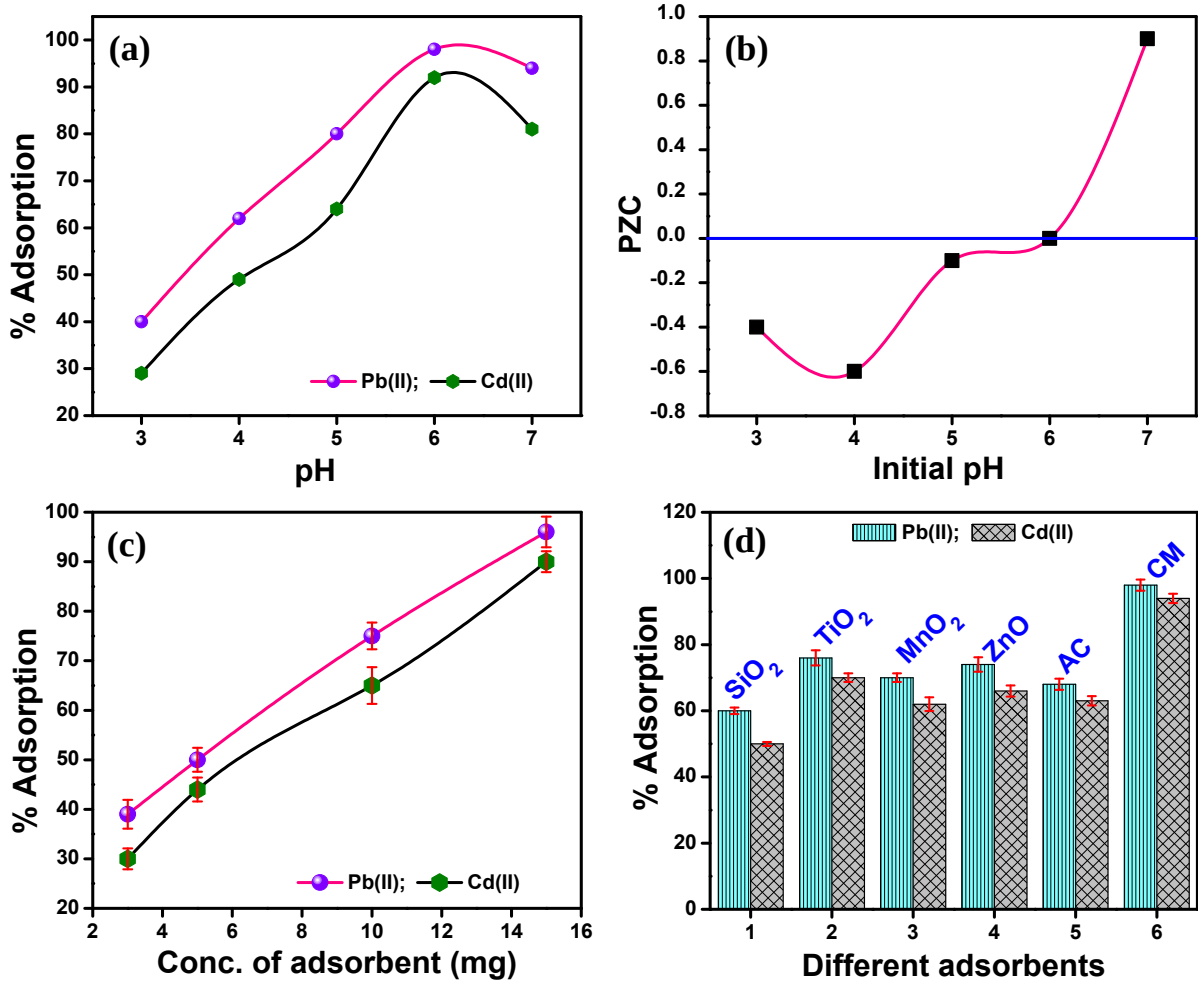

Fig. 3.22: a) Plot for effect of pH [adsorbent amount: 0.02 g/L]; b) plot showing point of zero charge (PZC) on CM, c) effect of adsorbent dose for carbon monoliths and d) comparative percentage adsorption of metal ions using different adsorbent. [agitation speed: 200 rpm, temperature: 25 °C].

3.11.2 Adsorption study

3.11.2.1 Effect of pH

In the adsorption process, pH parameter plays an important role in leading the Pb(II) and Cd(II) ion adsorption by influencing the surface charge. Here, the impact of pH on adsorption efficiency was investigated over the range from 2.0 to 7.0 because above pH 7, the surface of CM becomes negatively charged. From Fig. 3.22a, it is observed that the adsorption efficacy increases with increase of pH from 1 to 6. Under acidic conditions (below pH 6), most of the surface of CM get highly protonated and repulsive forces between metal ions and active sites increases and due to which the bond formation get interrupted among adsorbate and adsorbent. The obtained point of zero charge on the surface of CM has been shown in Fig. 3.22b. Here, adsorption of metal ions on the surface of CM can be explained on the basis of number of active/ vacant sites present.

3.11.2.2 Effect of adsorbent dosage

Mass of adsorbent also has a major persona in adsorption process. With the increase of dosage of adsorbent (3- 15 mg), increase in percentage of adsorbate (20 mg/L for both the metal ions) adsorption was observed. Fig. 3.22d shows that the removal of almost 100 % metal ions is attained by using 15 mg of CM in 50 ml metal ion solution, due to availability of high surface area and more active sites for adsorption. This result confirms that the removal efficacy of metal ions is directly proportional to the dosage of the CMs.

3.11.2.3 Comparative study of different adsorbent

In this study, we have used six different adsorbent materials e.g. SiO_2, MnO_2, TiO_2, ZnO, AC and CM to adsorb 50 ml of 20 mg/L of both the metal ion solutions. From Fig. 3.22d, it is clear that CM has the highest efficiency for adsorption of metal ions than SiO_2, MnO_2, TiO_2, ZnO and AC adsorbents.

3.11.2.4 Effect of contact time at different concentration of adsorbate

The optimization of contact time at different concentration of adsorbate has been shown in Fig. 3.23(a-b). The agitation time for all the concentration was kept 10-150 min. In this study, moderately fast adsorption of metal ions was observed in first 30 min (external surface adsorption) followed by the slow adsorption in which adsorption efficacy increases until equilibrium achieved (60 min). It was observed that the percentage adsorption was increased

with increase in concentration of adsorbate (for Pb, 5-50 mg/L and for Cd, 5-20 mg/L)[59]. The initial concentration offers the desired driving forces to overcome the resistance to mass transfer of Pb(II) and Cd(II) ions between aqueous and solid phase. Accordingly, increase in initial concentration also enhances the interaction between heavy metal ions and CM.

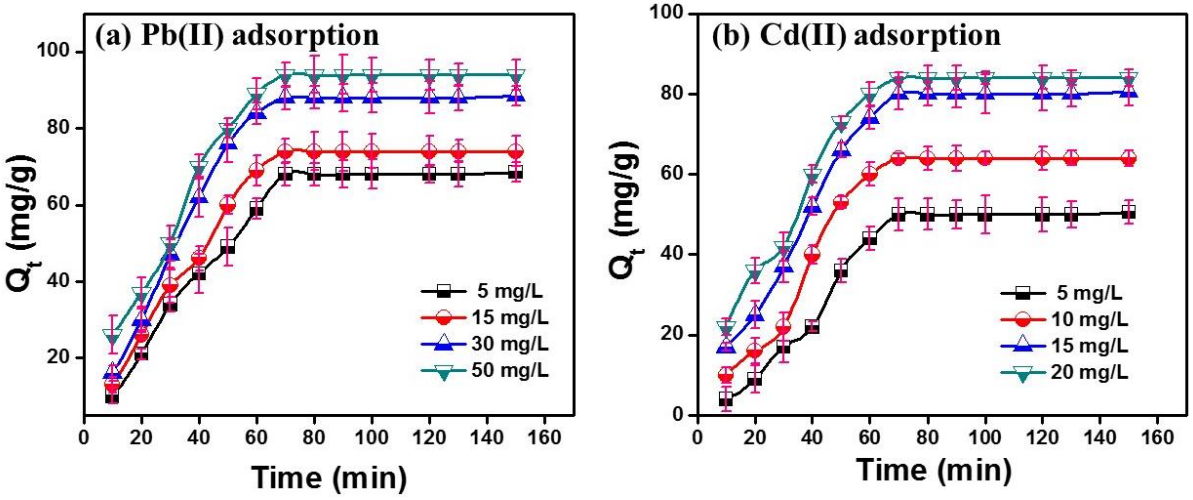

Fig. 3.23: Plot for effect of time along with different concentration of adsorbate (a- Pb(II)and b- Cd(II)) using carbon monoliths [adsorbate concentration: 0.02 g/L, agitation speed: 200 rpm, temperature: 25 °C].

3.11.2.5 Thermodynamic parameters

The influence of thermodynamic parameters like change in entropy, enthalpy and Gibb's free energy on heavy metal ions adsorption onto the surface of CM was investigated at temperature ranging from 298 to 313 K. The mathematical representation for free energy change and equilibrium distribution of adsorption can be described by Van't Hoff equation as follow [67]:

$$\Delta G^{\circ} = -RT \ln(\frac{Q_e}{C_e}) \quad (3.15)$$

Where R is the universal gas constant (8.314 $Jmol^{-1}K^{-1}$) and T is the absolute temperature. In other representation, change in entropy and enthalpy can be calculated by:

$$\ln(\frac{Q_e}{C_e}) = \frac{\Delta S}{R} - \frac{\Delta H}{RT} \quad (3.16)$$

Nature of adsorption process can be defined by evaluation of these thermodynamic parameters (Fig. 3.24a). For instance, the adsorption process is known as spontaneous and endothermic

when ΔG° has negative values and ΔH° has positive values. Thermodynamic parameters of adsorption for Pb(II) and Cd(II) are listed in Table 3.10. The increase of negative values of ΔG° along with increase of temperature represents better adsorption and favorable adsorption.

Table 3.10: Thermodynamic parameters for adsorption of Pb(II) and Cd(II) ions.

Metal-ions	Temperature (K)	Thermodynamic parameters		
		ΔH (kJ mol^{-1})	ΔS (J mol K^{-1})	ΔG (kJ mol^{-1})
Pd(II)	298	8.7	33.4	-1.17
	303			-1.34
	308			-1.5
	313			-1.6
Cd(II)	298	15.7	56.86	-1.23
	303			-1.52
	308			-1.81
	313			-2.09

3.11.3 Equilibrium studies and modeling

The interaction between adsorbate and adsorbent can be described by adsorption isotherm through optimization of adsorption process. In this study, adsorption data was evaluated by fitting Langmuir and Freundlich isotherm model. The batch experiments were executed at 298 K with 0.02 g/L adsorbent dose to provide better understanding for single or multi–layer adsorption mechanism.

Langmuir isotherm

Langmuir model is utmost well-known isotherm model for monolayer formation of adsorbate layer on the adsorbent surface. This model is based on the concept that binding energy of all active sites is constant and no transmigration is possible on the surface of adsorbate. Formerly, this model was recognized for gas phase adsorption phenomena, then it had been extensively efficient for adsorbate-adsorbent interaction in liquid phase. The Langmuir isotherm model is given as follows [62]:

$$\frac{C_e}{Q_e} = \frac{1}{Q_o b} + \frac{C_e}{Q_o} \qquad (3.17)$$

where C_e (mg/L) is the equilibrium of metal ions concentration, Q_e (mg/g) is the amount of adsorbate adsorbed per gram of adsorbent. Q_0 (mg/L) and b are the Langmuir constants correlated to maximum adsorption capacity and energy of adsorption, respectively. The slope and intercept of linear plots of C_e/Q_e vs. C_e defines the values of Q_0 and b. Plots for Langmuir isotherm for adsorption of Pb(II) and Cd(II) on CM are displayed in Fig. 3.24b.

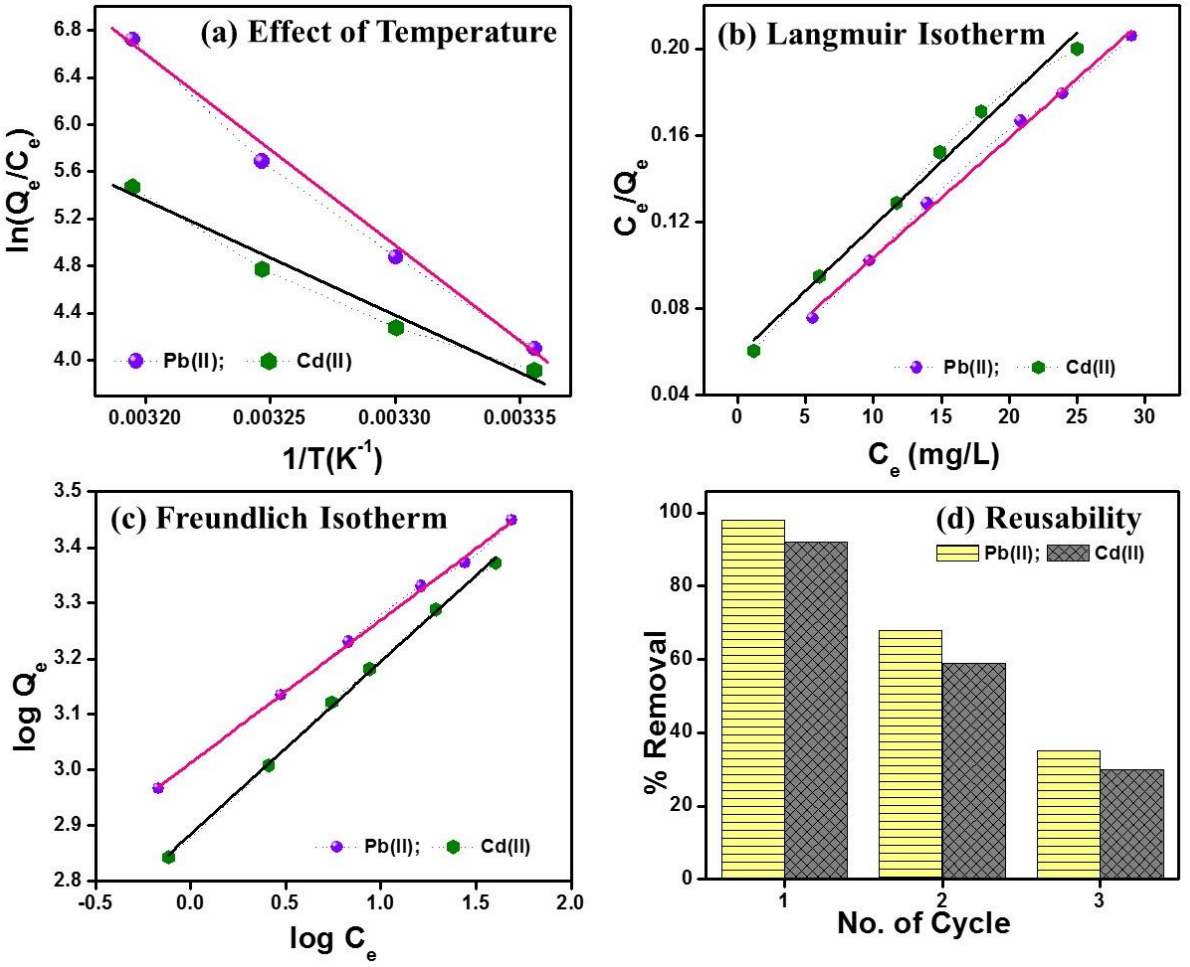

Fig. 3.24: a) plot showing effect of temperature for adsorption studies on carbon monoliths; Linear plots for b) Langmuir, c) Freundlich isotherms, and d) recyclability of monoliths. [Adsorbent concentration: 0.02 g/L, agitation speed: 200 rpm, pH: 6, temperature: 25 °C].

Freundlich isotherm

Freundlich model is used to define the adsorption process based on both homogeneous and heterogeneous surfaces. According to this model, strong binding site gets occupied first.

Meanwhile increase of degree of site occupation results in decrement of binding strength. It can be described as [63, 78]:

$$\log Q_e = \log K_f + \frac{\log C_e}{n} \quad (3.18)$$

Freundlich constants, K_f ($mg^{1-1/n}L^{1/n}\ g^{-1}$) and n depict the adsorption capacity at unit concentration and intensity, respectively and these constants can be evaluated through plot of log Q_e vs. log C_e. Freundlich isotherm plots for Pb(II) and Cd(II) adsorption on CM are shown in Fig. 3.24c.

The fitting constants and regression coefficients evaluated using Langmuir and Freundlich isotherms are given in Table 3.11. For promising results, 'n' values should lie between 1-10. By comparing the data of Pb(II) and Cd(II) ion adsorption and regression coefficients indicates better fitting to Freundlich adsorption model at equilibrium. A comparative study for maximum monolayer adsorption efficiency of different adsorbents for Pb(II) and Cd(II) ions are listed in Table 3.12 and here it could be concluded that the as-synthesized carbon monoliths could be employed as an alternative adsorbent for metal ions adsorption at low concentrations.

Table 3.11: Isotherm parameters for adsorption of Pb(II) and Cd(II) ions.

Model	**Parameters**	**CM**	
		Pd(II)	**Cd(II)**
Langmuir Model	Q_0	1128	989
	b	1.05	0.78
	R^2	0.990	0.986
Freundlich Model	K_f	20.33	17.86
	n	3.95	3.2
	R^2	0.995	0.998

Table 3.12: A comparative account for the adsorption efficiency of heavy metal-ions by different adsorbents.

Adsorbents	**Surface area (m^2/g)**	**Q_0 (mg/g)**		**Conditions**	**References**
		Pb(II)	**Cd(II)**		
IOARM	--	--	117.6	pH -6 Time-90 min Temp-20°C	[65]

TiO_2	220	857	770	pH-6 Temp-30 °C Time-80 min	[66]
CCM 8000	469.8	71.95	--	Time- 2000 min Temp- 30 °C	[79]
Activated carbon	1127	28.90	14.29	pH- 6.0-6.5	[80]
GO-TiO_2	--	65.6	72.8	pH- 5.6 Time- 12 h	[15]
Mesoporous silica	662	184.32	--	pH- 7	[81]
Silica nanotubes (SNT)	--	42.85	--	pH-4, 7, 9, Temp-30°C Time-240 min	[42]
Silica exhibiting DSDH	616	169.34	--	pH-5.2	[82]
CM	1103	1128	989	pH-6 Temp-30 °C Time-150 min	Present Study

3.11.4 Adsorption kinetics

In an attempt to study the adsorption process of Pb(II) and Cd(II) ions on solid CMs, various kinetic models like pseudo-first-order, pseudo-second-order, Elovich and intra particle diffusion were used to observe the adsorption mechanism. Based on literature, the proposed models define the adsorption process and adsorption efficacy of adsorbents. Linear kinetic equations for these models are as follow [60, 61]:

$$\log(Q_e - Q_t) = \log(Q_e) - \frac{K_1}{2.303} \times t \quad (3.19)$$

$$\frac{t}{Q_t} = \frac{1}{K_2 Q_e^2} + \frac{1}{Q_e} \times t \quad (3.20)$$

$$Q_t = \frac{1}{b}\ln(ab) + \frac{1}{b}\ln(t) \quad (3.21)$$

$$Q_t = k_i t^{0.5} + I \quad (3.22)$$

Where Q_e (mg/g) is the amount of metal-ions adsorbed at equilibrium, Q_t (mg/g) is the quantity of metal ions adsorbed at time t, K_1 is the rate constant for the pseudo-first order reaction for adsorption (min^{-1}), K_2 is the rate constant for pseudo-second order reaction (g/mg min), a is the

primary adsorption rate (mg/g min), b is the desorption constant (g/mg), k_i is the diffusion rate constant (mg/(g $min^{1/2}$)) and I is the intercept. The plot for intra particle diffusion for adsorption of Pb(II) and Cd(II) ions shows multi-linearity and adsorption process occurred in two steps. At first, in instantaneous diffusion stage adsorption process take place at external surface of adsorbent. After attaining equilibrium at surface, diffusion resistance increased leading to decrease in diffusion rate.

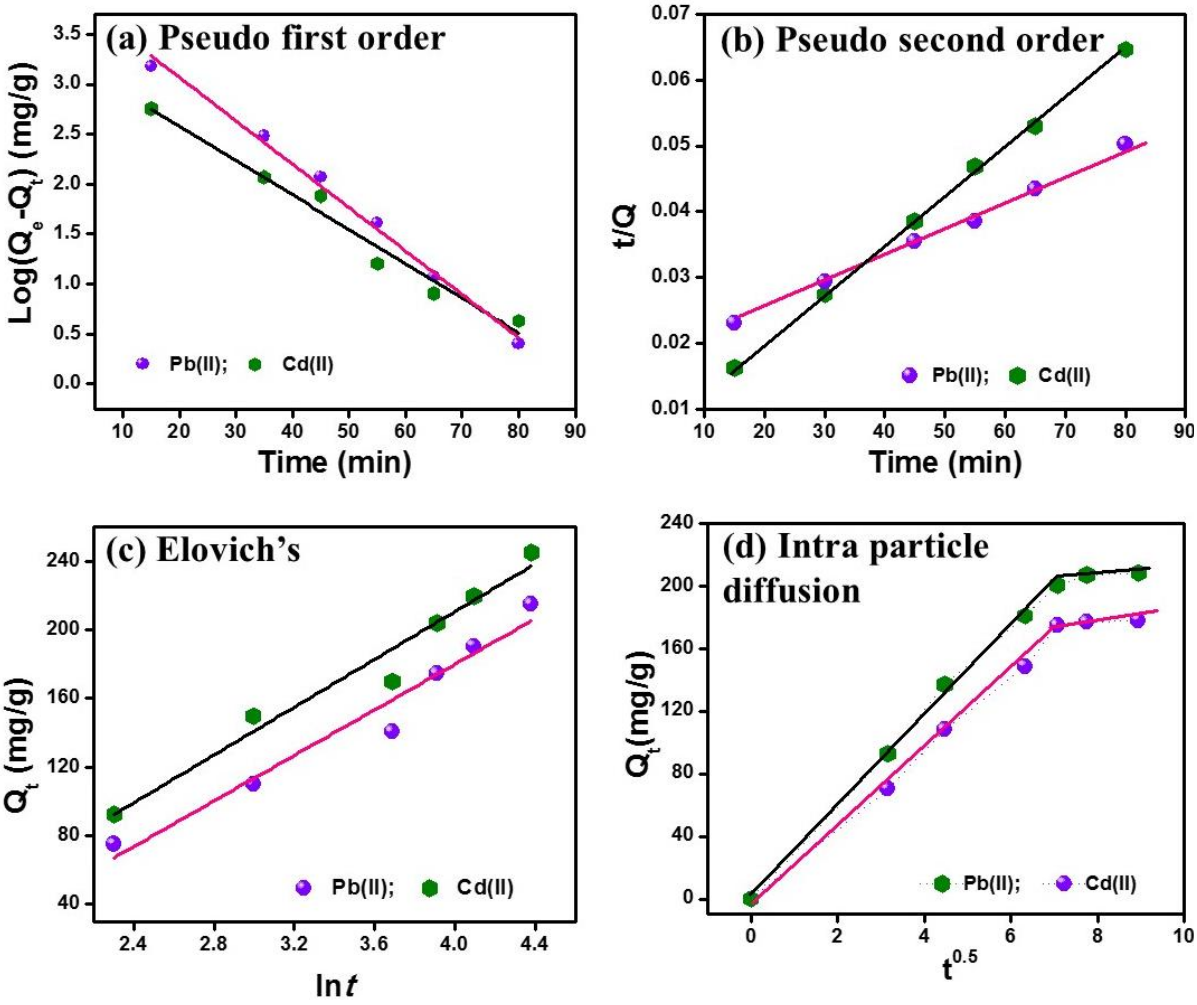

Fig. 3.25: Linear fit curves for (a) pseudo first order, (b) pseudo second order, (c) elovich's model and (d) intra-particle diffusion model for carbon monoliths [adsorbent concentration: 0.02 g/L, agitation speed: 200 rpm, pH: 6, temperature: 25 °C].

Plots of pseudo first order, pseudo second order for elovich's model and intra-particle diffusion model for CMs on the adsorption of Pb(II) and Cd(II) ions are shown in Fig. 3.25, respectively. For metal-ion adsorption on CM, pseudo-second order kinetic model shows better fitting corresponding to other models which suggests that adsorption process in this study characteristically controlled by chemisorption as displayed in Table 3.13.

Table 3.13: Kinetic parameters and correlation coefficients for the kinetic models.

Model	**Parameters**	**CM**	
		Pd(II)	**Cd(II)**
	Q_e (exp)	**50**	**20**
Pseudo-first order	Q_e (cal)	51.1	26.31
	K_1	0.091	0.078
	R^2	0.942	0.966
Pseudo-second order	Q_e(cal)	112.8	70.9
	K_2	0.0096	0.0010
	R^2	0.992	0.989
Elovich's model	a	90.42	67.9
	b	0.015	0.011
	R^2	0.951	0.957
Intra particle diffusion model	k_i	24.69	20.6
	I	1.3	0.5
	R^2	0.950	0.944

3.11.5 Reusability of adsorbent

To access the reusability of used CMs as adsorbent, their regeneration using NaOH (2M) [11] and reusability for adsorption of heavy metal-ions (Pb(II) and Cd(II)) were carried out up to 3 cycles which has been shown in Fig. 3.24d. The adsorption efficacy for both Pb(II) and Cd(II) ions decreases steadily with increased number of cycles because most of the adsorption sites get occupied due to bond formation between adsorbent and adsorbate. The good reusability of CM is due to the micrometer-sized structure with high surface area, which has a benefit of reducing overall cost for adsorption process. Furthermore, desorption conditions are more simple and accessible as no specific filtration techniques are required for adsorbent extraction due to its large size.

3.12 Conclusion

In summary, carbon monoliths are synthesized via nanocasting method show an excellent adsorption ability for removal of heavy metal ions from water. Equilibrium between CM and metal ion solution was achieved in approximately 60 min at pH 6. The maximum monolayer adsorption efficiency for Pb(II) and Cd(II) ions is 1128 mg/g and 989 mg/g, respectively. Kinetic data for the adsorption process shows best fit to pseudo second order. CM monoliths can be reusable as adsorbent (because of solid rock like structure) and become highly effective and economical adsorbent for heavy metal ion adsorption process.

References:

1. J. P. Zou, H. L. Liu, J. Luo, Q. J. Xing, H. M. Du, X. H. Jiang, X. B. Luo, S. L. Luo and S. L. Suib, *ACS applied materials & interfaces*, 2016, **8**, 18140-18149.
2. S. Khan, C. Chao, M. Waqas, H. P. Arp and Y. G. Zhu, *Environmental science & technology*, 2013, **47**, 8624-8632.
3. A. Mittal, J. Mittal, A. Malviya and V. K. Gupta, *Journal of colloid and interface science*, 2009, **340**, 16-26.
4. Z. L. He, X. E. Yang and P. J. Stoffella, *J Trace Elem Med Biol*, 2005, **19**, 125-140.
5. C. K. Ahn, D. Park, S. H. Woo and J. M. Park, *Journal of hazardous materials*, 2009, **164**, 1130-1136.
6. M. A. Alavi and A. Morsali, *Ultrasonics sonochemistry*, 2010, **17**, 441-446.
7. S. Mahdavi, M. Jalali and A. Afkhami, *Chemical Engineering Communications*, 2013, **200**, 448-470.
8. S. Debnath and U. C. Ghosh, *Desalination*, 2011, **273**, 330-342.
9. W. Si, Y. Wang, S. Zhao, F. Hu and J. Li, *Environmental science & technology*, 2016, **50**, 4572-4578.
10. L. Zhang, J. Lian, L. Wu, Z. Duan, J. Jiang and L. Zhao, *Langmuir : the ACS journal of surfaces and colloids*, 2014, **30**, 7006-7013.
11. J.-S. Hu, L.-S. Zhong, W.-G. Song and L.-J. Wan, *Advanced Materials*, 2008, **20**, 2977-2982.
12. T. A. Saleh and V. K. Gupta, *Environmental science and pollution research international*, 2012, **19**, 1224-1228.
13. M. I. Zaman, S. Mustafa, S. Khan and B. Xing, *Journal of colloid and interface science*, 2009, **330**, 9-19.
14. L. Dong, Z. Zhu, H. Ma, Y. Qiu and J. Zhao, *Journal of Environmental Sciences*, 2010, **22**, 225-229.
15. Y.-C. Lee and J.-W. Yang, *Journal of Industrial and Engineering Chemistry*, 2012, **18**, 1178-1185.
16. N. Wu, H. Wei and L. Zhang, *Environmental science & technology*, 2012, **46**, 419-425.
17. J. Hu and H. J. Shipley, *Environmental science and pollution research international*, 2013, **20**, 5125-5137.

18. J.-H. Smått, C. Weidenthaler, J. B. Rosenholm and M. Lindén, *Chemistry of Materials*, 2006, **18**, 1443-1450.
19. A. H. Lu, J. H. Smatt and M. Linden, *Adv Funct Mater*, 2005, **15**, 865-871.
20. A.-H. Lu, J.-H. Smått, S. Backlund and M. Lindén, *Microporous and Mesoporous Materials*, 2004, **72**, 59-65.
21. B. Tian, X. Liu, H. Yang, S. Xie, C. Yu, B. Tu and D. Zhao, *Advanced Materials*, 2003, **15**, 1370-1374.
22. G. Hasegawa, K. Kanamori, T. Kiyomura, H. Kurata, T. Abe and K. Nakanishi, *Chemistry of Materials*, 2016, **28**, 3944-3950.
23. J.-H. Smått, F. M. Sayler, A. J. Grano and M. G. Bakker, *Advanced Engineering Materials*, 2012, **14**, 1059-1073.
24. T. Sano and Y. Oumi, *Catalysis surveys from Asia*, 2004, **8**, 295-304.
25. Y. Sato, K. Nakanishi, K. Hirao, H. Jinnai, M. Shibayama, Y. B. Melnichenko and G. D. Wignall, *Colloids and Surfaces A: Physicochemical and Engineering Aspects*, 2001, **187-188**, 117-122.
26. S. Jana, S. Basu, S. Pande, S. K. Ghosh and T. Pal, *The Journal of Physical Chemistry C*, 2007, **111**, 16272-16277.
27. Z. Xu, C. Huang, L. Wang, X. Pan, L. Qin, X. Guo and G. Zhang, *Industrial & Engineering Chemistry Research*, 2015, **54**, 4593-4602.
28. N. K. Amin, *Desalination*, 2008, **223**, 152-161.
29. A. Mittal, D. Kaur and J. Mittal, *Journal of hazardous materials*, 2009, **163**, 568-577.
30. M. Sharma, A. Mishra, A. Mehta, D. Choudhury and S. Basu, *Journal of Nanoscience and Nanotechnology*, 2017, **17**, 1-11.
31. C. A. Başar, *Journal of hazardous materials*, 2006, **135**, 232-241.
32. S. Chatterjee, S. Chatterjee, B. P. Chatterjee and A. K. Guha, *Colloids and Surfaces A: Physicochemical and Engineering Aspects*, 2007, **299**, 146-152.
33. A. Shukla, Y.-H. Zhang, P. Dubey, J. Margrave and S. S. Shukla, *Journal of hazardous materials*, 2002, **95**, 137-152.
34. I. D. Mall, V. C. Srivastava, N. K. Agarwal and I. M. Mishra, *Chemosphere*, 2005, **61**, 492-501.
35. W. J. Thomson, *Introduction to transport phenomena*, Pearson College Division, 2000.

36. A. Mittal, D. Kaur and J. Mittal, *Journal of colloid and interface science*, 2008, **326**, 8-17.
37. M. J. Iqbal and M. N. Ashiq, *Journal of hazardous materials*, 2007, **139**, 57-66.
38. M. Xu, Y. Zhang, Z. Zhang, Y. Shen, M. Zhao and G. Pan, *Chemical Engineering Journal*, 2011, **168**, 737-745.
39. A. H. Chen, C. Y. Yang, C. Y. Chen and C. W. Chen, *Journal of hazardous materials*, 2009, **163**, 1068-1075.
40. X. Tan, X. Wang, M. Fang and C. Chen, *Colloids and Surfaces A: Physicochemical and Engineering Aspects*, 2007, **296**, 109-116.
41. S. Chella, P. Kollu, E. V. P. R. Komarala, S. Doshi, M. Saranya, S. Felix, R. Ramachandran, P. Saravanan, V. L. Koneru, V. Venugopal, S. K. Jeong and A. Nirmala Grace, *Applied Surface Science*, 2015, **327**, 27-36.
42. P. Wang, M. Du, H. Zhu, S. Bao, T. Yang and M. Zou, *Journal of hazardous materials*, 2015, **286**, 533-544.
43. X. Xue and F. Li, *Microporous and Mesoporous Materials*, 2008, **116**, 116-122.
44. M. R. Awual, T. Yaita, S. A. El-Safty, H. Shiwaku, S. Suzuki and Y. Okamoto, *Chemical Engineering Journal*, 2013, **221**, 322-330.
45. G. C. Panda, S. K. Das and A. K. Guha, *Journal of hazardous materials*, 2009, **164**, 374-379.
46. L.-S. Zhong, J.-S. Hu, A.-M. Cao, Q. Liu, W.-G. Song and L.-J. Wan, *Chemistry of Materials*, 2007, **19**, 1648-1655.
47. V. K. Gupta, P. J. M. Carrott, M. M. L. Ribeiro Carrott and Suhas, *Critical Reviews in Environmental Science and Technology*, 2009, **39**, 783-842.
48. F. Zhang, X. Chen, F. Wu and Y. Ji, *Colloids and Surfaces A: Physicochemical and Engineering Aspects*, 2016, **509**, 474-483.
49. V. K. Gupta and A. Nayak, *Chemical Engineering Journal*, 2012, **180**, 81-90.
50. S. S. Ahluwalia and D. Goyal, *Engineering in Life Sciences*, 2005, **5**, 158-162.
51. S. Hosseini, M. A. Khan, M. R. Malekbala, W. Cheah and T. S. Y. Choong, *Chemical Engineering Journal*, 2011, **171**, 1124-1131.
52. X. Xin, Q. Wei, J. Yang, L. Yan, R. Feng, G. Chen, B. Du and H. Li, *Chemical Engineering Journal*, 2012, **184**, 132-140.

53. Z. Sun, Y. Deng, J. Wei, D. Gu, B. Tu and D. Zhao, *Chemistry of Materials*, 2011, **23**, 2176-2184.
54. H. Cai, P. Liang, Z. Hu, L. Shi, X. Yang, J. Sun, N. Xu and J. Wu, *Nanoscale research letters*, 2016, **11**, 104.
55. S. Hernandez, V. Cauda, A. Chiodoni, S. Dallorto, A. Sacco, D. Hidalgo, E. Celasco and C. F. Pirri, *ACS applied materials & interfaces*, 2014, **6**, 12153-12167.
56. M. M. Momeni and Y. Ghayeb, *Journal of Applied Electrochemistry*, 2015, **45**, 557-566.
57. Y. Lei, G. Zhao, M. Liu, Z. Zhang, X. Tong and T. Cao, *The Journal of Physical Chemistry C*, 2009, **113**, 19067-19076.
58. A. Gomes, T. Frade, K. Lobato, M. E. M. Jorge, M. I. da Silva Pereira, L. Ciriaco and A. Lopes, *Journal of Solid State Electrochemistry*, 2011, **16**, 2061-2069.
59. J. Wang, G. Zhao, Y. Li, H. Zhu, X. Peng and X. Gao, *Dalton Trans*, 2014, **43**, 11637-11645.
60. M. H. A. Azqhandi, B. Vasheghani F, F. H. Rajabi and M. Keramati, *Results in Physics*, 2017, **7**, 1106-1114.
61. J. Aguado, J. M. Arsuaga, A. Arencibia, M. Lindo and V. Gascon, *Journal of hazardous materials*, 2009, **163**, 213-221.
62. A. Shahbazi, H. Younesi and A. Badiei, *Chemical Engineering Journal*, 2011, **168**, 505-518.
63. D. Alipour, A. R. Keshtkar and M. A. Moosavian, *Applied Surface Science*, 2016, **366**, 19-29.
64. S. Rajput, L. P. Singh, C. U. Pittman, Jr. and D. Mohan, *Journal of colloid and interface science*, 2017, **492**, 176-190.
65. T. A. Khan, S. A. Chaudhry and I. Ali, *Journal of Molecular Liquids*, 2015, **202**, 165-175.
66. M. Sharma, D. Choudhury, S. Hazra and S. Basu, *Journal of Alloys and Compounds*, 2017, **720**, 221-229.
67. C. Lei, X. Zhu, B. Zhu, C. Jiang, Y. Le and J. Yu, *Journal of hazardous materials*, 2017, **321**, 801-811.
68. S. P. Dubey, A. D. Dwivedi, M. Sillanpaa, H. Lee, Y. N. Kwon and C. Lee, *Chemosphere*, 2017, **169**, 99-106.

69. A. Smara, R. Delimi, E. Chainet and J. Sandeaux, *Separation and Purification Technology*, 2007, **57**, 103-110.
70. E. Erdem, N. Karapinar and R. Donat, *Journal of colloid and interface science*, 2004, **280**, 309-314.
71. D. K. V. Ramana, J. S. Yu and K. Seshaiah, *Chemical Engineering Journal*, 2013, **223**, 806-815.
72. L. Sun, C. Tian, L. Wang, J. Zou, G. Mu and H. Fu, *Journal of Materials Chemistry*, 2011, **21**, 7232.
73. M. Sharma, S. Hazra and S. Basu, *Journal of colloid and interface science*, 2017, **504**, 669-679.
74. M. R. Ganjali, L. H. Babaei, P. Norouzi, M. R. Pourjavid, A. Badiei, K. Saberyan, M. G. Maragheh, M. Salavati-Niasari and G. M. Ziarani, *Analytical Letters*, 2005, **38**, 1813-1821.
75. A. Jungbauer and R. Hahn, *Journal of separation science*, 2004, **27**, 767-778.
76. J. Urthaler, R. Schlegl, A. Podgornik, A. Strancar, A. Jungbauer and R. Necina, *Journal of Chromatography A*, 2005, **1065**, 93-106.
77. M. Sharma, P. Jain, A. Mishra, A. Mehta, D. Choudhury, S. Hazra and S. Basu, *Materials Letters*, 2017, **194**, 213-216.
78. J. Sharma, M. Sharma and S. Basu, *Journal of Environmental Chemical Engineering*, 2017, **5**, 3429-3438.
79. Y. P. Teoh, M. A. Khan and T. S. Y. Choong, *Chemical Engineering Journal*, 2013, **217**, 248-255.
80. S. Tangjuank, N. Insuk, J. Tontrakoon and V. Udeye, *World Acad. Sci. Eng. Technol.* , 2009, **52** 110-116.
81. M. R. Awual and M. M. Hasan, *Sensors and Actuators B: Chemical*, 2014, **202**, 395-403.
82. A. Shahat, M. R. Awual, M. A. Khaleque, M. Z. Alam, M. Naushad and A. M. S. Chowdhury, *Chemical Engineering Journal*, 2015, **273**, 286-295.

Chapter-4

Removal of Toxic Pollutants from Synthetic Waste Water using $ZnO@SiO_2$ Monoliths

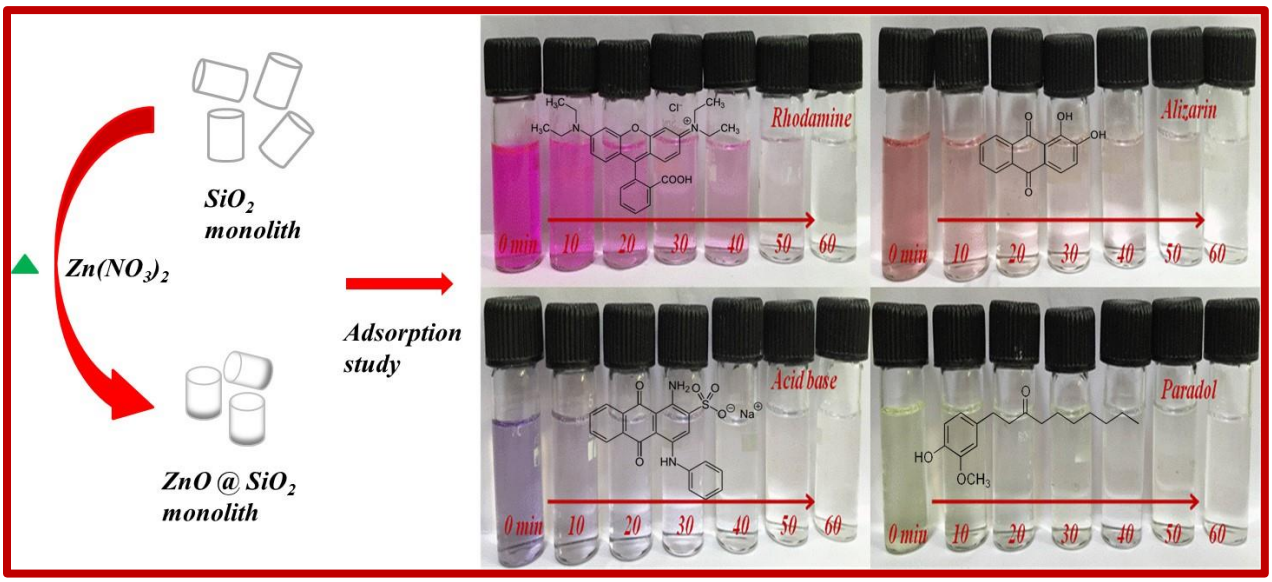

Removal of toxic effluents (like dyes and pesticides) by cost-effective and user-friendly method is needed to provide sustaining the environment for civilization. Here, low-cost mesoporous silica monolith (SiO_2) and silica supported metal-oxide ($ZnO@SiO_2$) monolith were synthesized to reduce the solemn impact of toxic effluents. Batch experiments were performed to remove Alizarin (AZ), Paradol (PD), Acid blue-113 (AB) and Rhodamine-B (RD) from aqueous solution via synthesized monoliths. The influence of various parameters (like pH, contact time, temperature and adsorbate concentration) has been optimized. The maximum adsorption capacity of $ZnO@SiO_2$ monolith is 625, 500, 714 and 555 mg/g for AZ, RD, AB, and PD respectively. The adsorption for AZ, PD, AB, and RD is spontaneous and exothermic. The adsorption process can be well described by the pseudo-second-order kinetic model (high regression coefficients) and the Freundlich isotherm model (R^2 = 0.97–0.99).

4.1 Introduction

In the recent era, water resources get polluted due to growth in population and industrial activities. Ground water and surface water gets contaminated by the excess release of toxic and some colored effluents like pesticides (substances used to destroy insects or pests) and organic dyes (unprocessed colored substances)[1]. These toxic wastes (agrochemical residues/organic pollutants) are highly hazardous to aquatic living, agriculture, animal and human health. Toxic effluents containing dyes and pesticides need to be treated before being delivered to the environment due to their toxic and carcinogenic effects on the living system including human beings by causing skin irritations, allergies etc.[2-4]. Among several physical or chemical methods, adsorption process can be used as a conventional method as it is utmost effective, cost effective, eco-friendly and easy to use. In this process, pollutants are transferred from aqueous medium onto the surface of the solid material. Also, adsorbents with high surface reactivity, surface area and with a high number of the vacant site are in demand. Several adsorbents (natural or synthetic) such as polymers, activated carbon, agro-industrial wastes, zeolite, CNTs etc.[5-7] have been used as adsorbents for the treatment of contaminated water.

Porous material, mainly those with bimodal porosity, used as an essential material to numerous important application including heterogeneous catalysis, adsorption and separation process. Due to the presence of a high number of reactive sites, porous composites are considered as a novel adsorbent for pre-concentration of toxic effluents[8-10]. Recently, mesoporous metal oxides (like Al_2O_3, MgO, SnO_2, Fe_3O_4, TiO_2 etc.) have gained huge attention for adsorption of organic pollutants because of their high surface area, reusability and more efficiency metal oxides other than ZnO have already been reported for toxic effluent removal[11, 12]. In literature, nano ZnO (metal-oxide) have been used for remediation of pollutants in water. Nonetheless, most of the literature has been focused on the photocatalytic activity of ZnO and studies regarding adsorptive affinity of ZnO in the direction of pollutant removal are still insufficient. Because of non-toxicity, easy producibility, and high adsorptive properties, mesoporous ZnO composites are considered as one of the most competent adsorbents for the removal of various toxic pollutants[13-15]. With controllable porosity, surface area and high available adsorption sites of ZnO nanocomposites enhance its utility for various other applications, especially for removal or adsorption of toxic pollutants[16-18].

ZnO can be synthesized by different methods including hydrothermal, sol-gel, microwave irradiation etc. Using nanocasting method, hierarchically porous ZnO monoliths of desired length scale can be synthesized. This process has already been used to prepare porous monoliths of carbon, NiO, TiO_2, Co_3O_4, SnO_2, MnO_2, ZrO_2, Al_2O_3, Cr_2O_3, In_2O_3, CeO_2, Fe_2O_3, Y_2O_3 and various mixed-oxides[19-25]. Ordered porous oxides because of their large surface areas, large pore volumes and ordered pore networks have a wide range of potential applications in energy storage, nanoreactors, semiconductors, electronic devices, catalysis and gas sensors[26]. Chitosan-polyaniline/ZnO hybrids were used as an adsorbent for removal of reactive orange-16 dye and the maximum adsorption efficiency was found 476.2 mg/g[27]. Removal of bromophenol red was investigated using ZnO nanoparticles loaded on activated carbon; maximum adsorption efficiency was found 200 mg/g[28]. Mostly, ZnO nanocomposites are available in powder form which has disadvantages since they make a miscible suspension with water. Therefore; the fast and economical method is needed for the growth of unsurpassed system for solid phase extraction from solution. So, in this regard, we tried to make mesoporous silica supported ZnO monoliths (solid rock style material) for pesticide and dye adsorption, which is cost effective. However, up to date, the efficient removal of organic toxic pollutants using solid ZnO@SiO_2 monoliths has not been studied yet. In this work synthesis of mesoporous ZnO@SiO_2 monoliths via nanocasting process from hierarchically porous parental silica monolith has been discussed in detail. The efficient removal of pesticides and dyes using solid ZnO@SiO_2 monoliths has been studied in detail. The effect of several physicochemical parameters, such as sorbent particle size, pH, contact time and pollutant concentration as well as the thermodynamic parameters are calculated and discussed. The kinetic data are modeled by the pseudo-first-order, pseudo-second-order, and Elovich's models. The Langmuir and Freundlich models were used to describe equilibrium isotherms. Our results indicate that the high adsorption capacity for pesticide and dye solutions will promote the application of ZnO@SiO_2 monolith as advanced adsorbent materials.

4.2.1 Synthesis of silica monoliths

Detailed synthesis procedure for silica monoliths has been explained in **Chapter 2, section 2.2.1**

4.2.2 Synthesis of $ZnO@SiO_2$ monoliths

$ZnO@SiO_2$ monoliths were synthesized via nanocasting method. Zinc nitrate hexahydrate (3.1 M) solution was impregnated into as prepared silica monoliths after degassing them under vacuum. The wet monoliths were heated at 150 °C for 10 h (1 °C/min). Impregnation process was repeated for at least five times to get uniform $ZnO@SiO_2$ monoliths. Later, synthesized composites were calcined at 400 °C for 5 h at a rate of 1 °C /min.

4.2.3 Characterization of monoliths

As synthesized silica and $ZnO@SiO_2$ monoliths were characterized by various techniques; details of the techniques are given in **Chapter 1, section 1.9**

4.2.4 Adsorption Study

Adsorption efficacy of synthesized adsorbents for organic dyes and pesticides was evaluated through UV-vis spectrophotometer; detail procedure has been given in **Chapter 1, Section 1.10.1**

4.3 Results and discussion

Bimodal interconnected porous structures were obtained via phase separation and gelation after successively completing interaction between gelling silica/CTAB micelles and water-soluble polymer (PEG). Fig. 4.1a shows the type IV, nitrogen sorption plot for SiO_2 and $ZnO@SiO_2$ monoliths which confirm the characteristics of mesoporous material. The characteristic parameters such as specific surface area, total pore volume and pore diameter of the synthesized monoliths are discussed in Table 1. The BJH pore size distribution indicates that the samples have pores in the range of 5–20 nm (Fig. 4.1b), which indicate the mesoporous nature of the materials.

Table 4.1: Textural characteristics for synthesized monoliths determined from nitrogen sorption measurements.

Monoliths	**S_{BET} ($m^2\ g^{-1}$)**	**d (nm)**	**V_g ($cm^3\ g^{-1}$)**
SiO_2	761	18.4	1.4
$ZnO@SiO_2$	125	6.5	0.3

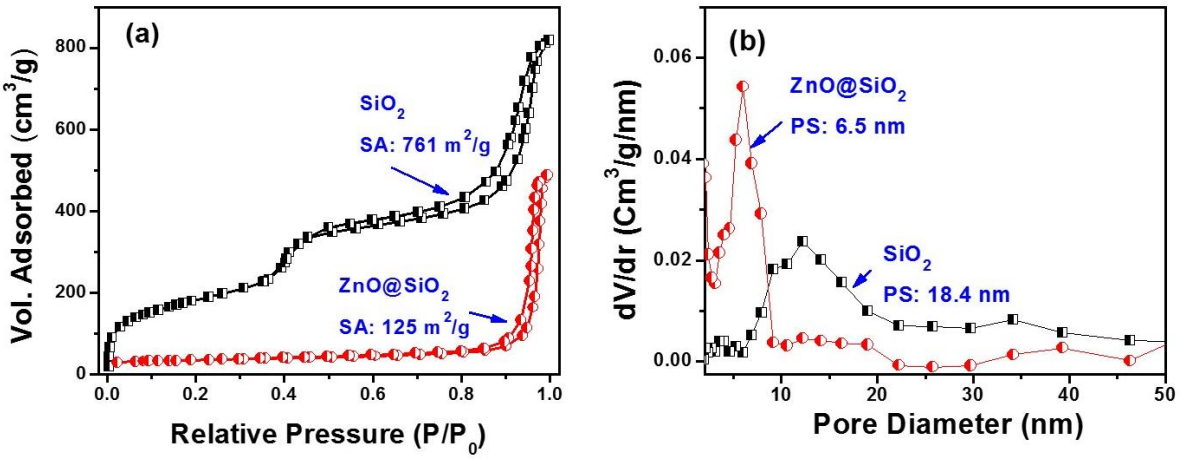

Fig. 4.1: a) Nitrogen adsorption desorption curve, b) Pore size distribution using BJH plot for SiO_2 and ZnO@SiO_2 monoliths.

The phase and purity of the synthesized ZnO@SiO_2 monoliths were confirmed by XRD analysis (Fig. 4.2a). XRD pattern confirms the formation of hexagonal structure of ZnO on the surface of SiO_2 monolith. ZnO@SiO_2 monolith shows dominant peaks for ZnO, 2Θ at 31.8°, 34.4°, 36.23, 47.5, 56.6 and 62.8° corresponding to lattice planes of (100), (002), (101), (102), (110) and (103) respectively, which is confirmed by JCPDS card no. 36-1451 [29]. Inset of Fig. 4.2a shows mesoporous nature of SiO_2 monoliths. No other diffraction peaks corresponding to $Zn(NO)_2 \cdot 6H_2O$ and $Zn(OH)_2$ or other impurities have been found in the samples, indicating that the precursor has completely transformed into ZnO. Diffused reflectance spectra (DRS) or absorbance as a function of wavelength shows exciton absorption edges at 346 nm for ZnO (Fig. 4.2b) and its optical band gap (E_g) was calculated using the following equation:

$$(\alpha h\nu)^2 = A(h\nu - E_g)^n \qquad (4.1)$$

where α is absorption coefficient, E_g represents optical band gap, A is a characteristic constant and hν is photon energy. The band gap of ZnO@SiO_2 monolith was evaluated according to intercept of the line obtained from Tauc plot (Fig. 4.2c). The presence of a single slope in the plot shows that the mesoporous monoliths have direct and allowed transitions.

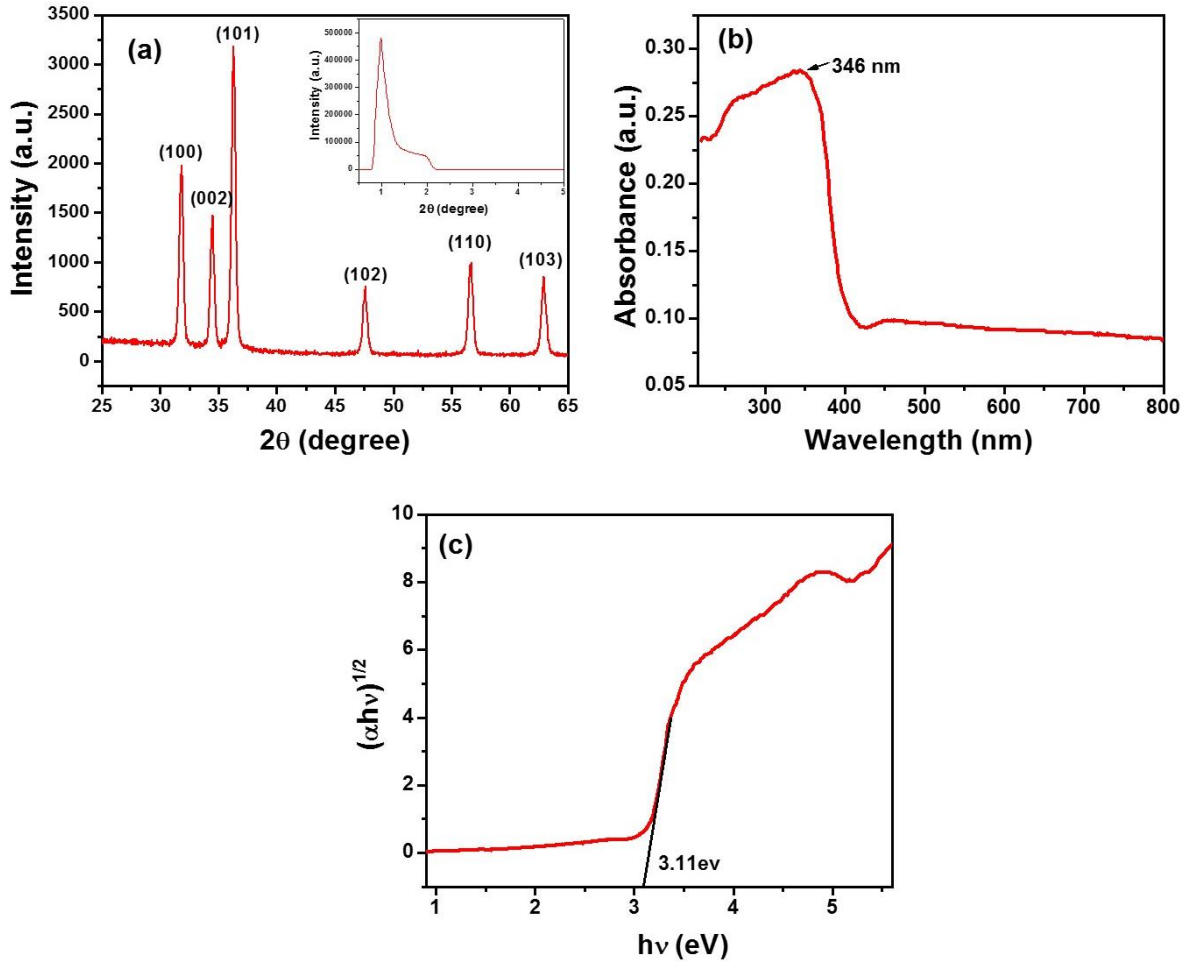

Fig. 4.2: a) XRD pattern b) UV-vis spectrum and c) Tauc plot for ZnO@SiO_2 monolith.

The optical band gap energy is obtained by extrapolating the straight line portion of the plot to zero absorption coefficient. The band gap value of ZnO was found to be 3.11 eV. FESEM images of the SiO_2 and ZnO@SiO_2 monoliths are shown in Fig. 4.3. The morphology of the macropores is very similar in both the cases. There appears to be fine mesopore structure within the walls of the macropores. The elemental composition of the synthesized monoliths was confirmed by EDS analysis (Fig. 4.3). Uniform distribution of the precursors throughout the core of the SiO_2 monoliths was responsible for chemical homogeneity.

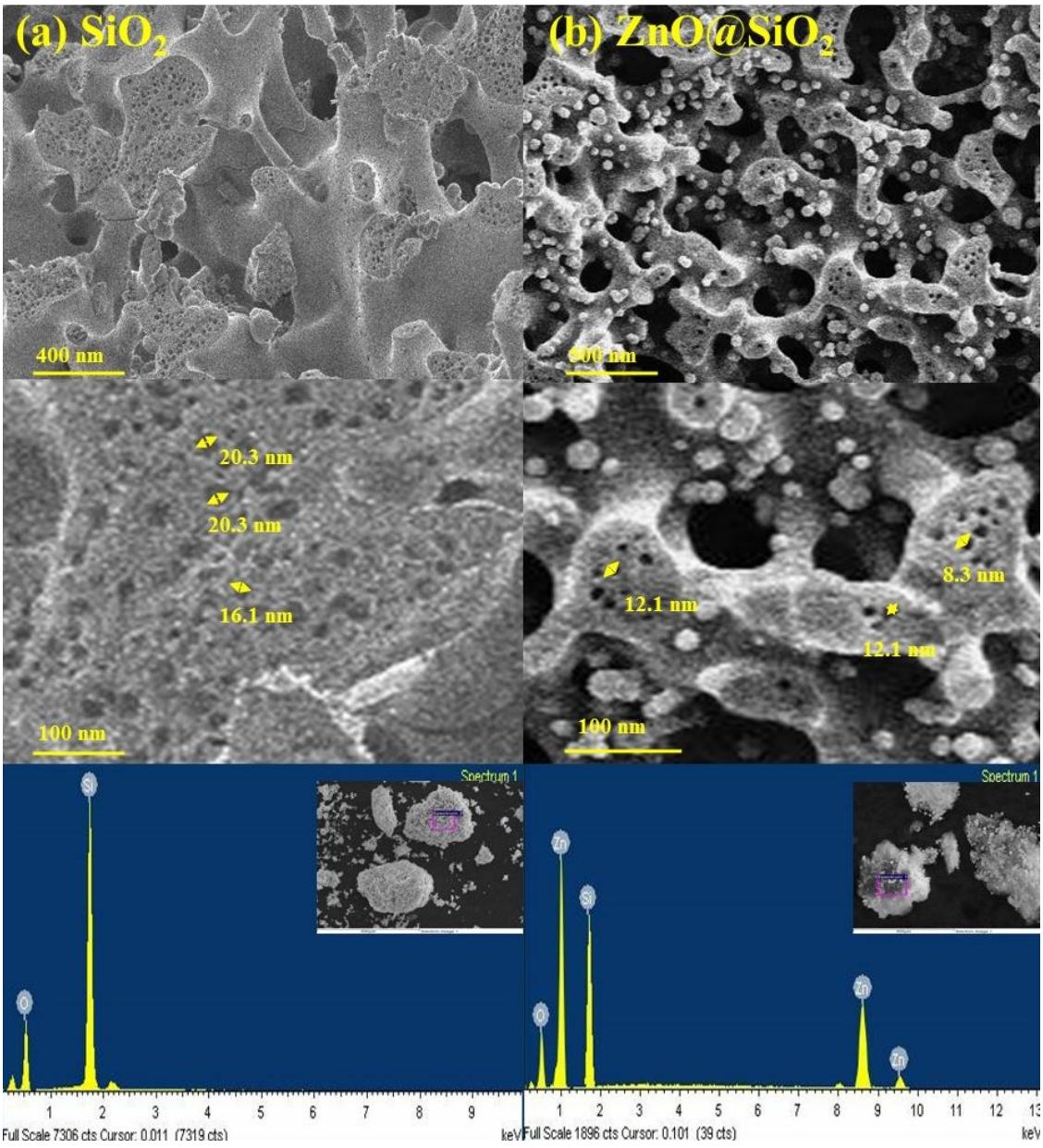

Fig. 4.3: FESEM and energy dispersive X-ray spectra for SiO_2 and $ZnO@SiO_2$ monoliths.

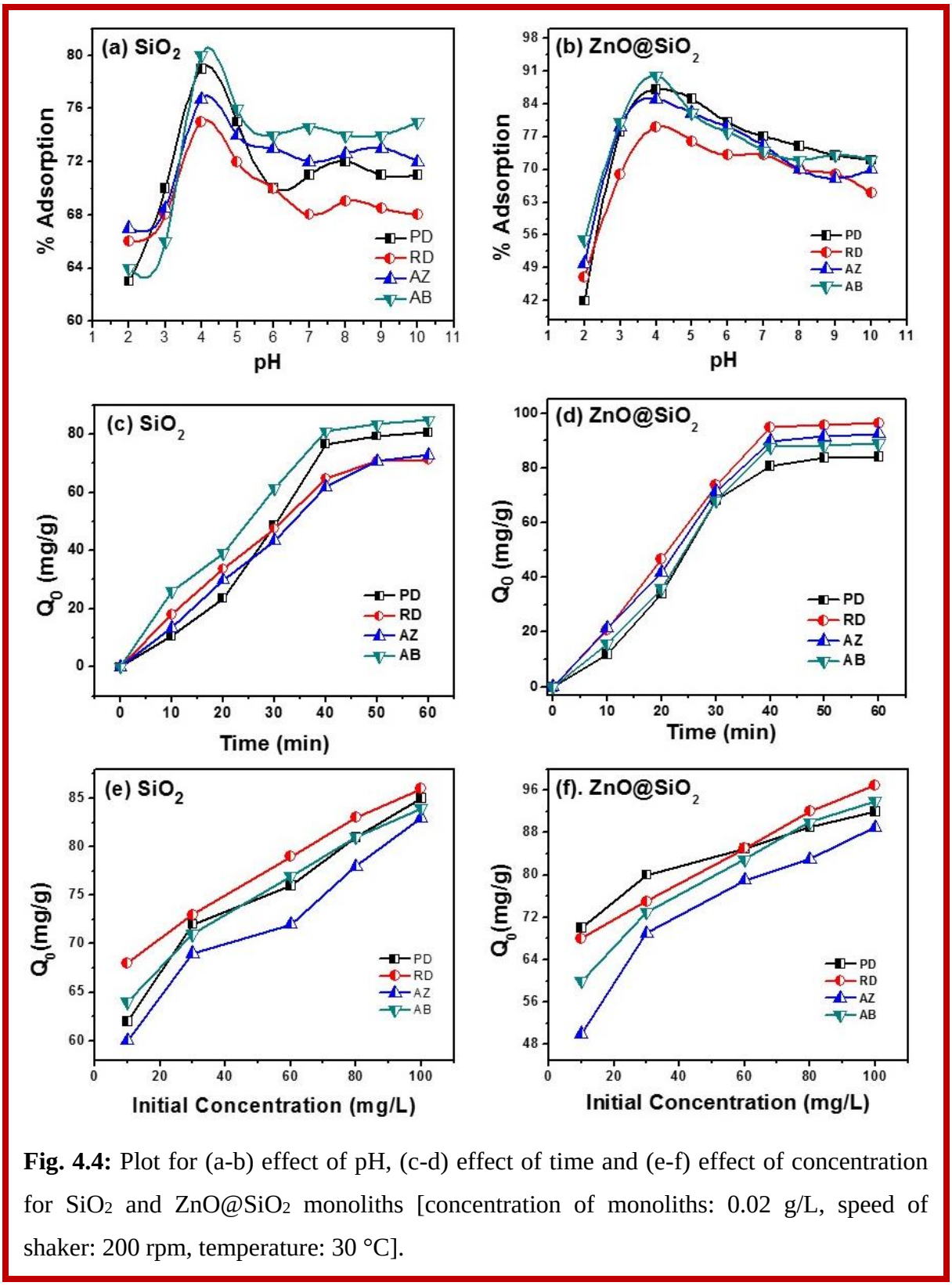

Fig. 4.4: Plot for (a-b) effect of pH, (c-d) effect of time and (e-f) effect of concentration for SiO_2 and $ZnO@SiO_2$ monoliths [concentration of monoliths: 0.02 g/L, speed of shaker: 200 rpm, temperature: 30 °C].

4.3.1 Adsorption studies

4.3.1.1 Effect of pH

Adsorption of dyes and pesticide in the pores of monoliths depends on the pH of the solution, due to different degree of ionization, surface binding sites of adsorbents. Adsorption of pollutants by different monolith was studied at a pH range from 3 to 10. pH values were adjusted by addition of either NaOH or HNO_3 on the synthetic solution of pollutants[30-32]. Fig. 4.4 (a-b) shows plots for the effect of pH on pollutant adsorption efficiencies of SiO_2 and ZnO@SiO_2 monolith. It was observed that the adsorption percentage increases with increase of pH (from pH 2 to 4). At pH 4, the adsorption process become highest, may be due to the maximum number of active sites present at the surface of adsorbent. Under the acidic conditions (at low pH), the surface of the adsorbents was surrounded by H^+ ions that interacts with anions of toxic pollutants. Higher adsorption for anionic dye (Acid blue), obtained at lower pH values may be due to electrostatic attraction between the negatively charged dye and positively charged adsorbent surface. Similarly, for the cationic dye (Rhodamine B) the interaction is very less and as a result the % adsorption is decreases. For neutral dye (Alizarin) and pesticide (Paradol) the interaction is not effective and as a result the % adsorption is moderate.

4.3.1.2 Effect of contact time

The effect of contact time was analyzed between 10 to 60 min for the adsorption of pollutants by SiO_2 and ZnO@SiO_2 monoliths. A physical change can be observed in Fig. 4.4(c-d). As the equilibrium time depends upon the initial concentration of pollutants, we have maintained the initial concentrations of the pollutants at 10 mg/L (pH 4). Pollutants were quantitatively adsorbed by the SiO_2 and ZnO@SiO_2 monoliths from the aqueous solution even after at a short time of exposure (<10 min). Since there was no significant increase in pollutants sorption after 40 min, the adsorption time of 60 min was kept for auxiliary experiments[33, 34].

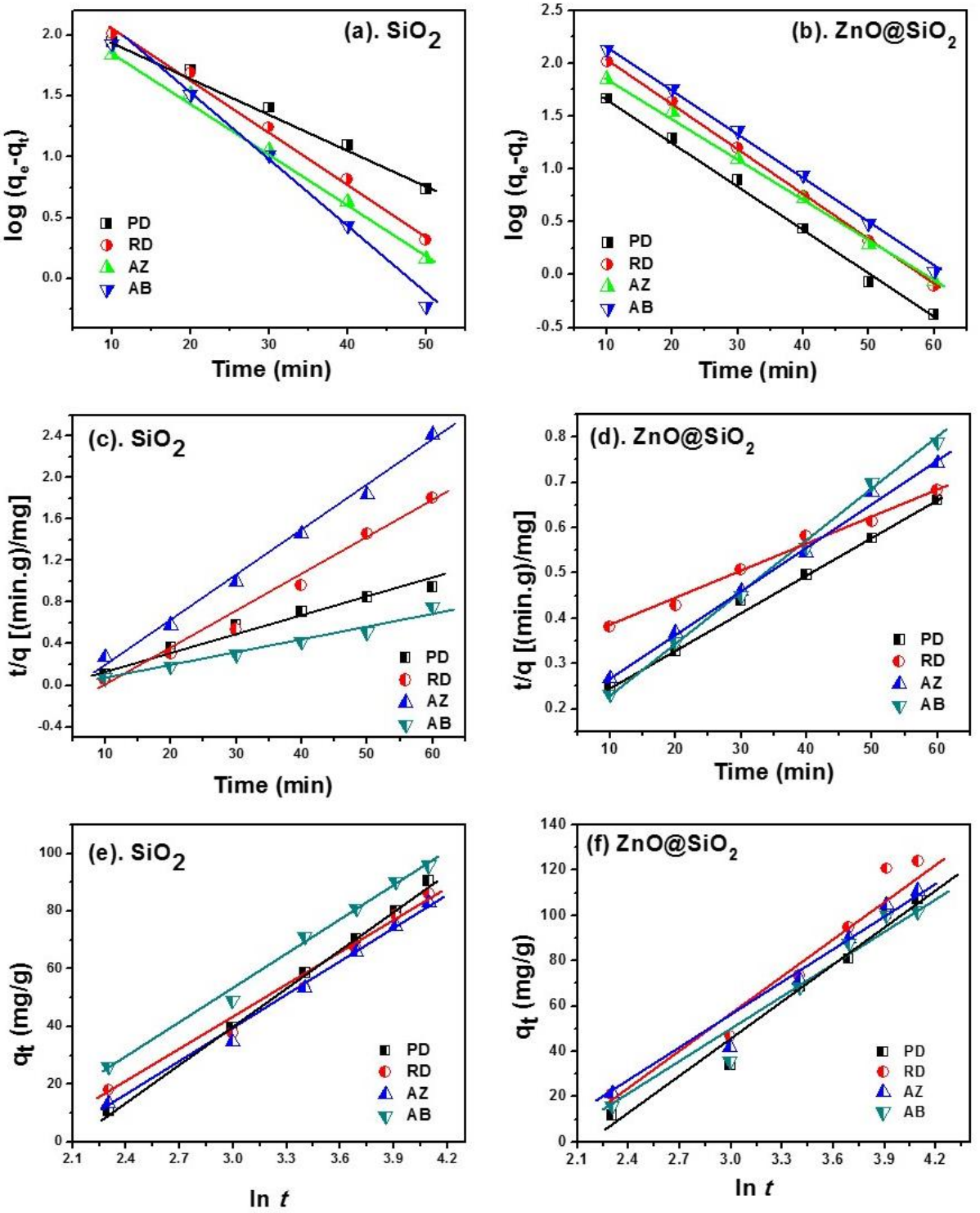

Fig. 4.5: Linear fit curves for (a-b) Pseudo first order, (c-d) Pseudo second order, (e-f) Elovich's model for SiO_2 and $ZnO@SiO_2$ monoliths [concentration of monoliths: 0.02 g/L, speed of shaker: 200 rpm, pH: 4, temperature: 30 °C].

4.3.1.3 Effect of initial concentration of pollutants

Effect of the initial concentration of pollutants on the monolith (0.02 g) was studied by changing the initial pesticide and dyes concentrations in the range of 10-100 mg/L at most effective pH 4 and at room temperature (Fig. 4.4(e-f)). The initial concentration offers the desired driving forces to overcome the resistance to mass transfer of pollutant ions between aqueous and solid phase. Accordingly, increase in initial concentration also enhances the interaction between pollutants and monoliths. The results confirmed that the removal of pollutants was directly proportional to the initial concentrations of pollutants [35, 36].

4.3.2 Adsorption Kinetics

The kinetics of different pollutants adsorption on SiO_2 and $ZnO@SiO_2$ monoliths were also evaluated using pseudo-first-order rate equation and pseudo-second-order kinetic model [37, 38]. The pseudo-first-order rate equation is usually used to predict adsorption kinetics and is expressed as;

$$\log(q_e - q_t) = \log(q_e) - \frac{K_1}{2.303} t \qquad (4.2)$$

where q_e and q_t are a number of pollutants (mg/g) adsorbed at equilibrium and at any given time t (min) respectively and K_1 is the rate constant for the pseudo-first-order reaction for adsorption (min^{-1}). Activated adsorption can be defined by Elovich's equation. Also, this equation has been used for relating adsorption of pollutants from aqueous solution and can be expressed as;

$$q_t = \frac{1}{b}\ln(ab) + \frac{1}{b}\ln(t) \qquad (4.3)$$

Where a and b are initial adsorption rate (mg/(g.min)) and a desorption constant (g/mg) respectively. If this equation applies, it should lead to a straight line by plotting q_t as a function of ln(t) [39-41].

The pseudo-second-order rate equation is expressed as;

$$\frac{t}{q_t} = \frac{1}{k_2 q_e^2} + \frac{t}{q_e} \qquad (4.4)$$

where q_e and q_t are a number of pollutants (mg/g) adsorbed at equilibrium and at any given time t (min) respectively and K_2 is the rate constant for pseudo-second order reaction for adsorption (g/mg min) [42]. Linear fit plots of pseudo-first-order, pseudo-second-order and Elovich's equation

for synthesized monoliths for the adsorption of different pollutants are shown in Fig. 4.5. Table 4.2 shows the parameters obtained from the pseudo-first-order equation (q_e and K_1) of Elovich's equation (a and 1/b) and of the pseudo-second-order kinetic model (K_2 and q_e). However, correlation coefficients (R^2) were found near to unity for all batches. But, the sorption kinetics can be described more appropriately by a pseudo-second-order model than other kinetic models for all the investigated pollutants, as adsorption process was mostly controlled by chemisorption.

Table 4.2: Kinetic parameters for adsorption of dyes and pesticide on different monoliths.

Adsorbent	**Pollutants**	**Pseudo-first order**			**Elovich's equation**			**Pseudo-second order**		
		q_e *	$K_1 \times(10^{-2})^+$	R^2	a$	1/b*	R^2	K_2@	q_e *	R^2
SiO_2	AZ	7.8	6.9	0.964	201.3	0.021	0.969	1.7×10^{-2}	32.5	0.990
	AB	9.6	9.6	0.985	291.3	0.024	0.953	3.4×10^{-2}	28.57	0.993
	RD	8.3	9.6	0.956	212.4	0.025	0.974	7.4×10^{-2}	23.8	0.983
	PD	10.7	12.2	0.880	265.5	0.026	0.936	0.18×10^{-2}	37.3	0.975
ZnO@ SiO_2	AZ	29.7	1.6	0.948	398.3	0.018	0.974	4.7×10^{-4}	111.1	0.995
	AB	33.6	1.86	0.960	431.9	0.018	0.977	10×10^{-4}	90.9	0.997
	RD	31.8	1.86	0.969	480.6	0.016	0.987	1.1×10^{-4}	166.6	0.999
	PD	28.2	1.8	0.986	477.6	0.017	0.949	3.7×10^{-4}	125	0.995

Where, * = mg/g; **@ =** g/(mg.min); $ = mg/(g.min); + = min^{-1}.

4.3.3 Adsorption isotherms

Adsorption isotherm gives proper quantitation of effectiveness of adsorption. The relationship between the concentrations of adsorbed and dissolved adsorbate at equilibrium along with the interactive behavior between the adsorbate and adsorbent can also describe by adsorption isotherm. In this study, Langmuir and Freundlich isotherm models were used to analyze the adsorption mechanisms, through which experimental results of pollutants can be explained in a wide range of concentrations. The Langmuir equation is expressed as follows;

$$\frac{C_e}{q_e} = \frac{1}{Q_o b} + \frac{C_e}{Q_o} \qquad (4.6)$$

where, the adsorption capacity at equilibrium is q_e (mg/g) and the maximum amount of the AZ, AB, RD and PD adsorbed per unit weight of the adsorbent is Q_0 (mg/g). When the surface is entirely covered with pollutants, Q_0 represents the adsorption capacity, helping in the assessment of adsorption act of different adsorbents.

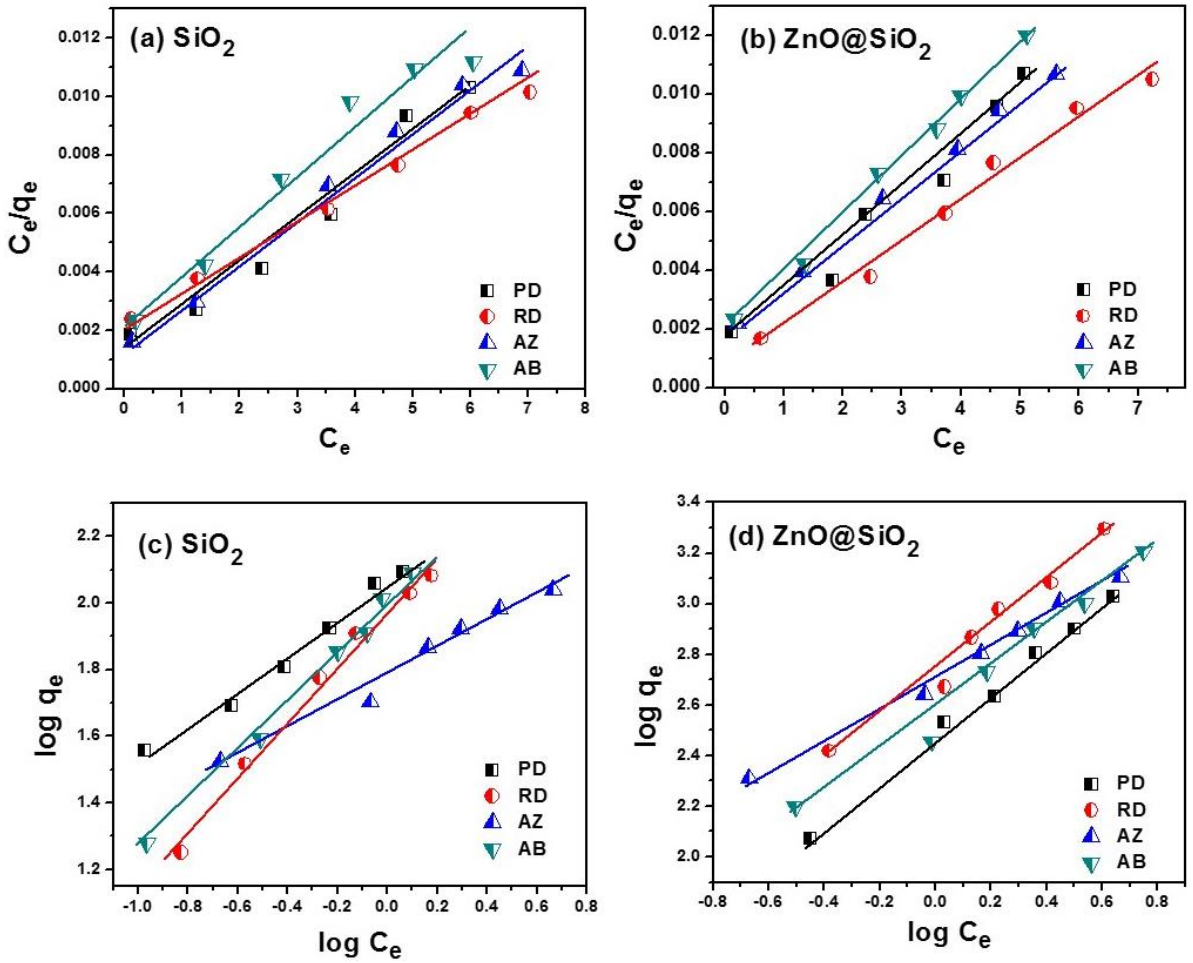

Fig. 4.6: Linear plots for isotherms (a-b) Langmuir and (c-d) Freundlich for SiO_2 and $ZnO@SiO_2$ monoliths [concentration of monoliths: 0.02 g/L, speed of shaker: 200 rpm, pH: 4, temperature: 30 °C].

Langmuir equilibrium constant (b) which is interrelated to the similarity of the connecting spots, shows the bond energy for the adsorption reaction. The linear plots of C_e/q_e vs. C_e propose the validity of the Langmuir isotherms and the values of Q_0 and b are obtained from slope and intercepts of the plots [43, 44]. Plots for Langmuir isotherm for adsorption of different pollutants on monoliths are shown in Fig. 4.6(a-b). The Freundlich isotherm is a resultant model of multilayer adsorption on the adsorbent. It can be described as:

$$\log q_e = \log K_f + \frac{\log C_e}{n} \qquad (4.7)$$

Freundlich constants, K_f ($mg^{1-1/n}L^{1/n}$ g^{-1}) and n, depict the adsorption capacity and intensity, respectively [45]. Freundlich isotherm plot for AZ, AB, RD and PD adsorption on different monoliths are shown in Fig. 4.6(c-d). Isotherm parameters for Langmuir and Freundlich models are listed in Table 4.3.

Table 4.3: Comparison of isotherm parameters and coefficients for different pollutants over monoliths at room temperature.

Adsorbent	Pollutants	Langmuir			Freundlich		
		Q_0 [+]	b	R^2	K_f [++]	n	R^2
SiO_2	AZ	102	0.05	0.991	4.8	1.1	0.997
	AB	123	0.14	0.979	6.9	1.5	0.996
	RD	83	0.04	0.966	6.9	1	0.980
	PD	96	0.19	0.990	7.3	1	0.999
ZnO@ SiO_2	AZ	625	0.84	0.987	14.9	1.62	0.993
	AB	714	1.05	0.896	12.9	1.20	0.978
	RD	500	2	0.986	15.1	1.16	0.994
	PD	556	1.5	0.966	11.8	1.14	0.996

Where, [+] = mg g^{-1}; [++] = $mg^{1-1/n}L^{1/n}$ g^{-1}

Adsorption is considered as satisfactory when the Freundlich constant n takes values within the range (1–10). The higher the value of R^2 for Freundlich model indicating the better applicability of Freundlich model. A comparative maximum monolayer adsorption efficiency of different nanostructures for different pollutants is listed in Table 4.4 and here it could be concluded that the as-synthesized monoliths could be employed as an alternative adsorbent for toxic pollutants at low concentrations.

Table 4.4: A comparative account of the adsorption efficiency of different pollutants by different nanostructures.

Adsorbents	Surface area (m^2/g)	Pollutant	Maximum adsorption (mg/g)	Conditions	References
CPA/ZnO hybride	45.9	Orange 16 dye	476.2	Time -60 min	[27]
ZnO-NR-AC	--	Bromophenol red	200	pH- 1-9 Time-24 min	[28]
Activated carbon	981	Pesticide (Methoxychlor)	112.0	pH-2 Temp-25°C Time -60 min	[46]

ZnO nanoparticles	--	Victoria Blue	163.9	pH- 2-10	[47]
$ZnO/ZnFe_2O_4$	94.4	Methylene Blue	37.27	pH- 3-11	[29]
ZnO nanopowder	--	Reactive black	27.6	pH- 3-9	[48]
MWCNTs	--	Alizarin red S	161.29	pH-1-6	[49]
Functionalized ZnO NPs		Brilliant blue R-250	59.9	pH-2-12	[50]
$ZnO@SiO_2$ monolith	110	Alizarin Acid Blue Rhodamine Paradol	625 714 500 555	pH-4, Time -80 min, Temp-25°C	Present study

4.3.4 Intra-particle diffusion model

The adsorption kinetics may be defined from the mechanistic point of view occasionally and mechanism of adsorption can be evaluated by Weber-Morris model [51]. Generally, adsorption process involves either by one or more steps: surface diffusion, pore diffusion, film diffusion and adsorption on the pore surface, or a combination of more than one step. In a batch process, experimental sorption rate data relates the diffusive mass transfer by an apparent diffusion coefficient. In general, a process is said to be diffusion-controlled, if the process rate is dependent on the diffusion rate of the two components [52]. Intra-particle diffusion model can be used to explore the possibility of intra-particle diffusion process and according to which the amount adsorbed at time t, q_t, reads;

$$q_t = k_i t^{1/2} + I \qquad (4.8)$$

where k_i is the diffusion rate constant (mg/(g $min^{1/2}$)) and I is the intercept. If Weber– Morris plot of q_t versus $t^{1/2}$ provides a straight line, it defines intra-particle adsorption process only. Whereas, if the data shows multiple linear plots (showing influence of two or more steps) in the adsorption process, it indicates that adsorption mechanism involves more than two steps. It is assumed in the early stage of adsorption; external force plays an important role in the accumulation of adsorbate encircling the surface of the adsorbent (represented by first linear portion). Second, linear portion shows the controlled intra-particle diffusion. Fig. 4.7(a-b) shows the plots of pollutants uptake (q_t) vs. $t^{1/2}$. The data points are related by two straight lines – the first straight portion depicting macropore and mesopore diffusion and the second representing micropore diffusion [53].

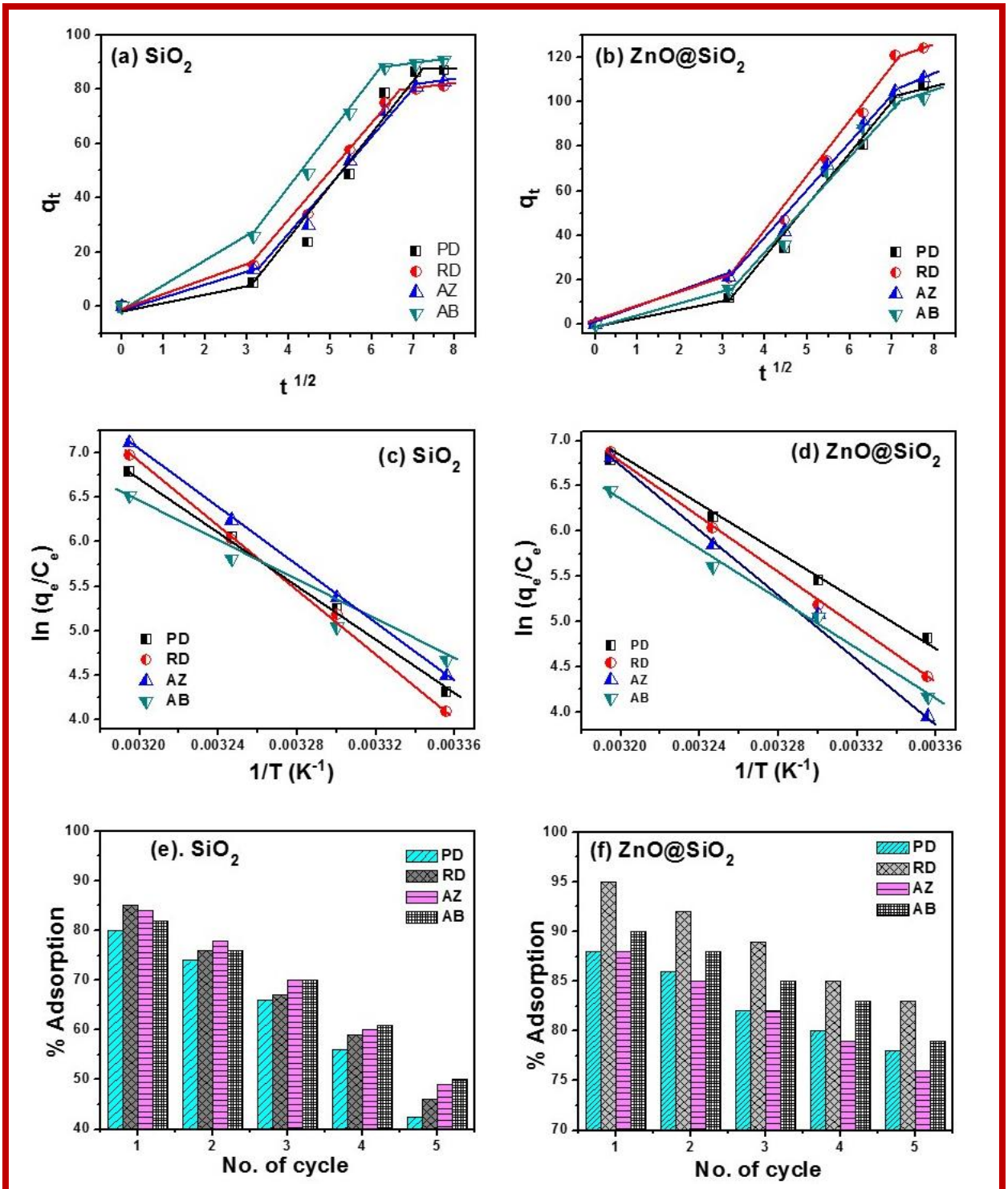

Fig. 4.7: Plot showing (a-b) Weber-Morris plot, (c-d) effect of temperature for adsorption studies on SiO_2 and $ZnO@SiO_2$ monoliths and (e-f) showing recyclability of monoliths [concentration of monoliths: 0.02 g/L, speed of shaker: 200 rpm, pH: 4, dye concentration: 10 mg/L].

The deviation of straight lines from the origin may be due to the difference in the rate of mass transfer in the initial and final stages of adsorption. Although, Pore diffusion is a fast process but this process does not contribute to control the total adsorption rate. Table 5 defines the intercept values indicating the thickness of boundary layers.

Table 4.5: Intra-particle diffusion parameters for the adsorption of dyes and pesticide.

Adsorbent	Pollutants	K_i	I	R^2
SiO_2	AZ	0.16	2.1	0.862
	AB	0.16	2.9	0.923
	RD	0.15	3.3	0.890
	PD	0.19	2.6	0.935
ZnO@SiO_2	AZ	0.20	4.5	0.985
	AB	0.24	4.9	0.965
	RD	0.20	5.2	0.987
	PD	0.22	5.8	0.983

4.3. 5 Effect of Temperature:

Temperature can also plays an important role/factor for adsorption of pollutants. To determine the nature of the adsorption process (endothermic or exothermic), adsorption for AZ, AB, RD and PD were done at different temperatures (303, 313, and 323 K). The increase in temperature results in a decrease of the values of $\ln(q_e/C_e)$ and also 1/T which specifies the exothermic nature of the adsorption process[54]. At different temperatures, the values of $\ln(q_e/C_e)$ are treated according to Van't Hoff equation;

$$\ln\left(\frac{q_e}{C_e}\right) = \frac{-\Delta H}{RT} + \frac{\Delta S}{R} \qquad (4.9)$$

where R is the universal gas constant (8.314 $Jmol^{-1}K^{-1}$) and T is the absolute temperature. The slope ($\Delta H/R$) and intercept ($\Delta S/R$) were evaluated from the plot between $\ln(q_e/C_e)$ and 1/T as shown in Fig. 4.7(c-d). At higher temperature, the adsorption process was also increased as toxic pollutants were adsorbed on the surface of monoliths. Table 4.6 shows the negative values of ΔG which confirms the spontaneity of the adsorption reactions.

Table 4.6: Thermodynamic parameters for different pollutants removal at different temperatures.

Adsorbent	Pollutants	ΔH (kJ mol^{-1})	ΔS (J mol K^{-1})	ΔG (kJ mol^{-1})		
				303(K)	313(K)	323(K)
SiO_2	AZ	-15.6	56.7	-1.07	-1.64	-2.2
	AB	-16.2	42.2	-1.16	-1.58	-2.0
	RD	-12.9	61.0	-0.94	-1.56	-2.1
	PD	-14.6	53.7	-1.05	-1.59	-2.6
ZnO@SiO_2	AZ	-16.7	60.2	-0.90	-1.5	-2.1
	AB	-13.2	48.7	-1.02	-1.5	-1.9
	RD	-14.7	55.0	-1.33	-1.88	-2.4
	PD	-11.8	44.5	-1.22	-1.66	-2.1

4.3.6 Reusability

Although, reusability of monoliths endures great challenges, still by treating the saturated rock like monoliths by 1 M NaOH, moderately regenerated monoliths can be achieved. Consequently, the reusability of monoliths was investigated by performing five consecutive adsorption cycles. After each cycle removal efficiency decreases up to 5-10 %. Here, for extraction of mesoporous particles, specific filtration techniques are not required because of their large size. In each cycle, pollutants were adsorbed by mesoporous SiO_2 or ZnO@SiO_2 monoliths, at room temperature for 60 min. Fig. 4.7 (e-f) shows reusability of SiO_2 or ZnO@SiO_2 monoliths, after 5 consecutive cycle of adsorption.

4.4. Conclusions

Mesoporous silica supported metal-oxide (ZnO@SiO_2) monoliths were synthesized and showed high absorption capacity and adsorption rate for removal of toxic effluents. Synthesized solid monoliths can be straightforwardly separated from aqueous solution due to their large size (0.5 cm in diameter and 0.8 cm in length) which gave a unique advantage in the form of efficient and low-cost recovery over existing systems. Adsorption and kinetic studies at pH 4 were performed for removal of AZ, PD, AB and RD in aqueous solution in batch experiments. The Freundlich model presented is the best fit to the auxiliary data for all the pollutants. Intra-particle diffusion model defines the surface diffusion occurs at the initial stage, later followed by the pore diffusion. The adsorption is controlled by chemisorption and it is thermodynamically favourable even at warmer temperatures. In conclusion, high adsorption capacity and rapid adsorption

suggested that silica supported metal-oxide ($ZnO@SiO_2$) monolith may be a promising adsorbent for removing several toxic pollutants from wastewater.

References:

1. J. Fu, Z. Chen, M. Wang, S. Liu, J. Zhang, J. Zhang, R. Han and Q. Xu, *Chemical Engineering Journal*, 2015, **259**, 53-61.
2. E. N. El Qada, S. J. Allen and G. M. Walker, *Chemical Engineering Journal*, 2008, **135**, 174-184.
3. L. Zhuannian, Z. Anning, W. Guirong and Z. Xiaoguang, *Chinese Journal of Chemical Engineering*, 2009, **17**, 942-948.
4. Z. Ajji and A. M. Ali, *Nuclear Instruments and Methods in Physics Research Section B: Beam Interactions with Materials and Atoms*, 2007, **265**, 362-365.
5. L. Ai, Y. Zhou and J. Jiang, *Desalination*, 2011, **266**, 72-77.
6. R. Ansari and Z. Mosayebzadeh, *J. Iran. Chem. Soc*, 2010, **7**, 339-350.
7. M. Hasan, A. Ahmad and B. Hameed, *Chemical Engineering Journal*, 2008, **136**, 164-172.
8. M. Ghaedi, H. Tavallali, M. Sharifi, S. N. Kokhdan and A. Asghari, *Spectrochimica acta. Part A, Molecular and biomolecular spectroscopy*, 2012, **86**, 107-114.
9. M. Ghaedi, M. N. Biyareh, S. N. Kokhdan, S. Shamsaldini, R. Sahraei, A. Daneshfar and S. Shahriyar, *Materials Science and Engineering: C*, 2012, **32**, 725-734.
10. M. Ghaedi, G. Negintaji, H. karimi and F. Marahel, *Journal of Industrial and Engineering Chemistry*, 2014, **20**, 1444-1452.
11. S. Kansal, M. Singh and D. Sud, *Journal of hazardous materials*, 2007, **141**, 581-590.
12. N. Modirshahla, A. Hassani, M. A. Behnajady and R. Rahbarfam, *Desalination*, 2011, **271**, 187-192.
13. P. Liang, L. Zhang, X. Zhao, J. Li, L. Liu, R. Cai, D. Yang and A. Umar, *Science of Advanced Materials*, 2015, **7**, 295-300.
14. C. Mondal, J. Pal, M. Ganguly, A. K. Sinha, J. Jana and T. Pal, *New Journal of Chemistry*, 2014, **38**, 2999.
15. K. Simeonidis, S. Mourdikoudis, E. Kaprara, M. Mitrakas and L. Polavarapu, *Environ. Sci.: Water Res. Technol.*, 2016, **2**, 43-70.
16. J. Choina, A. Bagabas, C. Fischer, G. U. Flechsig, H. Kosslick, A. Alshammari and A. Schulz, *Catalysis Today*, 2015, **241**, 47-54.

17. J. Liu, Z.-Y. Hu, Y. Peng, H.-W. Huang, Y. Li, M. Wu, X.-X. Ke, G. V. Tendeloo and B.-L. Su, *Applied Catalysis B: Environmental*, 2016, **181**, 138-145.
18. S. S. Patil, M. G. Mali, M. S. Tamboli, D. R. Patil, M. V. Kulkarni, H. Yoon, H. Kim, S. S. Al-Deyab, S. S. Yoon, S. S. Kolekar and B. B. Kale, *Catalysis Today*, 2016, **260**, 126-134.
19. A. H. Lu, J. H. Smått and M. Lindén, *Advanced Functional Materials*, 2005, **15**, 865-871.
20. B. Tian, X. Liu, H. Yang, S. Xie, C. Yu, B. Tu and D. Zhao, *Advanced Materials*, 2003, **15**, 1370-1374.
21. K. Zhu, B. Yue, W. Zhou and H. He, *Chemical Communications*, 2003, 98-99.
22. H. Yang, Q. Shi, B. Tian, Q. Lu, F. Gao, S. Xie, J. Fan, C. Yu, B. Tu and D. Zhao, *Journal of the American Chemical Society*, 2003, **125**, 4724-4725.
23. S. Laha and R. Ryoo, *Chemical Communications*, 2003, 2138-2139.
24. W. Cheng, F. Rechberger and M. Niederberger, *ACS nano*, 2016, **10**, 2467-2475.
25. J. H. Smått, F. M. Sayler, A. J. Grano and M. G. Bakker, *Advanced Engineering Materials*, 2012, **14**, 1059-1073.
26. T. Sano and Y. Oumi, *Catalysis surveys from Asia*, 2004, **8**, 295-304.
27. P. Kannusamy and T. Sivalingam, *Colloids and surfaces. B, Biointerfaces*, 2013, **108**, 229-238.
28. M. Ghaedi, M. Ghayedi, S. N. Kokhdan, R. Sahraei and A. Daneshfar, *Journal of Industrial and Engineering Chemistry*, 2013, **19**, 1209-1217.
29. J. Feng, Y. Wang, L. Zou, B. Li, X. He, Y. Ren, Y. Lv and Z. Fan, *Journal of colloid and interface science*, 2015, **438**, 318-322.
30. N. K. Amin, *Desalination*, 2008, **223**, 152-161.
31. A. Mittal, D. Kaur and J. Mittal, *Journal of hazardous materials*, 2009, **163**, 568-577.
32. M. Sharma, A. Mishra, A. Mehta, D. Choudhury and S. Basu, *Journal of Nanoscience and Nanotechnology*, 2017, **17**, 1-11.
33. C. A. Başar, *Journal of hazardous materials*, 2006, **135**, 232-241.
34. S. Chatterjee, S. Chatterjee, B. P. Chatterjee and A. K. Guha, *Colloids and Surfaces A: Physicochemical and Engineering Aspects*, 2007, **299**, 146-152.
35. A. Shukla, Y.-H. Zhang, P. Dubey, J. Margrave and S. S. Shukla, *Journal of hazardous materials*, 2002, **95**, 137-152.

36. I. D. Mall, V. C. Srivastava, N. K. Agarwal and I. M. Mishra, *Chemosphere*, 2005, **61**, 492-501.
37. W. J. Thomson, *Introduction to transport phenomena*, Pearson College Division, 2000.
38. A. Mittal, D. Kaur and J. Mittal, *Journal of colloid and interface science*, 2008, **326**, 8-17.
39. E. Hassan, *Chemistry International*, 2016, **2**, 89-102.
40. R. S. Juang, F. C. Wu and R. L. Tseng, *Journal of colloid and interface science*, 2000, **227**, 437-444.
41. S. Subramani and N. Thinakaran, *Process Safety and Environmental Protection*, 2017, **106**, 1-10.
42. M. J. Iqbal and M. N. Ashiq, *Journal of hazardous materials*, 2007, **139**, 57-66.
43. M. Xu, Y. Zhang, Z. Zhang, Y. Shen, M. Zhao and G. Pan, *Chemical Engineering Journal*, 2011, **168**, 737-745.
44. A. H. Chen, C. Y. Yang, C. Y. Chen and C. W. Chen, *Journal of hazardous materials*, 2009, **163**, 1068-1075.
45. X. Tan, X. Wang, M. Fang and C. Chen, *Colloids and Surfaces A: Physicochemical and Engineering Aspects*, 2007, **296**, 109-116.
46. V. K. Gupta, B. Gupta, A. Rastogi, S. Agarwal and A. Nayak, *Water research*, 2011, **45**, 4047-4055.
47. N. Kataria, V. K. Garg, M. Jain and K. Kadirvelu, *Advanced Powder Technology*, 2016, **27**, 1180-1188.
48. Z. Monsef Khoshhesab, K. Gonbadi and G. Rezaei Behbehani, *Desalination and Water Treatment*, 2014, **56**, 1558-1565.
49. M. Ghaedi, A. Hassanzadeh and S. N. Kokhdan, *Journal of Chemical & Engineering Data*, 2011, **56**, 2511-2520.
50. S. Chaudhary, Y. Kaur, A. Umar and G. R. Chaudhary, *Journal of Molecular Liquids*, 2016, **220**, 1013-1021.
51. F.-C. Wu, R.-L. Tseng and R.-S. Juang, *Chemical Engineering Journal*, 2009, **153**, 1-8.
52. G. Crini, H. N. Peindy, F. Gimbert and C. Robert, *Separation and Purification Technology*, 2007, **53**, 97-110.

53. L. Fan, C. Luo, X. Li, F. Lu, H. Qiu and M. Sun, *Journal of hazardous materials*, 2012, **215**, 272-279.
54. G. C. Panda, S. K. Das and A. K. Guha, *Journal of hazardous materials*, 2009, **164**, 374-379.

Chapter-5

Section-A: Green Synthesis of Biopolymer Capped Metallic Nanoparticles to Study Catalytic Activity

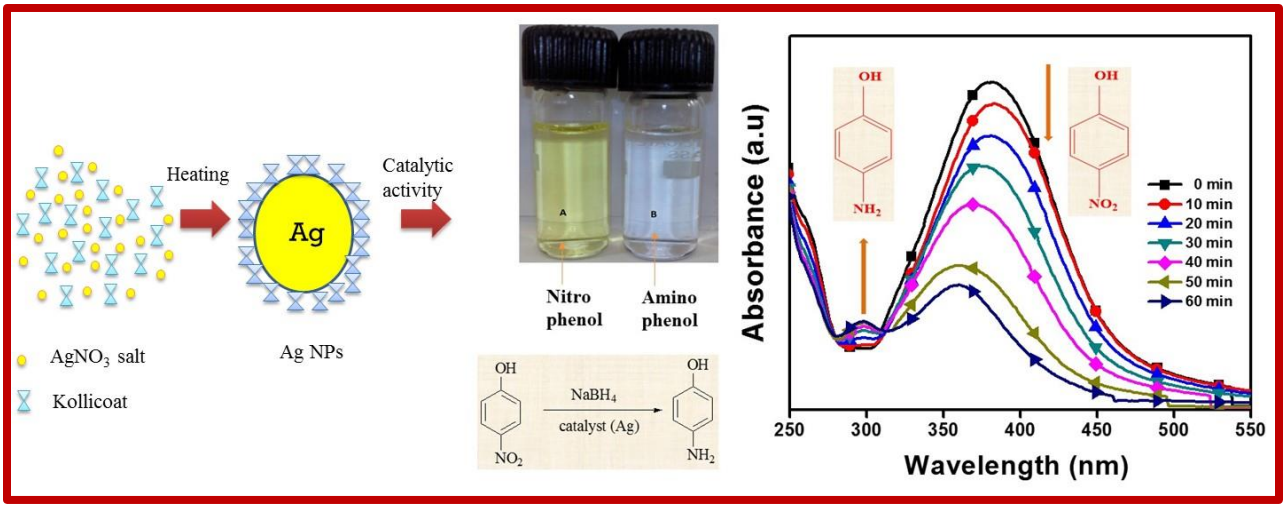

In this chapter, silver nanoparticles were synthesized by one-step process in the presence of kollicoat as capping, reducing and stabilizing mediator. The synthesized nanoparticles were characterized by using FTIR, TEM, DLS, XRD, EDS, and UV-vis spectroscopy. The resulted silver nanoparticles were having an incomparable colloidal stability against the salt addition and change of pH. The effect of different synthesis parameters and the catalytic property of the nanoparticles were examined.

5.1 Introduction

In recent years there has been going up interest in the study and preparation of highly stable metal nanoparticles (NPs), because of their exceptional electronic, optical, mechanical, magnetic and chemical properties that are significantly dependent on the size and shape[1-4]. The development of uniform nanometer size particles has been intensively pursued by reason of their technological and fundamental scientific importance[5, 6]. Amid the metal NPs, silver nanoparticles (Ag NPs) is one of the main remarkable materials because of its exceptional properties such as chemical stability, good conductivity, catalysis and antimicrobial activity[7]. These properties of Ag NPs acutely depend on their size and morphology. For the preparation of Ag NPs a variety of preparation routes have been stated; remarkable examples include, reverse micelles process[8], salt reduction, microwaves dielectric heating reduction, ultrasonic irradiation, radiolysis, solvo-thermal synthesis, electrochemical synthesis etc[9-12]. Several studies have made to know the size, stability, morphology and (chemical and physical) properties of the Ag NPs, which are strongly influenced by the experimental condition, the kinetics of contact of silver ions with reducing agents, and adsorption process of stabilizing agent with Ag NPs[13]. Generally, by changing the method of synthesis, stabilizing and reducing factors, specific control of the size, shape and distribution of the produced NPs is achieved[14, 15]. The most common accessible technique for the synthesis of Ag NPs with controlled size, specially round shape, is the reduction of Ag^+ ions directly in water with a reducing agent such as $NaBH_4$[16], ascorbic acid or citrate[17]. However, these aqueous synthesis strategies produce Ag NPs with a fairly broad size distribution and especially to different shapes varying from spheres to rods and even prisms. Up to date, only few synthesis strategies are available to produce spherical Ag NPs directly with small size in the water. Thus, it is very important to solve the critical challenge of preparing Ag NPs in water to achieve a quantitative investigation of the size-dependent properties of Ag NPs.

The various synthesis protocols used for Ag NPs production often necessitate the use of harsh organic solvents/surfactants and intense reducing agents (e.g., borohydride or hydrazine), which typically generate huge quantities of hazardous waste. The synthesis procedure that trim down the use of hazardous reagents and offer greener, more cost-effective alternatives are becoming more popular as the number of Ag NPs applications

increases. Hence, methods to provide stable Ag NPs dispersions that prevent aggregation in biological media and have elevated oxidation resistance are of significant importance. Kollicoat is a favorable grafted copolymer for medical applications because of its hydrophilic nature and biocompatibility[17]. Kollicoat can oftenly used to improve the biocompatibility due to its diverse range of molecular weights, outstanding solubility in aqueous medium, chain flexibility, low toxicity properties[18] and was able to act both as stabilizing as well as reducing agent. The usage of grafted copolymers are increasing in the research and industrial practice because of their hybrid functionality. Alkilany *et al*. has synthesized spherical gold nanopatricles using kollicoat as a stabilizing agent[19].

Manufacturing of several analgesic and antipyretic drugs needs 4-aminophenol (4-AP) as a potent intermediate. It is also used exceptionally as a photographic developer, corrosion inhibitor, anti corrosion-lubricant and hair-dyeing agent. Thus, being a regular precursor material for 4-AP, a newer and economical method for catalytic hydrogenation of 4-nitrophenol (4-NP) is always in demand. In the past two decades with the rapid and flourishing growth of nanotechnology, the borohydride reduction of 4-NP to 4-AP by metal NPs has received increasing consideration because this reaction can be finished in aqueous solution under mild condition[15, 20, 21].

In this chapter, we have described the simple strategy for the preparation of Ag NPs with special emphasis on exceptional colloidal stability. The work has been conducted to develop one step, cost-effective, biocompatible Ag NPs preparation. We have synthesized Ag NPs using kollicoat-IR as a reducing and capping agent. Here we also report the catalytic activity of Ag NPs as a selective catalyst for the reduction of 4-nitrophenol (4-NP) to the corresponding aminophenol with nearly 80% product yield.

5.2.1 Synthesis of Ag NPs

Typically, Ag NPs were prepared by boiling 25 ml aqueous solution (10, 50 and 100 mg) of kollicoat with 0.625 ml of 0.01M $AgNO_3$. The heating was maintained until a yellow color appeared (~80 minutes), indicating the formation of Ag NPs. For all the experiments, freshly prepared $AgNO_3$ stock solution was used.

5.2.2 Characterizations

As synthesized silver nanoparticles were characterized by various techniques; details of the techniques are given in **Chapter 1, section 1.9**

5.2.3 Catalytic Activity

The catalytic 4-NP reduction by synthesized Ag NPs, was carried out in a well-stoppered quartz cuvette in the presence of Ag NPs and borohydride solution. In a quartz cuvette, 2.77 ml water was mixed with 30 µl (10^{-2} M) 4-NP solution. Thereafter 200 µl of freshly prepared $NaBH_4$ solution (10^{-1} M) was added to it. Thus, the final concentration of 4-NP and $NaBH_4$ became 10^{-4} M and 6.67×10^{-3} M respectively. Once these solutions get mixed, 20 µl of the Ag NPs was added. The reaction was spectrophotometrically monitored at different time intervals.

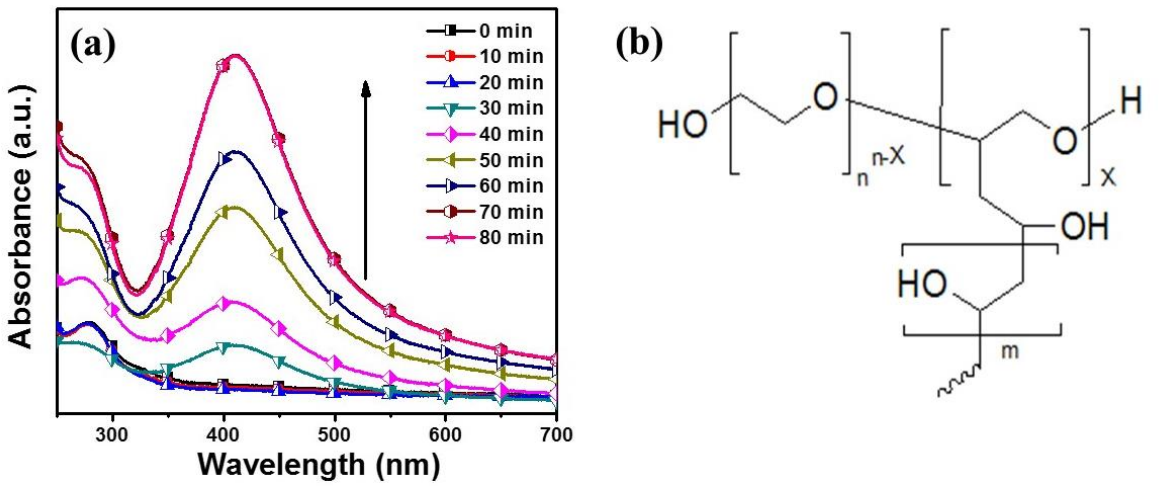

Fig. 5.1: (a) UV-vis spectra of Ag NPs evolution at various reaction times and (b) molecular structure of kollicoat.

5.3 Results and discussions

5.3.1 Characterization of synthesized Ag NPs

On reaction with kollicoat, at ~130°C for 80 min, the colorless silver nitrate solution turned deep yellow, indicating the reduction of Ag^+ to Ag^0 and the formation of Ag NPs. During the evolution of the Ag NPs from the silver salt, we recorded their UV-visible spectra at different reaction time.

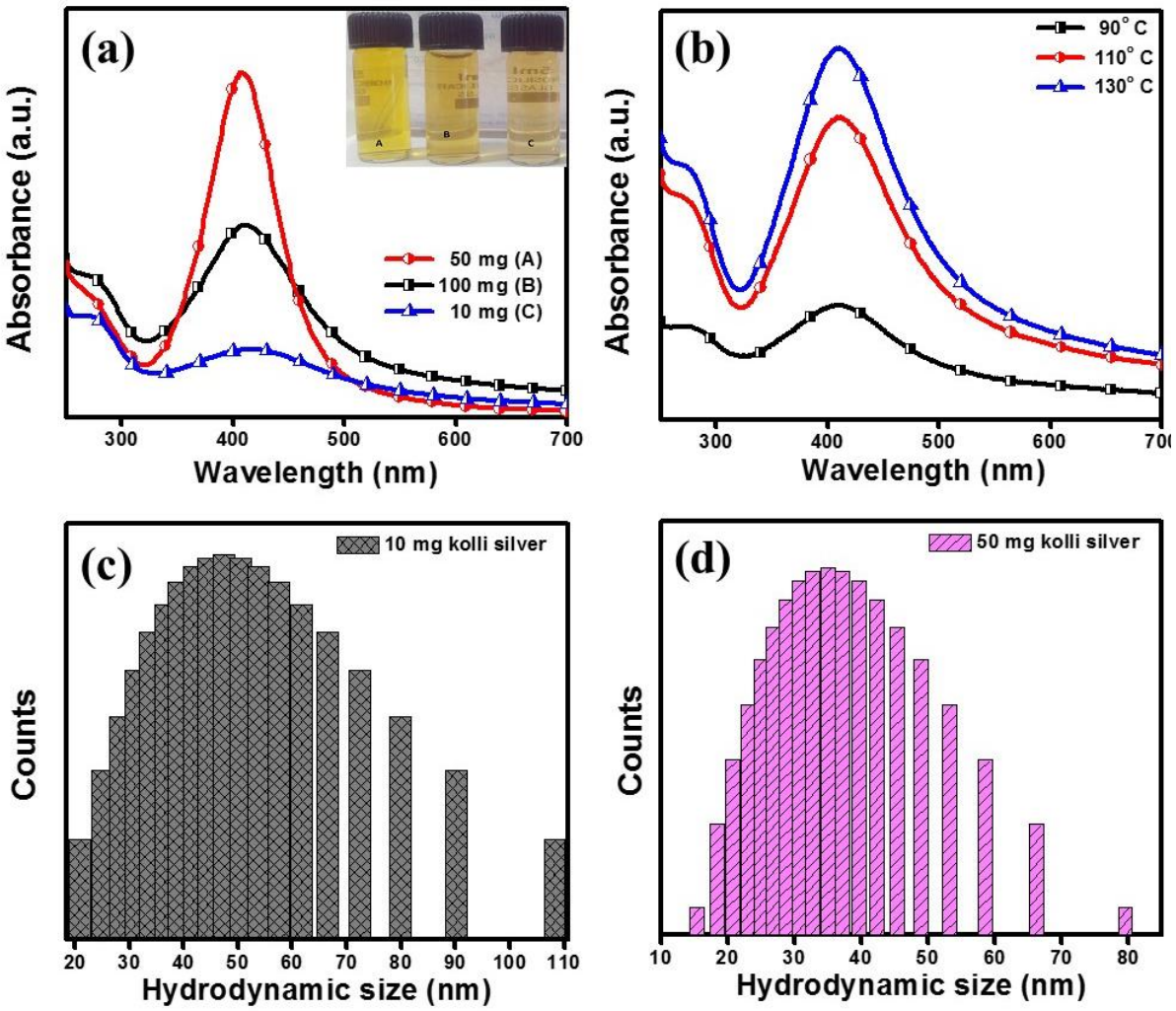

Fig. 5.2: (a) UV-vis spectra for Ag NPs with different concentration of kollicoat and inset shows their corresponding color, (b) UV-vis spectra of Ag NPs synthesized at different temperatures; Size distribution histogram of Ag NPs from particle size analyzer at different concentration of (c) 10 mg and (d) 50 mg kollicoat.

The surface plasmon absorption band in successive stages of formation of the Ag NPs is shown in Fig. 5.1(a). The colloidal solution shows a yellow color with an absorption band at 408 nm. The synthesis process is simple, fast and reproducible. Here, kollicoat was used as a reducing, capping, and stabilizing agent in a one-step synthesis of Ag NPs because of its unique structure, in which the PVA brushes (which may function as

reducing and capping moieties) are grafted from PEG backbone (which may function as a reducing and strong stabilizing agent)[22].

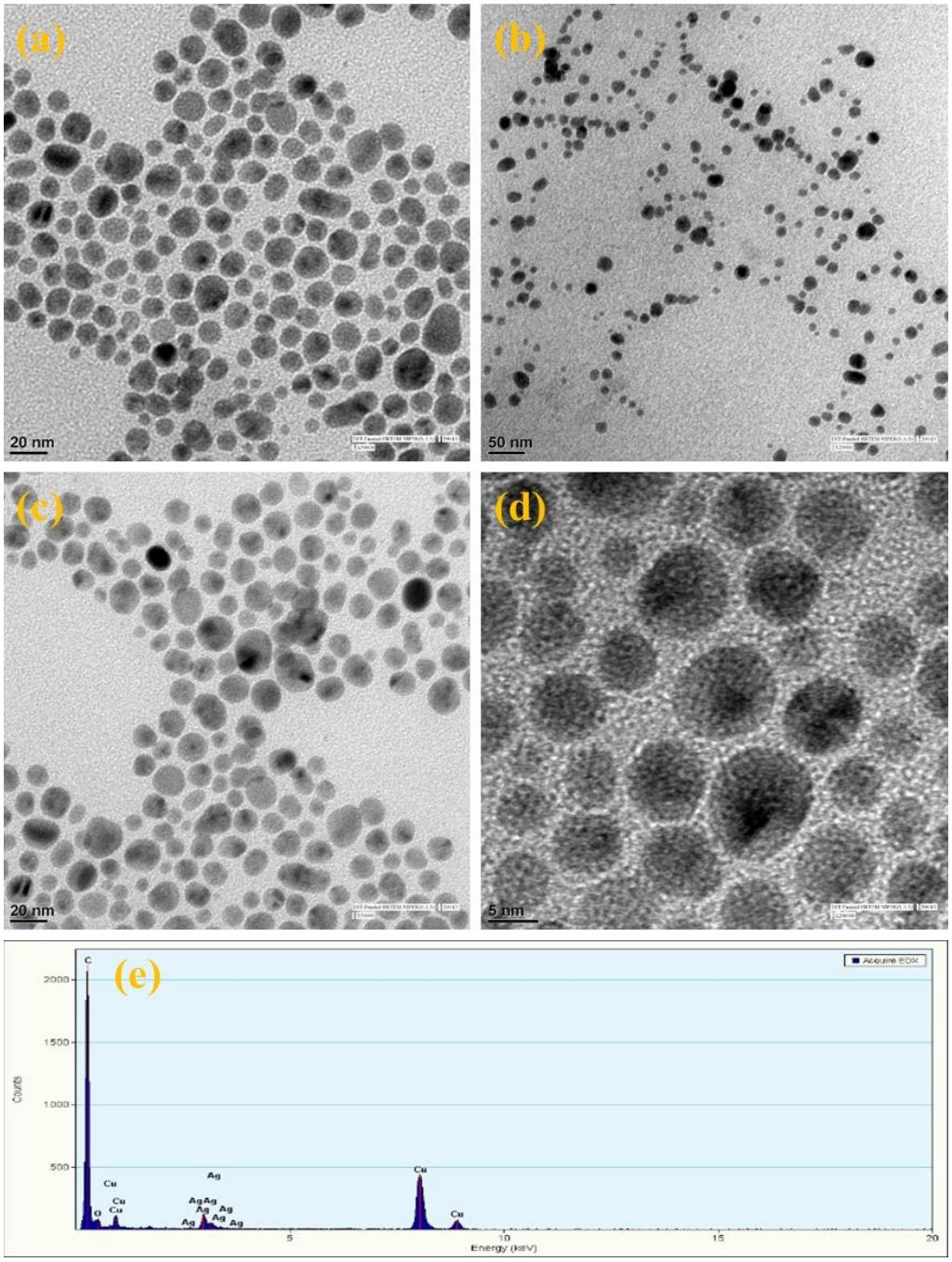

Fig. 5.3: TEM images of Ag NPs with different kollicoat concentration (a) 50 mg, (b) 100 mg, (c) 10 mg and (d) magnified details of image a and (e) Energy-dispersive spectrum (EDS) of Ag NPs.

The molecular structure of kollicoat is shown in Fig. 5.1(b). The particle size and the optical properties of as synthesized Ag NPs can be tuned straight away with varying the polymer/Ag-salt ratio. Fig. 5.2(a) shows the absorbance spectra of Ag NPs at different concentration of kollicoat. Ag NPs with different particle size (d=20±4 to 40±5.0 nm) were prepared by varying the kollicoat content from 10 to 100 mg at a constant silver salt concentration (0.01 M) as evident from various solution color (inset of Fig. 5.2(a)). Optimization studies were performed to check the effect of temperature on the resulting Ag NPs by evolution and wideness of their UV-vis spectra. It had been observed that a boiling condition (at 130°C) was required to assure a sharp plasmon peak around 408 nm. Where as decreasing the reaction temperature (90°C - 110°C) resulted in broadening plasmon peak (Fig. 5.3(b)). Higher temperature is well-known for faster and controlled reduction of Ag^+ ions and thus resulting in more uniform nucleation.

For 50 mg kollicoat concentration, the surface plasmon of Ag NPs showed a narrow band with a maximum at 408 nm. When the kollicoat concentration was less than 50 mg, the resulted Ag NPs were polydispersed and the NPs aggregated readily, where as the use of higher kollicoat concentrations (>50mg) may be resulted in smaller NPs with little polydispersed/aggregated form, which were evidented from broad and red shifted plasmon peak (Fig. 5.2(a)). So, at a particular polymer concentration (50 mg) the resulting spherical Ag NPs showed excellent uniformity which was also evidented from particle size analysis (Fig. 5.2(c and d)). The average particle size were found to be 35 nm and 45 nm for 50 mg and 10 mg kollicoat concentrations, respectively.

Fig. 3(a to c) show, TEM images of Ag NPs with different kollicoat concentration of 50 mg, 100 mg and 10 mg respectively. Fig. 5.3(d) shows the magnified image of Fig. 5.3(a). The TEM images indicate that the NPs are uniform in size, with mean diameters ~20 nm, 30 nm and 40 nm for 50 mg, 100 mg and 10 mg respectively. However, particles with diameter larger than 40 nm were formed because of aggregation, throughout preparation of the TEM holding grid. EDS spectrum of Ag NPs shown in Fig. 5.3 (e) confirms the purity of the synthesized Ag NPs. No other obvious peak attributable to contamination was spotted. EDS result showed that high-purity Ag NPs are synthesized. The Cu and C peaks were also detected by EDS due to interferance of carbon coated Cu TEM grid. Fig. 5.4 (a) shows the FTIR spectrum of Ag NPs stabilized by kollicoat. The

IR band at 1096, 2927, 1704 and 1461 cm^{-1} are characteristic vibration bands of kollicoat; and can be assigned to the vibration of the C–OH, C–H, C=O and C–O bonds[25]. The bands at 3611, 3743 and 3854 cm^{-1} can be assigned to –OH group. These IR bands confirmed the capping of kollicoat on the surface of Ag NPs.

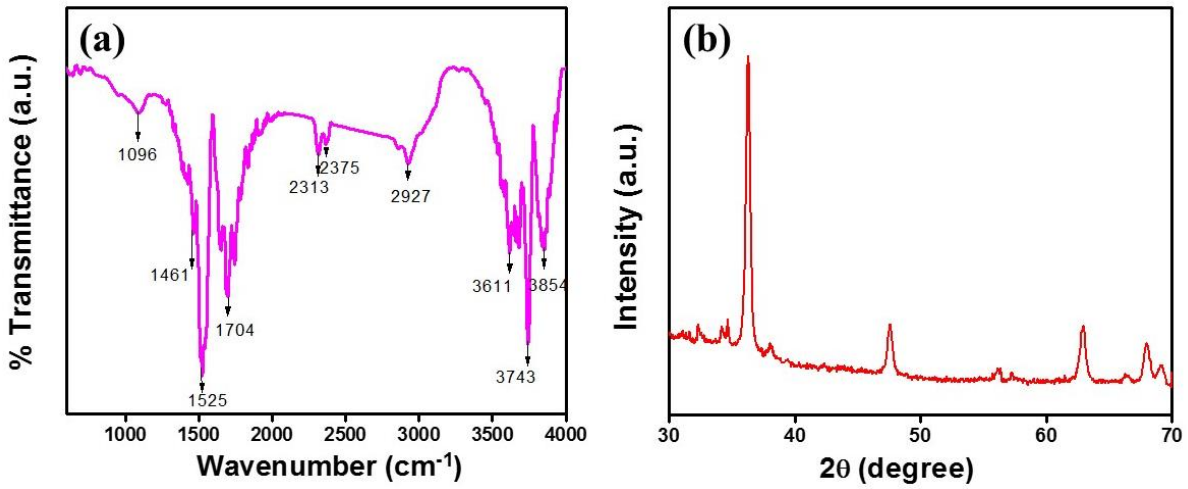

Fig. 5.4: (a) FTIR spectra of kollicoat capped Ag NPs (b) X-Ray diffraction pattern of kollicoat capped Ag NPs.

The XRD pattern shown in Fig. 5.4 (b), confirmed the formation of Ag NPs. Bragg's reflections at 2θ = 36.2°, 47.6°, 63.05°, and 68.02° indexed to (111), (200), (220) and (311) planes respectively, confirmed the formation of Ag NPs by comparison with the JCPDS card file no. 04-0783. It was also founded that there were some little peaks which match with the standard XRD data of Ag_2CO_3 (PDF No 26-0339). For XRD analysis, we had dried the sample on the XRD plate in open- atmosphere. So, the silver carbonate formation might be attributed due to the presence of carbon dioxide in atmosphere. The average size of the Ag NPs were calculated by using the Scherrer equation and found to be 37.42 nm correlating with our findings in TEM studies.

5.3.2 Stability against salt addition and change of pH

Colloidal stability of NPs is a critical factor verbalizing its physical, chemical, and biological properties[23]. Maintaining an excellent colloidal stability is advantageous for various applications. Unfortunately, many artificial routes for preparing Ag NPs do not

confirm a high stability of the resultant NPs. For instance, Ag NPs stabilized with sodium borohydride are greatest meta-stable[6], which frequently aggregate upon salt (1M NaCl) addition. Here we have compared the stability of as prepared Ag NPs with $NaBH_4$, PVA and PEG stabilized Ag NPs.

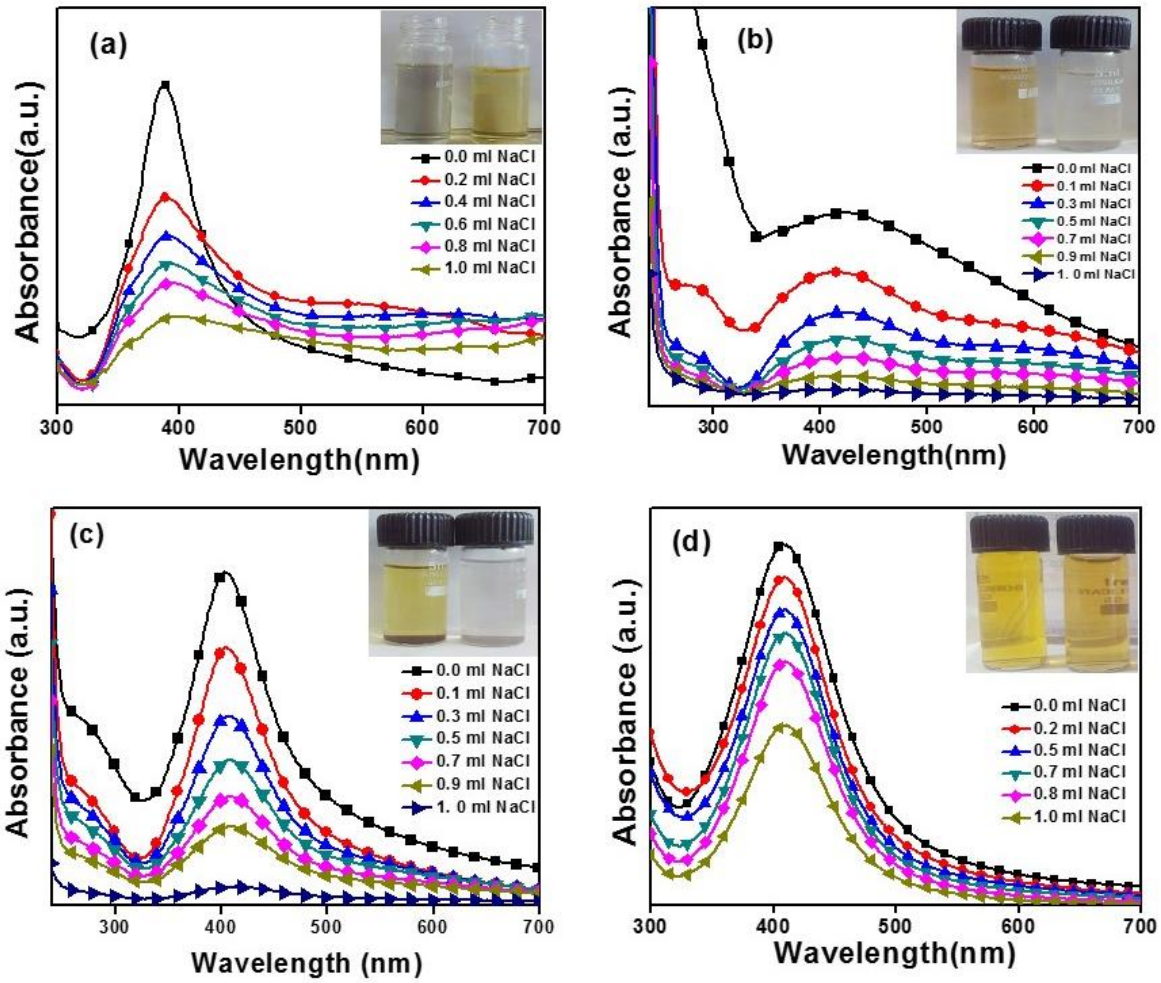

Fig. 5.5: UV-vis spectra of Ag NPs against salt (NaCl) addition: a) sodium borohydride b) PVA c) PEG and d) kollicoat stabilized Ag NPs and inset shows their corresponding color, before and after addition of NaCl (1M).

In our case, the aggregation of $NaBH_4$, PVA and PEG stabilized Ag NPs were evidenced from the colour change from yellow to blue (inset of Fig. 5.5 a-c) and associated red-shift as well as broadening in their surface plasmon peak (Fig. 5.5 a-c).

Herein, the resulting kollicoat capped Ag NPs were found to have incomparable colloidal stability without the precondition for any additional surface modification. The colloidal stability of kollicoat coated Ag NPs against the salt addition, was cleared from the constant yellow colour of their solutions (inset of Fig. 5.5d) and the superimposing UV-vis spectra (Fig. 5.5 d). The decrease in intensity in surface plasmon peak as well as the colour may be due to the dilution effect by addition of aqueous solution of NaCl. The comparative study concluded that, Ag NPs synthesized with kollicoat had much higher colloidal stability against the salt addition, than NPs synthesized by another chemical route ($NaBH_4$, PVA and PEG). Fig. 5.6 (a- b) show the TEM images of Ag NPs, capped by kollicoat before and after addition of NaCl. There was no sign of aggregation in their corresponding TEM images. The excellent colloidal stability of the kollicoat coated Ag NPs was due to the existence of polymeric covering of both PEG-PVA on the shell of Ag NPs that acted as a capping as well as stabilizing agent. It has been reported that both PVA and PEG can act as a surface stabilizers and capping agent for various colloidal systems[24, 25].

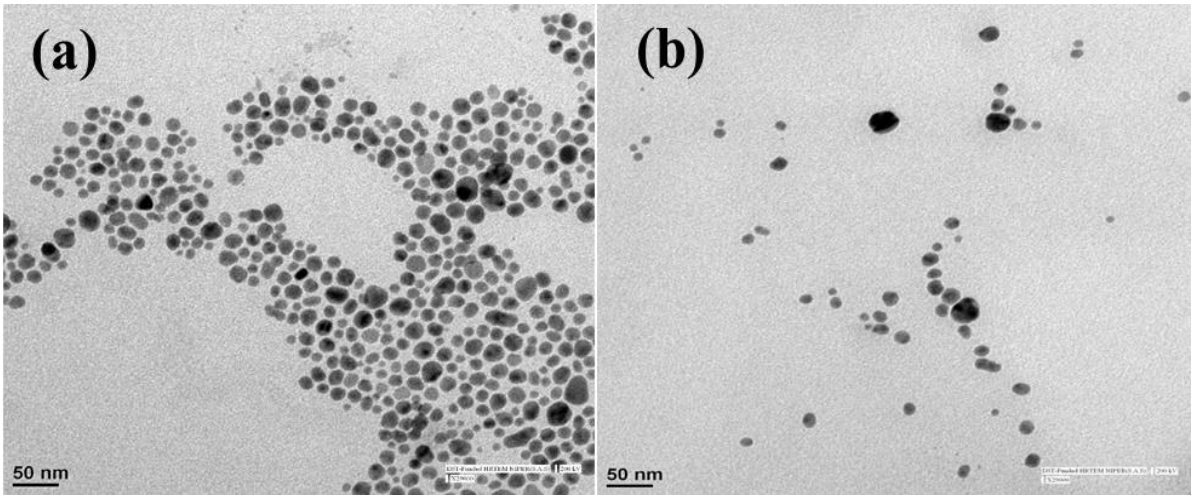

Fig. 5.6: TEM images of kollicoat capped Ag NPs a) before and b) after addition of NaCl.

The stability of the as synthesized Ag NPs was also checked at various pH. The pH change were done by addition of dilute HCl (0.1M) and NaOH (0.1M) solution[26]. The prepared Ag NPs were found to be highly stable at a wide pH range, starting from pH 2.5 to 10.6. The surface plasmon peak at λ_{max}= 408 nm was remained unaltered at this pH

range (pH 2.5 to 10.6), confirming the exceptional colloidal stability of the as prepared Ag NPs (Fig. 5.7). Also, the colour of the Ag NPs remained same at this pH range (inset of Fig. 5.7).

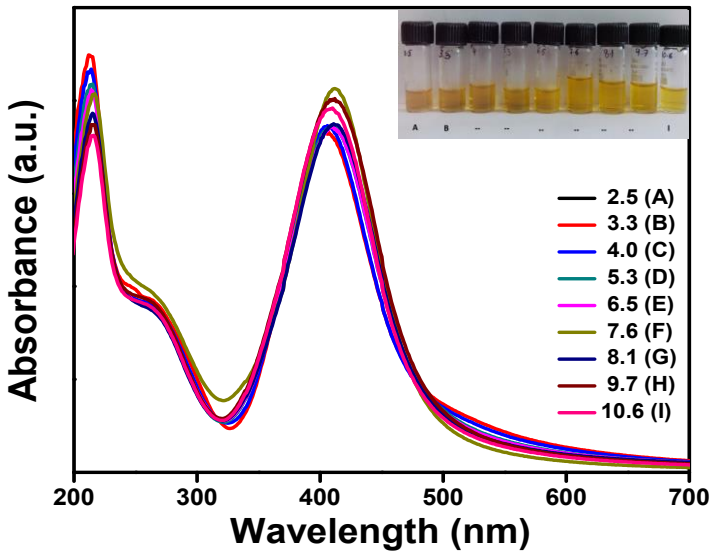

Fig. 5.7: UV-vis spectra of Ag NPs at different pH. Inset shows the colour of Ag NPs at different pH.

5.3.3 Catalytic Reactions

The catalytic activity of as-prepared polymer capped Ag NPs was authenticated through 4-NP reduction in the presence of borohydride as a reductant. The advantage of the catalytic reduction of 4-NP is the simple estimation of the reactant 4-nitrophenolate anion (λ_{max}= 400 nm) through spectrophotometry.

Although the reaction is a thermodynamically realistic method involving E_0 for 4-NP/4-AP = -0.76 V and H_3BO_3/BH_4^- = -1.33 V versus NHE, it is kinetically controlled (does not take place even in a couple of days' time) in the absence of a catalyst. But in the presence of a catalyst, it produces 4-aminophenol (4-AP). The time dependent spectra of catalytic activity of Ag NPs towards 4-NP reduction are shown in Fig. 5.8(a). The 4-nitrophenolate anion formation from 4-NP (pKa= 7.15) in the preliminary step upon addition of borohydride was determined when the peak at 317 nm (due to 4-NP) was shifted to 400 nm. Addition and proper mixing of Ag NPs to the reaction mixture caused a gradual waning and ultimate lighten of the yellow colour of the solution (inset of Fig. 5.8 (a)), which indicated ~80% conversion of 4-NP to 4-AP. The reduction could be visualized as the peak at 400 nm was vanishing with the concomitant appearance of a new peak at 295 nm, which substantiated the formation of 4-AP[27-29].

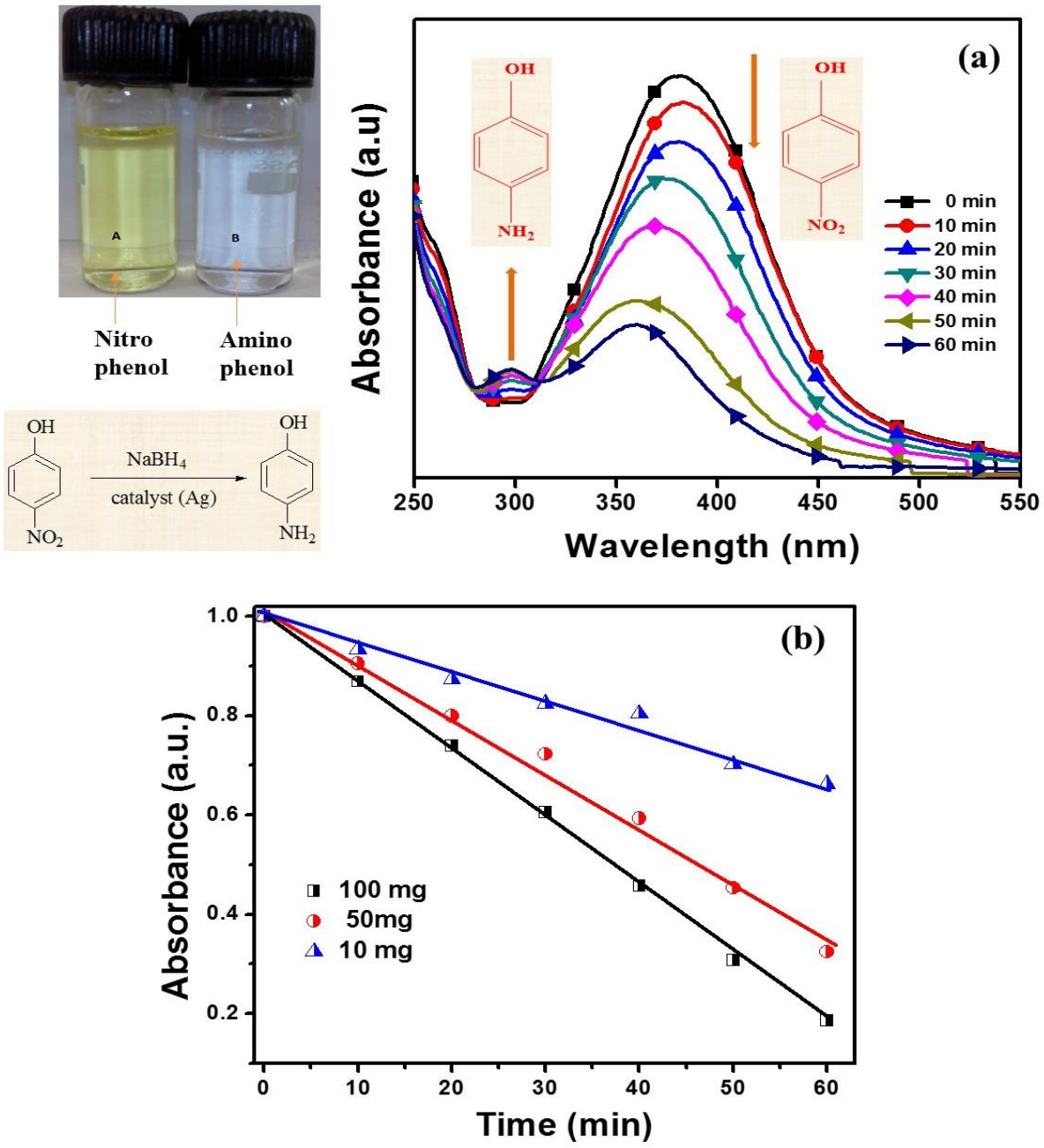

Fig. 5.8: (a) Reaction scheme and the time dependent absorption spectra for catalytic reduction of 4-NP and (b) Absorbance vs. time plot for 4-NP reduction by Ag NPs in different kollicoat concentration.

Absorbance versus time were plotted for the reduction of 4-NP by Ag NPs with different kollicoat concentrations, as shown in Fig. 5.8(b). The rate of reduction was lower for 10 mg kollicoat coated Ag NPs than 50 and 100 mg kollicoat coated Ag NPs. This may be due to the broad size distribution of 10 mg kollicoat coated Ag NPs than the others. As the primary concentration of sodium borohydride was at a high level, it remained essentially steady throughout the reaction. Therefore, for estimation of the catalytic rate pseudo-first-order kinetics with regard to 4-NP was used.

5.4 Conclusions

The green synthesis of Ag NPs with average size ~20 nm in one step heating process was demonstrated and explained in this section. The synthesized NPs showed high stability against the salt addition and change of solution pH. The NPs were characterized by UV-vis spectroscopy, XRD, FTIR, particle size analyser, EDS and TEM and they were found to be spherical, and with size of 20 nm. Optimization studies were performed to check the effect of temperature and the concentration of capping agent on the size of resulting Ag NPs. The effectiveness of the as prepared kollicoat stabilized Ag NPs as catalyst, for 4-NP reduction to nearly 80% yield of 4-AP by excess borohydride had been evaluated. The new as-prepared polymer-stabilized Ag NPs were highly stable, efficient, eco-friendly and easy to prepare and thus have the potential for several industrial applications.

Section-B: Enhanced Catalytic and Antibacterial Activity of Nanocasted Mesoporous Silver Monoliths

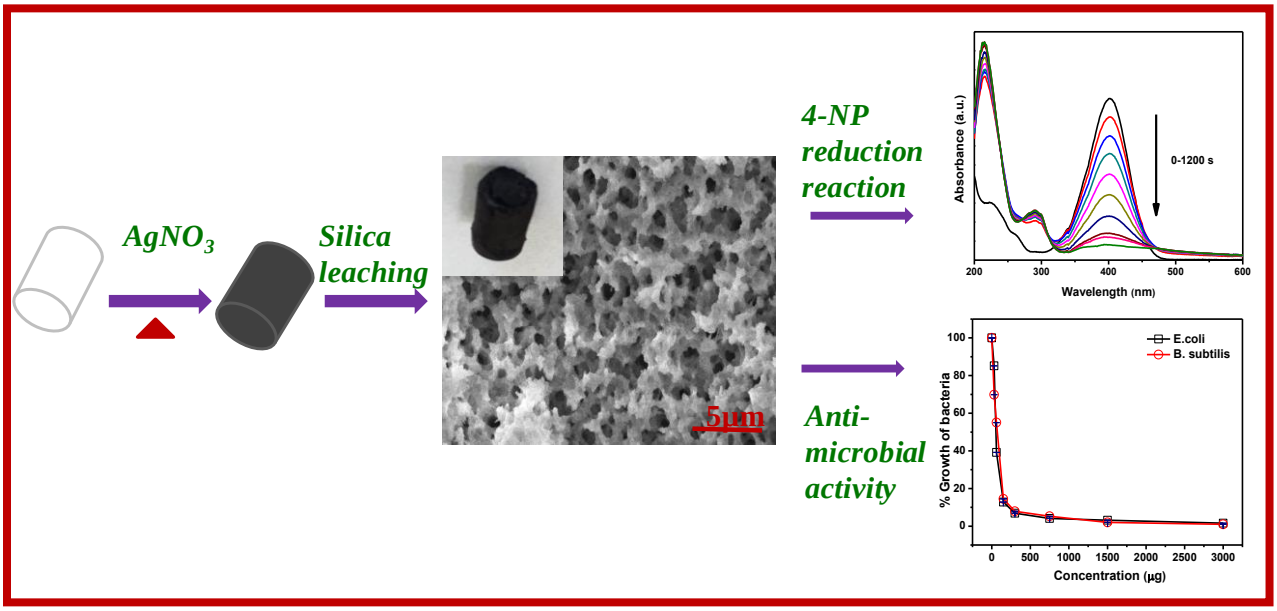

Use of low-cost heterogeneous renewable catalysts are essential for effective removal of chemical contaminants like 4-NP from water bodies. In the present study, for the first time use of surface enhanced (14 m^2/g) nanocasted mesoporous silver monolith (AgM) through impregnation into silica monoliths (prepared by sol-gel method) has been demonstrated for its catalytic and antibacterial activity. Highly efficient catalytic reduction rate (2.43 min^{-1}) of 4-NP to 4- AP has been demonstrated using 0.2 g/L of AgM catalyst. Enhancement of reduction rate is also observed with increase in temperature (from 25-40 °C). Removal of microbial contamination from drinking water is also a prime concern for water purification. Mesoporous AgM shows effective antimicrobial activity against gram negative (*E. coli*) and gram positive (*B. subtilis*) bacteria with IC_{50} values of 75.86 ± 0.173 and 74.56 ± 0.103 respectively at 24 h of incubation.

5.5 Introduction

Big water bodies are the major source of water for drinking and household works, cultivation and industry. But these water bodies often get contaminated with various toxic compounds and micro-organisms. Among the various organic pollutants, toxic aromatic nitro compounds such as 4-NP and nitrobenzene have been accepted as one of the main concern pollutants. Water gets contaminated with 4-NP from biological and chemical wastes such as paper, dye and pharmaceutical industries, etc[30, 31]. Pollutants in water effects human life by causing potential health risks[32] such as multiple organ damages, carcinogenic diseases etc[33]. So, removal of pollutants from water is very important to reduce the environmental toxicant load. With the emergence of nanoscience and nanotechnology in the last decade, several researches have been initiated to exploit the unusual and unique properties of nanomaterials for environmental remediation. In recent years the design of nanomaterials consisting of functional metals or metal oxides and different matrices is a promising research area for the fabrication of a variety of catalysts, adsorbents, and optical and electrical devices. Modern nanoclusters should be or have at least (i) specific size, (ii) well-defined surface composition, (iii) reproducible synthesis and properties, (iv) isolable and redissolvable ("Bottleable") and finally (v) high catalytic activities with long device lifetime with reproducible performance. The design of nanomaterials consisting of metal nanomaterials and adequate matrices is a challenge for the fabrication of recyclable catalysts[34].

Kinetic study of the catalytic properties of the heterogeneous catalyst with respect to the reduction of toxic aromatic nitro compounds such as 4-NP and nitrobenzene are of enormous importance. To reuse the 4-NP contaminated water; 4-NP can be converted to its useful derivatives such as 4-AP, a precursor of antipyretic and analgesic drugs using simple and fast catalytic reduction technique (waste-water)[28]. Thus, being a common precursor material for 4-AP, a newer and cheaper method for catalytic hydrogenation of 4-NP is always in demand. Pradhan *et al*. in 2002, for the first time, reported the catalytic reduction of 4-NP using $NaBH_4$ and silver nanoparticles at room temperature[35-37]. Saha *et al*. presented the kinetic study of 4-NP reduction reaction by varying concentrations of $NaBH_4$, 4-NP, and catalyst[27]. Formation of a single isosbestic point during kinetic study confirms the absence of any side reaction. Therefore; to check the catalytic activity of different nanostructures or nanoparticles of different shape and size, this process has become the gold standard.

Porous materials of noble metals such as Au, Pt and Ag are very effective for removal of organic toxicants. Porous noble metals with tunable porosity are widely used in heterogeneous catalysis, photocatalysis, medicines, bactericidal activity, biosensor technology, targeted drug delivery and tissue engineering[38-41]. Noble metal nanoparticles have engrossed massive attraction for their catalytic properties in different organic/inorganic reactions such as reduction of aromatic nitro compounds and conversion of benzene to phenol. In spite of huge demand and high surface to volume ratio of nanoparticles, during catalytic reactions nanoparticles make a missable suspension with water, get aggregated or coagulated and their surface state may get damaged. To overcome these problems, fabrication of porous monoliths of noble metals such as Au, Pt, and Ag are used for this purpose. Amongst these noble metals, silver monolith (as a heterogeneous catalyst) with high surface area and porosity is remarkable due to its noteworthy catalytic/antimicrobial activity, chemical stability and economic viability[42, 43]. Porous monoliths can be synthesized via a sol-gel method, sonication, microwave-irradiation, templating method (soft and hard templating) etc. Here, in the present study porous monoliths of desired length scale were synthesized via nanocasting method. In this method at first pores of the parental silica monoliths (synthesized via sol-gel method) were saturated with a choice of metal salt solution. Thereafter by heat treatments, the metal salt was converted to corresponding solid metal/ metal oxides. At the end, silica part gets removed by either HF or NaOH. Khan and Mann synthesized macroporous monoliths (silver, gold and copper oxide) using additives like silica particles, dextran etc[44]. Jiang *et al*. synthesized AgNPs in the scaffold of mesoporous silica (MCM-41) and found long-term antibacterial activity against both gram-negative and gram-positive microorganism even at low concentration[42]. Shen *et al*. achieved increased stability as well as increased antimicrobial activity of AgNPs by loading of AgNPs on silica shell[45]. Based on these perspectives, the synthesis of high surface area Ag superstructures and their application as a catalyst and the antibacterial agent could be investigated.

The surface area and porosity are the critical controlling factors for the catalytic and antimicrobial activity of the heterogeneous porous nanomaterials. In nanocasting method, by tuning the chain length of surface directing agents (such as PEG, CTAB etc.), one can control the porosity and surface area of the cast (parental metrical) which thereafter is used to generate the desired replica (AgMs / heterogeneous catalyst)[46, 47]. Here in this study, porous AgM of desired length scale were synthesized via nanocasting method. Thereafter; heterogeneous reduction of 4-

NP was monitored to study the catalytic activity of the AgM. Kinetic and thermodynamic parameters of catalytic reduction reaction have been studied in this work. In addition to that minimal inhibitory concentration (MIC) was also studied against both gram positive and negative bacteria using AgM to check its bactericidal activity.

5.6.1 Synthesis of AgM

The silica monoliths were prepared by the sol-gel method described by Smått *et al*. (2003) [26]. In brief, AgM was synthesized as follows: 3.1 M of silver nitrate solution impregnated in silica monoliths after degassing under vacuum. On completion of one cycle of impregnation, monoliths were found to be translucent. Heat treatment at 150 °C for 10 h was given to monoliths at a rate of 1 °C/min. This process was repeated for at least five times to get solid AgM. Afterward, the AgM were calcined at 250 °C for 5 h with 1 °C /min heating ramp. Finally, silica part was leached out from the composite to get AgM by using NaOH solution (2M).

5.6.2 Characterization of AgM

As synthesized AgM were characterized by various techniques; details of the techniques are given in **Chapter 1, section 1.9**

5.6.3 Catalytic reduction of 4-Nitrophenol

The catalytic efficiency of synthesized AgM for 4-NP to 4-AP was performed; detail procedure has been given in **Chapter 1, Section 1.10.3**

5.6.4 Antibacterial studies

The antibacterial effect of synthesized AgM against *E. coli* and *B. Subtilis* was checked; detail procedure has been given in **Chapter 1, Section 1.10.2**

5.7 Results and Discussion

Characterization of AgM

Fig. 5.9(a) shows the nitrogen adsorption-desorption isotherms plot of AgM. According to IUPAC classification type IV isotherm, the curve features the mesoporous characteristics of AgM. Specific surface area, pore diameter, and pore volume of AgM were found to be 14 m^2/g, 25.065 nm 0.04203 (cm^3/g) respectively using BET-surface analyzer studies.

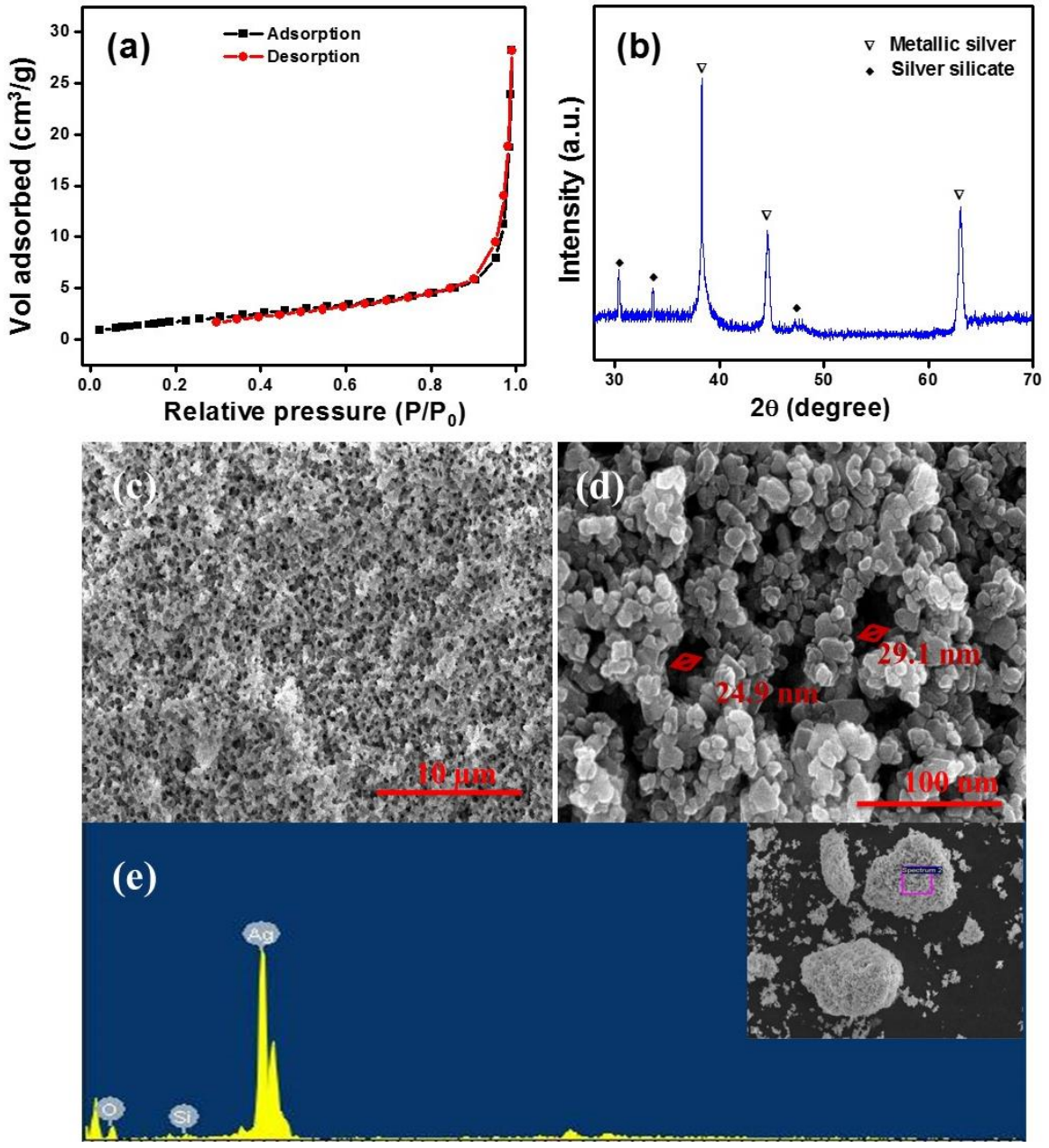

Fig. 5.9: (a) N_2 adsorption desorption curve, (b) XRD pattern, (c) & (d) FESEM image at different magnification and (e) EDX spectra for the AgM.

At low relative pressure, the maximum amount of nitrogen gas was adsorbed for evaluation of surface area. The crystal phases and purity of synthesized AgM was studied by XRD; shown in Fig. 5.9(b). In the prepared AgM, Ag showed dominant peaks 2Θ at 38.3°, 44.5°

and 62.9° corresponding to lattice planes of (111), (200) and (220) respectively, confirmed by JCPDS card no. 04-0783. The XRD data along with pure metallic Ag peak showed the existence of some other peaks, a set of which were of silver silicates ($Ag_{10}Si_4O_{13}$)[48].

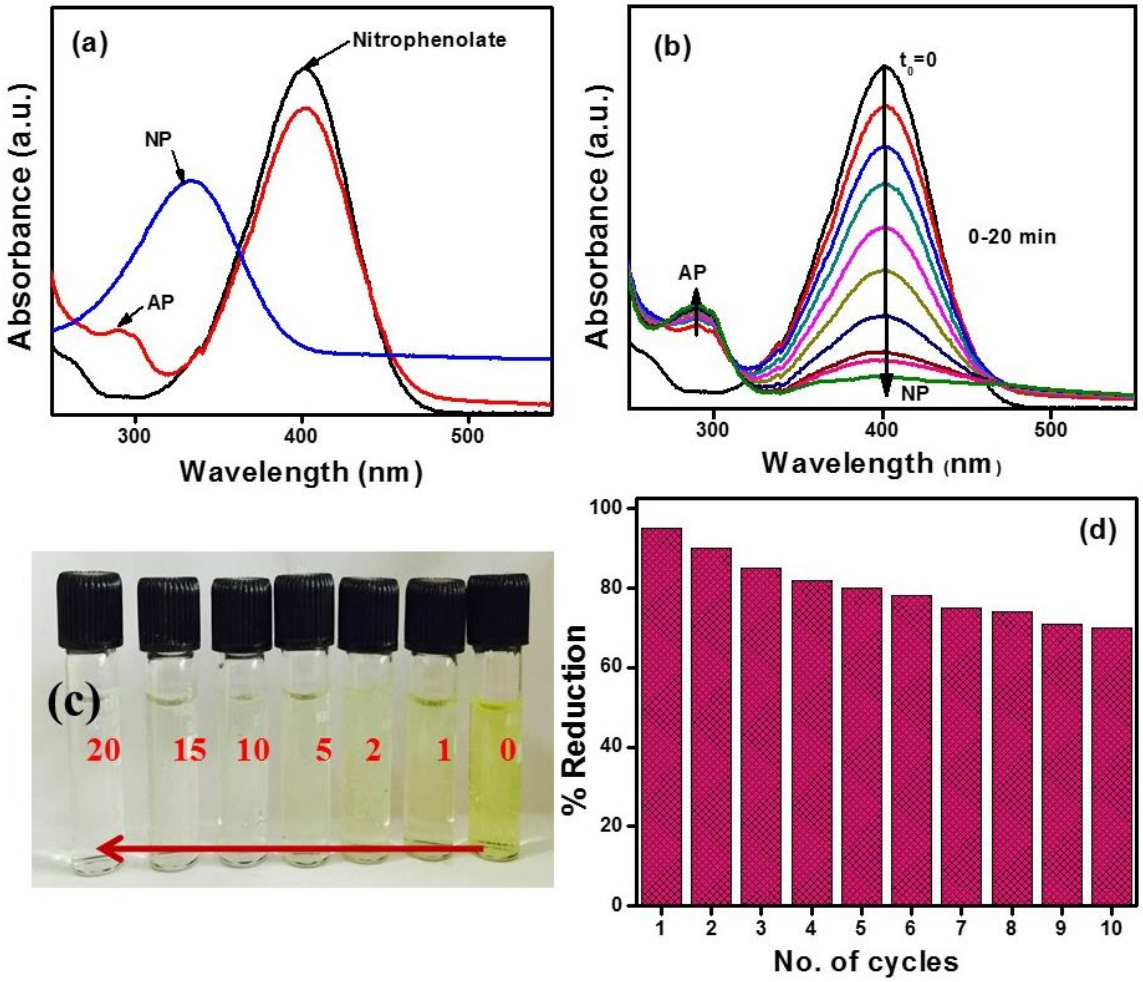

Fig. 5.10: UV-visible spectra showing 4-NP [1×10^{-3} M] reduction reaction using AgM [0.2 g/L]: (a) spectra showing 4-NP to nitrophenolate, (b) spectra for evolution of 4-AP with time and (c) conversion of 4-NP to 4-AP observed by visible color change and (d) percentage reduction against number of cycles.

To generate further structural information porous AgM were analyzed by FESEM. Fig. 5.9(c) & (d) showed the hierarchical network of pores with a mean diameter of 20-30 nm which were correlated with BET data. Elemental analysis of AgM shown in Fig. 5.9(e), suggested the

AgM composition with 80% silver. Probably the oxidation of Ag happened while heating which results in the formation of silver silicate (little amount).

Catalytic reduction

The catalytic model of 4-NP to 4-AP reduction reaction was performed in the presence of $NaBH_4$ and was studied using absorption in UV-visible range. Upon addition of freshly prepared $NaBH_4$ (0.1 M) solution in 4-NP (0.001 M), the sharp shift of λ_{max} from 317 nm to 400 nm was observed due to the conversion of 4-NP to 4-nitrophenolate (Fig. 5.10(a)). AgM showed instant degradation of 4-nitrophenolate to 4-AP which was characterized by a decrease of 400 nm peak and increase of 295 nm peak involving one single isosbestic point. The sharp drop of 400 nm peak was monitored even within the 30s of incubation. The peak at 295 nm is a characteristic of 4-AP and single isosbestic point suggests the involvement of single equilibrium (or no intermediate state). At room temperature, almost 95% of the 4-NP converted to 4-AP within 20 minutes of time (Fig. 5.10(b) &(c)). In control (no AgM) no change in intensity of 400 nm peak (corresponding to 4-nitrophenolate) was observed even after 8 weeks of RT incubation.

Kinetic study

To determine the rate of catalytic activity of AgM, reaction kinetic studies were performed. The catalytic rate constants (k) were calculated according to the pseudo-first-order kinetic model. The linear plot of $\ln(C/C_0)$ vs. time (in sec) obeys pseudo-first-order kinetic model (Fig. 5.11(a)) where C_0 and C are the initial and final concentration at time t of 4-nitrophenolate respectively. The rate constant (k) calculated from the slope of the logarithmic plot was 2.418 min^{-1}. A comparative analysis showed enhanced rate for conversion of 4-NP to 4-AP using our as synthesized AgM in compare with other published works (Table 5.1). Therefore, it could be conceived that AgM could be employed as alternative catalysts for the conversion of 4-NP to 4-AP at room temperature.

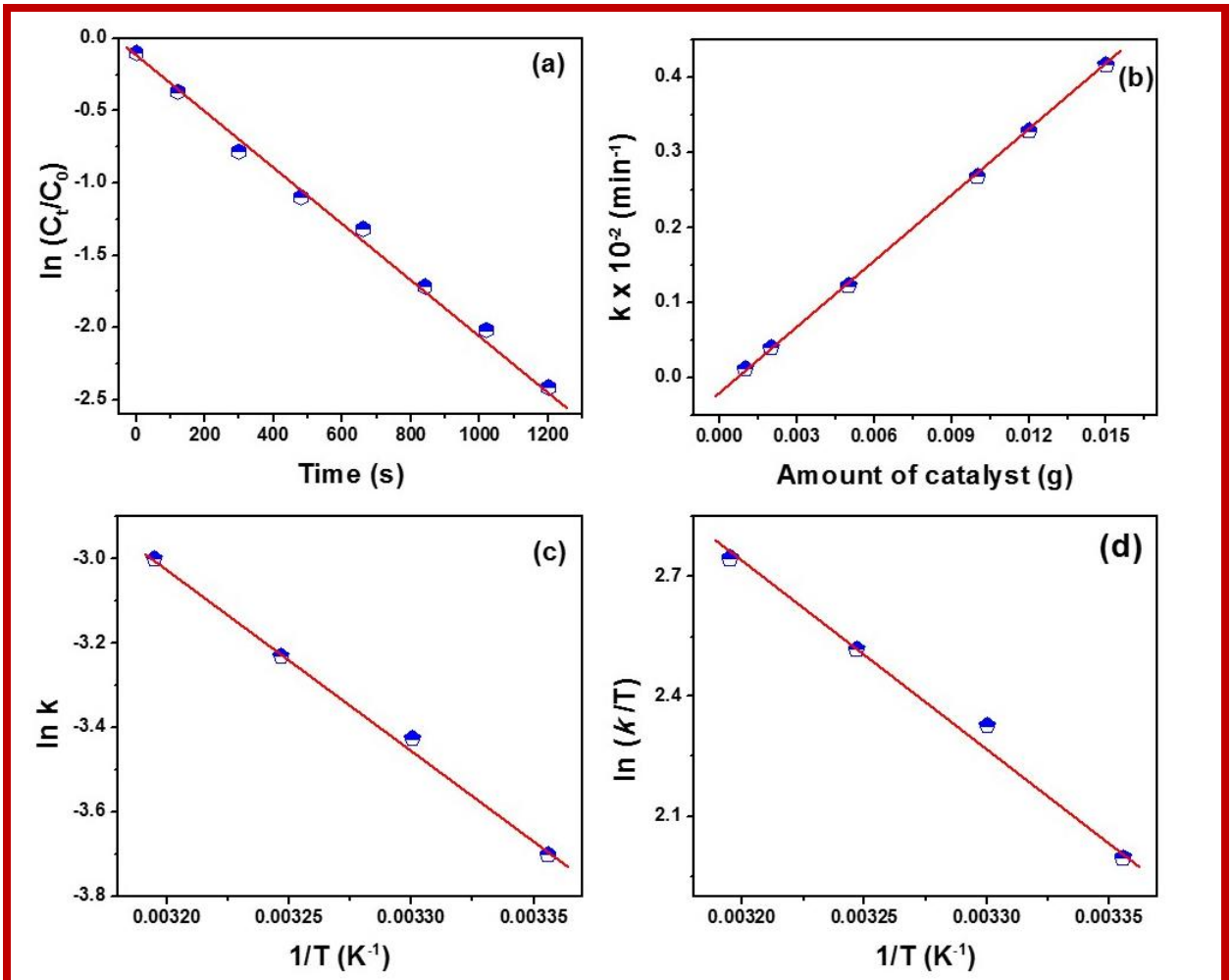

Fig. 5.11: Plots for kinetic study and to define thermodynamic parameters: (a) ln(C_t/C_0) vs. time, (b) rate constant (k) vs. amount of catalyst, (c) ln *k* vs. 1/*T* and (d) ln *k*/*T* against 1/*T*.

Table 5.1: A comparative account of the catalytic activity of the catalyst for 4-NP reduction.

Sample name	Type of catalyst	Catalyst amount (g/L)	$NaBH_4$ (M)	4-NP (M)	Rate (min^{-1})	TOF (molecule $g^{-1}s^{-1}$)	Reference
Au nanoparticles	Homogeneous	-	0.3	5×10^{-5}	0.05	-	30
Au/CA Ag/CA	Heterogeneous	1.2	0.1	1×10^{-4}	1.4×10^{-4} 0.1×10^{-4}	1.7×10^{16} 9.3×10^{16}	28
Au particle Au solution	Heterogeneous Homogeneous	0.6 -	0.1	10^{-2}	0.632×10^{-2} 0.201×10^{-2}	9.956×10^{7} -	49
Au@CMK-3-	Heterogen	0.15	0.06	0.27×1	0.274	-	50

O	eous			0^{-5}			
Ag nanoparticles	Homogeneous	-	0.1	10^{-2}	0.034	-	[51]
Ag monolith	Heterogeneous	0.200	0.1	10^{-3}	2.43	7.5×10^{17}	Current study

Effect of catalyst dose

Catalysis is a surface property and is directly proportional to the amount of surface availability. Therefore; concentration of the catalyst plays an important role in controlling the reaction rate. AgM induced conversion rate (K) of 4-NP to 4-AP is directly proportional to the amount of catalyst dose of AgM (Fig. 5.11(b)). As the pore size of the AgM remains same after immobilization, linear increase of rate can be observed with surface area.

Thermodynamic studies

Thermodynamic parameters for catalytic reduction were analyzed at different temperatures from 25 to 40 °C. Arrhenius equation was used to calculate the activation energy (E_a) of reduction reaction using AgM. Arrhenius activation energy equation for catalytic reduction reaction is:

$$\ln k = \ln A - \frac{E_a}{RT} \qquad (5.1)$$

where, E_a the activation energy, A is constant, k is rate constant at temperature T and R is the universal gas constant. The value of E_a was calculated from the slope of the linear plot of ln *k* vs. 1/*T* (Fig. 5.11(c)) and found to be 42.58 KJ mol^{-1} (Table 5.2)

The thermodynamic parameters were calculated by Erying equation:

$$\ln \frac{k}{T} = \ln \frac{k_B}{T} + \frac{\Delta S}{R} - \frac{\Delta H}{R}\left(\frac{1}{T}\right) \qquad (5.2)$$

where k_B is the Boltzmann constant, ΔH is enthalpy change and ΔS is entropy change. The slope of the linear plot of ln k/T against 1/T used to define the thermodynamic parameters (Fig. 5.11(d)).

Table 5.2: Temperature dependent rate of 4-NP reduction by $NaBH_4$ in the presence of AgM**.**

Temperature (°C)	k (min^{-1})	E_a (kJ mol^{-1})	ΔH (kJ mol^{-1})	ΔS (J mol^{-1} K^{-1})
25	2.47			
30	3.38	42.58	48.49	20.87
35	4.03			
40	4.98			

Turnover frequency

For the reduction of 4-NP many studies with the heterogeneous and homogeneous catalytic process have already been done [31]. Turnover frequency (TOF), the number of reactant molecules (4-NP) converts into the product (4-AP) per unit time per gram of catalyst (AgM) can generate useful information to quantify the catalytic activity of AgM. The measured TOF of AgM was 7.5×10^{17} molecules $g^{-1}s^{-1}$.

Reusability of AgM

Synthesized AgM was recyclable and can be reused for at least 10 times for the reduction of 4-NP. After completion of each catalytic cycle, AgM can easily be separated out simply by precipitation / centrifugation. The plot for % reduction against a number of cycles has been shown in Fig. 5.10(d).

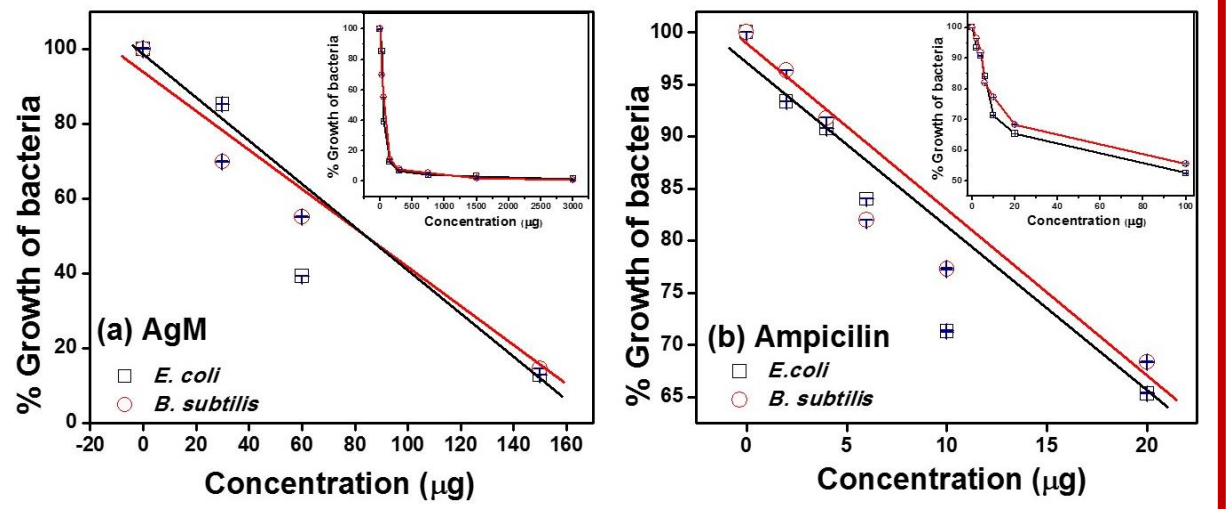

Fig. 5.12: Concentration vs. percentage of bacterial growth against *E. coli* & *B. subtilis* using (a) AgM and (b) ampicillin.

Antibacterial activity of AgM

The antibacterial activities of AgMs against *E. coli* and *B. subtilis* were shown in Fig. 5.12(a). The antibacterial activity of AgM was directly proportional to the concentration of the AgM used. Almost no growth was observed in presence of AgM (160 µg ml^{-1}) for both gram negative and positive bacteria. The IC_{50} values obtained after 24 h of AgM incubation for *E. coli* and *B. subtilis* were 75.86 ± 0.173 and 74.56 ± 0.103 µg ml^{-1} respectively. Ampicillin was taken as standard antibiotic to compare the activity of AgM and found it has IC_{50} values 17.83 ± 0.002 and 20.617 ± 0.005 µg ml^{-1} against *E. coli* and *B. subtilis* after 24 h of incubation respectively (Fig. 4(b)). The results were similar to the previous finding of Ruparelia *et al*. (2008) worked on bacterial sensitivity with nanoparticles against *E. coli* and *B. subtilis,* after 18 h (the IC_{50} values were 100 and 20 µg respectively)[51].

5.8 Conclusion

Heterogeneous catalyst with high surface area and porosity plays an important role in controlling catalytic activity and antimicrobial activity of the material. AgM (heterogeneous catalyst) synthesized via nanocasting method reported here has a very high surface area which gives maximum catalytic activity for 4-NP reduction reaction in the presence of $NaBH_4$ with a reaction rate of 2.43 min^{-1} corresponds to 0.2 g/L catalyst. The synthesized AgM shows enhanced rate for conversion of 4-NP to 4-AP as in compare with other published works in literature. The activation energy (E_a) of the catalytic reduction reaction has been measured (42.58 kJ mol^{-1}). The AgM structures are bigger than other reported once enabling them for easy separation and reuse. In addition to that nanocasted AgM has an efficient antimicrobial activity of silver particles against gram-negative (*E. coli*) and gram-positive bacteria (*B. subtilis*), which is an added advantage to it. Therefore, this work is worth practicing and commercialization for water body purification purposes.

Section-C: Bi-Metallic Monolithic System for Enhanced Catalytic and Antibacterial Activity

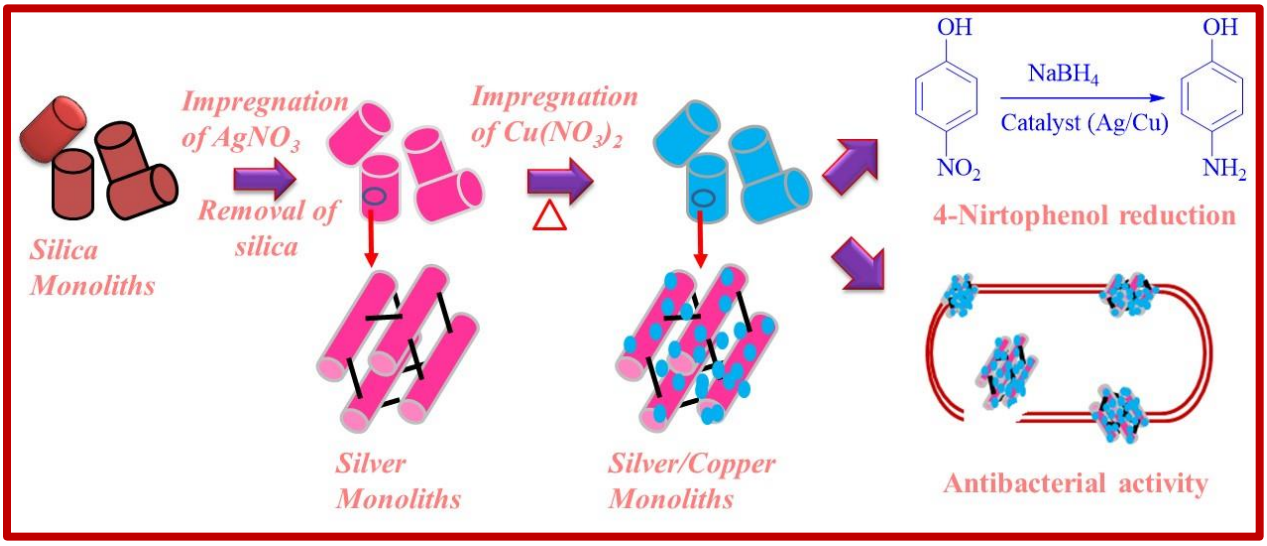

Combination of two or more metallic particles along with high surface area and porous structure exhibits enhanced catalytic as well as antibacterial activity. In this chapter, Ag-Cu bimetallic monoliths were synthesized by nanocasting method by strictly adjusting the molar ratio of Ag-Cu. This work is mainly focused on the effect of molar ratio (Ag:Cu) on surface area (14-110 m^2/g) and porous size of bimetallic monoliths, which has great influence on enhancement of catalytic and antimicrobial activity. The catalytic activity of bimetallic Ag-Cu monoliths was evaluated for the reduction of 4-nitrophenol (4-NP) to 4-aminophenol (4-AP) in the presence of excess $NaBH_4$. The reaction rate follows pseudo-first order for reduction of 4-NP with a reduction efficacy of ~95%. The effect of Ag:Cu molar ratio, and reaction conditions on the rate of reaction were investigated. In comparison with pristine Ag monometallic monoliths, bimetallic Ag-Cu monoliths exhibit high catalytic performance on the reduction of 4-NP. These heterogeneous catalysts were effortlessly recovered and reused (upto 8 cycles) after completion of catalytic reaction. As bimetallic Ag-Cu particles are well-known for antibacterial activity, so bactericidal properties of synthesized monoliths are tested against *E. coli* and *B. subtilis* bacteria by minimum inhibitory concentration method (MIC). The calculated IC_{50} (half maximum Inhibitory concentration) after 24 h of incubation, against *E. coli* and *B. subtilis* were 22.87 ± 0.015 and 23.33 ± 0.09 respectively.

5.9 Introduction

Manufacturing of several analgesic and antipyretic drugs needs aromatic amino compounds as a potent intermediate. These compounds are also used exceptionally as a photographic developer, anticorrosion-lubricant and hair-dyeing agent[52]. Thus, being a regular precursor material for aromatic amino compounds, a newer and economical method for catalytic hydrogenation of nitro-aromatic compound is always in demand. Also nitro aromatic compounds (like nitrophenols) are considered as most common organic pollutant in waste water introduced from pesticides, dyes, paper, pharmaceuticals and other chemical industries[53]. Nitrophenols has been considered as most toxic and hazardous pollutants by the US Environmental Protection Agency [54]. For removal of nitrophenols from water, an environment friendly system is required. Consequently, to convert these toxic pollutants into valuable amines, many research has been done on the synthesis of monometallic or bimetallic nanoparticles/ nanocomposites[55-59]. Even if metallic particles show good catalytic activity, but their applicability on a large scale was limited due to their high cost. To overcome this problem, bimetallic nanocomposites (two different metals bound to form one composite) are formed either in core-shell structure, alloys or mixture of two metals. Bimetallic nanocomposites are more attractive than individual metallic nanocomposites mostly because of enhanced catalytic properties and they exhibit different thermal, magnetic, electrical and optical properties due to synergistic or fine-tuning effects[60-62]. Bimetallic composites can be synthesized by reduction of two different metal ions at the same time in the presence/absence of surfactant/polymer [63] or straight reduction of one metal ion over the nuclei of other metal[64]. Based on different synthesis procedures, both alloy or core-shell structures can be synthesized. Some reported bimetallic combinations (like Ag-Cu, Ag-Au, Pd-Pt and Au-Pd) have applications in heterogeneous catalysis, fuel cell electro-catalysis and sensing[65].

Metallic elements like silver and copper are traditionally well known as bactericidal. The properties of these metal particles get amplified at nanoscale due to high surface area and volume ratio [66]. Metallic nanoparticles have a special potential to interact with microbial membrane, due to which they can be used as disinfectants for waste water treatment. Chen *et al*. have reported the synthesis of Cu-Ag core shell particles by chemical reduction of silver over commercial micrometric Cu particles to study the anti-oxidation and antibacterial properties[67]. Rousse *et al*. have studied the antibacterial properties of Cu-Ag bimetallic nanopowders using sonochemically synthesized Cu nanoparticles followed by coating of silver ions[68].

With regard to realistic applications as catalyst, porous materials became a hot topic for thorough study. Mesoporous metal nanoparticles as catalyst has advantage of very high surface area and large pore size distribution, which help in mass transfer and increase in number of active sites on the surface of nanomaterial. For catalytic function, numerous promising procedures can be used to synthesize mesoporous materials. Even though numerous papers have been published on synthesis of noble mesoporous metal composites, but hardly some are focused on bimetallic mesoporous monoliths like sliver with copper due to difficult and complex approach needed for the synthesis[69-71].

In this work, synthesis of mesoporous Ag-Cu bimetallic monoliths with varying molar ratio of Cu has been reported using previously synthesized silver monoliths. Synthesized porous Ag-Cu monoliths have been used as heterogeneous catalyst to study the catalytic reduction of nitroaromatic (4-NP) compound. Adding up to this, antibacterial activity against both gram positive and negative bacteria was also studied by minimal inhibitory concentration (MIC) using bimetallic monoliths.

5.10.1 Preparation of Ag-Cu Monolith

Detailed procedure for synthesis of silver monolith has been discussed in previous section. Cupric nitrate was used as precursor for Ag-Cu monolith synthesis. Cupric nitrate sol (in different molar ratios, which is defined in Table 1) along with a 0.1 M $NaBH_4$ was impregnated into silver monoliths in the presence of nitrogen atmosphere. Later, wet impregnated monoliths were dried for 10 h at 80 °C with a heating rate of 1 °C/min. Impregnation procedure was repeated for at least five times to get homogeneous impregnation of cupric solution into the pore of silver monoliths and to get solid Ag-Cu monoliths. At the time of drying, oxidation of Cu may result in formation of Cu_2O in a little amount on monolithic surface which is confirmed by UV-Vis spectroscopy and XRD analysis. Afterwards, composites of Ag-Cu monoliths were finally calcined at 200 °C for 6 h at the heating ramp of 1 °C /min.

5.10.2 Instrumentations

As synthesized Ag-Cu monoliths were characterized by various techniques; details of the techniques are given in **Chapter 1, section 1.9**

5.10.3 Antibacterial studies

The antibacterial effect of synthesized Ag-Cu monolith against *E. coli* and *B. Subtilis* was checked; detail procedure has been given in **Chapter 1, Section 1.10.2**

5.10.4 Catalytic reduction of nitro compound

The catalytic efficiency of synthesized Ag-Cu monolith for 4-NP to 4-AP was performed; detail procedure has been given in **Chapter 1, Section 1.10.3**

5.11 Results and discussion

5.11.1 Structural characterizations

According to IUPAC classification, all samples exhibited typical Langmuir type – IV isotherm (Fig. 5.13a). Table 5.3 displayed the textural properties of Ag-Cu monoliths (with different molar ratios) determined by N_2 –physisorption. The specific surface area of Ag-Cu monoliths regularly increases with the enhancement in molar ratio of Cu metal ions, which were calculated through multipoint BET equation. The data of pore size distribution specifies that Ag-Cu monoliths were mostly mesoporous in nature along with a small number of micropores as shown in Fig. 5.13b.

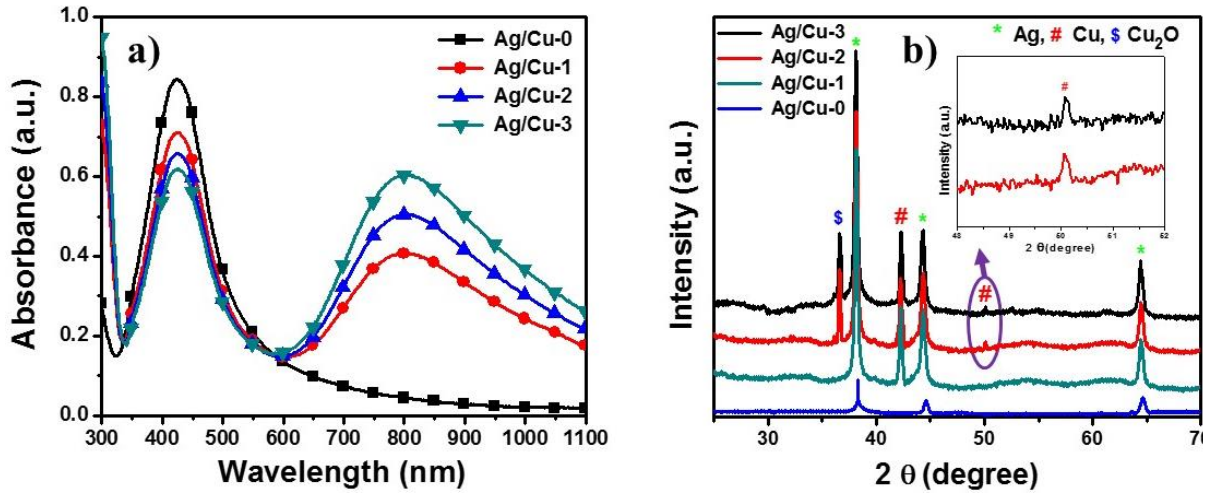

Fig. 5.14: (a) UV-visible spectra and (b) XRD pattern of Ag/Cu monoliths with different molar ratios.

Table 5.3: Textural properties of Ag-Cu monoliths

Monolith	Ratio (Ag:Cu)	S_{BET} ($m^2 g^{-1}$)	Mesopore diameter (nm)	Micropore diameter (nm)	Mesopore volume ($cm^3 g^{-1}$)	Micropore volume ($cm^3 g^{-1}$)
Ag/Cu-0	1:0	14	25.06	-	0.04	-
Ag/Cu-1	1:0.5	39	21.2	1.2	0.27	0.038
Ag/Cu-2	1:0.75	52	12.4	1	0.13	0.055
Ag/Cu-3	1:1	110	8.3	1.3	0.25	0.050

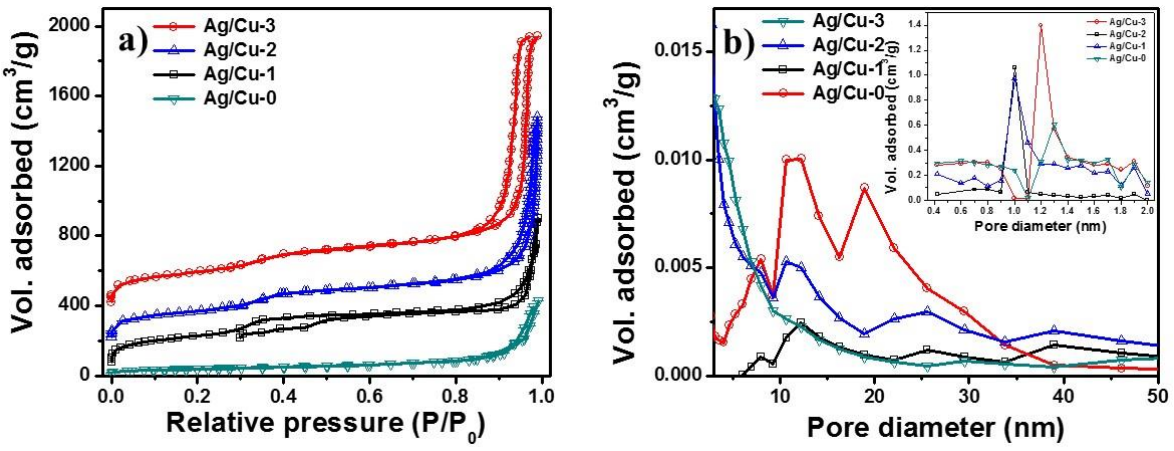

Fig. 5.13: (a) N_2 adsorption desorption isotherm and (b) mesopore distribution curves through BJH plot (inset contains micropore distribution curves through MP plot) for Ag/Cu monoliths with different molar ratios.

The UV-Visible spectra for Ag-Cu bimetallic monolith with different molar ratio (Fig. 5.14a) showed change in an absorption spectrum throughout the emergence of monometallic to bimetallic monolith. It is confirmed from literature, the peak at 424 nm was validated for Ag whereas peak at ~800 nm can be validated to Cu_2O [72, 73], which forms due to oxidation of Cu while heating/drying of Ag-Cu monoliths. Although no blue or red shift was observed with the change in molar ratio of Cu ions but change in intensity was noticed. In order to check the crystalline behavior of the synthesized Ag–Cu monoliths, X-ray diffraction measurements of the Ag-Cu monoliths (with different molar ratio) was carried out.

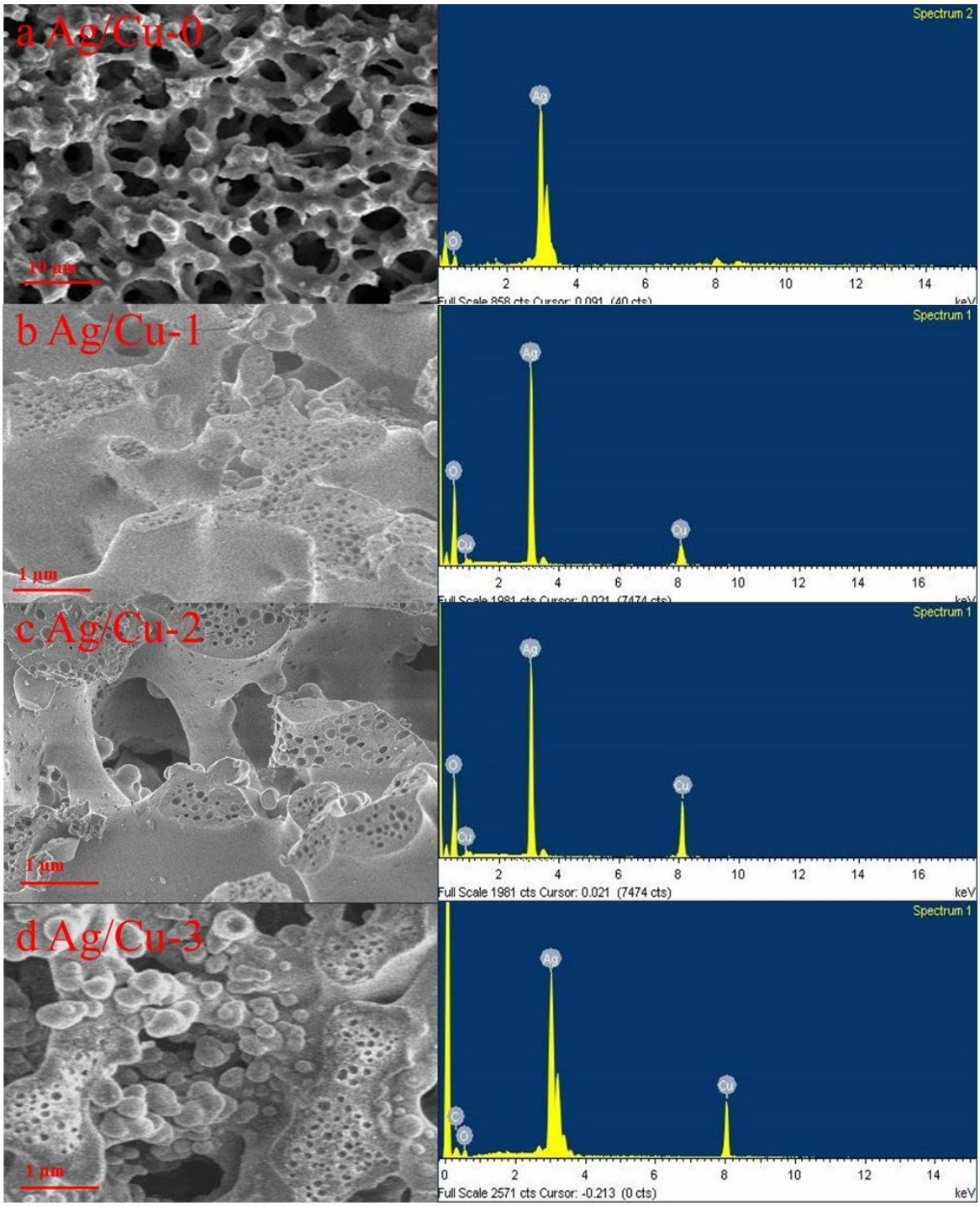

Fig. 5.15: SEM images and EDX spectrum for Ag/Cu monoliths with different molar ratios.

Fig. 5.14b clearly identify the crystal planes for both Cu and Ag. As shown in XRD pattern, three main characteristic diffraction peaks at 2Θ = 38.22, 44.34 and 64.36 corresponding to (111), (200) and (220) crystal planes of face centered cubic (fcc) phase for silver are observed (JCPDS card no. 4-783). Two characteristic diffraction peaks at 2Θ = 42.29 and 50.13 corresponding to (111) and (200) crystal planes of fcc phase for copper are observed (JCPDS card no. 4-836).

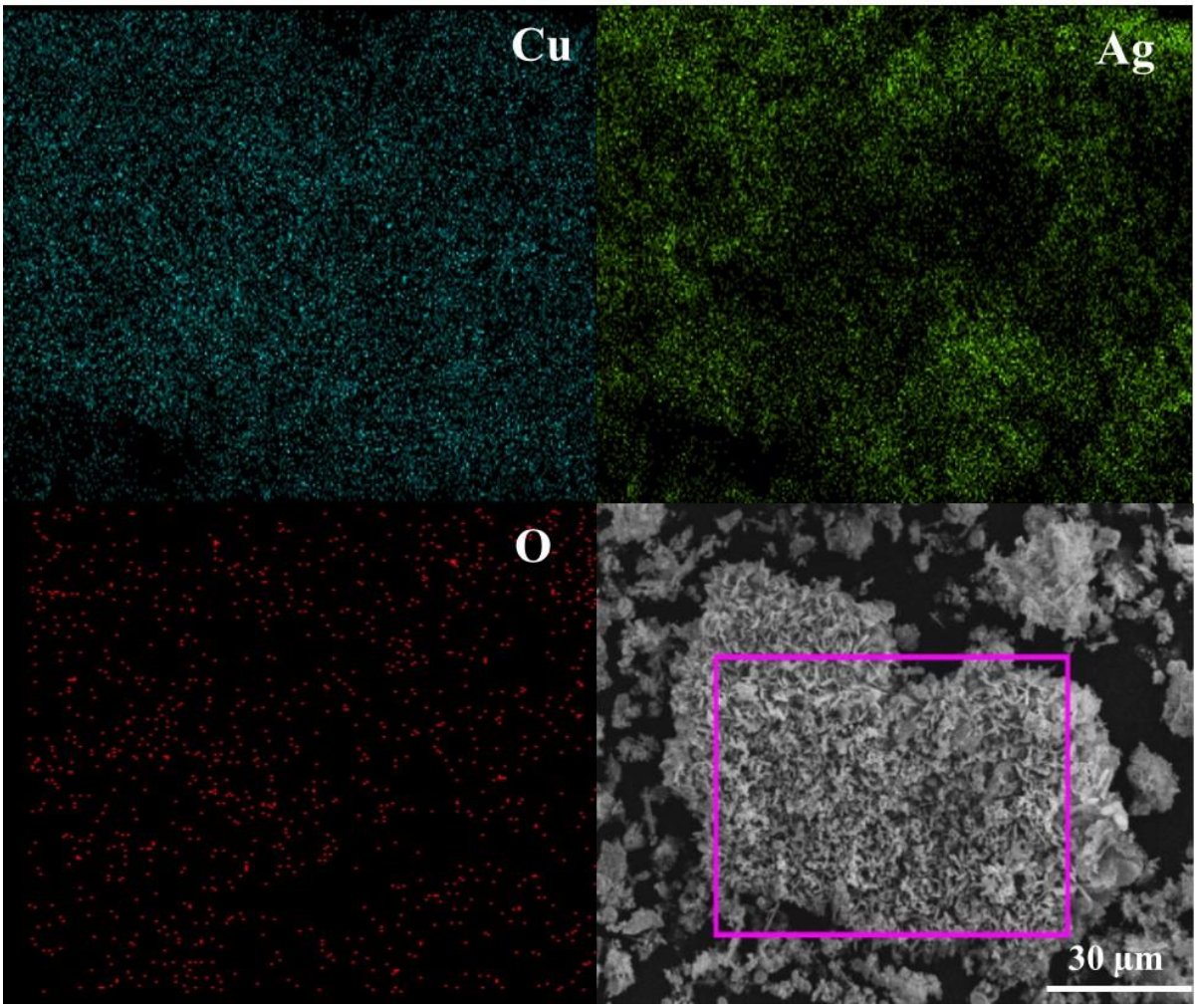

Fig. 5.16: SEM-EDS elemental mapping of Ag/Cu-3 bimetallic monolith.

A small peak of Cu_2O (111) was also found with increment of Cu molar ratio indicating a little oxidation of Cu. Surface micrographs (by SEM analysis) of Ag-Cu monoliths with different molar ratio are shown in Fig. 5.15. It can observe that the surface morphology and roughness of all samples are almost alike. But the pore size of all the monoliths are different which can be correlated through BJH pore distribution curve. It is also analyzed that with the increase of Cu molar ratio, surface area becomes high may be due to the aggregation of Cu particle. Further, EDS with elemental mapping was used to confirm the bimetallic structure and the distribution of Ag/Cu-3 monolith.

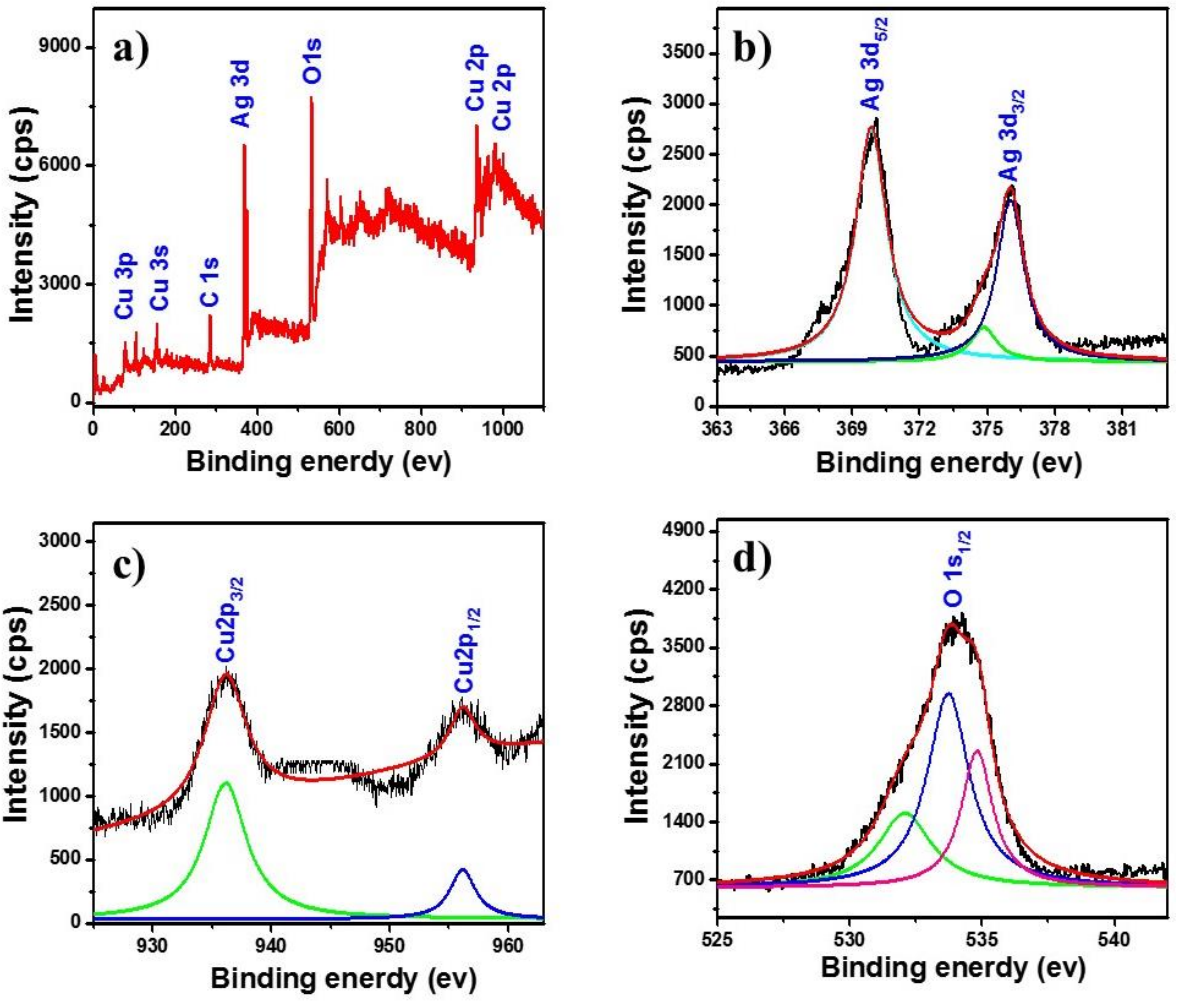

Fig. 5.17: (a) XPS spectra, (b) Ag 3d core level spectra, (c) Cu 2p core level spectra and (d) O 1s core level spectra for Ag/Cu-3 bimetallic monolith.

Fig. 5.16 shows the atoms of Ag and Cu have a homogeneous distribution. To find the elemental composition and oxidation states of Ag-Cu monolith, XPS of Ag/Cu-3 was performed. The XPS spectra showing the presence of Ag, Cu and O elemental composition in Fig. 5.17a.

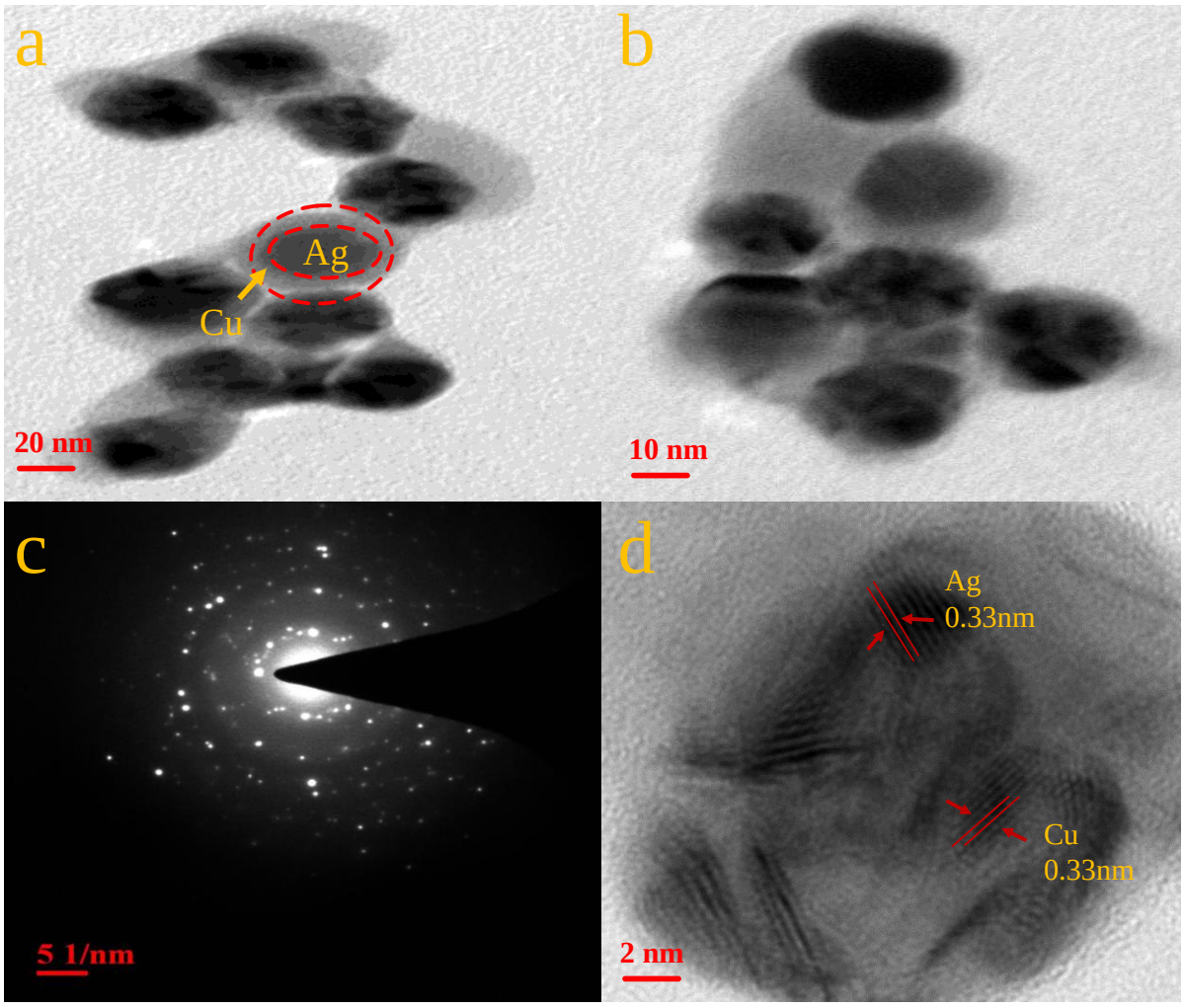

Fig. 5.18: HRTEM images of Ag/Cu-3 bimetallic monolith with (a) low, (b) high magnifications, (c) SAED pattern and (d) HRTEM image showing interface between Ag and Cu.

The core level of zero-valent Ag confirmed by binding energy values of two peaks, $Ag3d_{5/2}$ (367.6 eV) and $Ag3d_{3/2}$ (373.2 eV), as shown in Fig. 5.17b. Moreover, no traces of oxidation of Ag are measured due to the good symmetry and peak position. In the core level of Cu2p, two strong peaks for $Cu2p_{3/2}$ (932.3 eV) and $Cu2p_{1/2}$ (952.5 eV) associated with zero-

valent Cu are observed (Fig. 5.17c). Yet, most of the Cu present in Cu(0) state, slight shake-up lines are also observed due to Cu_2O at peak of 943.1 eV. So, a little amount of oxidation of Cu can be predicted which can be reliable with XRD. Besides, peak of $O1s_{1/2}$ with binding energy 531.7 eV corresponding to zero-valent O (Fig. 5.17d) may be the result from the adsorption of O from atmosphere at the time of heat treatment. TEM analysis was performed to investigate about the core shell structure formation in synthesized bimetallic monoliths. Fig. 5.18 (a-b) shows the core shell nature of Ag/Cu-3 monoliths. More fascinating thing is that in single shell, a few of Cu encapsulates more than one Ag particles. Fig. 5.18c shows the selected area electron diffraction (SAED) pattern of Ag/Cu-3 monoliths. SAED pattern supports the formation of bimetallic Ag-Cu monolith and confirms the fcc crystallite planes for Ag and Cu. HRTEM image presenting interface between Ag and Cu has been shown in Fig. 5.18d.

5.11.2 Antimicrobial activity:

Silver and copper has been known as antibacterial agent over decades. Due to low cytotoxicity and known antibacterial properties, researcher's interest has been renewed to work on silver and copper nanoparticle synthesis. The antibacterial effect of metallic nanoparticles has been widely studied but mechanism behind the action has not been interpreted fully.

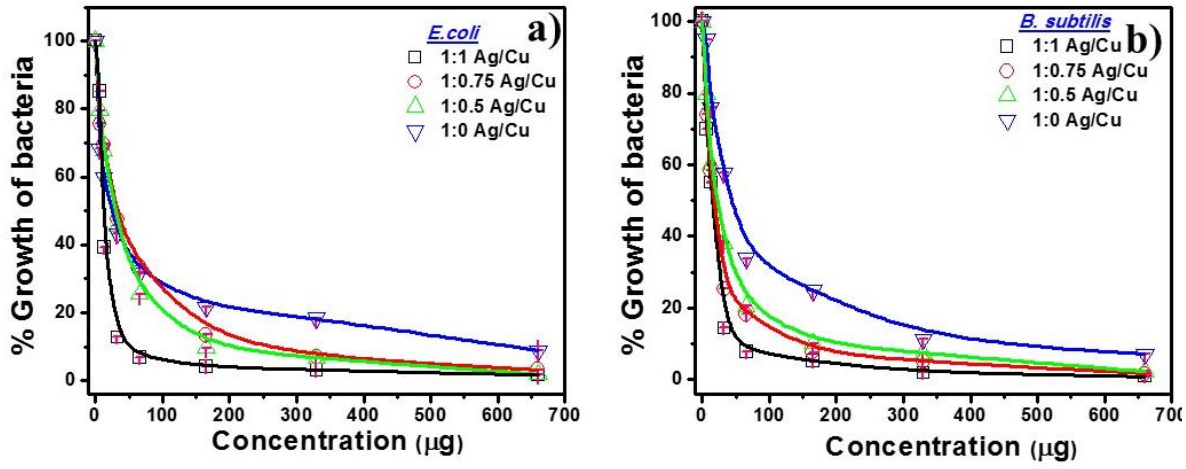

Fig. 5.19: Plots showing percentage of bacterial growth with respect to concentration of Ag/Cu monoliths with different molar ratios against gram negative (*E. coli*) and gram positive (*B. subtilis*) bacteria.

Maximum studies have emphasized that a direct contact between nanoparticles and bacteria results into bacterial cell-wall or membrane rupture and the ruptured cell wall permits the diffusion of nanoparticles inside the bacteria which enhances the changes in biomolecules. Metallic nanoparticles have antibacterial effect because of continuous release of generation of an oxidative stress by reactive oxygen species (ROS). Silver ions generates ROS and copper induces hydroxyl radicals which help them to rupture both DNA and proteins present in bacteria [74]. Recently, many researchers started working on synthesis of specific bimetallic nanoparticles (in core shell arrangement) with great chemical stability, very little cytotoxicity and long-term effect. Due to the core shell arrangement chance of oxidation of copper/silver is reduced. Here, in this work, in order to explore the antibacterial behavior of Ag-Cu bimetallic monoliths against *E. coli* and *B. subtilis*, a constant amount (0-660 µg) Ag-Cu bimetallic monolith was added to 5 ml of LB culture of bacteria. Fig. 5.19 shows the plot for percentage growth of bacteria (both *E. coli* and *B. subtilis*) vs. concentration of Ag-Cu bimetallic monolith. The measured IC_{50} (half maximum Inhibitory concentration) values of bimetallic monolith has been shown in Table 5.4.

Table 5.4: Antibacterial effect of Ag-Cu bimetallic monoliths against *E. coli* and *B. subtilis* measured by IC_{50}.

Monolith	***E. coli***	***B. subtilis***
Ag/Cu-0	40.85 ± 0.012	46.23 ± 0.1
Ag/Cu-1	38.056 ± 0.034	32.51 ± 0.07
Ag/Cu-2	33.86 ± 0.009	28.33 ± 0.16
Ag/Cu-3	22.87 ± 0.015	23.33 ± 0.09

5.11.3 Catalytic activity:

We are observant to the fact that water pollution by phenolic compounds is of massive anxiety. Among them nitrophenols have been considered as most rebellious and toxic pollutant which occurs in paper and pharmaceutical industrial waste water. Bimodal porous nature of synthesized monoliths fascinates us to explore their catalytic effect from the point of abatement of water pollution. Initially, freshly prepared $NaBH_4$ solution was added to a solution containing 4-NP and water mixture. The reduction process does not start at all but clear yellow color solution of 4-NP changes into greenish yellow color with the addition of $NaBH_4$, This change is

the resultant of increase in alkalinity (pH 9-10) of solution, due to this 4-NP transforms into nitrophenolate ions which remains stable if no catalyst is added. An instant change in color was observed after addition of catalyst in the solution and this change also recommends shift in the absorbance bands. Fig. 5.20(a-b) shows the UV-Vis spectra presenting the decrease in main peak for nitrophenolate ions at λ_{max} = 400 nm along with generation of another peak at λ_{max} = 295 nm indicating generation of 4-AP. The establishment of perfect isosbestic points at λ_{max} = 265 nm and 317 nm specifies that 4-AP is the only product formed. Generally, the 4-NP reduction reaction follows first order rate law kinetic model in order to quantify the reaction kinetics. Hence, the apparent reaction rate constant k values with respect to all synthesized catalysts were calculated from a linear plot between ln (C_t/C_0) and time (s) as shown in Fig. 5.20c and the rate constant (k) can be calculated according to Eq. 1

$$k = \frac{1}{t} \ln \frac{C_t}{C_0} \tag{5.3}$$

where C_0 and C_t are the initial and final concentration at time (t) of 4-NP respectively. Table 5.5 displays the apparent rate constant calculated from the logarithmic plot for all samples.

The catalytic activity and reduction rate follows in the order of Ag/Cu-3 > Ag/Cu-2 > Ag/Cu-1 > Ag/Cu-0. Due to the synergistic electronic effect, bimetallic composites have high electron density on surface by mean of electron transfer from one metallic state to other. When 4-NP interacts with Ag and Cu, bonding and anti-bonding interaction occurs as a result of overlapping between adsorbate state and metal state.

Moreover, bimetallic composites have stronger binding energy as compare to monometallic particles and attributed to strong binding energy bimetallic composites has faster reaction rate constant [75, 76]. Besides, high surface area and number of active sites are considered as other factors for the enhanced catalytic performance of Ag/Cu-3 monoliths.

Table 5.5: The rate constants and corresponding TOF values for the catalytic reduction of 4-NP over different Ag-Cu monoliths.

Monolith	S_{BET} (m^2 g^{-1})	Time (min)	Rate Constant (k, 10^{-2} s^{-1})	TOF (h^{-1})
Ag/Cu-0	14	20	0.46	37.5
Ag/Cu-1	39	15	2	52.1
Ag/Cu-2	52	10	3.7	80.6
Ag/Cu-3	110	8	5.5	116.6

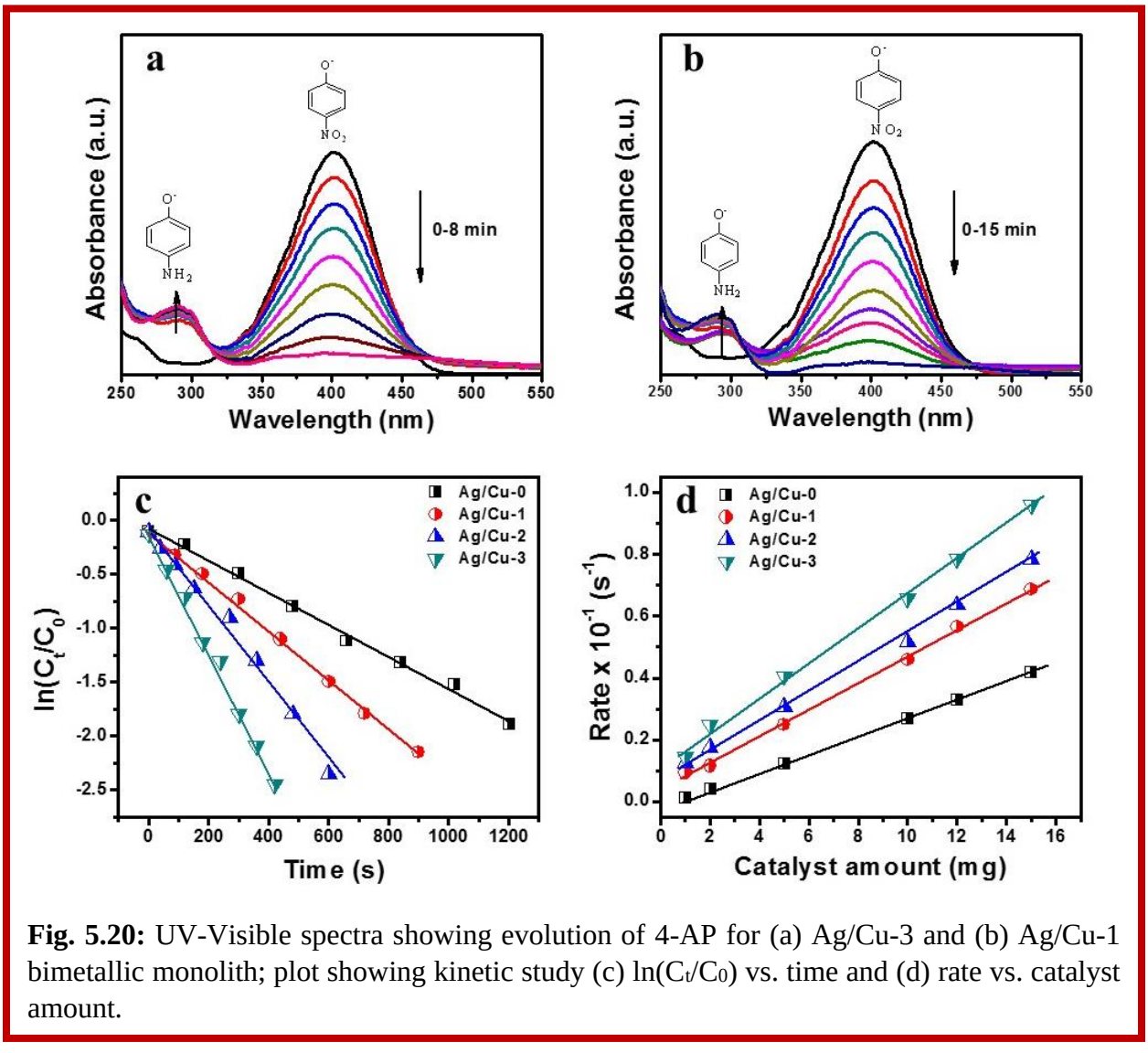

Fig. 5.20: UV-Visible spectra showing evolution of 4-AP for (a) Ag/Cu-3 and (b) Ag/Cu-1 bimetallic monolith; plot showing kinetic study (c) $\ln(C_t/C_0)$ vs. time and (d) rate vs. catalyst amount.

Here, a thought must be paid to a fact that, in all cases, no induction period (delay time t_0) was noticed and the reduction started immediately after addition of catalyst in the reaction mixture. This induction period is supposed to be the time needed for activation of catalyst in the

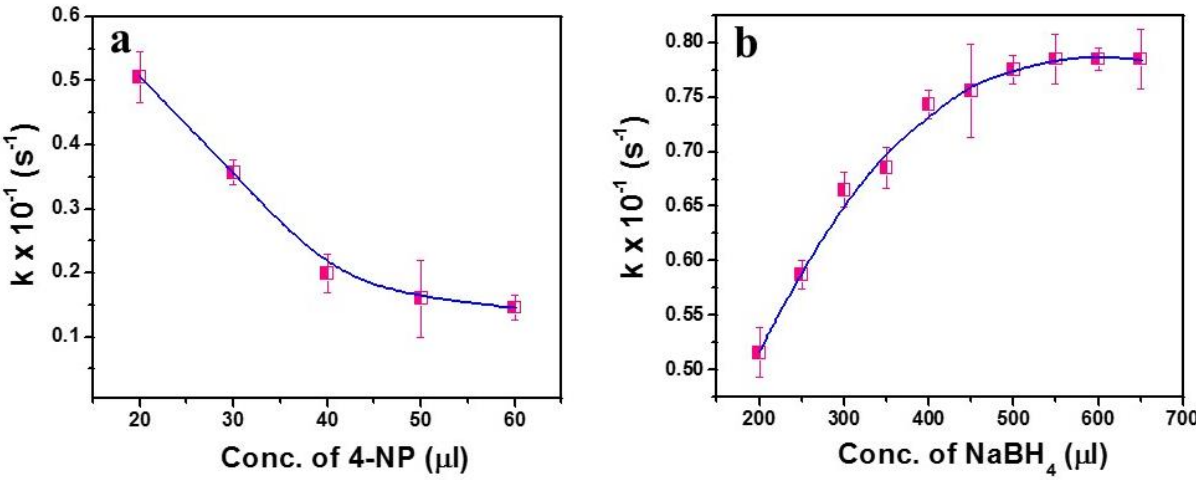

Fig. 5.21: Effect of concentration of (a) 4-NP and (b) $NaBH_4$ on rate of reduction reaction using Ag/Cu-3 monolith as catalyst [condition: dose of catalyst – 0.2g/L; agitation speed – 200 rpm; temperature – 25°C].

reaction mixture or for $NaBH_4$ to eliminate surface oxides on the catalyst. This is an opposite behavior to the other reported literature by some groups [77, 78]. In this case, hydrogen ions liberated from $NaBH_4$ purged out the air and stops the oxidation of 4-AP as all reactions were carried out in atmospheric conditions. Development of small bubbles on the surface of catalyst after addition of $NaBH_4$ helps in mixing of solution and provides optimum conditions for regular reaction to take place.

Amount of catalyst used for catalytic reduction also has a significant effect in controlling the rate of the reaction and to quantify this effect, amount of catalyst was altered keeping rest of the parameters constant. Rate of the reduction reaction escalates with simultaneous increase in catalyst amount. Rate vs. amount of catalyst plot is shown in Fig. 5.20d. Also, a connection between the concentration of either 4-NP or $NaBH_4$ and rate constant was acknowledged. Although keeping rest of the parameters constant, increase in concentration of 4-NP resulted in decrement in rate constant was observed (Fig. 5.21a) because high concentration of 4-NP fully occupied most of the surface of the catalyst and slowdowns the reaction whereas increase in

concentration of $NaBH_4$ results in escalation of rate (Fig. 5.21b). This report concludes that only H^- ions get absorbed and with more concentration of H^- ions on the surface of catalyst leads to enhancement of rate of reaction. But, above 500 µl concentration of $NaBH_4$ almost constant rate is observed due to the competitive adsorption of both 4-NP and $NaBH_4$ on the surface of Ag-Cu monoliths. Similar findings were detected by other research groups [27, 56, 79].

Turnover frequency:

For evaluating the catalytic efficiency of heterogeneous Ag-Cu monoliths, turnover number (TON) and turnover frequency (TOF) can be used [80]. TON is characteristically defined as the total number of reactant molecules passes through the catalytic cycle beforehand the catalyst gets inactivated.

$$TON = \frac{Number\ of\ \ reactant\ molecules}{Number\ of\ \ catalyst\ molecules} \times\ yield$$

$$TOF = \frac{TON}{Time}$$

TOF is characteristically defined as the total number of reactant molecules converted into desired product per unit time (s) per gram of Ag-Cu monoliths. Table 5.5 shows the catalytic efficiency with TOF of Ag-Cu monoliths.

Thermodynamic study:

Thermodynamic parameters (like activation energy) for catalytic reduction of 4-NP for all monoliths, were evaluated at various temperatures (283K, 288K, 293K and 298K). Non-linear increase in rate constant was observed by mean of increase in temperature (Fig. 5.22a). Activation energy (E_g) of 4-NP reduction reaction was calculated using Arrhenius equation:

$$\ln k = -\frac{E_a}{RT} + \ln A \qquad (5.4)$$

where, k is rate constant at temperature (T), A is absorbance and R is the molar gas constant. The calculated E_a using Ag-Cu bimetallic monolith as heterogeneous catalyst was found to be 82.7 KJ mol^{-1}. Thermodynamic parameters like enthalpy change (ΔH) and entropy change (ΔS) were also calculated (Table 5.6) and the reaction was found to be endothermic which is not related to the catalyst used because measured ΔH values were more than zero.

Table 5.6: Temperature dependent rate of 4-NP reduction using Ag/Cu-3 monoliths**.**

Temperature (K)	k (s^{-1}) × 10^{-2}	E_a (KJ mol^{-1})	ΔH (KJ mol^{-1})	ΔS (J mol^{-1} K^{-1})
283	2.4	82.7	11.2	45.12
288	3.6			
293	4.0			
298	4.9			

In comparison with other published works, the as synthesized Ag-Cu bimetallic monoliths showed a high rate for conversion of 4-NP to 4-AP (Table 5). Therefore, it could be considered that Ag-Cu bimetallic monoliths could be employed as alternative catalysts for the conversion of 4-NP to 4-AP at room temperature.

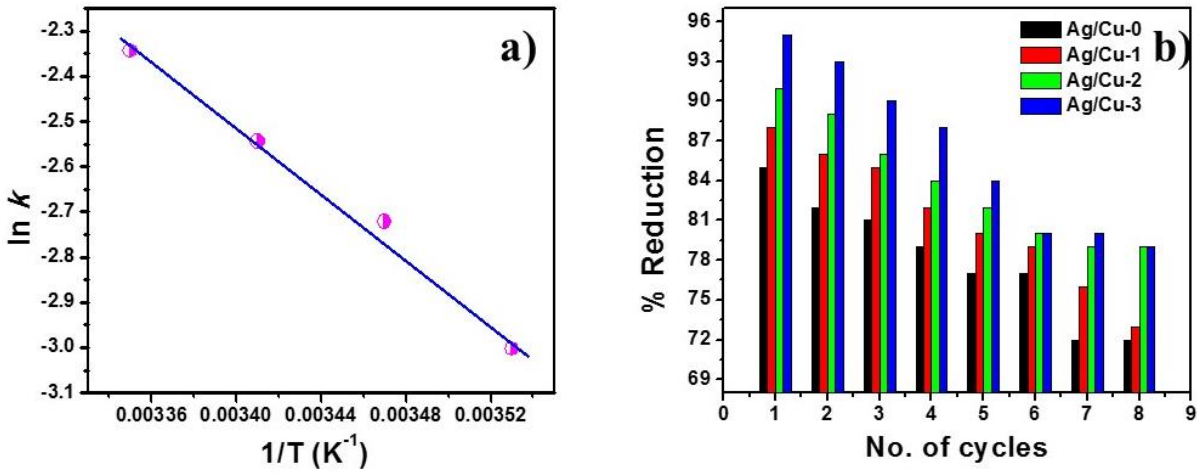

Fig. 5.22: Plots of (a) ln k vs. 1/T to define the thermodynamic parameters for Ag/Cu-3 monolith and (b) percentage reduction vs. no. of cycles to check the reusability of the catalyst.

Table 5.7: A comparative account for the catalytic activity of the catalyst for 4-NP reduction.

Catalyst	4-NP (M)	Rate (s^{-1})	Ea (KJ mol^{-1})	Reference
Cu- DENs	0.6×10^{-3}	2.43×10^{-2}	65.5	[56]
Ag- DENs		0.7×10^{-2}	45.7	
Au/PMMA	9×10^{-5}	7.9×10^{-3}	38	[57]
Au/g-C_3N_4	1×10^{-2}	0.6180×10^{-3}	-	[81]
Au-SPB	1×10^{-4}	2.301×10^{-4}	49	[82]
Ag/Cu-3	10^{-2}	5.23×10^{-2}	82.7	Current study

Reusability of catalyst:

To check the reusability of the catalysts in consecutive catalytic cycles, Ag-Cu bimetallic monoliths were reused at least 8 times for 4-NP reduction reaction. From Fig. 5.22b it is cleared that Ag-Cu bimetallic monoliths can directly be separated by filtration and the reduction rate was maintained over 60-75 % after 8 cycles.

5.12 Conclusion:

Mesoporous bimetallic Ag-Cu monoliths with a small amount of micropores were synthesized via nanocasting method. Of interest is that the synthesized monoliths showed effective bactericidal against *E. coli* and *B. Subtilis* and calculated IC_{50} using Ag/Cu-3 bimetallic monolith after 24 h of incubation were found to be 22.87 ± 0.015 and 23.33 ± 0.09 respectively. Furthermore, kinetic catalytic reduction reactions of 4-NP in the presence of bimetallic Ag-Cu monolith (with different molar ratio) by $NaBH_4$ were performed. Additionally, kinetic rate constant and activation energy were also evaluated to be $2\text{-}5.5\times10^{-2}$ (s^{-1}) and 82.7 KJ mol^{-1}. The catalyst efficiency was determined on the basis of TOF and recyclability. The new as-prepared mesoporous bimetallic Ag-Cu catalysts are stable, efficient, easy to prepare, and recyclable and thus have potential for industrial applications.

References

1. E. I. Alarcon, M. Griffith and K. I. Udekwu, *Springer*, 2015.
2. M. Mazur, *Electrochemistry Communications*, 2004, **6**, 400-403.
3. Z. T. Hu Yougen, Zhu Pengli, Liang Xianwen, Sun Rong, Wong Ching-Ping, *RSC Adv.*, 2015, **5**, 58-67.
4. N. G. Bastús, F. Merkoçi, J. Piella and V. Puntes, *Chemistry of Materials*, 2014, **26**, 2836-2846.
5. S. Basu, S. Pande, S. Jana, S. Bolisetty and T. Pal, *Langmuir : the ACS journal of surfaces and colloids*, 2008, **24**, 5562-5568.
6. S. Basu, S. Jana, S. Pande and T. Pal, *Journal of colloid and interface science*, 2008, **321**, 288-293.
7. A. Pal, S. Shah and S. Devi, *Colloids and Surfaces A: Physicochemical and Engineering Aspects*, 2007, **302**, 483-487.
8. Y. Xie, R. Ye and H. Liu, *Colloids and Surfaces A: Physicochemical and Engineering Aspects*, 2006, **279**, 175-178.
9. S. Panigrahi, S. Praharaj, S. Basu, S. K. Ghosh, S. Jana, S. Pande, T. Vo-Dinh, H. Jiang and T. Pal, *J Phys Chem B*, 2006, **110**, 13436-13444.
10. G. S. Kristl M., Kristl J., *Materials Express*, 2015, **5**, 359-366.
11. I. A. Wani, S. Khatoon, A. Ganguly, J. Ahmed, A. K. Ganguli and T. Ahmad, *Materials Research Bulletin*, 2010, **45**, 1033-1038.
12. M. Starowicz, B. Stypula and J. Banas, *Electrochemistry Communications*, 2006, **8**, 227-230.
13. H. R. Ghorbani, A. A. Safekordi, H. Attar and S. M. R. Sorkhabadi, *Chemical and Biochemical Engineering Quarterly*, 2011, **25**, 317-326.
14. W. Z. Zhang, X. L. Qiao, J. G. Chen and H. S. Wang, *Journal of colloid and interface science*, 2006, **302**, 370-373.
15. Z. Zhang, C. Shao, Y. Sun, J. Mu, M. Zhang, P. Zhang, Z. Guo, P. Liang, C. Wang and Y. Liu, *J. Mater. Chem.*, 2012, **22**, 1387-1395.
16. R. Eising, A. M. Signori, S. Fort and J. B. Domingos, *Langmuir : the ACS journal of surfaces and colloids*, 2011, **27**, 11860-11866.

17. S. Yamamoto, Y. Kaneo, T. Ishizu, Y. Yamaguchi and H. Haraguchi, *J Drug Deliv Sci Tec*, 2013, **23**, 591-596.
18. E. de Souza Costa-Junior, M. M. Pereira and H. S. Mansur, *Journal of materials science. Materials in medicine*, 2009, **20**, 553-561.
19. A. M. Alkilany, A. I. Bani Yaseen and M. H. Kailani, *Journal of Nanomaterials*, 2015, **2015**, 1-9.
20. L. Q. Zhao X. H., Ma X. M., Xiong Z., Quan F. Y., Xia Y. Z., *RSC Advances*, 2015, **5**, 49534-49540.
21. Z. Y. Zhou W., Liang Y., Feng H. X., Zhou H., *RSC Advances*, 2015, **5**, 50505-50511.
22. F. F. Heuschmid, S. Schneider, P. Schuster, B. Lauer and B. van Ravenzwaay, *Food Chem Toxicol*, 2013, **51**, S14-S23.
23. J. W. Krumpfer, T. Schuster, M. Klapper and K. Mullen, *Nano Today*, 2013, **8**, 417-438.
24. A. S. Karakoti, S. Das, S. Thevuthasan and S. Seal, *Angew Chem Int Edit*, 2011, **50**, 1980-1994.
25. E. S. Abdel-Halim, H. H. Alanazi and S. S. Al-Deyab, *Int J Biol Macromol*, 2015, **75**, 467-473.
26. A. H. K. Tyagi, A. Kumar and M. Aslam, PVA stabilized gold nanoparticles using ascorbic acid as a reducing agent, 2011.
27. S. Saha, A. Pal, S. Kundu, S. Basu and T. Pal, *Langmuir : the ACS journal of surfaces and colloids*, 2010, **26**, 2885-2893.
28. S. Panigrahi, S. Basu, S. Praharaj, S. Pande, S. Jana, A. Pal, S. K. Ghosh and T. Pal, *The Journal of Physical Chemistry C*, 2007, **111**, 4596-4605.
29. S. Jana, S. Ghosh, S. Nath, S. Pande, S. Praharaj, S. Panigrahi, S. Basu, T. Endo and T. Pal, *Applied Catalysis A: General*, 2006, **313**, 41-48.
30. Y. P. Li, H. B. Cao, C. M. Liu and Y. Zhang, *Journal of hazardous materials*, 2007, **148**, 158-163.
31. V. K. Gupta, N. Atar, M. L. Yola, Z. Üstündağ and L. Uzun, *Water research*, 2014, **48**, 210-217.
32. S. Khan, C. Chao, M. Waqas, H. P. H. Arp and Y.-G. Zhu, *Environmental science & technology*, 2013, **47**, 8624-8632.

33. A. Mittal, J. Mittal, A. Malviya and V. Gupta, *Journal of colloid and interface science*, 2009, **340**, 16-26.
34. M. Armbrüster, R. Schlögl and Y. Grin, *Science and technology of advanced materials*, 2014, **15**, 034803.
35. N. Pradhan, A. Pal and T. Pal, *Colloids and Surfaces A: Physicochemical and Engineering Aspects*, 2002, **196**, 247-257.
36. A. Fedorczyk, J. Ratajczak, O. Kuzmych and M. Skompska, *Journal of Solid State Electrochemistry*, 2015, **9**, 2849-2858.
37. S. Tang, S. Vongehr and X. Meng, *The Journal of Physical Chemistry C*, 2009, **114**, 977-982.
38. G. A. Naikoo, R. A. Dar and F. Khan, *J. Mater. Chem. A*, 2014, **2**, 11792-11798.
39. B. Y. Xia, W. T. Ng, H. B. Wu, X. Wang and X. W. D. Lou, *Angewandte Chemie*, 2012, **124**, 7325-7328.
40. R. A. Dar, G. A. Naikoo, P. K. Kalambate, L. Giri, F. Khan, S. P. Karna and A. K. Srivastava, *Electrochimica Acta*, 2015, **163**, 196-203.
41. Y. Wei, J. Liu, Z. Zhao, A. Duan, G. Jiang, C. Xu, J. Gao, H. He and X. Wang, *Energy & Environmental Science*, 2011, **4**, 2959.
42. K. J. Kim, W. S. Sung, B. K. Suh, S. K. Moon, J. S. Choi, J. G. Kim and D. G. Lee, *Biometals : an international journal on the role of metal ions in biology, biochemistry, and medicine*, 2009, **22**, 235-242.
43. I. Subhankari and P. Nayak, *World Journal of Nano Science & Technology*, 2013, **2**, 10-13.
44. M. U. D. Sheikh, G. A. Naikoo, M. Thomas, M. Bano and F. Khan, *Journal of Sol-Gel Science and Technology*, 2015, **76**, 572-581.
45. F. Khan and S. Mann, *The Journal of Physical Chemistry C*, 2009, **113**, 19871-19874.
46. Y. Tian, J. Qi, W. Zhang, Q. Cai and X. Jiang, *ACS applied materials & interfaces*, 2014, **6**, 12038-12045.
47. N. L. Netzer, R. Gunawidjaja, M. Hiemstra, Q. Zhang, V. V. Tsukruk and C. Jiang, *ACS nano*, 2009, **3**, 1795-1802.
48. J.-H. Smått, F. M. Sayler, A. J. Grano and M. G. Bakker, *Advanced Engineering Materials*, 2012, **14**, 1059-1073.

49. H. Yang, Y. Liu, Q. Shen, L. Chen, W. You, X. Wang and J. Sheng, *Journal of Materials Chemistry*, 2012, **22**, 24132.
50. P. Guo, L. Tang, J. Tang, G. Zeng, B. Huang, H. Dong, Y. Zhang, Y. Zhou, Y. Deng, L. Ma and S. Tan, *Journal of colloid and interface science*, 2016, **469**, 78-85.
51. M. Sharma, A. Mishra, V. Kumar and S. Basu, *Nano*, 2016, **11**, 1650046.
52. Y. Du, H. Chen, R. Chen and N. Xu, *Applied Catalysis A: General*, 2004, **277**, 259-264.
53. Y.-P. Li, H.-B. Cao, C.-M. Liu and Y. Zhang, *Journal of hazardous materials*, 2007, **148**, 158-163.
54. Z. V. Feng, J. L. Lyon, J. S. Croley, R. M. Crooks, D. A. V. Bout and K. J. Stevenson, *J. Chem. Educ*, 2009, **86**, 368.
55. N. Pradhan, A. Pal and T. Pal, *Langmuir : the ACS journal of surfaces and colloids*, 2001, **17**, 1800-1802.
56. M. Nemanashi and R. Meijboom, *Journal of colloid and interface science*, 2013, **389**, 260-267.
57. K. Kuroda, T. Ishida and M. Haruta, *Journal of Molecular Catalysis A: Chemical*, 2009, **298**, 7-11.
58. M. Sharma, A. Mishra, V. Kumar and S. Basu, *Nano*, 2016, **11**, 1-10.
59. A. Mehta, M. Sharma, A. Kumar and S. Basu, *Nano*, 2016, **11**, 1-9.
60. T. P. Ang and W. S. Chin, *The journal of physical chemistry. B*, 2005, **109**, 22228-22236.
61. J. Zhao, D. Zhang and X. Zhang, *Surface and Interface Analysis*, 2015, **47**, 529-534.
62. Z. Khan and A. Y. Obaid, *RSC Adv.*, 2016, **6**, 29116-29126.
63. N. N. Kariuki, J. Luo, M. M. Maye, S. A. Hassan, T. Menard, H. R. Naslund, Y. Lin, C. Wang, M. H. Engelhard and C. J. Zhong, *Langmuir : the ACS journal of surfaces and colloids*, 2004, **20**, 11240-11246.
64. L. Rivas, S. Sanchez-Cortes, J. V. García-Ramos and G. Morcillo, *Langmuir : the ACS journal of surfaces and colloids*, 2000, **16**, 9722-9728.
65. I. Najdovski, P. R. Selvakannan, S. K. Bhargava and A. P. O'Mullane, *Nanoscale*, 2012, **4**, 6298-6306.
66. K.-Y. Yoon, J. Hoon Byeon, J.-H. Park and J. Hwang, *Science of The Total Environment*, 2007, **373**, 572-575.

67. K.-t. Chen, D. Ray, Y.-h. Peng and Y.-C. Hsu, *Current Applied Physics*, 2013, **13**, 1496-1501.
68. C. Rousse, J. Josse, V. Mancier, S. Levi, S. C. Gangloff and P. Fricoteaux, *RSC Advances*, 2016, **6**, 50933-50940.
69. D. Wang, Q. Peng and Y. Li, *Nano Research*, 2010, **3**, 574-580.
70. R. Hao, R. Xing, Z. Xu, Y. Hou, S. Gao and S. Sun, *Adv Mater*, 2010, **22**, 2729-2742.
71. A. Taguchi and F. Schuth, *Microporous and Mesoporous Materials*, 2005, **77**, 1-45.
72. H. R. Nikabadi, N. Shahtahmasebi, M. R. Rokn-Abadi, M. Karimipour and M. M. B. Mohagheghi, *B Mater Sci*, 2014, **37**, 527-532.
73. A. A. Dubale, C.-J. Pan, A. G. Tamirat, H.-M. Chen, W.-N. Su, C.-H. Chen, J. Rick, D. W. Ayele, B. A. Aragaw, J.-F. Lee, Y.-W. Yang and B.-J. Hwang, *J. Mater. Chem. A*, 2015, **3**, 12482-12499.
74. C. Rousse, J. Josse, V. Mancier, S. Levi, S. C. Gangloff and P. Fricoteaux, *RSC Adv.*, 2016, **6**, 50933-50940.
75. W. Wu, M. Lei, S. Yang, L. Zhou, L. Liu, X. Xiao, C. Jiang and V. A. L. Roy, *J. Mater. Chem. A*, 2015, **3**, 3450-3455.
76. F. Zaera, *Chemical Society reviews*, 2013, **42**, 2746-2762.
77. Y. Mei, Y. Lu, F. Polzer, M. Ballauff and M. Drechsler, *Chemistry of Materials*, 2007, **19**, 1062-1069.
78. Y. Mei, G. Sharma, Y. Lu, M. Ballauff, M. Drechsler, T. Irrgang and R. Kempe, *Langmuir : the ACS journal of surfaces and colloids*, 2005, **21**, 12229-12234.
79. S. Wunder, F. Polzer, Y. Lu, Y. Mei and M. Ballauff, *The Journal of Physical Chemistry C*, 2010, **114**, 8814-8820.
80. H. Wu, Z. Liu, X. Wang, B. Zhao, J. Zhang and C. Li, *Journal of colloid and interface science*, 2006, **302**, 142-148.
81. Y. S. Fu, T. Huang, B. Q. Jia, J. W. Zhu and X. Wang, *Appl Catal B-Environ*, 2017, **202**, 430-437.
82. S. Wunder, Y. Lu, M. Albrecht and M. Ballauff, *ACS Catalysis*, 2011, **1**, 908-916.